



**HAL**  
open science

## Remotely powered and readable sensors

Romain Alcesilas

► **To cite this version:**

Romain Alcesilas. Remotely powered and readable sensors. Optics / Photonics. Université Grenoble Alpes [2020-..], 2024. English. NNT : 2024GRALT007 . tel-04584876

**HAL Id: tel-04584876**

**<https://theses.hal.science/tel-04584876>**

Submitted on 23 May 2024

**HAL** is a multi-disciplinary open access archive for the deposit and dissemination of scientific research documents, whether they are published or not. The documents may come from teaching and research institutions in France or abroad, or from public or private research centers.

L'archive ouverte pluridisciplinaire **HAL**, est destinée au dépôt et à la diffusion de documents scientifiques de niveau recherche, publiés ou non, émanant des établissements d'enseignement et de recherche français ou étrangers, des laboratoires publics ou privés.

THÈSE

Pour obtenir le grade de

**DOCTEUR DE L'UNIVERSITÉ GRENOBLE ALPES**

École doctorale : EEATS - Electronique, Electrotechnique, Automatique, Traitement du Signal (EEATS)

Spécialité : Optique et Radiofréquences

Unité de recherche : Laboratoire d'Electronique et de Technologie de l'Information (LETI)

**Capteurs télé-alimentés et interrogeables à distance**

**Remotely powered and readable sensors**

Présentée par :

**Romain ALCESILAS**

Direction de thèse :

**Christophe DELAVEAUD**  
Directeur de recherche, CEA-LETI

Directeur de thèse

**Patrice REY**  
CEA

Co-encadrant de thèse

**Camille JOUVAUD**  
CEA

Co-encadrante de thèse

**Marc SANSA PERNA**  
Ingénieur Docteur, CEA - LETI

Co-encadrant de thèse

Rapporteurs :

**Hervé AUBERT**  
PROFESSEUR DES UNIVERSITES, TOULOUSE INP

**Jaume VERD MARTORELL**  
ASSOCIATE PROFESSOR, Universitat de les Illes Balears

Thèse soutenue publiquement le **5 février 2024**, devant le jury composé de :

**Skandar BASROUR,**  
PROFESSEUR DES UNIVERSITES, UNIVERSITE GRENOBLE  
ALPES

Président

**Christophe DELAVEAUD,**  
DIRECTEUR DE RECHERCHE, CEA CENTRE DE GRENOBLE

Directeur de thèse

**Hervé AUBERT,**  
PROFESSEUR DES UNIVERSITES, TOULOUSE INP

Rapporteur

**Jaume VERD MARTORELL,**  
ASSOCIATE PROFESSOR, Universitat de les Illes Balears

Rapporteur

**Bernard LEGRAND,**  
DIRECTEUR DE RECHERCHE, CNRS DELEGATION OCCITANIE  
OUEST

Examineur

**Gaëlle LISSORGUES,**  
PROFESSEURE DES UNIVERSITES, UNIVERSITE GUSTAVE  
EIFFEL

Examinatrice

Invités :

**Rachid JAOUI**  
Direction générale de l'armement





# Contents

Table of contents . . . . .	3
<b>Introduction</b>	<b>1</b>
<b>1 State of the art of passive wireless sensors</b>	<b>4</b>
1.1 General introduction . . . . .	6
1.2 State of the art of passive wireless sensors . . . . .	7
1.2.1 Inductive coupling sensors . . . . .	7
1.2.2 Wireless sensors based on acoustic waves . . . . .	9
1.2.3 Electromagnetic transduction-based wireless sensors . . . . .	11
1.3 Definitions and general information about antennas . . . . .	13
1.3.1 Working principle of an antenna . . . . .	13
1.3.2 Equivalent electrical model of an antenna . . . . .	13
1.3.3 Antenna gain and directivity . . . . .	15
1.3.4 Radiation pattern . . . . .	16
1.3.5 Radar Cross-Section and Radar Equation . . . . .	17
1.3.6 Antenna miniaturization and impact on its quality factor . . . . .	18
1.3.7 Printed antenna . . . . .	20
1.3.8 Antenna materials for harsh environments . . . . .	21
1.4 Introduction to MEMS sensors . . . . .	21
1.4.1 MEMS technology . . . . .	21
1.4.2 Microfabrication process . . . . .	22
1.4.3 Working principle of capacitive pressure sensors . . . . .	24
1.5 MEMS-based passive wireless sensors . . . . .	24
1.5.1 MEMS positioning on the antenna . . . . .	25
1.5.2 Impact of the MEMS on the antenna . . . . .	25
1.5.3 Choice of the resonance frequency of the antenna . . . . .	26
1.5.4 Main parameters of wireless passive sensors . . . . .	26
1.6 Conclusion . . . . .	27
References . . . . .	28
<b>2 MEMS design and integration with the antenna</b>	<b>33</b>
2.1 Introduction . . . . .	35
2.2 Strategy for the MEMS design . . . . .	35
2.3 MEMS geometry . . . . .	36
2.4 Design of the MEMS . . . . .	37
2.4.1 Methodology . . . . .	37
2.4.2 Modeling of the MEMS . . . . .	37
2.4.3 Determination of the MEMS dimensions . . . . .	39
2.4.4 Validation of the model . . . . .	40
2.5 Microfabrication process and masks designs . . . . .	42
2.5.1 Process flow . . . . .	42

## Table of contents

---

2.5.2	MEMS designs	45
2.6	Finite element simulations of the MEMS	46
2.6.1	De-embedding and ABCD matrixes	46
2.6.2	Simulated structures of MEMS	48
2.6.3	Dimensioning of the CPW lines	51
2.6.4	Properties of the lines	52
2.6.5	Conclusion	56
2.7	Integration with the antenna and impact on the performances	56
2.7.1	Impact of the antenna structural mode	56
2.7.2	Impact of antenna size/quality factor	56
2.7.3	Impact of the resistance of the MEMS on the sensitivity	59
2.7.4	Impact of the wire-bonding	59
2.7.5	Analysis of an enhanced version of the sensor	61
2.7.6	Conclusion on the optimization of the performance of the sensor	62
2.8	Conclusion	63
	References	63
<b>3</b>	<b>MEMS characterization</b>	<b>65</b>
3.1	Introduction	66
3.2	In-line metrology	66
3.2.1	Etching of the hole of the reference sensors	67
3.2.2	Surface defects of the deposited metal	69
3.2.3	Synthesis of the in-line metrology	69
3.3	Electrical characterization of materials	70
3.3.1	Sheet resistance of conductors (Van der Pauw)	70
3.3.2	Contact resistance between two conductors (CBKR)	72
3.3.3	Over-etching and continuity of the metal	73
3.3.4	Conclusion	74
3.4	Changes made to the process flow	74
3.4.1	Verification of the metal layer	74
3.4.2	Etching of membrane to create reference MEMS	75
3.5	MEMS characterization procedure	76
3.5.1	RF characterization at atmospheric pressure	76
3.5.2	RF characterization under vacuum	81
3.5.3	Measurement of the membrane deflection	83
3.6	Conclusion	83
<b>4</b>	<b>Antenna design and sensor characterization</b>	<b>87</b>
4.1	Introduction	88
4.2	Sensor design	88
4.2.1	MEMS selection criteria	88
4.2.2	Antenna design and simulations	89
4.2.3	Summary of the properties of the antennas	95
4.3	Frequency response of the sensors in anechoic chamber	96
4.3.1	Generalities about characterization in anechoic chamber	96
4.3.2	Algorithm of signal processing	97
4.3.3	Frequency response of the sensors	98
4.4	Pressure response of the sensors in anechoic chamber	100
4.4.1	Measurement setup in anechoic chamber	100
4.4.2	Frequency response of the vacuum chamber	100
4.4.3	Modification of the time-gating algorithm to extract the pressure response	101

---

4.4.4	Analysis of the raw measurements . . . . .	102
4.4.5	Pressure response of the sensors . . . . .	104
4.4.6	Estimation of the reading range . . . . .	108
4.4.7	Estimation of the resolution . . . . .	109
4.5	Conclusion . . . . .	109
<b>5</b>	<b>Wireless interrogation of resonant MEMS</b>	<b>113</b>
5.1	Introduction . . . . .	115
5.2	General principle and interest for wireless measurement . . . . .	115
5.2.1	Reading in real environment and clutter isolation issue . . . . .	115
5.2.2	General principle . . . . .	116
5.3	Complete theoretical model . . . . .	117
5.3.1	Incident signal and voltage at the MEMS terminals . . . . .	118
5.3.2	Membrane mechanical resonance and actuation . . . . .	120
5.3.3	Equivalent capacitance of the MEMS and reflection coefficient . . . . .	124
5.3.4	Variation of Radar Cross Section . . . . .	125
5.3.5	Shape of the backpropagated signal . . . . .	126
5.3.6	On the necessity to calculate by recurrence . . . . .	126
5.3.7	Conclusion on the complete model . . . . .	127
5.4	Linearized model for the co-design . . . . .	127
5.4.1	Approximations used . . . . .	127
5.4.2	Simplification and linearization of the model . . . . .	128
5.5	Analysis of the models . . . . .	130
5.5.1	Analysis of the equation of the signal received . . . . .	130
5.5.2	Interrogation of multiple MEMS on one antenna . . . . .	131
5.5.3	Amplitude of the peaks in the frequency spectrum . . . . .	132
5.6	Example of numerical applications of the models . . . . .	132
5.6.1	Geometries used for this analysis . . . . .	132
5.6.2	Validation of the voltage on the antenna . . . . .	134
5.6.3	Validation of the linear model . . . . .	134
5.6.4	Example of a received signal . . . . .	135
5.6.5	Choice of the interrogation frequency . . . . .	135
5.7	Measurement of the resonance of the MEMS . . . . .	137
5.7.1	Resonance frequency and pressure . . . . .	137
5.7.2	Quality factor of the MEMS . . . . .	138
5.7.3	MEMS resonance and intermodulation . . . . .	140
5.7.4	Conclusion on the measurements . . . . .	140
5.8	Conclusion . . . . .	142
	<b>Conclusion and perspectives</b>	<b>145</b>
	<b>Table of figures</b>	<b>148</b>
	<b>List of tables</b>	<b>157</b>
<b>A</b>	<b>Appendix 1 : Python codes</b>	<b>159</b>
A.1	Time-gating algorithm for the frequency response . . . . .	160
A.2	Time-gating algorithm for the pressure response . . . . .	160

---



# Introduction

With the advent of the *Fourth Industrial Revolution*, or *Industry 4.0*, where billions of objects are connected thanks to RF communications, microelectronics or artificial intelligence, consumption is a key factor in the development of new devices. This is even more the case with the challenges of climate change. In this new paradigm, data has never been more important, especially when it comes to sensing information about the outside world. These new issues related to the Internet of Things require the development of new types of sensors with very low power consumption, and where computing power is centralized.

Sensors are the eyes, ears, and touch of electronic devices, allowing them to perceive and interact with the world around them. From smartphones to self-driving cars, sensors gather data about everything from temperature and light to motion and proximity. This data empowers devices to adapt, optimize, and enhance their functionality, making them more intuitive, efficient, and user-friendly.

In recent years, there has been increasing demand in sensors and actuators designed to function effectively in harsh environmental conditions, including high temperatures, extreme pressures, and remote or inaccessible environments. This heightened interest has been largely driven by their critical roles in military and industrial applications, such as clean-room instrumentation and aeronautical systems. Using a cable to connect the sensor to the data processing unit can be challenging, or even impossible in certain situations. In such cases, it becomes essential to opt for wireless measurement acquisition, especially when dealing with high temperatures where the use of electronics or batteries could potentially harm the sensor.

Micro-Electro-Mechanical Systems (MEMS)-based sensors have revolutionized the field of sensor technology by offering a remarkable level of adaptability and robustness, making them highly suitable for operation in harsh and challenging environments. Their miniaturized design, which incorporates mechanical and electronic components on a single microchip, can be designed to withstand extreme conditions. Coupled to an antenna, they offer a way to create passive wireless sensors which are very suitable for harsh environments applications.

The measurement must then be performed by a totally passive system, powered by an incident electromagnetic wave. These components operate in the microwave frequency range, between 300 MHz and 30 GHz. The sensor will then "send back" a part of the signal, which will be used to acquire the measurement. By connecting directly the sensor to the antenna, there are not any CMOS electronics, and the only high-temperature constraints are those linked to the materials used for the antenna and the sensor. As a result, higher operating temperatures can be achieved (>500°C, or even higher with the right choice of materials) which increases the range of applications reachable.

When a MEMS sensor is combined with an antenna (which can be miniature), we have a technology which merge low-cost and high performances, which seems promising to work in harsh environments, and more specifically in high temperatures. It can be adapted to different physical quantity to measure and with different transduction principle such as resistive or capacitive. The computing power and data processing is therefore transferred from the sensor to the reader, far

from where the measurement is taken. In this configuration, a co-design is then necessary to reach the highest performances possible.

The goal of this thesis is to develop a novel approach of high-performance wireless sensing based on a MEMS sensor coupled with an antenna without electronic circuitry, which can increase the interrogation distance between the reader and the remotely powered sensor. The challenge is to couple and integrate these silicon sensors with an antenna architecture in a co-design approach.

The objective is to develop a MEMS capacitive pressure sensor and a miniature antenna, designed to work at subatmospheric pressure at 868 MHz. The use of MEMS for far-field wireless passive sensors is not often studied in the literature. Even if the achievable performances seem very interesting, the combination of antennas and MEMS requires a good expertise of fields such as mechanics, radio-propagation, electronics and signal processing. For this, the project takes place between two laboratories of CEA-Leti: the sensor and actuator laboratory and the antenna laboratory.

In this manuscript, after a general introduction on wireless passive sensors, I will make a survey of the sensors present in the bibliography, explicit the motivation of the choices made and explain the key concepts surrounding antennas (and their miniaturization) and MEMS sensors. These will then lead to the study of a type of sensor, based on electromagnetic transduction and composed of a MEMS transducer and an antenna. In the second chapter, the design and the process flow of the MEMS sensors are presented. The conception of the MEMS was done in order to work in radio-frequencies and to be wire-bonded to an antenna. Analytical studies are presented to understand the impact of key parameters of the co-design on the performances. The MEMS are then characterized in chapter 3, in order to extract their impedance and their behavior with pressure. Then, in chapter 4, using the results of characterization, the antenna is designed specifically for a MEMS. This is followed by characterization of the sensor in an anechoic chamber, and the analysis of the results. Finally, an alternative method of interrogation is presented in the last chapter, based on the mechanical resonance of non-linear MEMS sensors. This interrogation offers several advantages in harsh environments. An analytic model is expressed, finally linearized to understand the key parameters of the co-design.



# 1

## State of the art of passive wireless sensors

---

*In this first chapter, I present the important concepts surrounding passive wireless sensors. Passive wireless sensor can be represented as a system composed of a sensor part, which is the sensitive part of the system, and an antenna part, which ensures the communication with an interrogator. Therefore, I start by presenting a synthesis of the bibliographical study which allowed us to choose the type of remote-fed sensor. Then I define key concepts surrounding this thesis by separating the key definitions between those related to the antenna, and those related to the sensor.*

---

### Contents

---

<b>1.1</b>	<b>General introduction</b>	<b>6</b>
<b>1.2</b>	<b>State of the art of passive wireless sensors</b>	<b>7</b>
1.2.1	Inductive coupling sensors	7
1.2.2	Wireless sensors based on acoustic waves	9
1.2.3	Electromagnetic transduction-based wireless sensors	11
<b>1.3</b>	<b>Definitions and general information about antennas</b>	<b>13</b>
1.3.1	Working principle of an antenna	13
1.3.2	Equivalent electrical model of an antenna	13
1.3.3	Antenna gain and directivity	15
1.3.4	Radiation pattern	16
1.3.5	Radar Cross-Section and Radar Equation	17
1.3.6	Antenna miniaturization and impact on its quality factor	18
1.3.7	Printed antenna	20
1.3.8	Antenna materials for harsh environments	21
<b>1.4</b>	<b>Introduction to MEMS sensors</b>	<b>21</b>
1.4.1	MEMS technology	21
1.4.2	Microfabrication process	22
1.4.3	Working principle of capacitive pressure sensors	24

---

<b>1.5</b>	<b>MEMS-based passive wireless sensors</b>	<b>24</b>
1.5.1	MEMS positioning on the antenna	25
1.5.2	Impact of the MEMS on the antenna	25
1.5.3	Choice of the resonance frequency of the antenna	26
1.5.4	Main parameters of wireless passive sensors	26
<b>1.6</b>	<b>Conclusion</b>	<b>27</b>
	<b>References</b>	<b>28</b>

---

## 1.1 General introduction

Passive wireless sensors are devices that can detect and measure various physical parameters, such as temperature, humidity, pressure, or motion, but do not require a battery or any other external power source to operate. Instead, they rely on energy wirelessly harvested from the surrounding environment, such as an incoming radio frequency (RF) signal, light, or temperature gradients, to power their electronics and to communicate.

Passive wireless sensors offer a number of advantages over traditional active sensors. For example, they do not require batteries, which means they do not need to be replaced, they can be used in harsh environments where CMOS electronics cannot be used, and they are more cost-effective. They also have a longer lifespan and can be implemented in a wider variety of applications.

Passive wireless sensors can be broadly classified into two categories: those that rely on energy harvesting and those that rely on backscattering:

- Energy harvesting sensors: these sensors use a small energy harvesting module that converts energy from the surrounding environment into electricity. This electricity is then used to power the electronics of the sensor and its communication. Examples of energy harvesting technologies include:
  - RF energy harvesting: this technology captures energy from RF (Radio Frequency) signals and converts it into electricity. RF energy harvesting can be used in RFID (Radio Frequency IDentification) and NFC (Near Field Communication) applications. It can also use ambient RF energy [1] to power the sensor.
  - Solar energy harvesting: this technology captures energy from the sun and converts it into electricity [2, 3]. Solar energy harvesting is mainly used in outdoor applications.
  - Vibration energy harvesting: this technology captures energy from vibrations and converts it into electricity [4]. Vibration energy harvesting is often used in transportation or industrial machinery.
  - Thermal energy harvesting: this technology captures energy from temperature gradients and converts it into electricity [5]. Thermal energy harvesting is often used in applications where there is a large temperature difference, such as in geothermal or waste heat recovery systems.
- Backscattering sensors: these sensors reflect a portion of the received energy to convey information about the physical or environmental parameters being measured. Backscattering is often used in RFID, NFC, and other wireless communication technologies. It operates at a very low power and does not require an external power source, it modulates the reflected signal, allowing for data to be transmitted. Backscattering sensors can be divided into :
  - Inductive Coupling Sensors (or LC Sensors): this technology is based on a capacitive sensor and an inductive loop in series, forming a resonant circuit. The reading is done by inductive coupling with a reading loop.
  - Acoustic Wave Sensors: this technology is based on an acoustic sensor, for example Surface Acoustic Wave (SAW) or Bulk Acoustic Wave sensors (BAW), powered by an antenna. The sensing procedure can be done based on the travel time of the acoustic signal or the resonance frequency of a piezoelectric resonator.
  - Electromagnetic Transduction Sensors: this technology uses directly the electromagnetic (EM) signal as a support for the measurement. The sensing part will directly modify the EM properties of the antenna.

A passive wireless sensor can also use a combination of these two technologies to achieve a balance of performance and power consumption.

Passive wireless sensors can be used in a wide range of industries such as agriculture, building automation, industrial automation, healthcare, and military. For instance, they can be used to monitor the temperature and humidity in a green house, the vibration and temperature of a machine, the pressure and flow of fluids in a pipeline, or the occupancy of a room in a building. The data collected by the sensor will be wirelessly sent to a reading antenna, connected to a data processing unit in order to extract the value of the physical quantity.

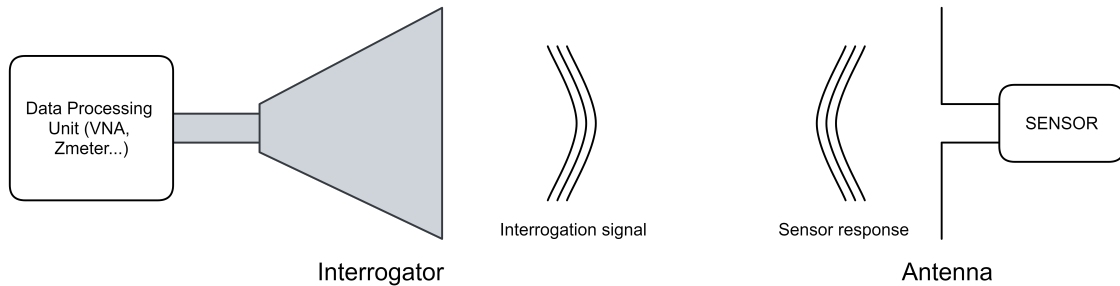


*Figure 1.1: Simplified representation of a reading procedure of a Passive Wireless Sensor using the backscattering technique. A reading antenna sends an EM signal, and the antenna-sensor will reflect a part of this power. This power will be received back by the reader and linked to the value of the physical quantity measured by the sensor.*

For this thesis, we have chosen to develop a sensor based on the backscattering technique, because of the great versatility of this operating principle, which can be used in several types of environments. We can split this kind of sensors in two parts, as shown in Figure 1.1: the antenna, which capture and sends back the incident RF electromagnetic wave, and the sensor, which modifies the electromagnetic properties of the antenna depending on an external physical phenomenon. This way the sensor will modify the behavior of the antenna or, in other words, the way it reflects an incident electromagnetic wave. By studying the response of the wireless sensor to an incident EM signal, the value of the physical quantity can be deduced. Moreover, in some technologies, the antenna itself acts like a sensor, for example when it is printed in a substrate with a temperature-dependent permittivity. The sensor can also operate at high temperatures, in our case at temperatures higher than the operating temperatures of the CMOS electronics ( $> 120^{\circ}\text{C}$ ). For this range of applications, the usage of CMOS electronics or batteries is excluded on the wireless sensor.

The next section presents the study of each type of backscattering sensors, how they work and their advantages and disadvantages, which will orient the choice of the passive wireless sensor developed in this thesis, which will be the combination of a MEMS capacitive pressure sensor and a miniature antenna. The MEMS consists of a membrane and a fixed electrode. The membrane will deflect under the effect of pressure, which will modify the response of the antenna.

To avoid any ambiguity in this manuscript, the capacitive MEMS sensor will be referred to as "MEMS", while the term "sensor" will refer to the antenna+MEMS system.

## 1.2 State of the art of passive wireless sensors

### 1.2.1 Inductive coupling sensors

The use of inductive coupling for wireless reading of a capacitive sensor was proposed as early as 1967 by Collins [6]. More commonly known as LC sensors, the use of a LC resonant circuit as a wireless sensor only gained interest in the 1990s with the development of microelectronics

[7], [8]. These sensors are composed of a capacitor whose value varies with the measurand, and an inductive loop, forming a resonant circuit whose frequency shift due to the capacitance change. The reading is then done by inductive coupling by approaching a reading loop near the sensor.

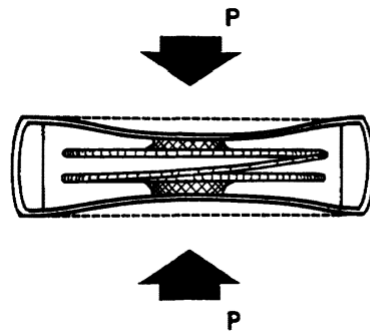


Figure 1.2: LC pressure sensor proposed by Collins [6], which consist of two coils trapped between two membranes. The pressure brings the coils closer together and changes the capacitance between them.

Because of its relative ease of design, this type of sensor is still being developed at present. The applications are diverse and range from pressure sensors [9] [10] [11], to strain sensors [12], to temperature sensors [9] [13]. The use of micro-fabrication processes allows obtaining very good performances, allowing the use of these sensors in harsh environments.

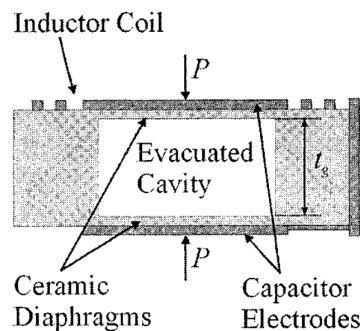


Figure 1.3: LC pressure sensor proposed by Fonseca [11] for high-temperature applications. The sensors consists of two electrodes on two diaphragms, separated by a vacuum-sealed cavity, thus forming a capacitor, connected to a coil on one side of the sensor.

However, this type of sensor has some disadvantages that can be problematic depending on the application. The first one is the very short reading distance (less than 10 cm) due to the near-field reading requirement. The other one is the large size of the sensor with regards to the operating frequencies which are very low (generally lower than 30 MHz). A summary of the advantages and disadvantages of Inductive coupling sensors is presented in Table 1.1.

Sensor type	Advantages	Disadvantages
Inductive coupling sensors	Easy to design	Near-field operation
	Operation in harsh environments	Large space requirement
	Compatible with micro-fabrication processes	Low operating frequency

Table 1.1: Summary table of advantages and disadvantages of LC sensors.

### 1.2.2 Wireless sensors based on acoustic waves

Surface acoustic wave (SAW) or bulk acoustic wave (BAW)-based devices play a major role in filter design because of their high bandwidth, low manufacturing cost and high reproducibility. The operating principle is based on the propagation of an acoustic wave in a piezoelectric material. These properties make them very good candidates for use as passive sensors [14], especially in wireless operation.

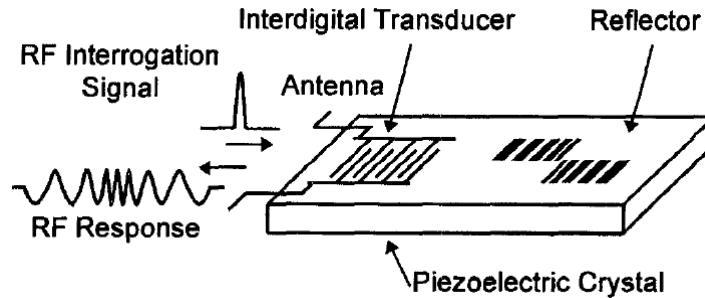


Figure 1.4: Working principle of a wireless surface acoustic wave sensor [15].

The principle of operation of an acoustic wave (AW) wireless sensor is presented in Figure 1.4. A radio frequency wave is sent to an antenna connected to an acoustic wave sensor. An interdigital transducer converts the signal into an acoustic wave which propagates on the piezoelectric material. This wave is reflected, then converted again into an electromagnetic signal, which will be back-propagated by the antenna. The sensing is done through the measurement of the acoustic signal which is sensitive to the measurand, for example with the variation of its propagation time. The theory behind the interrogation of these wireless sensors is presented by Reindl et al [15].

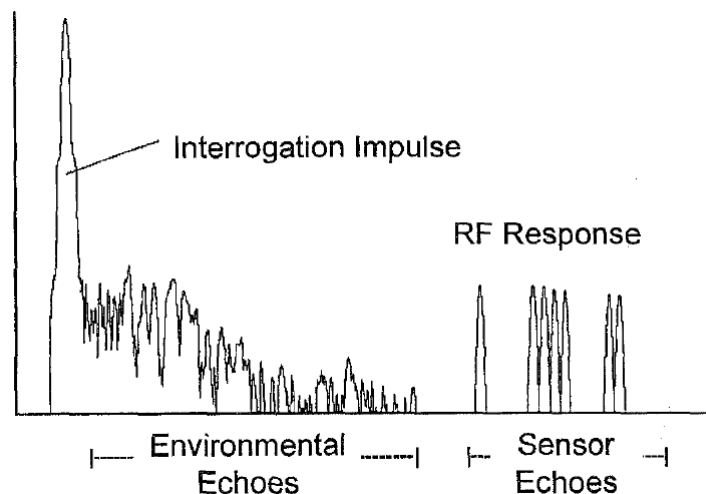


Figure 1.5: Time domain response of an AW wireless sensors based on a delay line [15].

We can identify three main categories of designs for AW transponders used as wireless sensors :

- Delay line: the measurement is based on the variation of the signal propagation on the piezoelectric material due to changes in the environment. The reading procedure is done in time domain by reading the delayed response of the signal backpropagated by the antenna. The physical quantity change the speed of propagation of the signal on the piezoelectric

material and thus, the delay time of the response. An example of this is shown in Figure 1.5. This technique offers a good isolation from residual echos arising from the environment (clutter isolation) as the antenna response is received later due to the difference between the speed of light and speed of sound. A linear change in the delay time  $\Delta\tau$  due to a change  $\Delta y$  of the physical quantity  $y$  can be expressed as :

$$\tau(y + \Delta y) = \tau(y)(1 + S_y \Delta y) \quad (1.1)$$

With  $S_y$  the sensor sensitivity.

- Resonator: the measurement is based on the variation of the resonance frequency of an AW resonator due to changes in the environment. The reading procedure is done in the frequency domain by shifting the interrogation frequency. Multiple sensors can be powered by the same antenna in order to do a differential measurement or to measure different physical quantities. The variation  $\Delta f$  of the resonance frequency  $f$  can be expressed as :

$$\Delta f = -f(y)S_y \Delta y \quad (1.2)$$

- Impedance Sensors: the measurement is based on the variation of the impedance of an external sensor connected to the interdigital transducer, as shown in Figure 1.6. A change in the sensor impedance change the reflection coefficient of the interdigital transducer. This reflectivity change due to the load impedance  $Z_L$  can be expressed using the P-Matrix representation [16], as :

$$P_{11}(Z_L) = P_{11}^{sc} + \frac{P_{13}^2}{P_{33} + \frac{1}{Z_L}} \quad (1.3)$$

AW wireless sensors present several advantages and disadvantages, as summarized in Table 1.2. Its main disadvantage is its lack of integration flexibility compared to MEMS based wireless passive sensors where you can also have, for example, a configuration with a MEMS on the radiating part of the antenna and a fixed load (see next section). Here, it is because the sensor is placed where the current is maximal to supply it (i.e. at the load). The AW sensor must also be match the antenna with the acoustic wave frequency in addition to the impedance match. There is also losses due to the propagation of the acoustic wave, losses due to the double conversion acoustic-electromagnetic in addition to the conduction losses, impedance miss-match losses and antenna substrate losses.

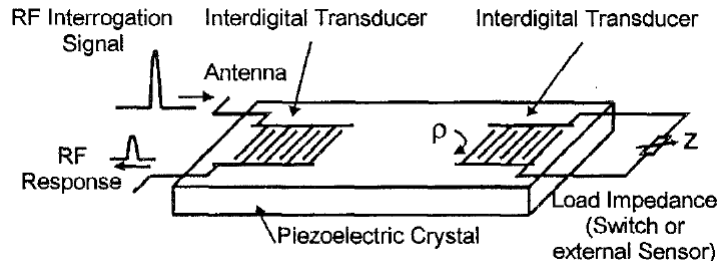


Figure 1.6: Representation of an external sensor connected to a SAW device. The sensor impedance will change the reflection coefficient of the interdigital transducer. [15]

Sensor type	Advantages	Disadvantages
AW wireless sensors	Clutter isolation Mature technology Multiple sensors on the same antenna	Sensor placed where the current is maximal Sensitive to other physical quantities Acoustic-EM conversion losses

Table 1.2: Summary table of advantages and disadvantages of AW wireless sensors.

### 1.2.3 Electromagnetic transduction-based wireless sensors

#### Operating principle

Electromagnetic transduction sensors works directly on modifying the electromagnetic signal. The operating principle is based on the measurement of the variation of the properties of an antenna. This can be done in different ways, by introducing an element that varies the impedance of the antenna, by having a substrate whose permittivity varies with the measurand or by varying the effective length of the antenna.

The reading principle is similar to the one used for acoustic wave sensors: a reader send an electromagnetic wave to the antenna. The sensor modify this wave which is backpropagated by the antenna. The reader then deduce the measurand by studying the variation of this wave. This can be done in two ways, either by studying the backpropagated power at the transmission frequency (using a sensor that varies the RCS of the antenna), or by studying the variation of the resonance frequency of the antenna, which means the frequency at which the RCS is maximum. The possibility of using one type of reading or the other depends on the type of sensor, and is developed in the following subsection.

#### Classification of electromagnetic transduction based wireless sensors

As said before, electromagnetic transduction wireless sensors can use different operating principles. Within the framework of the bibliographical study, they can be classified in two different categories, divided into several sub-categories:

- Those that vary the impedance of the antenna. In this case the sensor is placed on the antenna, and it can be seen as a variable impedance. The variation of the measurand will cause a variation of the properties of the antenna, due to the impedance mismatch between the antenna and the load. The variation can come from :
  - A variation in resistance, which will cause a variation in the power backpropagated by the antenna. We then work at a single frequency (the resistance variation does not modify the resonance frequency of the antenna). However, these sensors generally consume more power than a capacitive sensor. Furthermore, this type of sensors have usually high resistance values, which limits the sensitivity of the antenna-sensor. They also tends to have a high temperature sensitivity, which is usually compensated through a compensation circuit. The use of a variable resistor, placed as an antenna load, as a temperature sensor was developed by Victor Engelhardt in his PhD thesis [17].
  - A variation in capacitance will cause a variation in the power backpropagated and the resonance frequency of the antenna. Indeed, a variation in capacitance implies a variation in the frequency at which the imaginary part of the impedance of the sensor and the antenna cancel each other. Temperature sensors [18] and strain sensors [19] based on this transduction method have been designed in the literature. Capacitive sensors combines high sensitivity, low power consumption, almost hysteresis-free and low temperature sensitivity [20, 21].

- A variation of mechanical resonance frequency. However, due to the mechanical resonance frequencies of MEMS (usually below MHz), which are very small compared to the resonance frequencies of the antennas, it is not possible to directly drive the sensors at resonance. Viikari et al [22], [23] have presented a method for actuating resonant sensors by intermodulation. By sending two RF signals to the antenna, they use the non-linearities present in the electric force in capacitive sensors to set it in resonance at a frequency which is the difference of the frequencies of the two incident signals. However, no sensor has been developed using this operating principle.
- Those which modify the environment of the antenna. The antenna being highly sensitive to its environment, a sensitive element can be inserted outside the antenna to make the measurement. The sensor is therefore not present in charge of the antenna. The objective is mainly either to vary the actual length of the antenna, or the effective permittivity of the antenna environment, which shifts its resonance frequency. These sensors can also be divided into several categories, depending on whether the variation comes from :
  - A capacitive coupling between the antenna and a conductive membrane, forming a parallel capacitance. Rogers et al [24] have developed a pressure sensor for harsh environments based on this principle. Applying pressure to the membrane cause it to deflect, resulting in a change in the value of the equivalent capacitance.
  - The variation of the thickness of air above a resonator, which causes the variation of the effective electrical permittivity and thus a change in the resonance frequency of the resonator. References [25] [26] [27] present sensors based on this principle.
  - The variation of the permittivity of the substrate of the antenna. The permittivity of these substrates often varies with temperature or humidity. Henry et al. [28] developed a humidity sensor and Kou et al. [29] developed temperature and humidity sensors. The performance (measurement range, sensitivity...) of these types of sensors is however limited by the properties of the substrate.
  - From the expansion of a fluid. These sensors based on micro-fluidics are mainly used as temperature sensors as in the articles by Rifai et al. [30] and Virtanen et al. [31]. Like sensors based on the variation of substrate permittivity, they are limited the properties of the fluid, both in terms of performance and in terms of physical quantities they can measure.
  - The deformation of the substrate, as in the case of the strain sensor developed by Thai et al. [13]. However, the materials employed in this approach are generally not suitable for high-temperature applications.

---

Sensor type	Advantages	Disadvantages
EM transduction based	No conversion loss Design flexibility... Reading range Diversity of operating principle	... but can be very complex

---

*Table 1.3: Summary of advantages and disadvantages of wireless sensors based on electromagnetic transduction.*

The advantages and disadvantages of EM transduction passive wireless sensors are summarized in Table 1.3. It offers a great flexibility in terms of design and transduction principle. It

can have a sensitive element on the antenna, or the antenna itself can also act as the sensor, if it is printed on a temperature-sensitive substrate for example. It is for example compatible with MEMS technologies. With a MEMS, the sensor can be the antenna load or considered as a part of the antenna. The main design constraints in harsh environments are those related to material, which should be carefully chosen for the specific application.

## 1.3 Definitions and general information about antennas

### 1.3.1 Working principle of an antenna

The *IEEE Standard for Definitions of Terms for Antennas* [32] define an antenna as "That part of a transmitting or receiving system that is designed to radiate or to receive electromagnetic waves. The term antenna is sometimes used for electromagnetic devices that couple over distances less than that associated with radiated fields.". This section will focus solely on far-field radiating antennas.

At its core, an antenna functions by converting electrical signals into electromagnetic waves for transmission or vice versa for reception. This process involves the interaction between the electric and magnetic fields generated by the current flowing through the antenna.

To understand the operation of an antenna, it is helpful to consider a simple example: the dipole antenna. A dipole antenna consists of two conductive elements, typically straight rods or wires, that are symmetrically arranged. The length of each element is typically a fraction of the wavelength of the signal and it is designed to transmit or receive.

For transmitting, an alternating current in the antenna causes the electrons in the conductive elements to oscillate back and forth. This oscillation generates a time-varying electric field around the antenna which propagate away from the antenna as an electromagnetic wave. As the electric field changes, it induces a magnetic field perpendicular to it, creating an electromagnetic wave. That is these accelerated charges which produces the radiation, and because the current is sinusoidal, the EM field created will be also sinusoidal.

For receiving, the varying electric and magnetic fields induce an alternating current in the antenna. This current is then extracted and processed by the receiver to retrieve the transmitted information.

Balanis [33] gave a simplified but clear illustration of how the electric field is radiated, shown in Figure 1.7. After a period of  $T/4$ , the charges travel a distance of  $\lambda/4$  over the fed point of the antenna. The charges distribution is at its maximal value and the current distribution on the antenna create an electric field represented with three lines in subfigure (a). After another period of  $T/4$ , these three lines travel another distance of  $\lambda/4$  and the charges density decreases to became null. It can be represented as if additional charges of opposite signs are added, represented in dashed lines in subfigure (b). The dashed lines has travelled a distance of  $\lambda/4$  and the solid lines a distance of  $\lambda/2$ . At  $T/2$ , there is no any charges on the antenna, the lines cannot stay on the dipole, they must so detach from the antenna as shown in subfigure (c). The electric field is then radiated, and will induce a magnetic field and create a propagating electromagnetic wave.

### 1.3.2 Equivalent electrical model of an antenna

An antenna can be represented electrically using an equivalent circuit. Equivalent circuit of a loaded antenna is shown in Figure 1.8. The load impedance is expressed as  $Z_L = R_L + jX_L$ . The impedance of an antenna is defined as the ratio of voltage to current seen at its terminal when there is no load attached, defined as :

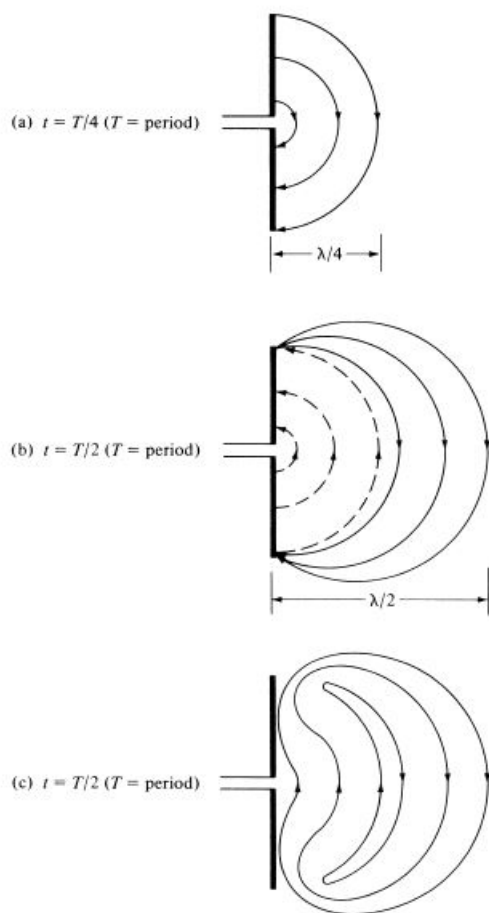


Figure 1.7: Example of radiation of a short dipole [33]

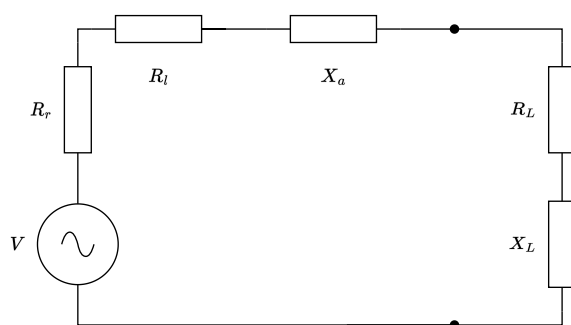


Figure 1.8: Equivalent circuit of a loaded antenna.

$$Z_a = R_a + jX_a \quad (1.4)$$

With  $R_a$  the antenna resistance and  $X_a$  the antenna reactance at the terminals. The antenna equivalent resistance can be splitted in two parts, such as :

$$R_a = R_r + R_l \quad (1.5)$$

with  $R_r$  the radiation resistance and  $R_l$  the loss resistance of the antenna. The IEEE definition of the radiation resistance is "the ratio of the power radiated by an antenna to the square of the RMS (Root Mean Square) current of the antenna referred to a specified point" [32]. A higher radiation resistance means that more electrical power is being radiated as electromagnetic energy for a given current circulating on the antenna. This definition does not take in account the intrinsic losses of the antenna, which are represented through the loss resistance. Loss resistance includes dielectric loss and conduction losses that occurs mainly by Joule heating in conductors. It is hard to measure conduction losses and dielectric losses independently, so they are usually expressed together using a single loss resistance. By reducing the loss resistance, the antenna system can be made more efficient and the amount of radiated energy can be increased. The antenna radiation efficiency  $e_{cd}$ , due to conduction and dielectric losses can be then expressed as :

$$e_{cd} = \frac{R_r}{R_r + R_l} \quad (1.6)$$

Another source of losses can occur arising from signal reflection at the terminals due to the impedance mismatch between the antenna and the load (with an impedance  $Z_L = R_L + jX_L$ ). This mismatch is represented with the reflection coefficient  $\Gamma$ , which is equal, in case of loaded antenna, to:

$$\Gamma = \frac{Z_a - Z_L^*}{Z_a + Z_L} \quad (1.7)$$

When the load impedance is the complex conjugate of the impedance of antenna , there are matched and there are no reflection losses. In practice, a perfect adaptation is impossible, but it is possible to get close to it, and the radiation efficiency  $e_r$  is expressed as :

$$e_r = (1 - |\Gamma|^2) \quad (1.8)$$

The expression of the total efficiency of the antenna is :

$$e_0 = e_r e_{cd} = \frac{R_r}{R_r + R_l} (1 - |\Gamma|^2) \quad (1.9)$$

### 1.3.3 Antenna gain and directivity

The antenna gain, usually denoted  $G$ , refers to its ability to concentrate radio energy in a particular direction., or in other words, the part of the radiation intensity in a given direction and polarization compared to the intensity radiated by an ideal isotropic antenna, which is an idealized theoretical antenna that radiates equally in all directions. The antenna gain is measured commonly in isotropic decibels (dBi). A higher gain antenna will have a higher signal strength in a particular direction, while a lower gain antenna will have a weaker signal in the same direction. The gain is expressed as :

$$G = 4\pi \frac{U}{P_{in}} \quad (1.10)$$

with  $U$  the radiation intensity in Watt per Steradian (W/sr), and  $P_{in}/4\pi$  the mean radiation intensity of a perfect isotropic antenna.

---

Directivity, on the other hand, usually denoted as  $D$ , refers to the ability of an antenna to focus its energy in a specific direction, while rejecting signals from other directions. The directivity of an antenna is often characterized by its beamwidth, which is the angle between the half-power points (3 dB points) of the main lobe of the antenna's radiation pattern. A narrower beamwidth means that the antenna is more directional and focuses more of its energy in a specific direction, while a wider beamwidth means that the antenna is less directional and radiates more energy in multiple directions. It is expressed as :

$$D = 4\pi \frac{U}{P_0} \quad (1.11)$$

With  $P_0$  the mean radiation intensity of the antenna. According to IEEE Standards [32] : "Gain does not include losses arising from impedance and polarization mismatches and does not depend on the system to which the antenna is connected.". The relationship between IEEE gain and directivity is then  $G_{IEEE} = e_{cd}D$  with  $e_{cd}$  the radiation efficiency of the antenna. Another definition is the realized gain, which is equal to  $e_0D$ , which represent the gain including all sources of losses.

Both of these parameters are important in designing a passive wireless sensor as they define the reading range and the directions in which the antenna can be interrogated.

### 1.3.4 Radiation pattern

The radiation pattern of an antenna is a graphical representation of the way in which an antenna radiates energy into space, usually in far-field. It shows the relative strength of the radio waves emitted by the antenna in different directions, and it is often represented as a three-dimensional plot or a two-dimensional polar plot.

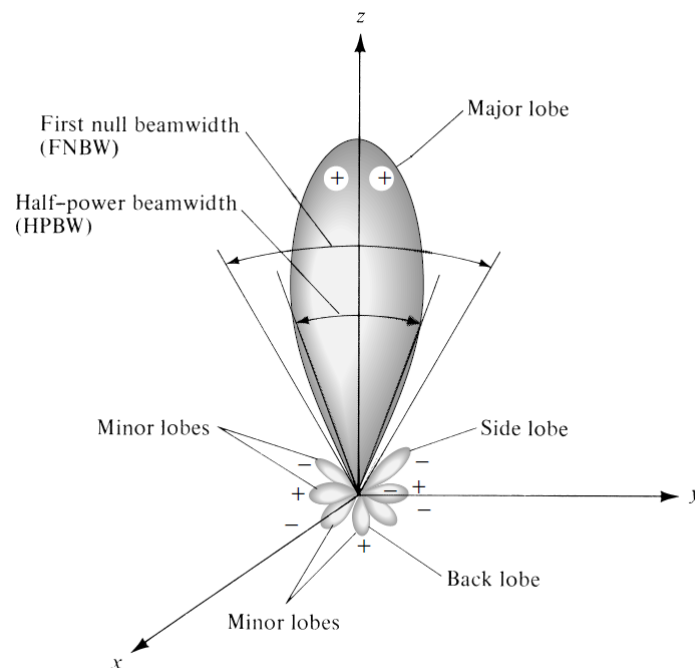


Figure 1.9: 3D representation of a radiation pattern [33].

The radiation pattern can be divided into several regions, such as shown in Figure 1.9 :

- The main lobe is the region where the majority of the energy is radiated, and it is typically pointed in the direction of the intended signal reception or transmission.

- The side lobes are smaller regions of radiation located on either side of the main lobe, and they can cause unwanted interference with other signals.
- The back lobe is at the opposite direction of the main lobe. Usually, the goal is to make the back lobe the smallest as possible.

A directional antenna, for example, will have a more focused radiation pattern with a narrower main lobe and stronger energy in one direction. Its maximal gain is greater than 1. On the other hand, an omni-directional (or isotropic) antenna will have a more dispersed radiation pattern and will radiate the energy relatively equally in all directions. A perfect isotropic antenna has a gain of 1.

### 1.3.5 Radar Cross-Section and Radar Equation

When an RF wave arrives at the surface of a medium having a different dielectric constant from its propagation medium, a reflection takes place. This phenomenon is the basis of radar communication between two antennas. The ability of an object to reflect an electromagnetic signal at a particular frequency is called the Radar Cross-Section (RCS).

The Radar Cross-Section is an intrinsic property of any object that describes how detectable it is by radar: the larger the RCS of an object, the more detectable it will be. The RCS depends on many parameters such as:

- The material of the object
- The size of the object
- The angle of incidence of the wave emitted by the radar
- The angle of reflection of the radar signal
- The wavelength of the radar signal
- The polarization of the radar wave

The RCS, usually denoted  $\sigma$  is homogeneous to a surface and it is defined as  $\sigma = p_r/p_i$  with  $p_r$  the reflected power per unit solid angle and  $p_i$  the surface power received by the object. It can also be defined through the radar equation as :

$$\sigma = \frac{P_r(4\pi)^3 R^4}{\lambda^2 P_t G_t G_r} \quad (1.12)$$

With :

- $P_t$  the power emitted by the radar
- $P_r$  the power received by the radar, which was reflected by the object
- $G_r$  and  $G_t$  the gain of the radar in reception and in transmission respectively
- $R$  the distance between the radar and the object
- $\lambda$  the wavelength of the signal sent.

For antennas, the RCS can be divided in two parts: the antenna mode RCS and the structural RCS. The antenna mode RCS is the part of RCS which varies with the antenna load, while the structural RCS does not vary. Under perfect impedance matching between the antenna and the load, the RCS of the antenna is purely structural. Another way to express the RCS using this separation is:

$$\sigma = \frac{\lambda^2 G_A^2}{4\pi} |\Gamma - A|^2 \quad (1.13)$$

With  $A$  the structural mode of the antenna and  $G_A$  its gain. Table 1.4 gives some examples of RCS values of common objects, for the X-band (8-12 MHz).

Object	RCS [ $m^2$ ]
Pick-up	200
Car	100
Commercial airplane	40
Small fighter plane	2
Adult man	1
Bird	0.01
Insect	0.00001

Table 1.4: Examples of RCS values in the X-band [34].

### 1.3.6 Antenna miniaturization and impact on its quality factor

The concept of antenna miniaturization refers to the reduction of the antenna size at a specified frequency. This means that the electrical size of the antenna decreases at its working frequency or, in other words, its effective wavelength. These antennas are called "Electrically Small Antennas" (ESA). This notion of electric size, as well as the notion of ESA, was first introduced by Wheeler in 1947 [35]. An antenna is usually said to be electrically small if  $ka < 1$ , with  $k = 2\pi/\lambda$  and  $a$  the radius of the smallest sphere containing the antenna. Later, Adler, Chu and Fano [36] defined the short dipole as a dipole whose length  $l = 2a$  is less than  $\lambda/2\pi$ , which implies that the criteria for an ESA is  $ka < 0.5$ .

The main impacts of miniaturization are the increase of the quality factor, the reduction of radiation efficiency and the reduction of the maximal gain. The quality factor represents the ability for a resonator to keep the energy inside of it. It is defined as the ratio of the energy initially stored in it over the energy loss for each radian of the cycle of the oscillation. Moreover, higher is the quality factor, lower is the bandwidth of the antenna, as shown in Figure 1.10

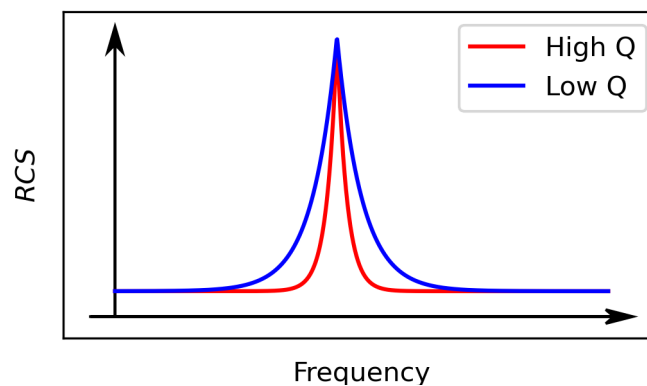


Figure 1.10: Comparison of the curves of the transfer functions of the antenna for high and low quality factors

The general expression for the quality factor, in analogy with the expression for linear circuits, is :

$$Q = \frac{2\omega \max(W_e, W_m)}{P_{rad}} \quad (1.14)$$

With  $\omega = 2\pi f$  the resonance frequency of the antenna,  $W_e$  and  $W_m$  respectively the stored electric and magnetic energy and  $P_{rad}$  the power radiated by the antenna. A high quality factor means, therefore, a relatively higher amount of power radiated by the antenna.

Wheeler firstly described the link between antenna size and bandwidth by introducing the "Radiation Power Factor"  $P$ , which is approximately equal to the relative bandwidth  $BW$ , and, if  $P < 0.2$  :

$$P = \frac{R}{|X|} = \frac{1}{Q} \approx BW \approx \frac{\Delta f}{f} \quad (1.15)$$

With  $R + jX$  the antenna impedance and  $Q$  the antenna quality factor. The bandwidth is equal to the ratio of difference between the highest and the lowest frequency of the bandwidth  $\Delta f$  over the resonance frequency of the antenna  $f$ . It was obtained using two simple models : a cylindrical volume with capacitor plates and a multitransformer inductor.

To link the quality factor and the electrical size of the antenna, Chu [37] did an analysis in 1948 using TE and TM spherical modes (respectively Transverse Electric and Transverse Magnetic). For a single low order TE or TM mode, the expression of the quality factor is minorized by :

$$Q_{min,Chu} = e_{cd} \left( \frac{1}{ka} + \frac{1}{k^3 a^3} \right) \quad (1.16)$$

Different approaches were taken by others after, such as Harrington [38], Collin and Rothschild [39] of Kalafus [40]. Later, McLean has shown that in case of circular polarization, the quality factor is minorized :

$$Q_{min,McLean} = \frac{1 + 3k^2 a^2}{2(1 + k^2 a^2)k^3 a^3} \quad (1.17)$$

MacLean has also expressed the limitation of the antenna efficiency in case of high miniaturization. This confirms the assumption of Harrington [38] that the efficiency of an antenna reduce when its size decrease.

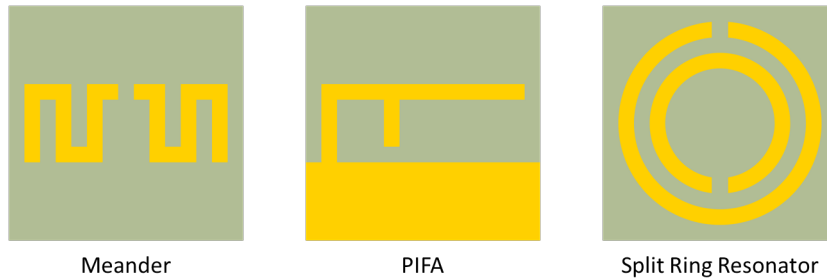


Figure 1.11: Examples of miniature antennas geometries.

When designing a ESA, there is a necessity to find a trade-off between the key parameters of the antenna: electrical size  $ka$ , efficiency  $\eta$  and bandwidth  $1/Q = \Delta f/f$ . If we take the Chu expression of the quality factor in (1.16) and the approximation of an ESA of electrical size  $ka \ll 0.5$ , there is the relationship :

$$e_{cd} \frac{\Delta f}{f} \approx (ka)^3 \quad (1.18)$$

In practice, several techniques are used for antenna miniaturization :

- Topology-based techniques: where the antenna geometry is modified in order to reduce its electrical size. We can cite for example meander antennas, or fractal antennas.
- Material-based techniques: where the focus is placed on changing directly the electrical and magnetic properties of the antenna. It can be done by using a high-permittivity substrate, or by using metamaterials (artificial materials with properties rarely observed in naturally occurring materials, such as an effective negative permittivity and permeability).
- Techniques based on slowing the wave propagation: they allow designing antennas which are physically small but electrically large. This can be done by placing a capacitor or an inductance on the antenna, by engineering the ground plane, or by using distributed loading.

### 1.3.7 Printed antenna

Printed antennas (or microstrip antennas) are designed from PCB etching processes mainly used in the microwave range (300 MHz - 30 GHz). They are often used in wireless communication devices, such as cell phones, Wi-Fi routers, and GPS devices, due to their low cost and ease of manufacturing. They are also attractive for integration with other technologies such as RFID, sensors and IoT. They can also be made flexible, which makes them suitable for use in wearable devices and other portable electronics. The use of this type of antennas for embedded systems has many advantages [41] such as:

- Compactness (planar technology);
- Ease and low cost of manufacture;
- Integration with electronic components;
- Possibility of printing on flexible substrates;
- Easy networking of antennas.

The main disadvantages include:

- A large bandwidth requires a complex design of the antenna
- Power losses, especially those related to dielectric losses, which reduce the radiation efficiency of the antenna
- Difficulties to have an accurate polarization if the antenna is miniaturized.

It is worth noting that despite these disadvantages, the use of printed antennas is growing in popularity because of their low cost and ease of manufacturing. There is also ongoing research to improve their performance.

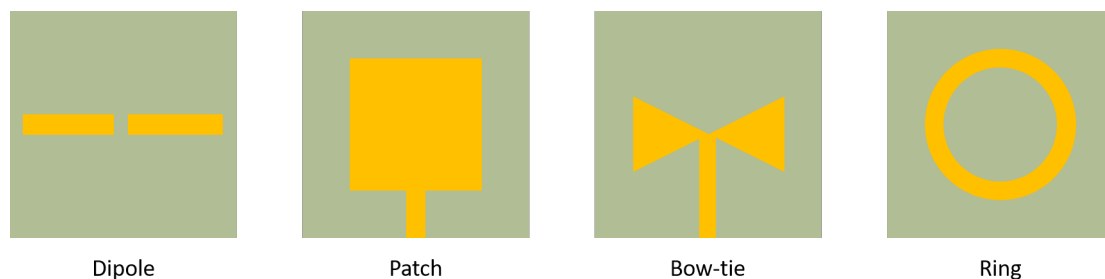


*Figure 1.12: Example of planar antenna geometries.*

There are several different geometries that are commonly used in the design of printed antennas, the most well-known being the dipole, the patch, the ring or the Yagi antenna (Figure 1.12). Many other more complex geometries that have been proposed for specific applications or to achieve precise properties, some of them based on metamaterials and other advanced techniques like fractal or evolved antennas.

### 1.3.8 Antenna materials for harsh environments

In order to build planar antennas for harsh environments, it is important to pay special attention to the materials of the substrate and conductive parts. Recent advances allow having materials with good performance in harsh environment, which means high melting point and low losses. For example, Younes et al. [42] present a very good overview of the materials available for antenna design for high-temperature applications.

For high temperature applications, some common characteristics desired for the dielectric are a constant permittivity in the temperature range, a melting point inferior to the highest temperature of the medium, low dielectric losses and low thermal conductivity. Commonly used materials for the substrate are ceramics or laminate. Some materials are also flexible, such as E-Strate substrate. An example of a slot antenna designed on this substrate is shown in [43].

In order to choose the conductive material, the key parameters are a low electric resistivity, a low thermal conductivity and a high melting point. Some metals such as gold, copper or molybdenum are well-suited for high temperature applications.

## 1.4 Introduction to MEMS sensors

Understanding the operating principle of an antenna highlights important parameters to be taken into account when designing the antenna: gain, quality factor and operating frequency, among others. These parameters are often interdependent, and a compromise must be found at the design stage. However, it is necessary to understand the working principle of MEMS in order to grasp all the aspects of sensor design. This section presents generalities around MEMS, their microfabrication process and then the key equations around MEMS capacitive pressure sensors.

### 1.4.1 MEMS technology

The Microelectromechanical Systems (MEMS) are a family of components involving the use of miniaturized mechanical and electro-mechanical elements which are fabricated using semiconductor manufacturing techniques. The term "MEMS" was introduced in 1986 by S.C. Jacobsen (PI) and J.E. Wood (Co-PI) through a proposal to DARPA titled "Micro Electro-Mechanical Systems (MEMS)" that was granted to the University of Utah on 15 July 1986. A year later, in November 1987, S.C. Jacobsen presented the term "MEMS" in an invited talk titled "Micro Electro-Mechanical Systems (MEMS)" at the IEEE Micro Robots and Teleoperators Workshop in Hyannis, MA. Additionally, the term was published in a submitted paper by J.E. Wood, S.C. Jacobsen, and K.W. Grace titled "SCOFSS: A Small Cantilevered Optical Fiber Servo System" [44] in the IEEE Proceedings Micro Robots and Teleoperators Workshop held in Hyannis, MA.

They typically consist of a mobile part with dimensions ranging from few micrometers to a millimeter. Electrical transducers are used to control and detect its motion and convert it into an electric signal. Common transducers includes :

- Capacitive transducers: Where the motion is measured through a variation of capacitance. Classical geometrics of capacitive transducers include interdigitated capacitors, beams or

membranes.

- Piezoelectric transducers: Which utilize the piezoelectric effect, where certain materials generate an electric charge in response to mechanical stress. The electric signal generated will be proportional to the applied stress.
- Piezoresistive transducers: Which utilize the piezoresistive effect, where certain materials exhibit a change in resistance when subjected to mechanical stress. For example, strain gauges are resistive transducers that change their resistance in response to applied strain or deformation.

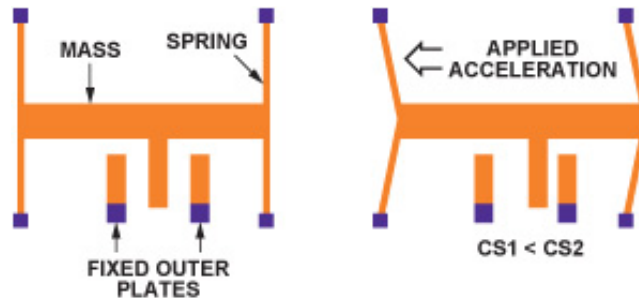


Figure 1.13: Working principle of a 1-axis MEMS accelerometer. The acceleration will move the mobile part, which will change the capacitance at the outer plates.

MEMS are often used in sensing applications. An example of a 1-axis accelerometer is shown in Figure 1.13. The acceleration will move the mobile part, which will change the capacitance at the outer plates.

Usually, MEMS sensors are integrated in package with their own electronics to condition the signal. In the case of passive wireless sensors, the sensor is only connected to the antenna, without electronic components. This antenna can be more or less sensitive to the variation of the sensor impedance, which proves once again the importance of the co-design between the sensor and the antenna.

MEMS technology has increased the performance of many sensor families, while reducing the cost of manufacturing due to the high-volume manufacturing process. We can cite mobile telephony (gyroscope, microphones...), automotive (car tire pressure sensors, airbag sensors...) as areas that have greatly benefited from this technology.

#### 1.4.2 Microfabrication process

A MEMS process flow is the succession of several elementary steps based on microelectronics, which are most often carried out on silicon substrate, leading to the manufacturing of the desired geometry. The most common processes are :

- Photolithography: this is the basis of micro- and nano-fabrication technologies, and it refers to the process of imprinting a pattern onto a light-sensitive substance by selectively exposing it to radiation, usually light. A light-sensitive substance, also known as a photosensitive material, undergoes alterations in its physical properties upon exposure to radiation. By selectively exposing the photosensitive material to radiation, such as by using a mask to shield certain areas, the pattern of the radiation is transferred onto the material. If the photoresist is positive, then the light will weaken the material, if it is negative, it will protect the enlightened parts. Then, another process can be done only on the areas exposed. After the process, the photoresist is removed using a stripping solution. Figure 1.14 shows an example of the etching of a motif using photolithography.

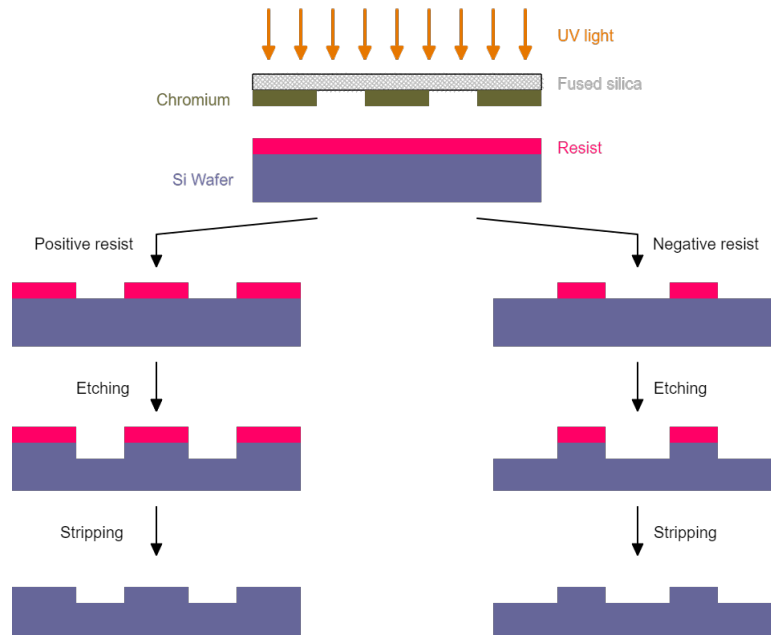


Figure 1.14: Example of etching process using photolithography depending on the photoresist polarity.

- Deposition: the ability to deposit thin film materials on a substrate is another key element of microfabrication. The deposited films are in a range of few nanometers to 100 micrometers. There are two main categories of deposition :
  - Physical Vapor Deposition (PVD): in which the atoms are removed from a solid or liquid source, go into a vapor phase, and then deposit on the substrate. There are many different techniques to perform PVD, such as sputtering, in which a plasma is used to pull the atoms from the surface of the source material, or Electron-beam physical vapor deposition (EBPVD) in which an electron beam is used.
  - Chemical Vapor Deposition (CVD): in which the wafer is exposed to a reactive medium in order to grow a high-quality and solid material. It is used to grow materials such as  $\text{SiO}_2$ ,  $\text{SiN}$ ,  $\text{SiC}$  on silicon, or to create nanotubes or nanofilms of carbon.
- Etching: in which a material is removed from the substrate. It can be divided in two main categories :
  - Wet etching: in which a reactive liquid solution is used to selectively etch a material. The etching can be anisotropic or isotropic depending on the solution used and the material etched. For example, KOH (potassium hydroxide) is used to etch anisotropically the silicon ( $\text{Si} \langle 111 \rangle$  planes etch 100 times slower than other planes). To etch  $\text{SiO}_2$ , HF (Hydrofluoric acid) is commonly employed, for example to remove native oxide at the surface of a silicon wafer.
  - Dry etching: in which the wafer is placed on a reactive gas plasma medium in order to bombard it with ions. It can create very high aspect ratio structures with Deep Reactive-Ion Etching (DRIE). For example, Xenon Difluoride  $\text{XeF}_2$  is commonly used to dry-etch silicon.

Wet etching	Dry etching
High selectivity	High reproducibility
Cheaper	More expensive
Isotropic or anisotropic	Can perform high aspect ratio structures
Slower	Faster

Table 1.5: Comparison of dry and wet etching.

- Thermal processes and doping: which use high temperature in order to diffuse oxidative species on silicon to grow  $\text{SiO}_2$ , or to diffuse dopants such as boron or phosphorus in order to create impurities. These impurities create free charges on the silicon and, then, increase locally the conductivity inside the material.

### 1.4.3 Working principle of capacitive pressure sensors

Pressure sensor is one of the most common technology of MEMS sensor. It can measure different kinds of pressure, such as absolute pressure, vacuum or differential, using different transduction principles : capacitive, piezoresistive, piezoelectric, optical etc.

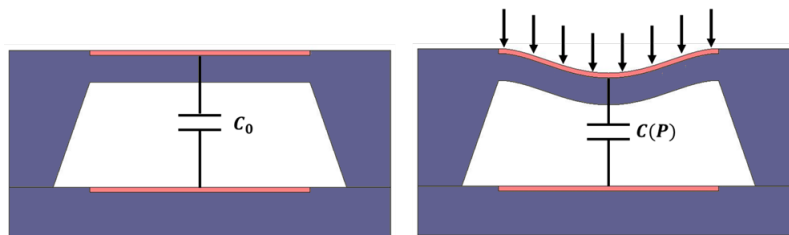


Figure 1.15: Operating principle of a capacitive pressure sensor. The membrane will deflect due to applied pressure. The deflection changes the value of the capacitance between the two electrodes (in pink).

For a capacitive pressure sensor, the capacitor is composed of the membrane and a fixed electrode. Usually, the membrane shape is square, rectangular or circular. In case of absolute pressure measurement, the cavity between the membrane and the fixed electrode is vacuum-sealed. The pressure applied deflects the membrane, which changes the value of the gap between the electrodes. This cause a change of the value of the capacitance created between the two electrodes, as shown in Figure 1.15.

## 1.5 MEMS-based passive wireless sensors

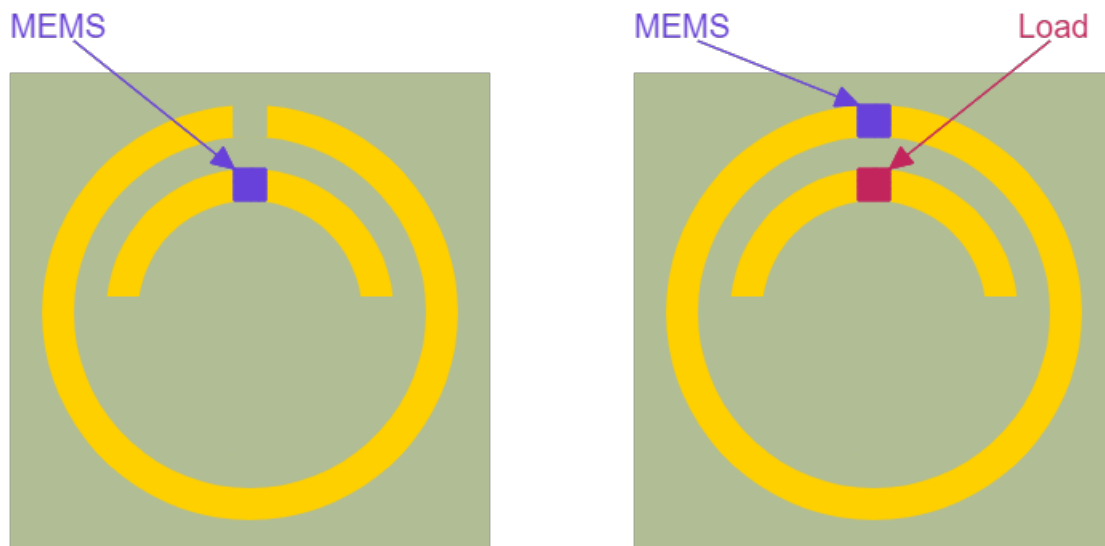
Now that the theory behind antenna and behind MEMS sensor has been presented, this part focus on the integration between the antenna and the MEMS, in order to understand more in general how this technology of passive wireless sensors works.

### 1.5.1 MEMS positioning on the antenna

The positioning of the MEMS on the antenna is a crucial aspect in order to optimize the performances. Two configurations can be identified in order to position the MEMS on the antenna.

- Where the MEMS is considered as the load : The MEMS is then placed where the current is highest, or in other words, where the cables would be connected in the case of an antenna that would be connected to a circuit. The impedance-matching is done between the antenna and the MEMS.
- Where the MEMS is considered as a part of the antenna : The MEMS is then placed on the radiative part of the antenna, and seen as an element which modify directly the electrical length of the antenna. An additional constant load is then necessary, which can be seen as an additional parameter that can be manipulated to improve sensor performance. The impedance-matching is, here, done between the load on the one hand, and the antenna and the MEMS on the other hand (the MEMS impedance is included in the parameter  $Z_a$  in the reflection coefficient  $\Gamma$  (Eq. 1.7)).

These two configurations are illustrated in Figure 1.16 on a Capacitive Loaded Loop (CLL), which is a structure of planar miniature antenna where the outer loop is the radiative element. This loop is coupled to an inner arc where we put the load.



(a) CLL antenna with the MEMS as the load without additional element

(b) CLL antenna with the MEMS on the radiating part and an additional load

Figure 1.16: Example of the two positioning configurations of the MEMS for the same antenna

### 1.5.2 Impact of the MEMS on the antenna

This subsection focus on the understanding of how the MEMS will modify the response of the antenna. This can be explained in two ways :

- Using the reflection coefficient  $\Gamma$  (Eq. 1.7) : if the MEMS is the antenna load, the pressure will change the value of the capacitance and thus the impedance of the MEMS. Consequently, it will change the value at which the reflection coefficient is closest to zero. This is also the case if the MEMS is considered as part of the antenna, but this is the impedance of the antenna that will change, and the impedance of the load will be constant.

- Using the current : Equivalently, a capacitor can be seen as an element "which slows" down charges. In order words, it will shift negatively the value of the phase of the current where the capacitor is. By changing the value of the capacitance, this phase shift also varies. Using the example of the dipole, the boundary conditions require the current to be zero at the edges of the dipole at resonance, i.e. the phase  $\phi$  to be a multiple of  $\pi$ . Thus, a variation of the value of the MEMS capacitance will change the value of the frequency which respects this boundary condition. This can be applied to all geometries of antennas.

This change of the resonance frequency of the antenna will also change the response of the antenna, which means the curve of its RCS. Because the value of the frequency at which the RCS is maximal is strongly linked to the resonance frequency of the antenna, it will also shift with the variation of capacitance.

### 1.5.3 Choice of the resonance frequency of the antenna

While the MEMS is designed to operate over a whole frequency band, because its frequency behavior will depend mainly on the dimensions of the lines to which it is connected (the in-plane and out-of-plane dimensions of the MEMS are small compared with the wavelength), the antenna will resonate at a single frequency. The choice of this frequency is a key parameter which depends:

- On the regulations governing the use of frequency bands and the power that can be sent. The frequency bands that can be used depends on the application. In our case, the regulator in France is the Agence Nationale des Fréquences Radio (National Radio Frequencies Agency), and the 868MHz is on a ISM band (industrial, scientific, and medical).
- On the reading range desired. By re-arranging the equation 1.12 we have:

$$\frac{P_r}{P_t} = \left( \frac{\lambda}{4\pi R} \right)^4 G_A^2 G_r G_t |\Gamma - A|^2 \quad (1.19)$$

This equations shows that the attenuation depends on the fourth power of the wavelength. A higher frequency means higher attenuation in free-space. But the reading range does not depend solely on the frequency: it depends on the gain of the antenna, its RCS, the gain of the interrogator, the sensitivity of the measuring instrument or power regulation as explained above..

- On the size of the antenna. If the size of the antenna is a critical design factor, two different strategies can be put forward: work with a relatively high frequency or miniaturize the antenna. Having a higher operating frequency has an impact on free-space losses, as seen above. But a miniature antenna with a lower resonance frequency tends to have a lower gain and a lower RCS. In our case, the choice has been made to work at 868 MHz (wavelength of approximately 34.5 cm) in order to design antenna which can be miniature or not and compare the performances. The impact of the miniaturization on the performances of the sensor is studied more in details in chapter 2.

### 1.5.4 Main parameters of wireless passive sensors

As presented in the state of the art, there is a huge variety of working principles of passive wireless sensors with different types of transduction, physical parameters to measure, methods of interrogation etc. However, some general parameters can be identified as important in order to determine the performances of a passive wireless sensor:

- **Sensitivity / Full Span** : The sensitivity and full span are classical parameters used to compare sensors performances. Sensitivity can be seen as the variation of resonance frequency

of the antenna, or the variation of the power at a given frequency, depending on the working principle of the passive wireless sensor.

- **Precision** : In case of passive wireless sensors, the antenna bandwidth is also a critical parameter, because bandwidth is directly related to the width of the peak of the RCS frequency response. Thus, a low bandwidth is important to differentiate two measurements of two close values of the physical parameter, in case of a working principle based on a variation of the resonance frequency. If the parameter measured is the variation of the power back-propagated at a given frequency, it allows to have a good precision on the value of the value of the maximum amount of power measured.
- **Accuracy** : As an antenna is very sensitive to its environment, its response can be modified by other external parameters than the physical quantity to measure. It is also the case for a MEMS sensor for example. Differential measurement between a passive wireless sensor and a reference can be done to take into account this effects.
- **Reading range** : The reading range of the wireless sensors is a parameters which depends on many other ones, such as working frequency, reader gain, maximal power which can be sent by the VNA and its sensitivity. To a greater extent, another parameter that can have a greater impact on reading distance for far-field measurement is the environment around the antenna. As shown in [45], in real environments, the limitation of reading range is the ratio between the power sent back by the antenna over the power reflected by the environment. The Radar Cross Section seems to be a good parameter to discriminate passive wireless sensors which works in far-field, but it strongly depends on the size of the antenna. However, this parameter is almost never mentioned in the literature. Finally, it seems that reading range is a parameters which is really difficult to quantify, because of its dependence to many other external parameters. The reading range can be really discriminated depending on the working principle of the interrogation, i.e. by coupling or by far-field.
- **Dimensions** : Size of the antenna-sensor can be a good parameter as it is often an important parameter while conceiving a sensor for a specific application. Moreover, the size of the global system is mainly fixed by the size of the antenna, which is dependent on the working frequency and impact the other parameters such as the amount of power backpropagated, the sensitivity, the antenna bandwidth etc. Two different strategies are possible in order to reduce the size of the antenna : using miniaturization techniques or increasing the resonance frequency of the antenna, which was presented in section 1.5.3.

## 1.6 Conclusion

In this chapter, an overview of the literature around passive wireless sensors has been made, with their great diversity of working principle, their strengths and weaknesses. Bearing in mind all the possibilities and the constraints of operating in a harsh environment, we have chosen to develop a MEMS capacitive pressure sensor co-designed with a miniature antenna, working at 868 MHz. This choice is motivated by the possibility of measurement by reading the resonance frequency of the antenna, or by looking at the variation of power backpropagated at a single frequency. Other motivations are the performances of MEMS sensors, combined with the compactness of miniature antenna, and the flexibility offered by these two technologies for co-design purposes. MEMS EM transduction-based passive wireless sensors based are less developed in the literature, despite the performance that can be achieved by combining MEMS and miniature antennas, mainly due to the

complexity of design and the facilities required. The parameters determining the performances of the sensor were presented: it must have high sensitivity, low bandwidth and a reading distance as long as possible. The chapter two is focused on the definition of constraints and requirements, and the quantification of the key parameters in order to achieve those performances. Analyses are then done in order to understand which parameters of the antenna and the MEMS impact the performances of the sensor. These studies are leading to a better understanding of how the sensor works, and how to co-design the antenna and the MEMS. It leads to the design of the MEMS and its microfabrication process flow which are then simulated on the software Ansys HFSS.

## References

- [1] Hakim Takhedmit. “Ambient RF power harvesting: Application to remote supply of a batteryless temperature sensor”. In: *2016 IEEE International Smart Cities Conference (ISC2)*. 2016, pp. 1–4. DOI: [10.1109/ISC2.2016.7580800](https://doi.org/10.1109/ISC2.2016.7580800).
- [2] J. M. Williams et al. “Solar and RF Energy Harvesting Design Model for Sustainable Wireless Sensor Tags”. In: *2020 IEEE Topical Conference on Wireless Sensors and Sensor Networks (WiSNeT)*. 2020, pp. 1–4. DOI: [10.1109/WiSNeT46826.2020.9037497](https://doi.org/10.1109/WiSNeT46826.2020.9037497).
- [3] Sai Nithin R. Kantareddy et al. “Long Range Battery-Less PV-Powered RFID Tag Sensors”. In: *IEEE Internet of Things Journal* 6.4 (2019), pp. 6989–6996. DOI: [10.1109/JIOT.2019.2913403](https://doi.org/10.1109/JIOT.2019.2913403).
- [4] B. Andò et al. “A wireless sensor node powered by nonlinear energy harvester”. In: *SENSORS, 2014 IEEE*. 2014, pp. 1583–1586. DOI: [10.1109/ICSENS.2014.6985320](https://doi.org/10.1109/ICSENS.2014.6985320).
- [5] Juan M. Lopera et al. “Practical Issues in the Design of Wireless Sensors Supplied by Energy Harvesting Thermoelectric Generators”. In: *IEEE Transactions on Industry Applications* 55.1 (2019), pp. 996–1005. DOI: [10.1109/TIA.2018.2867810](https://doi.org/10.1109/TIA.2018.2867810).
- [6] C.C. Collins. “Miniature Passive Pressure Transensor for Implanting in the Eye”. In: *IEEE Transactions on Biomedical Engineering* BME-14.2 (1967), pp. 74–83. DOI: [10.1109/TBME.1967.4502474](https://doi.org/10.1109/TBME.1967.4502474). URL: <https://www.scopus.com/inward/record.uri?eid=2-s2.0-0014080792&doi=10.1109%2fTBME.1967.4502474&partnerID=40&md5=4e003fbe11fbbc5bfc26f47dea4a5532>.
- [7] Y. Bäcklund et al. “Passive silicon transensor intended for biomedical, remote pressure monitoring”. In: *Sensors and Actuators: A. Physical* 21.1-3 (1990), pp. 58–61. DOI: [10.1016/0924-4247\(90\)85011-R](https://doi.org/10.1016/0924-4247(90)85011-R). URL: <https://www.scopus.com/inward/record.uri?eid=2-s2.0-0025698114&doi=10.1016%2f0924-4247%2890%2985011-R&partnerID=40&md5=00e653cb69798724a9c16dc2f2588e34>.
- [8] L. Rosengren et al. “A system for wireless intra-ocular pressure measurements using a silicon micromachined sensor”. In: *Journal of Micromechanics and Microengineering* 2.3 (1992), pp. 202–204. DOI: [10.1088/0960-1317/2/3/021](https://doi.org/10.1088/0960-1317/2/3/021). URL: <https://www.scopus.com/inward/record.uri?eid=2-s2.0-0026913146&doi=10.1088%2f0960-1317%2f2%2f3%2f021&partnerID=40&md5=4992f4f5a614d9bbb5f3c83a52e30a7e>.
- [9] Qiulin Tan et al. “A Wireless Passive Pressure and Temperature Sensor via a Dual LC Resonant Circuit in Harsh Environments”. In: *Journal of Microelectromechanical Systems* PP (Jan. 2017), pp. 1–6. DOI: [10.1109/JMEMS.2016.2642580](https://doi.org/10.1109/JMEMS.2016.2642580).
- [10] Li Qin et al. “A Wireless Passive LC Resonant Sensor Based on LTCC under High-Temperature/Pressure Environments”. In: *Sensors* 15 (July 2015), pp. 16729–16739. DOI: [10.3390/s150716729](https://doi.org/10.3390/s150716729).

- 
- [11] Michael Fonseca et al. “Wireless micromachined ceramic pressure sensor for high-temperature applications”. In: *Microelectromechanical Systems, Journal of* 11 (Sept. 2002), pp. 337–343. DOI: [10.1109/JMEMS.2002.800939](https://doi.org/10.1109/JMEMS.2002.800939).
- [12] John C. Butler et al. “Wireless, passive, resonant-circuit, inductively coupled, inductive strain sensor”. In: *Sensors and Actuators A: Physical* 102.1 (Dec. 2002), pp. 61–66. ISSN: 0924-4247. DOI: [10.1016/S0924-4247\(02\)00342-4](https://doi.org/10.1016/S0924-4247(02)00342-4). URL: <http://www.sciencedirect.com/science/article/pii/S0924424702003424>.
- [13] T. T. Thai et al. “Design and Development of a Novel Passive Wireless Ultrasensitive RF Temperature Transducer for Remote Sensing”. In: *IEEE Sensors Journal* 12.9 (Sept. 2012), pp. 2756–2766. ISSN: 1558-1748. DOI: [10.1109/JSEN.2012.2201463](https://doi.org/10.1109/JSEN.2012.2201463).
- [14] A.J. Ricco and S.J. Martin. “Thin metal film characterization and chemical sensors: monitoring electronic conductivity, mass loading and mechanical properties with surface acoustic wave devices”. In: *Thin Solid Films* 206.1-2 (1991), pp. 94–101. DOI: [10.1016/0040-6090\(91\)90399-I](https://doi.org/10.1016/0040-6090(91)90399-I). URL: <https://www.scopus.com/inward/record.uri?eid=2-s2.0-0026367115&doi=10.1016%2f0040-6090%2891%2990399-I&partnerID=40&md5=ec977dd7f94a96836602e79bd5410e43>.
- [15] L. Reindl et al. “Theory and application of passive SAW radio transponders as sensors”. In: *IEEE Transactions on Ultrasonics, Ferroelectrics, and Frequency Control* 45.5 (1998), pp. 1281–1292. DOI: [10.1109/58.726455](https://doi.org/10.1109/58.726455).
- [16] G. Tobolka. “Mixed Matrix Representation of SAW Transducers”. In: *IEEE Transactions on Sonics and Ultrasonics* 26.6 (1979), pp. 426–427. DOI: [10.1109/T-SU.1979.31128](https://doi.org/10.1109/T-SU.1979.31128).
- [17] Victor Engelhardt. “Contribution au développement d’antennes miniatures intégrant des fonctionnalités de capteurs”. PhD thesis. 2018. URL: <http://www.theses.fr/2018INPT0067/document>.
- [18] Sean Scott and Dimitrios Peroulis. “A capacitively-loaded MEMS Slot element for wireless temperature sensing of up to 300°C”. In: *2009 IEEE MTT-S International Microwave Symposium Digest*. Boston, MA, USA: IEEE, June 2009, pp. 1161–1164. ISBN: 978-1-4244-2803-8. DOI: [10.1109/MWSYM.2009.5165908](https://doi.org/10.1109/MWSYM.2009.5165908). URL: <http://ieeexplore.ieee.org/document/5165908/> (visited on 01/20/2021).
- [19] Trang Thai et al. “A newly developed radio frequency wireless passive highly sensitive strain transducer”. In: *Proceedings of IEEE Sensors* (Oct. 2011), pp. 211–214. DOI: [10.1109/ICSENS.2011.6127239](https://doi.org/10.1109/ICSENS.2011.6127239).
- [20] Robert Puers. “Capacitive sensors: When and how to use them”. In: *Sensors and Actuators A: Physical* 37-38 (1993), pp. 93–105. ISSN: 0924-4247. DOI: [https://doi.org/10.1016/0924-4247\(93\)80019-D](https://doi.org/10.1016/0924-4247(93)80019-D). URL: <https://www.sciencedirect.com/science/article/pii/092442479380019D>.
- [21] G. Blazquez, P. Pons, and A. Boukabache. “Capabilities and limits of silicon pressure sensors”. en. In: *Sensors and Actuators* 17.3-4 (May 1989), pp. 387–403. ISSN: 02506874. DOI: [10.1016/0250-6874\(89\)80026-5](https://doi.org/10.1016/0250-6874(89)80026-5). URL: <https://linkinghub.elsevier.com/retrieve/pii/0250687489800265> (visited on 04/13/2021).
- [22] Ville Viikari and Heikki Seppä. “RFID MEMS sensor concept based on intermodulation distortion”. In: *IEEE Sensors Journal* 9 (Jan. 2010). DOI: [10.1109/JSEN.2009.2031809](https://doi.org/10.1109/JSEN.2009.2031809).
- [23] Ville Viikari et al. “Review of passive wireless sensors utilizing the intermodulation communication”. In: *2014 IEEE RFID Technology and Applications Conference (RFID-TA)*. Tampere, Finland: IEEE, Sept. 2014, pp. 56–61. ISBN: 978-1-4799-4680-8. DOI: [10.1109/RFID-TA.2014.6934200](https://doi.org/10.1109/RFID-TA.2014.6934200). URL: <http://ieeexplore.ieee.org/document/6934200/> (visited on 01/20/2021).
-

- [24] John Rogers et al. “A Passive Wireless Microelectromechanical Pressure Sensor for Harsh Environments”. In: *Journal of Microelectromechanical Systems* PP (Nov. 2017), pp. 1–13. DOI: [10.1109/JMEMS.2017.2774000](https://doi.org/10.1109/JMEMS.2017.2774000).
- [25] M.M. Jatlaoui et al. “Working principle description of the wireless passive EM transduction pressure sensor”. In: *The European Physical Journal Applied Physics* 56.1 (Oct. 2011), p. 13702. ISSN: 1286-0042, 1286-0050. DOI: [10.1051/epjap/2011100220](https://doi.org/10.1051/epjap/2011100220). URL: <http://www.epjap.org/10.1051/epjap/2011100220> (visited on 01/20/2021).
- [26] Mohamed Jatlaoui et al. “Wireless interrogation techniques for a passive pressure micro-sensor using an EM transducer”. In: Pages: 056. Nov. 2009. ISBN: 978-1-4244-4748-0. DOI: [10.1109/EUMC.2009.5296233](https://doi.org/10.1109/EUMC.2009.5296233).
- [27] Julien Philippe et al. “In-Situ Wireless Pressure Measurement Using Zero-Power Packaged Microwave Sensors”. In: *Sensors* 19 (Mar. 2019), p. 1263. DOI: [10.3390/s19061263](https://doi.org/10.3390/s19061263).
- [28] Dominique Henry et al. “Long range wireless interrogation of passive humidity sensors using Van-Atta cross-polarization effect and 3D beam scanning analysis”. In: *2017 IEEE MTT-S International Microwave Symposium (IMS)*. Honolulu, HI, USA: IEEE, June 2017, pp. 816–819. ISBN: 978-1-5090-6360-4. DOI: [10.1109/MWSYM.2017.8058703](https://doi.org/10.1109/MWSYM.2017.8058703). URL: <http://ieeexplore.ieee.org/document/8058703/> (visited on 01/20/2021).
- [29] Hairong Kou et al. “A wireless slot-antenna integrated temperature-pressure-humidity sensor loaded with CSRR for harsh-environment applications”. en. In: *Sensors and Actuators B: Chemical* 311 (May 2020), p. 127907. ISSN: 09254005. DOI: [10.1016/j.snb.2020.127907](https://doi.org/10.1016/j.snb.2020.127907). URL: <https://linkinghub.elsevier.com/retrieve/pii/S0925400520302549> (visited on 01/20/2021).
- [30] Ayoub Rifai et al. *Wireless chipless passive microfluidic temperature sensor*. Pages: 1027. June 2013. DOI: [10.1109/Transducers.2013.6626944](https://doi.org/10.1109/Transducers.2013.6626944).
- [31] Juha Virtanen et al. “Temperature sensor tag for passive UHF RFID systems”. In: *2011 IEEE Sensors Applications Symposium*. San Antonio, TX, USA: IEEE, Feb. 2011, pp. 312–317. ISBN: 978-1-4244-8063-0. DOI: [10.1109/SAS.2011.5739788](https://doi.org/10.1109/SAS.2011.5739788). URL: <http://ieeexplore.ieee.org/document/5739788/> (visited on 01/20/2021).
- [32] “IEEE Standard for Definitions of Terms for Antennas”. In: *IEEE Std 145-2013 (Revision of IEEE Std 145-1993)* (2014), pp. 1–50. DOI: [10.1109/IEEESTD.2014.6758443](https://doi.org/10.1109/IEEESTD.2014.6758443).
- [33] Constantine A Balanis. *Antenna theory: analysis and design*. John Wiley & sons, 2015.
- [34] J.A. Adam. “How to design an ‘invisible’ aircraft”. In: *IEEE Spectrum* 25.4 (1988), pp. 26–31. DOI: [10.1109/6.4529](https://doi.org/10.1109/6.4529).
- [35] H.A. Wheeler. “Fundamental Limitations of Small Antennas”. In: *Proceedings of the IRE* 35.12 (Dec. 1947), pp. 1479–1484. ISSN: 2162-6634. DOI: [10.1109/JRPROC.1947.226199](https://doi.org/10.1109/JRPROC.1947.226199).
- [36] Richard B. Adler, Lan Jen Chu, and Robert M. Fano. “Electromagnetic Energy Transmission and Radiation”. In: *American Journal of Physics* 29.3 (1961), pp. 214–215. DOI: [10.1119/1.1937726](https://doi.org/10.1119/1.1937726). eprint: <https://doi.org/10.1119/1.1937726>. URL: <https://doi.org/10.1119/1.1937726>.
- [37] L. J. Chu. “Physical Limitations of Omni-Directional Antennas”. In: *Journal of Applied Physics* 19.12 (1948). \_eprint: <https://doi.org/10.1063/1.1715038>, pp. 1163–1175. DOI: [10.1063/1.1715038](https://doi.org/10.1063/1.1715038). URL: <https://doi.org/10.1063/1.1715038>.
- [38] Roger F. Harrington. “Effect of antenna size on gain, bandwidth, and efficiency”. In: *Journal of Research of the National Bureau of Standards, Section D: Radio Propagation* (1960), p. 1.

- 
- [39] R. Collin and S. Rothschild. “Evaluation of antenna Q”. In: *IEEE Transactions on Antennas and Propagation* 12.1 (1964), pp. 23–27. DOI: [10.1109/TAP.1964.1138151](https://doi.org/10.1109/TAP.1964.1138151).
- [40] R. Kalafus. “On the evaluation of antenna quality factors”. In: *IEEE Transactions on Antennas and Propagation* 17.6 (1969), pp. 729–732. DOI: [10.1109/TAP.1969.1139558](https://doi.org/10.1109/TAP.1969.1139558).
- [41] S. Drabowitch et al. “Printed antennas”. In: *Modern Antennas*. Ed. by S. Drabowitch et al. Boston, MA: Springer US, 1998, pp. 117–139. ISBN: 978-1-4757-2758-6. DOI: [10.1007/978-1-4757-2758-6\\_6](https://doi.org/10.1007/978-1-4757-2758-6_6). URL: [https://doi.org/10.1007/978-1-4757-2758-6\\_6](https://doi.org/10.1007/978-1-4757-2758-6_6).
- [42] Bachir Younes et al. “HIGH TEMPERATURE ANTENNAS: A REVIEW”. en. In: *Progress In Electromagnetics Research B* 95 (2022), pp. 103–121. ISSN: 1937-6472. DOI: [10.2528/PIERB22030704](https://doi.org/10.2528/PIERB22030704). URL: <http://www.jpier.org/PIERB/pier.php?paper=22030704> (visited on 02/14/2023).
- [43] María Gómez et al. “Zirconia-Based Ultra-Thin Compact Flexible CPW-Fed Slot Antenna for IoT”. In: *Sensors* 19 (July 2019), p. 3134. DOI: [10.3390/s19143134](https://doi.org/10.3390/s19143134).
- [44] JE Wood, SC Jacobsen, and KW Grace. “SCOFFS: a small cantilevered optical fiber servo system”. In: *Proc. IEEE Micro Robots and Teleoperators Workshop*. 1987, pp. 9–11.
- [45] Nicolas Barbot, Olivier Rance, and Etienne Perret. “Classical RFID Versus Chipless RFID Read Range: Is Linearity a Friend or a Foe?” In: *IEEE Transactions on Microwave Theory and Techniques* 69.9 (Sept. 2021), pp. 4199–4208. ISSN: 1557-9670. DOI: [10.1109/TMTT.2021.3077019](https://doi.org/10.1109/TMTT.2021.3077019).



# 2

## MEMS design and integration with the antenna

---

*This chapter focuses on the MEMS design and the definition of the microfabrication process. The key elements to design the MEMS are presented, in order to be later integrated on an antenna specifically designed for each MEMS. Studies are done in order to understand which parameters of the antenna and the MEMS impact the performances of the global system.*

---

### Contents

---

<b>2.1</b>	<b>Introduction</b>	<b>35</b>
<b>2.2</b>	<b>Strategy for the MEMS design</b>	<b>35</b>
<b>2.3</b>	<b>MEMS geometry</b>	<b>36</b>
<b>2.4</b>	<b>Design of the MEMS</b>	<b>37</b>
2.4.1	Methodology	37
2.4.2	Modeling of the MEMS	37
2.4.3	Determination of the MEMS dimensions	39
2.4.4	Validation of the model	40
<b>2.5</b>	<b>Microfabrication process and masks designs</b>	<b>42</b>
2.5.1	Process flow	42
2.5.2	MEMS designs	45
<b>2.6</b>	<b>Finite element simulations of the MEMS</b>	<b>46</b>
2.6.1	De-embedding and ABCD matrixes	46
2.6.2	Simulated structures of MEMS	48
2.6.3	Dimensioning of the CPW lines	51
2.6.4	Properties of the lines	52
2.6.5	Conclusion	56
<b>2.7</b>	<b>Integration with the antenna and impact on the performances</b>	<b>56</b>
2.7.1	Impact of the antenna structural mode	56
2.7.2	Impact of antenna size/quality factor	56
2.7.3	Impact of the resistance of the MEMS on the sensitivity	59

2.7.4	Impact of the wire-bonding . . . . .	59
2.7.5	Analysis of an enhanced version of the sensor . . . . .	61
2.7.6	Conclusion on the optimization of the performance of the sensor . . . . .	62
<b>2.8</b>	<b>Conclusion</b> . . . . .	<b>63</b>
	<b>References</b> . . . . .	<b>63</b>

---

## 2.1 Introduction

The previous chapter presented the global aspects of MEMS-based passive wireless sensors, and some general elements of design. An important factor to consider when designing MEMS and antennas in the context of this thesis is the difference in terms of manufacturing time. While the antennas developed here are designed using conventional printed circuit board manufacturing processes, the MEMS are designed using clean room microfabrication processes. These manufacturing times are not negligible compared to the duration of the thesis (of the order of one year).

With this in mind, it was decided to design the MEMS first, integrating as much as possible the constraints associated with the antenna. The antennas were then designed in a second phase, after the characterization of the MEMS to take in account the process variability. Therefore the MEMS was designed using theoretical and generic antenna models, representing the general behavior of an antenna without considering a particular geometry.

The integration with the antenna is not the only criterion taken into account when designing MEMS; there are, for example, those related to microfabrication itself or the possibility of measuring at high temperatures. Finally, as mentioned in the first chapter, this passive wireless sensor technology can be adapted to different types of MEMS or physical quantities to be measured, which gives freedom in the design of the sensor. All these aspects guided the design of the MEMS and the design of the antennas in a second phase.

Based on the manufacturing process and the design of the MEMS photolithography masks, analytical models and simulations can be used to determine the behavior of the sensors in RF and as a function of pressure.

Even if the antennas are designed at a later stage, studies can be carried out to guide their design and highlight possible improvements to the sensors that could lead to even better performance.

This chapter presents each step of the design of the MEMS, by firstly defining the strategy, then the global geometry which leads to the modeling of the MEMS. Based on the dimensions obtained by modeling, the microfabrication process and the layout are defined. It allows to obtain precise geometries of MEMS which can be then simulated. Finally, in order to have a better understanding about the interactions between the MEMS and the antenna, analytical studies were performed to conclude on a strategy of design to optimize the performances of the sensor.

## 2.2 Strategy for the MEMS design

Starting from the choice of designing a capacitive pressure sensor to measure subatmospheric pressures, it is convenient to define more precisely the constraints and requirements, with the aim of achieving specific MEMS geometries. A particular emphasis is placed on the trade-offs between the best possible performance and the technological risks linked to microfabrication. Some studies have been carried out to identify which aspects are more important to focus on than others. However, design choices still take into account these aspects, which are considered secondary, even if they are not studied as thoroughly as other aspects of the MEMS.

- Due to the time constraints of MEMS microfabrication in clean room (usually around a year), the MEMS was designed using general models of antennas, i.e., without choosing a particular geometry. Then, the geometry of the antennas were studied and defined after the characterization of the MEMS. This allows an antenna geometry tailored to each MEMS in order to have an optimized performance.
- The materials must be chosen when establishing the manufacturing process to overcome the

limit of 120°C of maximal temperature of CMOS electronics (in our case, mainly silicon and  $SiO_2$ , in addition to metal).

- The impedance of the MEMS must be carefully chosen to allow the design of the antenna adapted to the MEMS. The high limit of the impedance was set to be 500  $\Omega$  in real and imaginary part at 868 MHz, frequency chosen as resonance frequency of the antenna, with particular emphasis on reducing the value of the real part of the impedance. The structure of the MEMS was therefore defined as consisting of a large circular membrane and small gap values, and special attention was paid to the doping steps when establishing the manufacturing process.
- The MEMS must operate in the UHF-SHF band (300 MHz - 30 GHz), which means it must have an impedance which allows the matching with the antenna in this frequency range. The MEMS are then be connected to coplanar line structures whose dimensions are judiciously chosen to allow in particular the characterization under RF probes. These lines must have an input impedance of 50 $\Omega$  in order to prevent signal reflections during probing measurements.
- The MEMS are connected to the antenna by wire-bonding, so the lines which connect the MEMS to the antenna must be sufficiently wide, i.e., at least 100  $\mu\text{m}$  wide.

## 2.3 MEMS geometry

Having defined the constraints and requirements that the MEMS must meet, the global geometry of the MEMS was then selected to set up the equations to precisely define its dimensions.

The primary purpose is to meet the impedance matching necessity and mitigate fabrication risks. This involves maintaining stringent control over each microfabrication stage to prevent any deviations from specifications, performance degradation, or even compromised functionality. The goal is to ensure optimal impedance matching and minimize potential fabrication issues, thereby safeguarding the overall performance and functionality of the system. The geometry of the MEMS which is chosen is based on a variable capacitor created by a circular membrane with a conductive part on it and a fixed electrode. The membrane is vacuum-sealed in order to make the pressure between the membrane and the bottom electrode the most possible close to vacuum. If the gap between those two electrodes is sealed (i.e. constant pressure), a pressure applied on the membrane causes its deflection, resulting in a change in the capacitance value. This principle is illustrated in Figure 2.1.

This choice of geometry allows using a relatively mature Capacitive Micromachined Ultrasonic Transducer (CMUT) process flow, developed at CEA-Leti, with very few modifications. A CMUT is a type of (MEMS) device that converts electrical signals into ultrasonic waves or vice versa, utilizing the capacitance variations between closely spaced conductive layers on a flexible membrane to generate or detect acoustic waves. In order to lower the imaginary part of the impedance, the capacitor can be defined by a large electrode and thin gap. This common geometry of pressure sensor has the advantage of being well-studied, and analytical equations to describe its behavior are readily available. Three dimensions can be changed to design different variants of MEMS: the radius of the membrane, denoted by  $R$ ; the gap between the membrane and the lower electrode, denoted by  $g_0$  and the thickness of the membrane denoted by  $h$ .

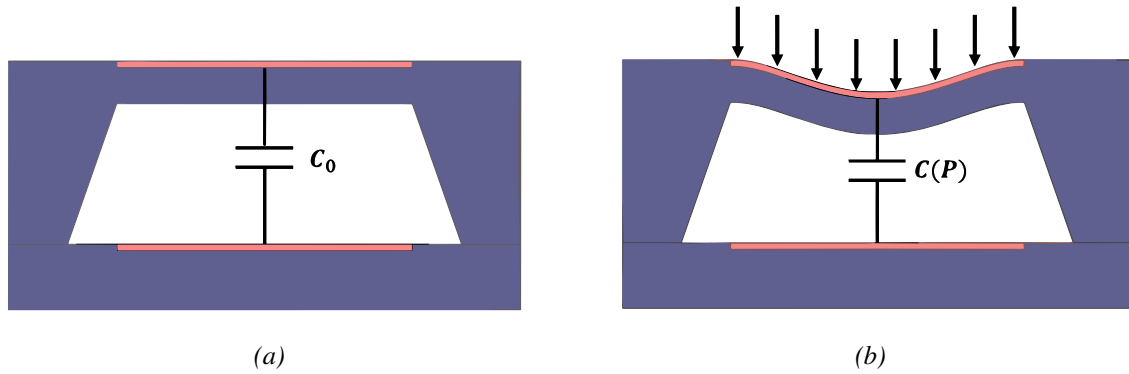


Figure 2.1: Working principle of the capacitive pressure sensor: under vacuum (a), the membrane and the bottom electrode are parallel, while applying a pressure on the membrane (b), it will deflect and change the value of the capacitance.

## 2.4 Design of the MEMS

In the previous sections, the overall geometry of the MEMS has been defined with the strategy of design, in order to respect the listed constraints and requirements. The objective of this part is to define the geometrical parameters of the design in which the constraints are respected. Precise dimensions of MEMS were chosen, in order to define the manufacturing process and the layout of the photolithography masks of the MEMS.

### 2.4.1 Methodology

To define the dimensions for the MEMS, I add to the above list of requirements more numerical requirements, e.g. that the deflection at 1 bar must be less than the gap value, or that the maximum stress on the membrane must be less than the stress at break. It is then possible to determine the sets of dimensions of the MEMS that meet all the requirements described above. The key equations that define those set of dimensions must be then defined and are presented in the next sections.

### 2.4.2 Modeling of the MEMS

In this theoretical analysis, the MEMS is modeled as a circular membrane of radius  $R$  and thickness  $h$ , separated by a distance of  $g_0$  from a fixed electrode with the same surface as the membrane. The pressure is applied on the upper face of the membrane, while the lower face is considered to be under a perfect vacuum. The following equations are defined under the small displacement assumption, i.e., the deformation is lower than membrane thickness.

#### Deflection of a circular membrane

Under the effect of a difference of pressure between its two faces, a membrane deflects. This deflection depends on a parameter called the stiffness. The stiffness of a membrane is its ability to resist deformation. The stiffer a membrane is, the less it deforms when subjected to an external force. The stiffness of a membrane is determined by its material, thickness, and area. For a circular membrane, it is defined as:

$$k_m = \frac{16\pi E h^3}{3(1-\nu^2)R^2} \quad (2.1)$$

with  $E$  the Young's modulus and  $\nu$  the Poisson's ratio of silicon, and  $h$  the thickness of the membrane.

In the case of a circular membrane, the deflection  $w$  of each point  $r$  of the radius  $R$  (supposing a deflection much smaller than the membrane thickness  $h$ ) when a pressure  $P$  is applied uniformly on it is given by [1] :

$$w(P, r) = \frac{\pi R^2}{k_m} P \left( \left( \frac{r}{R} \right)^4 - 2 \left( \frac{r}{R} \right)^2 + 1 \right) \quad (2.2)$$

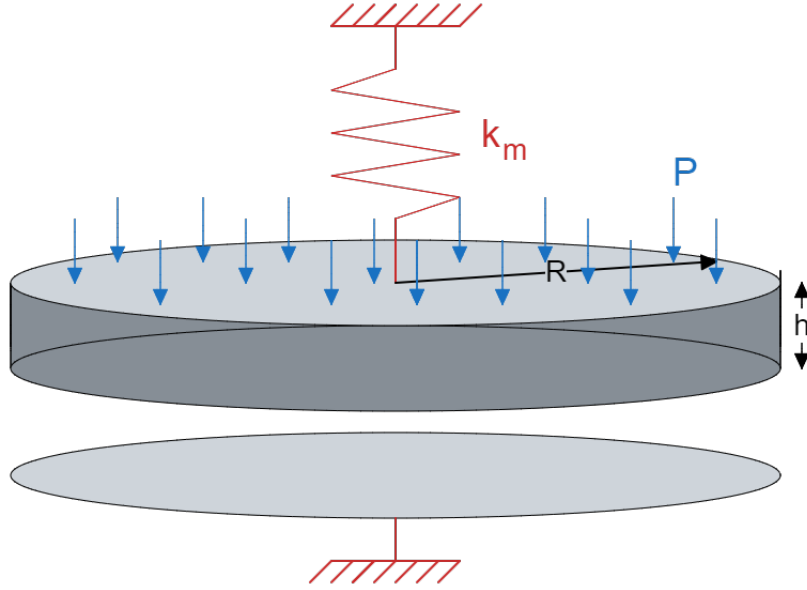


Figure 2.2: Spring model of a circular membrane of surface  $S$  under a pressure  $P$ , modeled with a stiffness  $k_m$ .

Equation 2.2 applied at  $r = 0$  shows that the center of the membrane can be modeled as a spring of stiffness  $k_m$  on which a pressure  $P$  is applied on a surface  $S = \pi R^2$ , as shown in Figure 2.2.

### Variation of capacitance with pressure

Due to the deflection of the membrane with pressure, the capacity between the MEMS and the lower electrode changes:

$$C_S = \int_0^R \frac{2\pi r \epsilon_0}{g_0 + \frac{h}{\epsilon_r} - w(P, r)} dr \quad (2.3)$$

with:  $\epsilon_0$  the vacuum permittivity,  $\epsilon_r$  the permittivity of the material of the membrane,  $g_0$  the value of the gap, i.e., the thickness of the void between the bottom electrode and the membrane and  $w$  the deflection under a pressure  $P$  defined by equation 2.2. The integral is present in the equation because the deflection is not constant over the membrane surface.

### Stress in membrane

On an other way, the pressure applied on the membrane creates internal constraint (or stress)  $\sigma$  within the material of the membrane. This internal stress arises due to the deformation of the membrane material as it attempts to accommodate the applied pressure. This stress is maximum at the surface of the membrane, and can be deduced from the curvature  $\frac{\partial^2 w(P, r)}{\partial r^2}$  [1]:

$$\sigma(r) = 2 \frac{Eh}{1-\nu^2} \frac{\pi}{k_m} P \left( 3 \left( \frac{r}{R} \right)^2 - 1 \right) \quad (2.4)$$

In case of circular membrane, the stress at its surface is maximal at the edge, where the membrane is clamped, i.e. for  $r = R$ .

### 2.4.3 Determination of the MEMS dimensions

Based on the equations of the previous section, the MEMS can be defined by three dimensions: the radius of the membrane, denoted by  $R$ ; the gap between the membrane and the lower electrode, denoted by  $g_0$  and the thickness of the membrane denoted by  $h$ . Each variant of the MEMS can be therefore characterized by this triplet  $(R, h, g_0)$ . From the requirements defined in the previous sections, a Python script was written to determine the sets of triplets that meet the requirements. Key parameters of the MEMS (for example its resonance frequency of deflection) can be plotted as a function of these parameters in order to find valid designs, as shown in Figure 2.3.

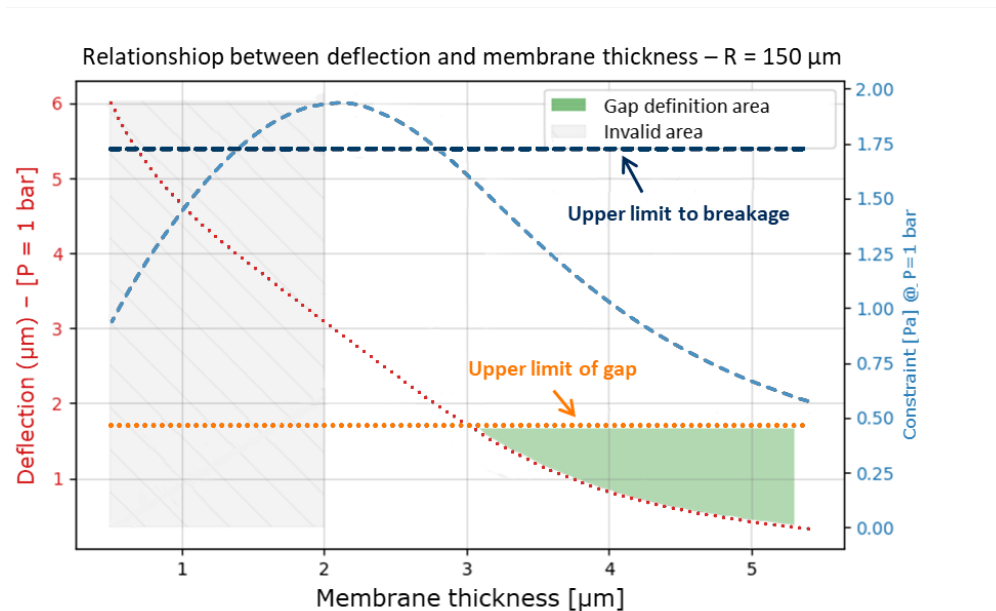


Figure 2.3: Example of curves used to determine MEMS dimensions sets for a radius  $R = 150\mu m$ . The green area represents the zone where the thickness (in x-axis) and the gap (in y-axis) can be extracted. In this area, the triplet  $(R, g_0, h)$  are considered as valid, as the deflection (red curve) is lower than the upper limit of the gap (orange line), and the stress (blue curve) is lower than the upper limit to breakage (dark blue line).

The curves can be analyzed as:

- On the x-axis there is the thickness of the membrane for a defined value of radius  $R$ , the figure shows as an example a radius  $R = 150\mu m$ .
- The red curve represents the deflection of the membrane at 1 bar as a function of its thickness.
- The orange horizontal line represents the limit value of the gap above which the imaginary part of the MEMS impedance exceeds the limit value of  $500\Omega$  at 868 MHz. The chosen gap value must then be lower than this value and lower than the deflection at 1 bar.
- The curve in blue is the value of the maximum stress in the membrane at 1 bar extracted from equation 2.4, and the dark blue horizontal line is the limit to breakage of silicon.

- The shaded area represents the area where the equation for the maximum stress in the membrane is no longer valid. In fact, by reducing the thickness of the membrane, the maximum stress can only increase, not decrease as shown here. This is because the deflection at 1 bar has become much greater than the membrane thickness, so the small displacement approximation used to determine the stress equation is no longer valid.
- Finally, the green area represents the set of parameters in which the values of the gap and the thickness can be chosen and which respect the requirements. In this area, the theoretical deflection at 1 bar is smaller than the gap between the membrane and the lower electrode, and the maximal stress in the membrane does not break it. Also, the value of the reactance is less than  $500\Omega$  in absolute value at 868 MHz.

For this value of radius of the membrane, a triplet of dimensions is then determined by taking a point in the green zone, for this value of radius, the thickness is determined thanks to the abscissa of the point and the gap thanks to the ordinate of this point. By varying the radius  $R$ , several of these graphs were plotted to determine the parameter sets. In order to have different behaviors of MEMS, while lowering the fabrication risks, four values of gap and four values of membrane thickness were chosen, then forming eight different triplets  $(R, h, g_0)$ . The dimensions sets chosen are summarized in Table 2.4.3.

Set 1			Set 2		
Radius $R$	Gap $g_0$	Thickness $h$	Radius $R$	Gap $g_0$	Thickness $h$
75 $\mu\text{m}$	0.3 $\mu\text{m}$	2.5 $\mu\text{m}$	100 $\mu\text{m}$	0.5 $\mu\text{m}$	3 $\mu\text{m}$
100 $\mu\text{m}$	0.3 $\mu\text{m}$	3.5 $\mu\text{m}$	125 $\mu\text{m}$	0.5 $\mu\text{m}$	4 $\mu\text{m}$
100 $\mu\text{m}$	0.7 $\mu\text{m}$	2.5 $\mu\text{m}$	125 $\mu\text{m}$	1 $\mu\text{m}$	3 $\mu\text{m}$
125 $\mu\text{m}$	0.7 $\mu\text{m}$	3.5 $\mu\text{m}$	150 $\mu\text{m}$	1 $\mu\text{m}$	4 $\mu\text{m}$

Table 2.1: Table of the dimensions triplet chosen for the MEMS

#### 2.4.4 Validation of the model

In order to validate the chosen dimensions of the membranes, the membranes were simulated on the Ansys Mechanical software. The goal was to verify the deflection and the maximal constraint on the membrane. The membrane is made of silicon and the mean value of the Young's modulus is 162.7 MPa, while the Poisson's ratio is 0.27.

An example of the simulation at 1 bar of the membrane with dimensions of  $(R = 100\mu\text{m}, g_0 = 0.3\mu\text{m}, h = 3.5\mu\text{m})$  is shown in Figures 2.4 and 2.5. Simulations were done between 0.1 and 1 bar and the maximum value of the deflection (i.e., at the center of the membrane) and the maximum value of the constraint (i.e., at the edge of the membrane) was extracted.

The dimensions chosen for the membranes were then validated, based on the good correlation between the results of simulation and from analytical model. Based on those dimensions, the process flow can be defined, in order to obtain the complete MEMS geometry, which is used in simulation to extract the MEMS impedance.

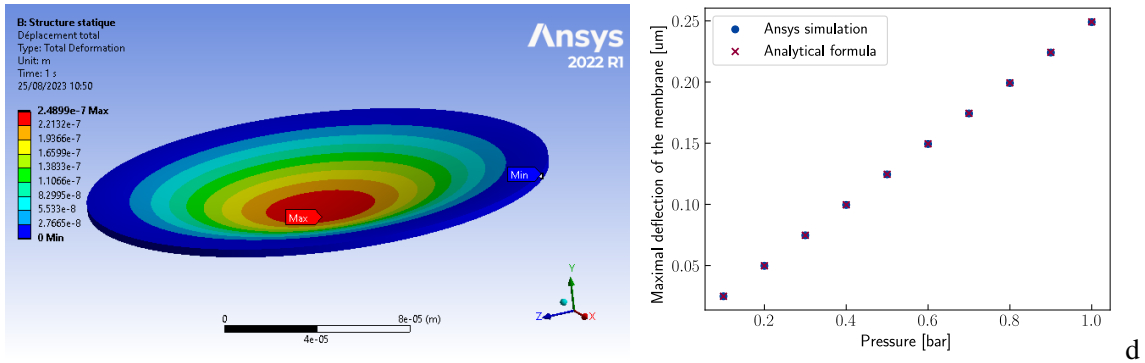


Figure 2.4: Simulation on Ansys Mechanical of the deflection of the membrane of the MEMS with dimensions of ( $R = 100\mu\text{m}$ ,  $g_0 = 0.3\mu\text{m}$ ,  $h = 3.5\mu\text{m}$ ) at 1 bar and comparison between the maximal deflection extracted from simulation and from equation 2.2.

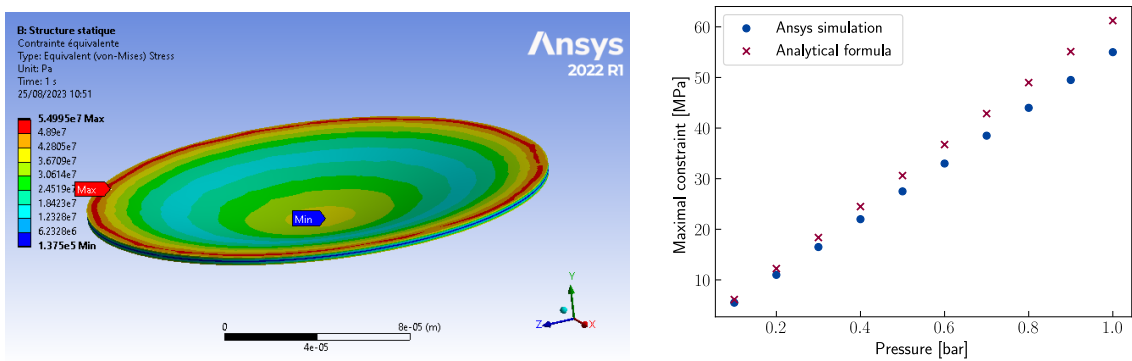


Figure 2.5: Simulation on Ansys Mechanical of the constraint on the membrane of the MEMS with dimensions of ( $R = 100\mu\text{m}$ ,  $g_0 = 0.3\mu\text{m}$ ,  $h = 3.5\mu\text{m}$ ) at 1 bar and comparison between the maximal constraint extracted from simulation and from equation 2.4.

## 2.5 Microfabrication process and masks designs

Now that the global geometry of the MEMS has been chosen, this part focuses on the MEMS fabrication process flow and the masks design.

### 2.5.1 Process flow

The process flow developed here is based on a CMUT process flow, adapted to be compatible with the constraints presented at the beginning of this chapter. It contains around 100 steps of fabrication, and 10 masks of photolithography. Figures 2.6 to 2.14 present the main steps of the fabrication process. In these figures, the dimensions in the z axis for each step are relatively 6 times larger than the real dimensions to be more easily visible. Also, the thickness of the wafer is lower than the real thickness (725  $\mu\text{m}$ ). On each wafer, there are 45 photorepetition fields, with 121 cells of  $2 \times 2 \mu\text{m}$  on each field.

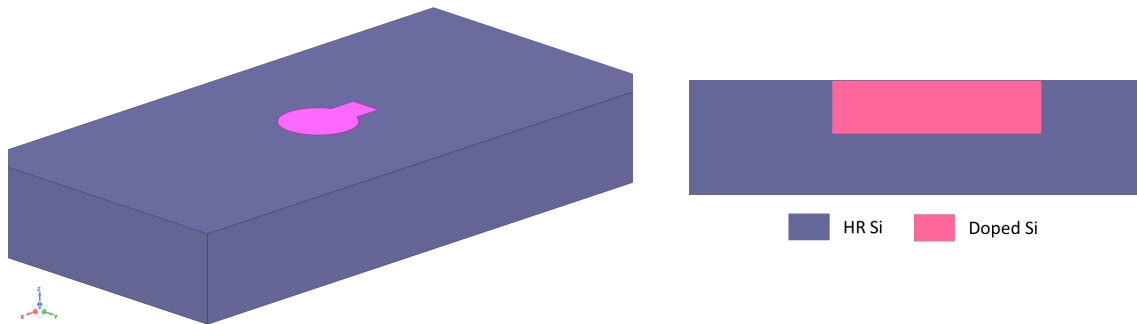


Figure 2.6: Photolithography and dopant implantation of Boron atoms at a concentration of  $5 \times 10^{15}$  atoms/cm<sup>2</sup> and an energy of 240 keV on a 200mm high-resistivity (HR) silicon wafer to define the lower electrode, fixing the value of the radius  $R$ . The implantation creates an area with free charges which locally increase the conductivity. It is followed by an annealing step at 1000°C for 12 hours, to activate and diffuse the doping agents in depth. The AlCu metallization is not possible for the lower electrode as few of the subsequent manufacturing stages include annealing at temperatures higher than the melting point of AlCu.

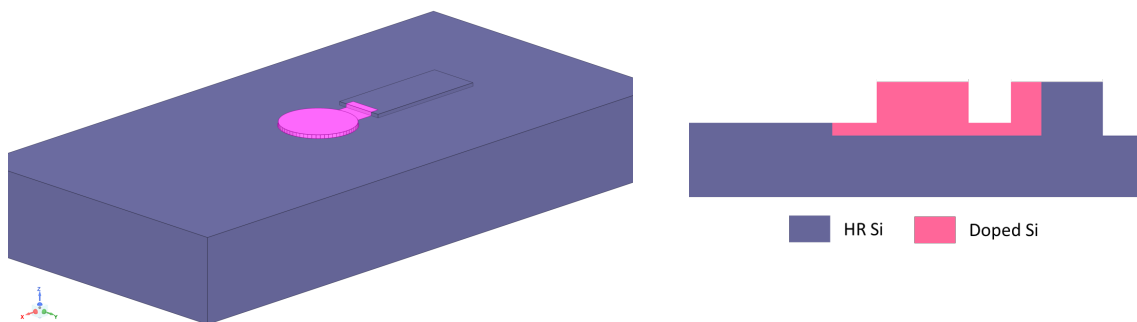


Figure 2.7: Photolithography and silicon dry etching to prepare for the SiO<sub>2</sub> deposition. This SiO<sub>2</sub> is used in a subsequent step to bond the membrane.

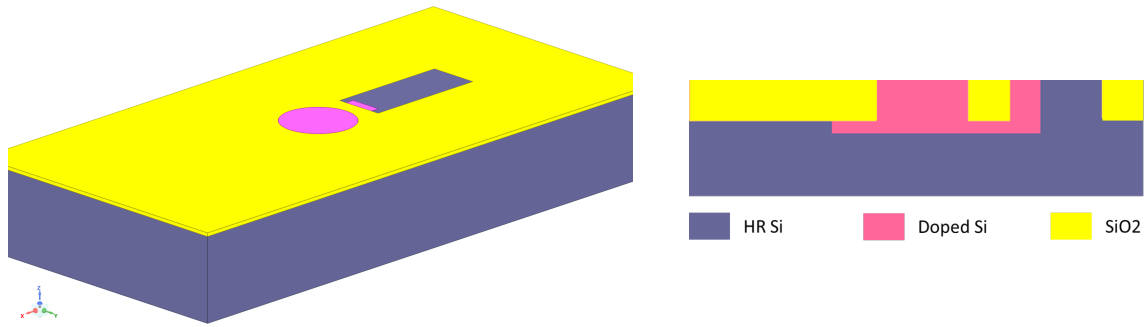


Figure 2.8:  $\text{SiO}_2$  deposition using Plasma-Enhanced Chemical Vapor Deposition (PECVD). The etched parts of the previous steps are filled with  $\text{SiO}_2$ . A Chemical Mechanical Polishing (CMP) is done in order to planarize the oxide.

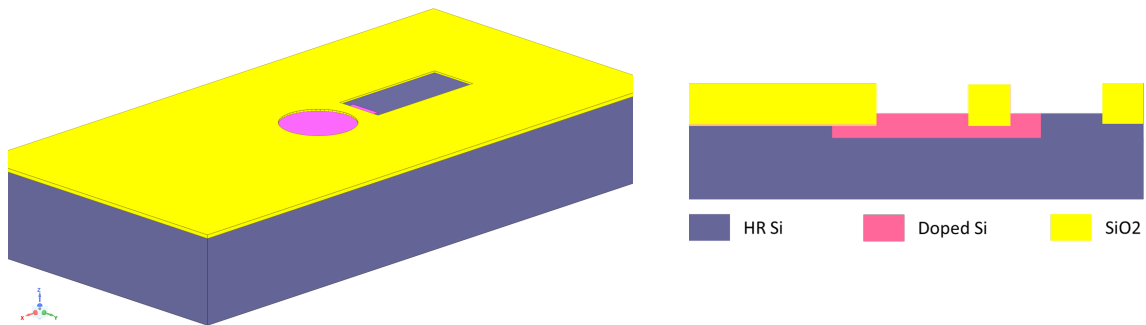


Figure 2.9: Silicon etching to fix the values of the capacitor gap  $g_0$ . The silicon is etched in the areas where there is no oxide. Two etching splits using two different masks are made on each wafer to get two different gap values.

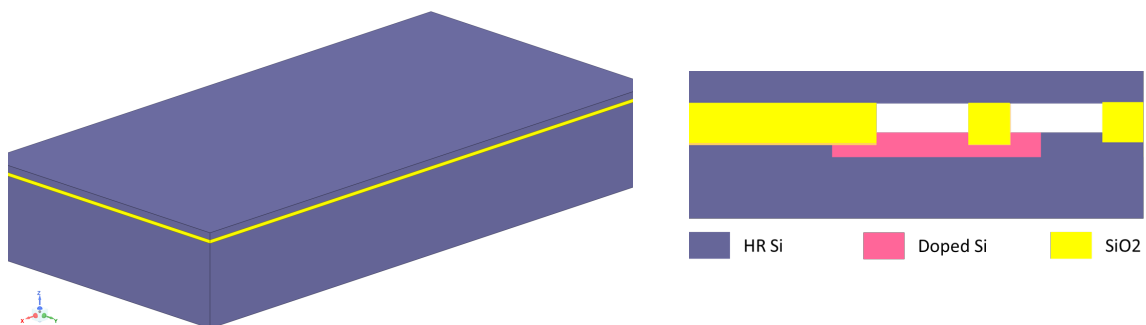


Figure 2.10: Direct bonding under vacuum ( $P = 5 \times 10^{-2} \text{ mbar}$ ) of a SOI wafer and thinning to create the pressure sensor highly resistive membrane layer  $4\mu\text{m}$  thick. The buried oxide layer of the SOI wafer is  $1\mu\text{m}$  thick and the top silicon  $4\mu\text{m}$  thick. The bonded surfaces needs to be as planar as possible to have a high-quality bonding. After the bonding, the bulk is grinded in order to reduce its thickness up to  $10\mu\text{m}$ . A wet etching is then performed to etch the remaining  $10\mu\text{m}$  of silicon, followed a dry etching to remove the oxide  $1\mu\text{m}$  thick.

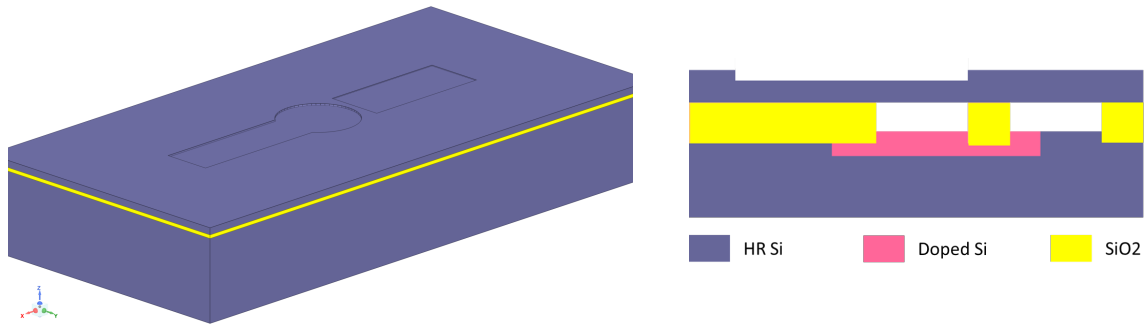


Figure 2.11: Localized thinning of the top Si to fix the value of the membrane thickness  $h$ . Two different etching steps with two different photolithography masks are done for each wafer in order to create two different values of membrane thickness.

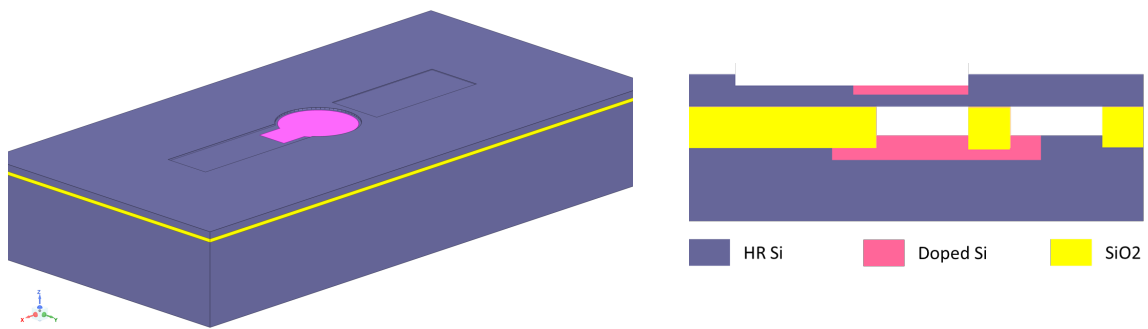


Figure 2.12: Surface implant through a photoresist mask to create the upper electrode on the membrane. The implant dose is  $2 \times 10^{15}$  atoms/cm<sup>2</sup> at an energy of 75 keV. The activation annealing is at 1000°C for 15 min.

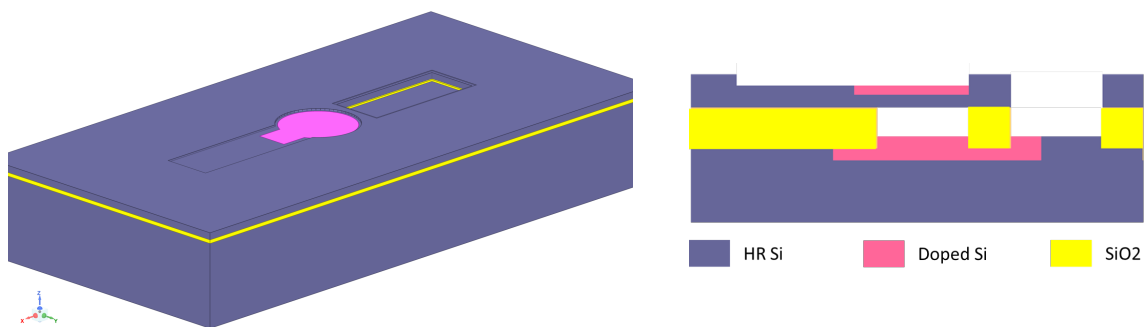


Figure 2.13: Photolithography and Si top dry etching to access the contact of the lower electrode. A hole is also etched at the center of the membrane of reference sensors (for them to be insensitive to pressure).

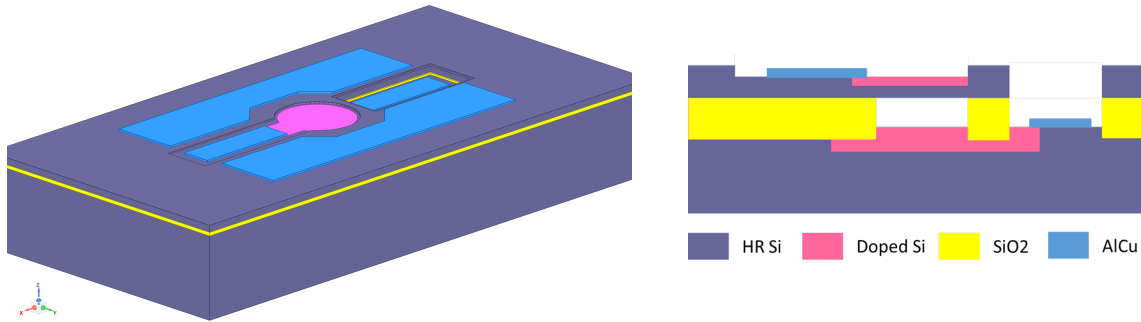


Figure 2.14: Deposition of AlCu for the metallization of contact pads, electrical lines and test structures. The input impedance of the transmission lines is  $50\Omega$ . A deoxidation using Hydrofluoric acid (HF) is carried out before the metal deposition in order to remove any thin layer of native oxide.

The set of parameters that defines the membrane geometry (Table 2.4.3) is adjusted through:

- The implantations set the radius  $R$  of the electrodes (Figures 2.6 and 2.12).
- The etchings shown in Figure 2.9 set the two gaps.
- The etchings shown in Figure 2.11 set the membrane thickness.

### 2.5.2 MEMS designs

For each MEMS with a single triplet of dimensions  $(R, h, g_0)$ , three variants are implemented on the photorepetition field (Figure 2.15): one with the membrane doped by implantation as presented in Figure 2.14, one with the membrane doped by implantation and then metallized and the third one with the membrane metallized but without doping. The metallization steps are used to lower the global resistive part of the MEMS impedance.

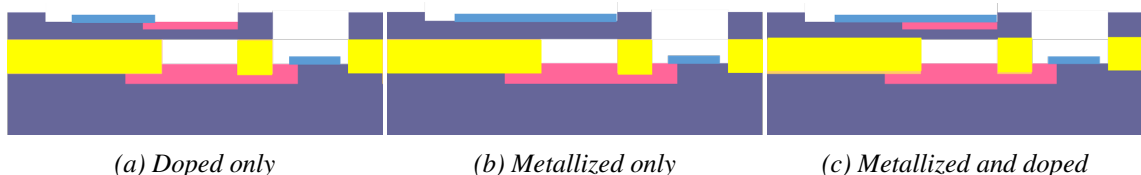


Figure 2.15: Variants of membrane stacks

Each MEMS present also three variants in the lines connected to them: the first one, presented in the last section, used CPW (Coplanar Waveguide Structures) designed to have a  $50\Omega$  input impedance, designed to be characterized using Ground-Signal-Ground probes. The center line is the signal line and is connected to each electrode of the MEMS, and the ground planes are on each side of the center line. The second variant has the same lines but without the ground planes, which can be wire-bonded to the antennas in differential mode or characterized at low frequencies. The last one present a CPW structure with of the two ends short-circuited. It has an important advantages because, in an ideal case, the MEMS impedance is easier to be extracted. There variants are presented in Figure 2.16. There are 240 MEMS on each field, for a total of around 10800 MEMS per wafer.

Figure 2.17 shows the other cells in the photo-repetition field, which contains test RF structures such as open lines, through or short. These structures are used for the de-embedding of MEMS, a procedure which is presented in subsection 2.6.1. Finally, a zone containing the technological test

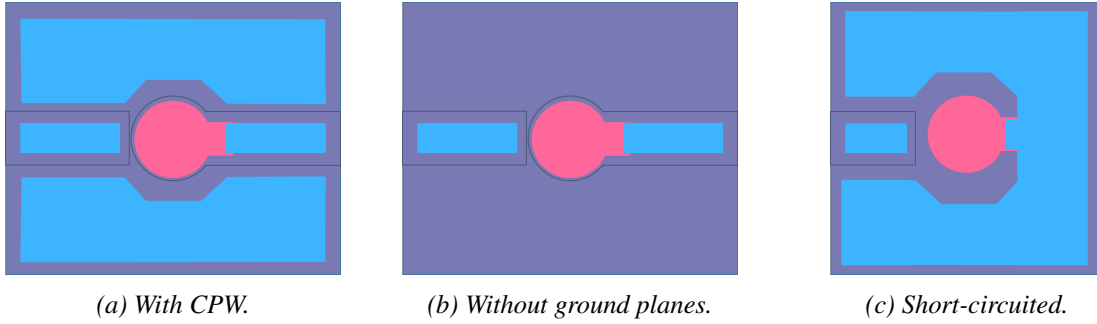


Figure 2.16: Variants of the lines of the MEMS on the wafer.

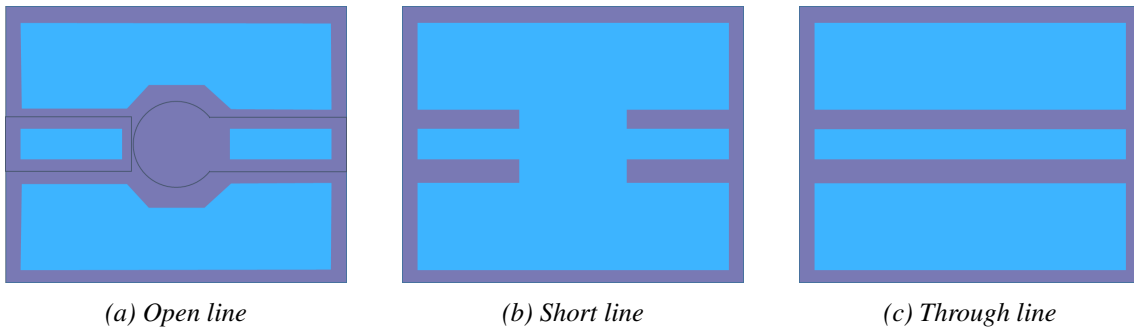


Figure 2.17: Variants of RF test structures on the wafer.

structures was included in order to characterize contact resistances between conductive parts, and the resistivity of the different materials.

## 2.6 Finite element simulations of the MEMS

The geometries of the MEMS presented in the previous section were then implemented in the Ansys HFSS FEM simulation software in order to simulate their RF behavior and extract their equivalent impedance to compare them with the analytical model. The goal of these simulations is to extract the lumped representation of the MEMS and the dependence of the lumped parameters on the pressure. As HFSS is not a multiphysics simulation system, eq. 2.2 was implemented to simulate the deflection of the membrane with the pressure. These equivalent circuits can then be used for the antenna simulations to reduce the simulation time, because the small dimensions and variations of the MEMS with respect to wavelength (around  $\lambda/(10^5)$  in order of magnitude for the value of the gap) imply that the mesh has to be very dense and convergence is more difficult.

### 2.6.1 De-embedding and ABCD matrixes

To extract the equivalent impedance of the MEMS, it is necessary to be in the reference plane of the MEMS, or in other words, mathematically compensate the influence of the CPW lines. In the simulation (and equivalently in the measurement under probes) the signal is sent and received at the ends of the lines, and those lines affect the measurement of the signal. However, the aim is to extract the impedance of the MEMS alone. To do that, two simulations are used: one of the CPW line and one of the MEMS with the CPW. The scattering matrixes  $S$  of the CPW line and the MEMS with the lines are then extracted from the simulations, respectively named  $S_{cpw}$

and  $S_{s+cpw}$ . Finally, the scattering matrix of the MEMS alone  $S_s$  can be deduced. This operation is usually called "de-embedding". The simulated geometries and their equivalence in terms of  $S$  matrixes are presented in Figure 2.18.  $Z$  matrix,  $Y$  matrix or  $ABCD$  matrix representations can also be used equivalently.

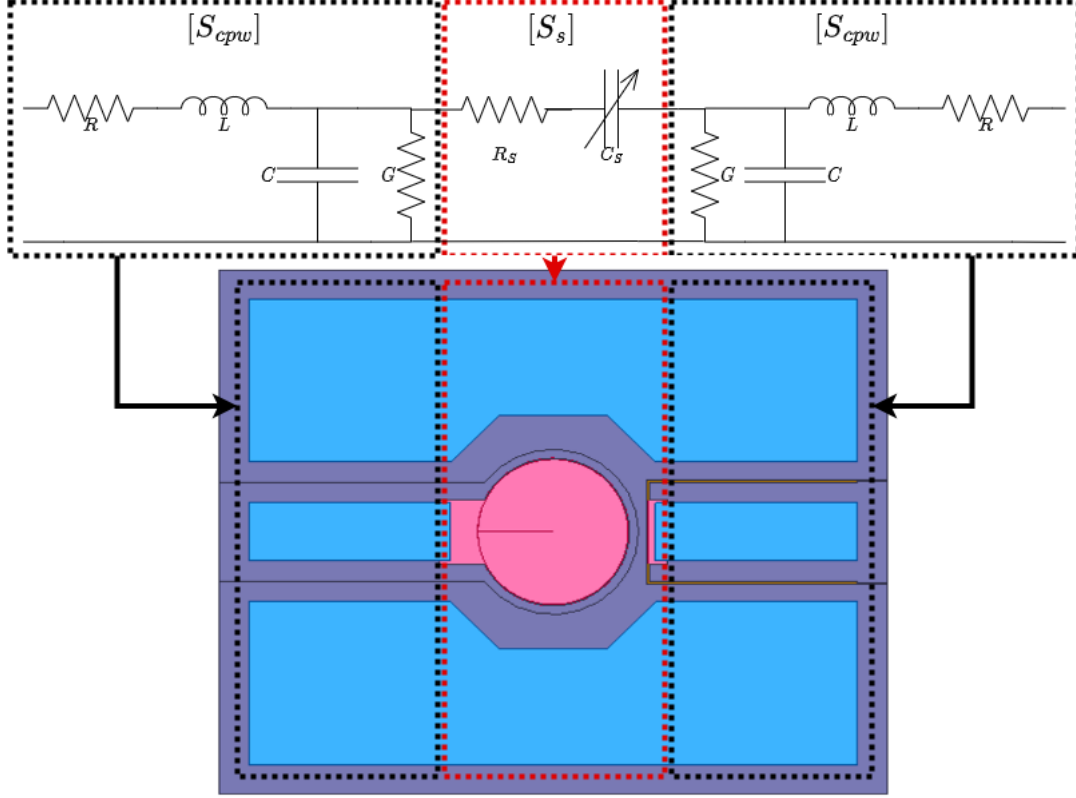


Figure 2.18: Simulated structures with their corresponding  $S$  matrixes and equivalent circuit. The ground planes are neglected in the representation of the MEMS itself.

The easiest way to extract MEMS impedance with de-embedding is to convert the  $Z$  or  $Y$  matrix extracted from HFSS to an other equivalent representation: the  $ABCD$  matrix. For a two-port system, such as our MEMS, the relation between  $ABCD$  matrix and  $Z$  matrix is:

$$\begin{pmatrix} A & B \\ C & D \end{pmatrix} = \begin{pmatrix} \frac{Z_{11}}{Z_{21}} & \frac{|Z|}{Z_{21}} \\ \frac{1}{Z_{21}} & \frac{Z_{22}}{Z_{21}} \end{pmatrix} \quad (2.5)$$

with  $|Z| = |Z_{11}Z_{22} - Z_{12}Z_{21}|$  the determinant of the  $Z$  matrix.

The  $ABCD$  matrix presents two very interesting properties for our requirements:

- The  $ABCD$  matrix of  $N$  cascaded quadripoles is the product of the  $ABCD$  matrix of each individual quadripole. For our MEMS, the  $ABCD$  matrix of the global structure is:

$$[ABCD_{s+cpw}] = [ABCD_{cpw}] \times [ABCD_s] \times [ABCD_{cpw}] \quad (2.6)$$

- The MEMS impedance can be easily extracted from the  $ABCD$  matrix in very common cases. For example, in our case (which is shown later), the MEMS can be seen as a serial impedance. The  $ABCD$  matrix of a serial impedance  $Z$  is:

$$[ABCD] = \begin{pmatrix} 1 & Z \\ 0 & 1 \end{pmatrix} \quad (2.7)$$

## 2.6.2 Simulated structures of MEMS

In order to simulate the RF response of the MEMS, their geometries are implemented on HFSS based on the layout used for the photolithography masks. To simulate each electrode, the conductivity was averaged over the thickness of the implantation. Because Ansys HFSS is not a multiphysics software, the deformation of the membrane due to the pressure is implemented using an equation-based geometry, using the equation of the deflection of the membrane (Eq. 2.2). This model is fully parameterized in order to automatically change the dimensions of the structure for all the dimensions of the MEMS (i.e., the membrane radius, thickness and the gap between the membrane and the lower electrode). The deflection is also automatically calculated based on the sets of MEMS dimensions.

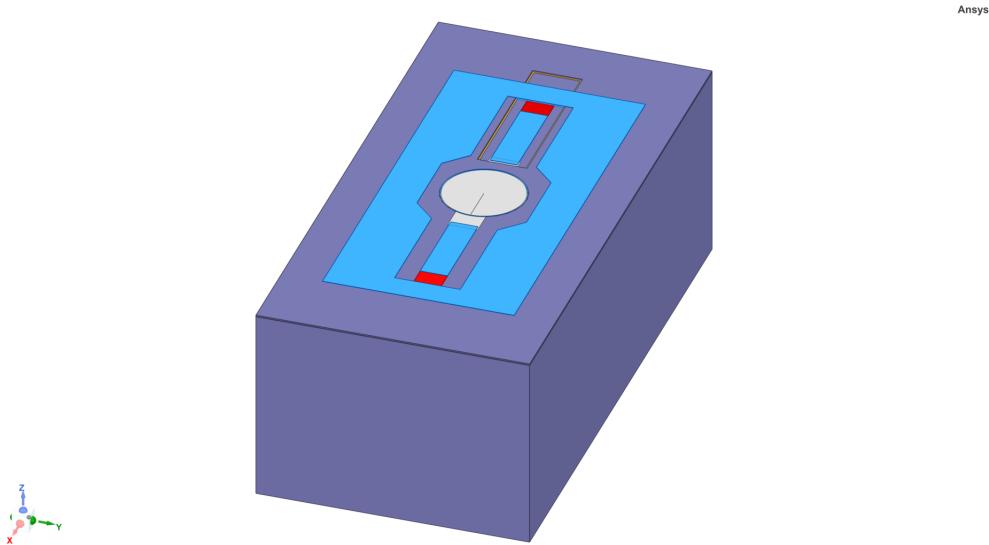


Figure 2.19: MEMS geometry simulated on Ansys HFSS. The red rectangles are the lumped ports.

Then, to simulate the probes used for the characterization, the ground planes are connected behind the central line and a lumped port is used between the signal line and the ground plane. The structure is shown in Figure 2.19. A particular attention is paid to the mesh of the gap between the membrane and the lower electrode: as the variation of capacitance is caused by the variation of the field in this gap, and because the deflection of the membrane is very small compared to the wavelength, the mesh must be very dense to detect this capacitance variation.

The MEMS are simulated over the 1 mbar - 1 bar pressure range. Using the results files extracted from simulations and the `skrf` Python module, the  $S$  matrixes of the MEMS connected with the CPW lines and the CPW lines alone are converted into  $ABCD$  matrixes, named respectively  $[ABCD_{s+cpw}]$  and  $[ABCD_{cpw}]$ . The deembedded  $ABCD$  matrixes of the MEMS are then extracted using Eq. 2.6. These matrixes have the form of a series RC circuit. Figures 2.20 and 2.21 shows the capacitances extracted from simulation in comparison with those extracted with the analytical representation. The analytical results are obtained by combining equations 2.2 and 2.3, and integrating on them the parameters of Table 2.4.3. Then, the value of the capacitance can be estimated as well as its variation with pressure. Both analytical formulas and simulations shows a capacitance with the same variation and the same order of magnitude, with a slight difference between simulation and analytical results.

The observed differences can be explained by several hypotheses or facts:

- The electrodes of the MEMS are made of highly doped silicon, which is not equivalent to the perfect metallic electrodes of the parallel plate capacitor.

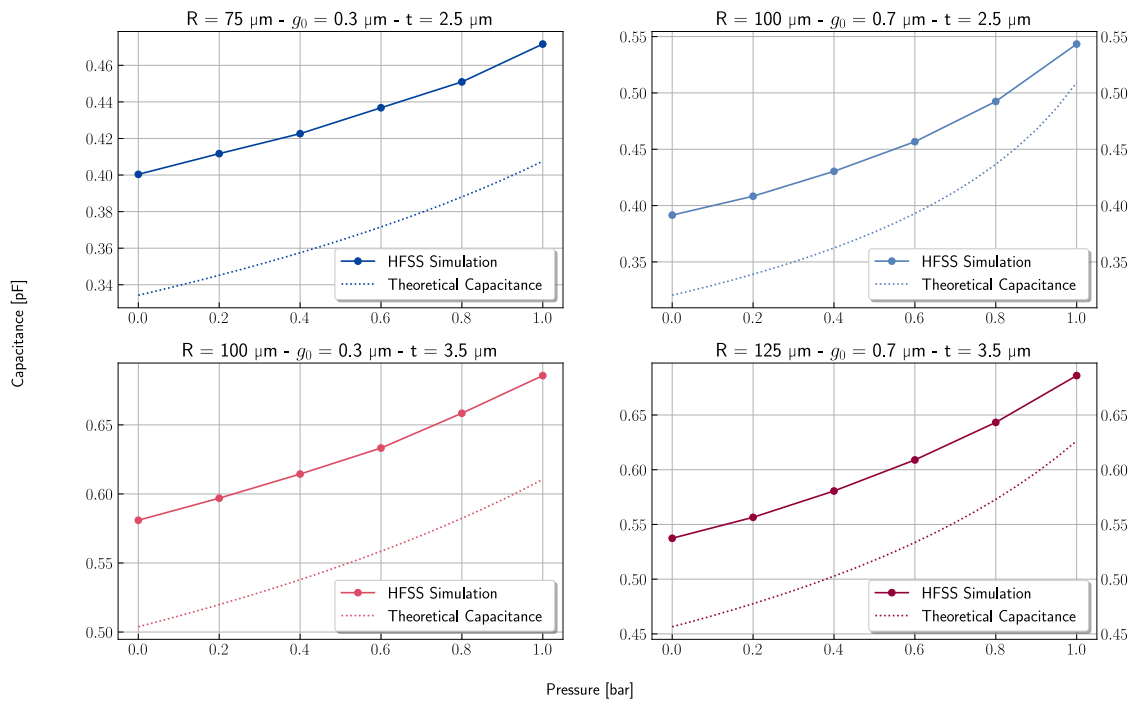


Figure 2.20: Simulated equivalent capacitance of the MEMS of the first set and comparison with analytical results.

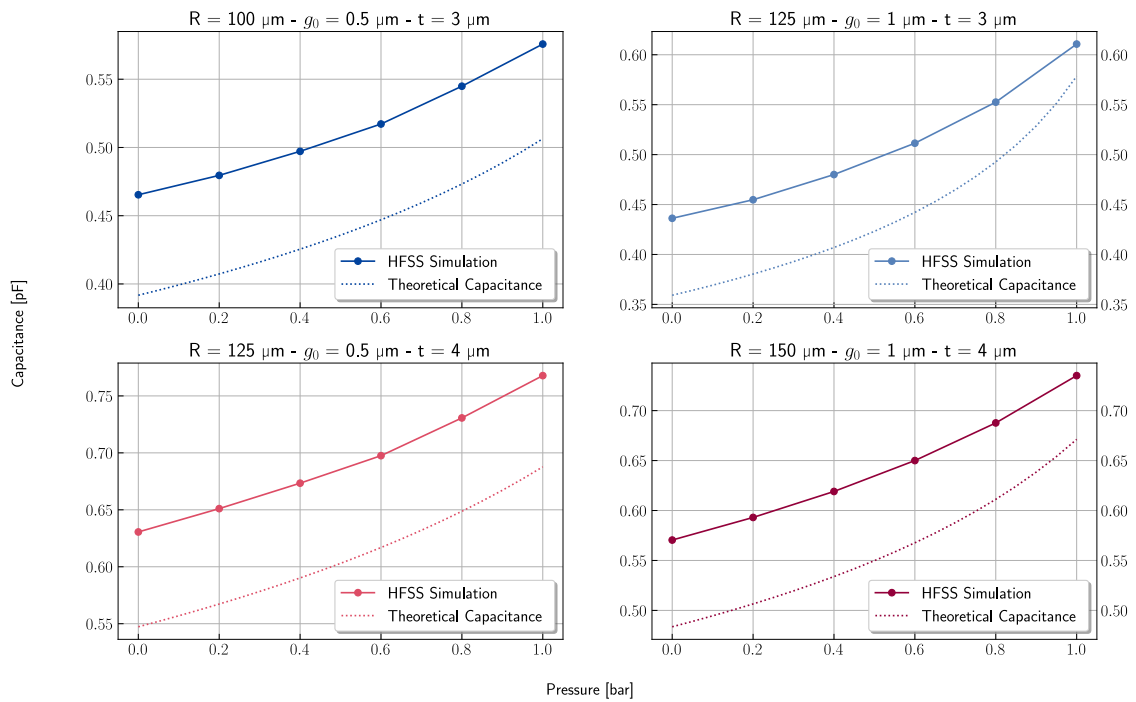


Figure 2.21: Simulated equivalent capacitance of the MEMS of the second set and comparison with analytical results.

- A non-uniform repartition of the current on the electrodes, due to skin effect in radiofrequency.
- To a lesser extent, simulation inaccuracies due to the small gap variation with pressure compared to the wavelength.

The MEMS were designed to have a behavior dependent on pressure, which is confirmed in the capacity variation curves. The MEMS have different capacitance values and different variation of capacitance with pressure.

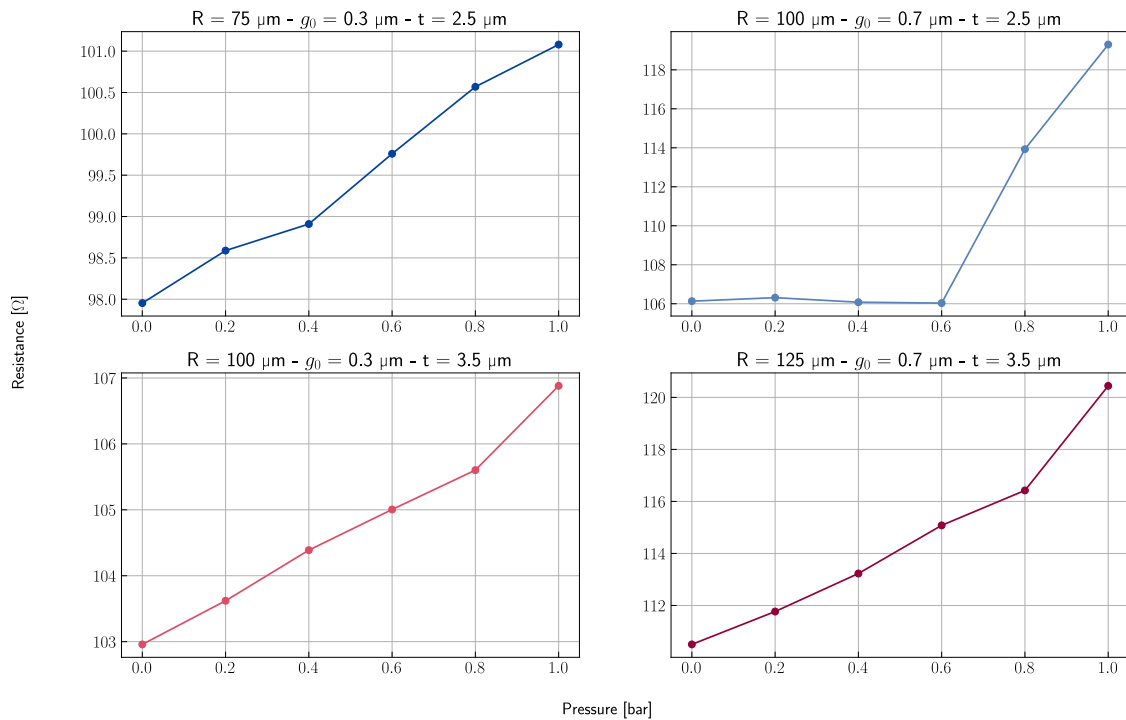


Figure 2.22: Simulated resistance of the MEMS of the first set.

The equivalent resistances of the MEMS were only obtained on simulation, and they are around 100Ω, (their evolutions are shown in Figure 2.22 and 2.23). This resistance is relatively similar for the sensor with the metallized membrane. It shows that it comes mainly from the bottom electrode doping.

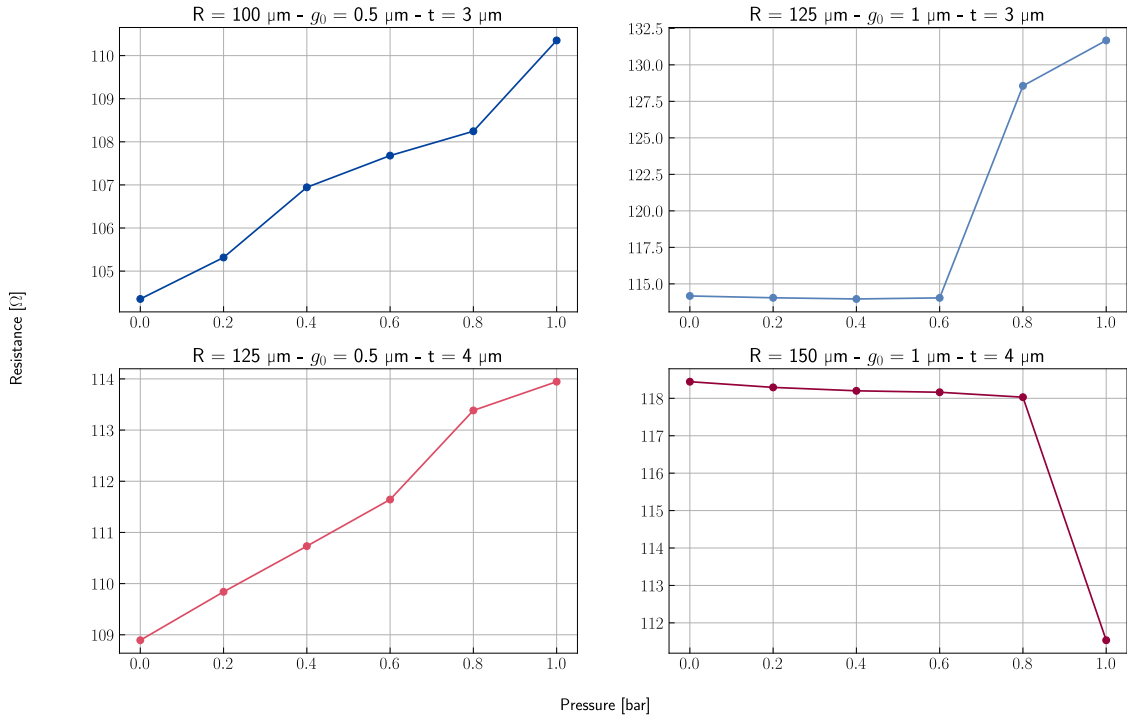


Figure 2.23: Simulated resistance of the MEMS of the second set.

### 2.6.3 Dimensioning of the CPW lines

To allow proper probing characterization, the lines structures must have a characteristic impedance  $Z_0 = 50\Omega$ . The dimensions of each cell on the wafer are  $2 \times 2 \text{mm}$ , with two MEMS per wafer and a margin of  $150\mu\text{m}$  at each edge for wafer dicing. The width  $W$  of the signal line is defined as  $100\mu\text{m}$  to allow wire-bonding with the antenna. Taking all this into account, the sum of the width of the ground plane  $W_g$  and the gap between the signal line and the ground plane  $S$  must be equal to  $300\mu\text{m}$ . The characteristic impedance of a CPW line depends only on  $S$ , on  $W$ , on the substrate thickness  $H = 725\mu\text{m}$  and on its relative permittivity  $\epsilon_r = 11.9$ , and is defined as [2]:

$$Z_0 = \frac{30\pi}{\sqrt{\epsilon_{eff}}} \frac{K(k')}{K(k)} \quad (2.8)$$

where

$$\epsilon_{eff} = 1 + \frac{\epsilon_r - 1}{2} \frac{K(k')K(k_1)}{K(k)K(k'_1)} \quad (2.9)$$

and

$$k = \frac{W}{W + 2S} \quad (2.10)$$

$$k_1 = \frac{\sinh \frac{\pi W}{4H}}{\sinh \frac{\pi(W+2S)}{4H}} \quad (2.11)$$

with  $K$  the complete elliptic integral of the first kind, and  $k' = \sqrt{1 - k^2}$ .

Using this model, the obtained width of the gap  $S$  is equal to  $70\mu\text{m}$ , and a ground lines width  $W_g$  of  $230\mu\text{m}$ .

### 2.6.4 Properties of the lines

The model presented above assumes the ground plane is infinite, which is of course not feasible in practice. The geometry of CPW with narrow ground planes is named Finite Ground Coplanar Waveguide (FGC). Ponchak [3] studied the properties of this structure of line with backside metalization, and concludes that "FGC waveguide has low attenuation, low dispersion, and no parasitic resonances if the ground plane width is at least twice the center conductor width and the total line width is less than  $\lambda_d/4$ ". This part focuses on comparing the properties of the CPW and FGC lines.

#### Characteristic impedance of the FGC structure

The model presented above is used to determine the dimensions of the line and the characteristic impedance must be verified in simulation with narrower ground planes. The simulated FGC line has dimensions  $W = 100\mu m$ ,  $S = 70\mu m$ ,  $W_g = 230\mu m$  and a length of 1mm. The metal is aluminum of  $1\mu m$  thickness over a  $725\mu m$  thick silicon. Two wave-ports are used for the excitation. Figure 2.24 shows the characteristic impedance of the FGC line. It shows that the impedance is very close to  $50\Omega$ , which confirms the model and the dimensions used. Because the line is very short compared to the wave-length, the characteristic impedance is constant, as the resistance and conductance of losses per unit length are very low compared to the capacitance and inductance in the transmission-line representation.

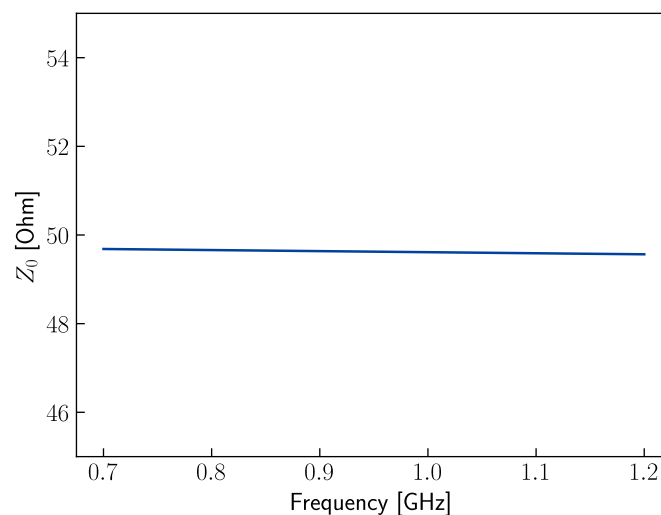


Figure 2.24: Characteristic impedance of a 1mm-long line

#### Attenuation

To compare the attenuation of FGC and CPW lines, a 1mm-long FGC line with the dimensions defined above is simulated and compared with a CPW structure with a width of ground planes of  $480\mu m$ . The simulated lines with their mesh and the electric field are shown in Figure 2.25.

The lines were excited using a wave port on one side of the lines (port 1), and another wave port on the other side (port 2) to study the propagation properties of each line. The  $S_{21}$  parameters, which represents the relative amount of power sent by port 1 to port 2 are shown in Figure 2.26.

The losses in the two geometries are very low, but they are even lower for the FGC structure with the width of ground planes of  $230\mu m$ . These results confirm the assumption made in the section 2.6.4 above the low resistance and conductance of losses of the line. This geometry of FGC lines with ground planes of  $230\mu m$  was then chosen.

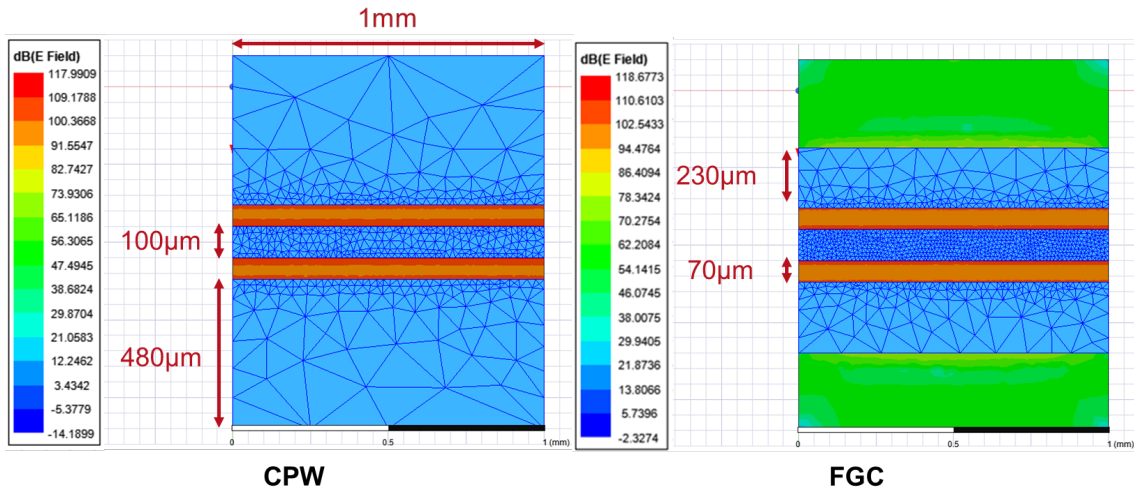


Figure 2.25: EM simulation using Ansys HFSS of CPW and FGC lines with their dimensions and the electric field.

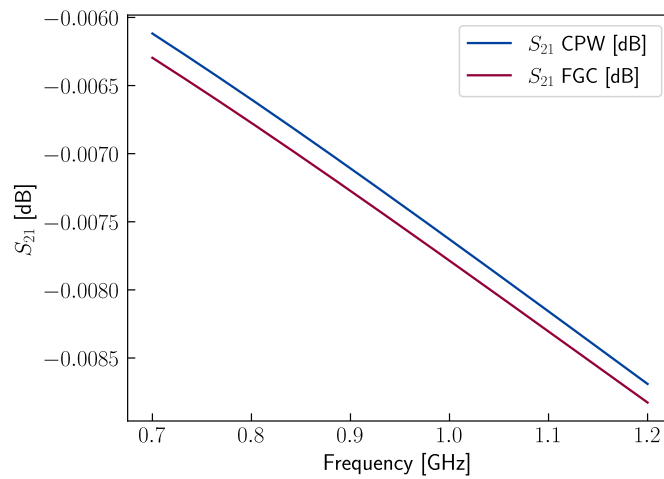


Figure 2.26: Transmission properties of the two types of lines

### Cross-talk

As described above, there are two MEMS in each chip of  $2 \times 2 \mu\text{m}$ , with a distance of  $300 \mu\text{m}$  between the upper ground plane of one MEMS and the lower ground plane of the other. Pappalopoulos studied the cross-talk between two FGC lines [4], and made the same conclusion as Ponchak [3], which is that the width of the ground plane must be at least 2 times larger than the central line to obtain a good insulation.

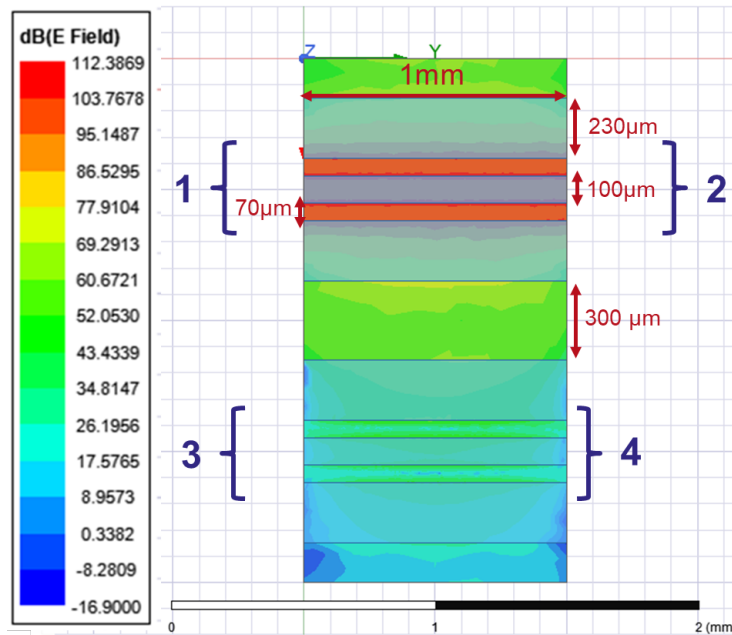


Figure 2.27: FGC lines simulated to evaluate the cross-talk, with the electric field, the dimensions in red and the port number in blue.

To evaluate the cross-talk, two FGC structures with a distance of  $300 \mu\text{m}$  between them are simulated, as shown in Figure 2.27. The dimensions are shown in red. Wave-ports are used on each boundary of the lines, and they are numbered from 1 to 4 as shown in the figure. The excitation is made in the port 1.

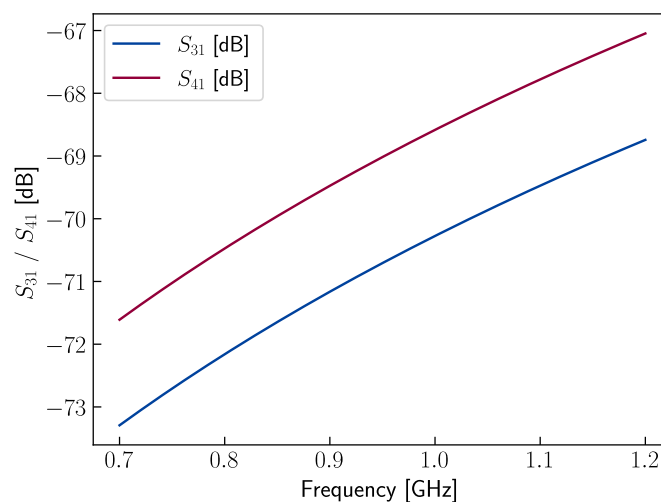


Figure 2.28: Cross-talk between two lines on the same chip separated by  $1000 \mu\text{m}$  between the center of the signal lines.

To evaluate the insulation,  $S_{31}$  and  $S_{41}$  are plotted in Figure 2.28. For the two scattering parameters, the values are around -70 dB, which confirms the good insulation between the two lines. The magnitude of the electric field is much lower outside of the line than between the ground planes and the signal line. This confinement of the electric field prevents cross-talk between the lines, i.e., good insulation between the two lines. Furthermore, in order to confirm the insulation, two MEMS on a single chip are then simulated. The structure with the magnitude of the electric field is shown on Figure 2.29. The total length of the geometries (sensor + lines) is 1700 $\mu\text{m}$ .

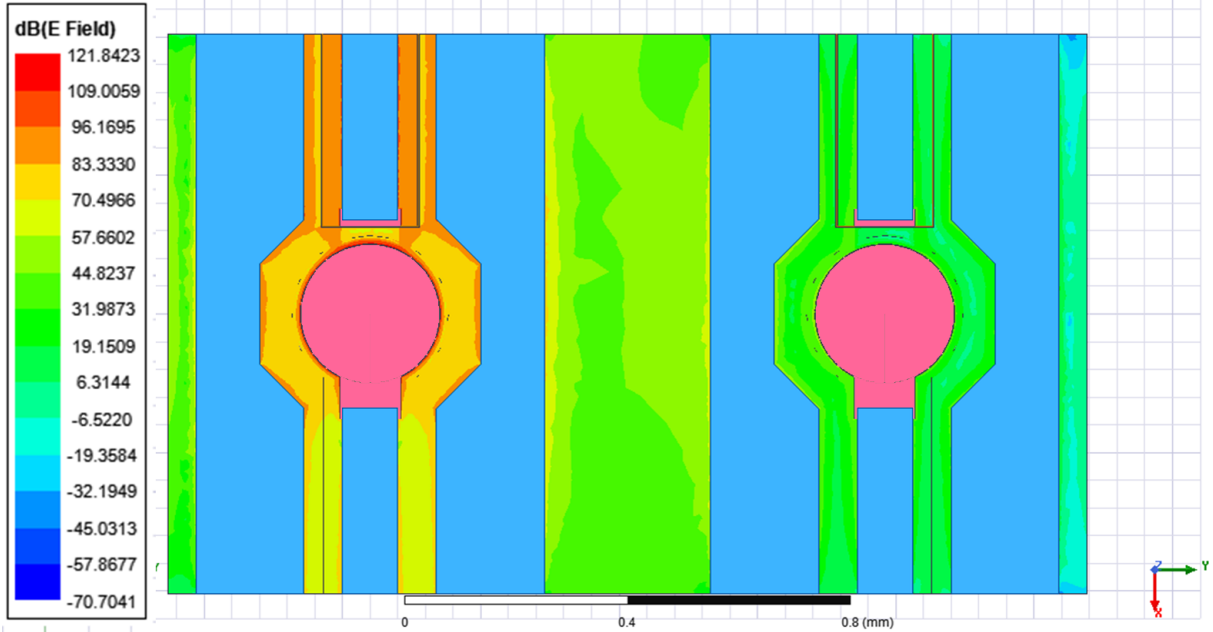


Figure 2.29: EM simulation of two MEMS on Ansys HFSS to simulate the cross-talk, with the electric field plotted.

The cross-talk is then plotted on Figure 2.30, and is lower than that between the lines alone. This confirms that the measurement or the excitement of one sensor on a chip does not influence the other one significantly.

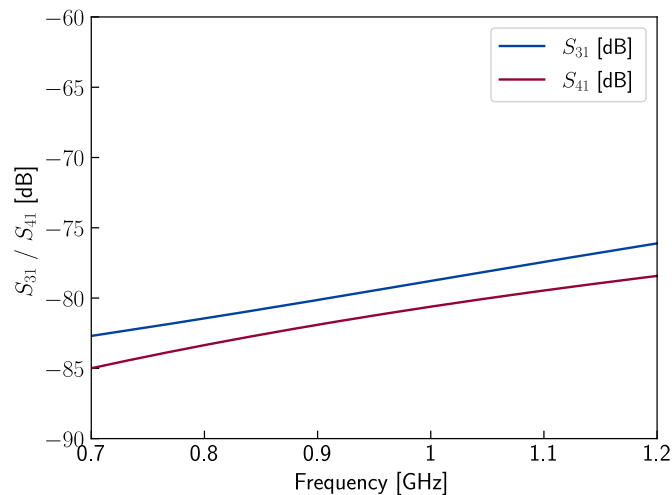


Figure 2.30: Cross-talk between two MEMS on the same chip separated by 1000 $\mu\text{m}$  between the center of the signal lines.

### 2.6.5 Conclusion

As a conclusion, the simulations enabled to obtain a precise geometry of the MEMS and their lines. These lines show low attenuation and cross-talk between the MEMS has been shown to be negligible. The MEMS were simulated to extract their variation of impedance with the pressure, based on a parameterized geometry of the membrane implemented on Ansys HFSS. For this thesis, the simulated impedance were used to define the strategy of design of the antenna thanks to analytical models and simulations, which are presented in the following section. For greater clarity, the lines present on the MEMS will be referred to as CPW in the rest of the manuscript.

## 2.7 Integration with the antenna and impact on the performances

The aim of this section is to study the impact of the MEMS, the antenna and their on the global performance of the system, and more precisely on the sensor resolution. For this technology of sensors, high resolution means high sensitivity and low bandwidth. A better understanding of the system is necessary in order to know the key parameters of the antenna and which aspects should be prioritized to improve the resolution of the global system in the future. It is important to highlight that the precise antenna designs were chosen after the characterization of the MEMS, in order to enhance the performances of the system (better impedance adaptation, sensitivity, bandwidth...). In the following analysis, the resonance frequency is defined as the frequency where the reflection coefficient between the antenna and the load is at its minimal value. The sensitivity is defined as the variation of resonance frequency as a function of pressure, between vacuum and 1 bar. The bandwidth is equal to the difference of the two frequencies where the magnitude of the reflection coefficient is equal to -20 dB. The MEMS is considered to be the antenna load, which means the reflection coefficient is calculated from the MEMS impedance and the antenna impedance.

### 2.7.1 Impact of the antenna structural mode

As explained in section 1.3.5, the RCS of an antenna can be separated in two parts: the structural mode and the antenna mode. The structural mode is inherent to any object, and it is primarily influenced by its physical shape and composition. It is represented by the term  $A$  in Eq. 1.13. The antenna mode is the part of the power that is dependent on the way the incident wave is modified by the MEMS itself, it is then dependent on the load, in our case the MEMS.

As the structural mode is a constant parameter, it does not impact the variation of resonance frequency of the antenna.

### 2.7.2 Impact of antenna size/quality factor

The first study presented here focuses on the impact of antenna size on the resolution of the sensor. As the quality factor is strongly linked with the size of the antenna, two different analyses were done:

- One with a geometry of an antenna whose electrical size can be easily modified. The electrical size of the antenna was changed by adding a lumped element (capacitor or inductance), which allows its dimensions to be changed in order to resonate at 868 MHz.
- One with a generic equivalent model of an antenna: a parallel RLC. The values of the capacitance and the inductance were modified to change the quality factor of the antenna while keeping the resonance frequency at 868 MHz.

For each analysis, the MEMS model used was the RC equivalent circuit obtained by simulations.

### Analysis on a particular antenna geometry

For this analysis, a geometry of Capacitive Loaded Loop (CLL) antenna is used [5], based on an outer parasitic loop (the radiative element) coupled with an inner arc, used in our case to reduce the size of the antenna. The antenna is made of copper printed on a FR4 substrate. This geometry is well suited for our requirements because its electrical size can be easily modified. Here, the MEMS is the antenna load, and it is positioned in the middle of the inner arc. A lumped element (a capacitance or an inductance) is also connected to the outer loop, as shown in Figure 2.31. The MEMS is assimilated to a series RC with a constant resistance value of  $100\Omega$  and a capacitance which varies between  $0.57\text{ pF}$  and  $0.73\text{ pF}$ . The global system is designed to resonate at  $868\text{ MHz}$ .

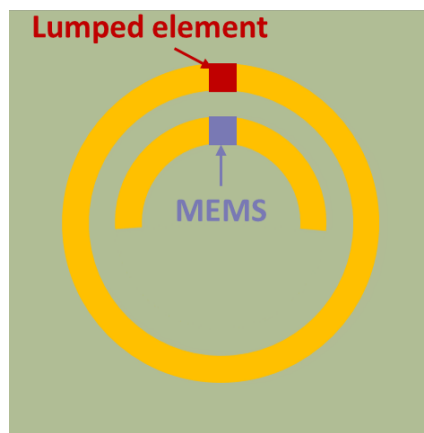


Figure 2.31: CLL antenna used for the analysis of the impact of the electrical size, with the position of the elements

By modifying the value of the lumped element from  $0.1\text{ pF}$  to  $0.4\text{ pF}$  for the capacitor, and from  $90\text{ nH}$  to  $300\text{ nH}$  for the inductance, the resonance frequency of the antenna is shifted, so the dimensions of the antenna must be tuned to make it resonant at the targeted frequency, i.e.,  $868\text{ MHz}$ . Another simulation was done in open circuit (i.e. without lumped element). Figure 2.32 shows the sensitivity of the sensor for a capacitance variation of the MEMS between  $0.57\text{ pF}$  and  $0.73\text{ pF}$  versus the electrical size of the antenna.

It is observed that the sensitivity tends to decrease when the electrical size decreases. This result seems to limit the use of miniature antennas with the MEMS, but it is important to highlight that the bandwidth of the antenna becomes narrower with the decrease of its electrical size, because of the size-dependence of an antenna quality factor. There is less variation of resonance frequency, but the peak of the antenna radar signature is thinner and, so, the maximum can be detected more precisely. Moreover, the detectability is limited by the reduction of the radiation efficiency with the increase of the quality factor. Further studies are needed to determine the impact of miniaturization on the performance.

### Analysis on an equivalent circuit

As explained in section 1.3.6, the quality factor of an antenna is strongly linked to its electrical size. This second analysis is still focused on the variation of resonance frequency, but now by varying the quality factor of the antenna on a more general representation. Here, the antenna is modeled by a RLC parallel circuit, as shown in the Figure 2.33. The condition of matching

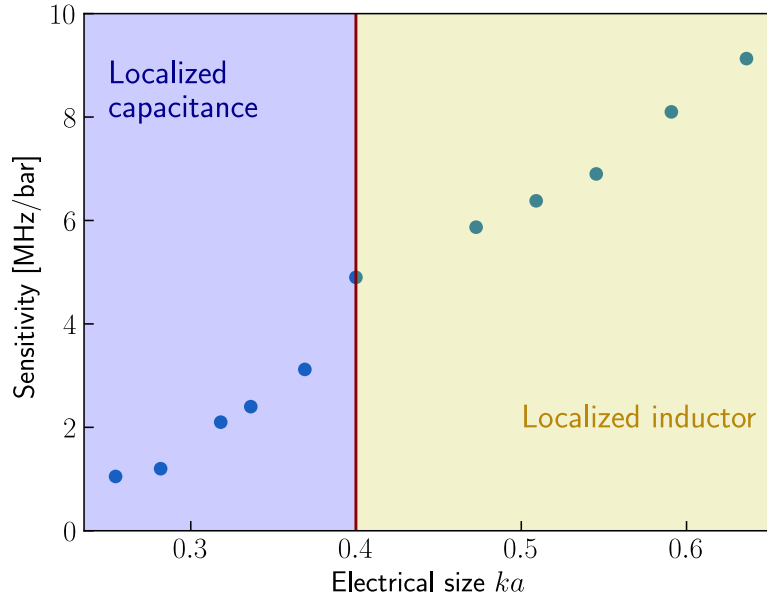


Figure 2.32: Sensitivity of the sensor vs antenna electrical size

impedance is assumed for the lowest value of the MEMS capacitance. The antenna inductance is defined as  $L = \frac{R}{Q_{ant} \omega_{ant}}$  and its capacitance as  $C = \frac{Q_{ant}}{R \omega_{ant}}$ .

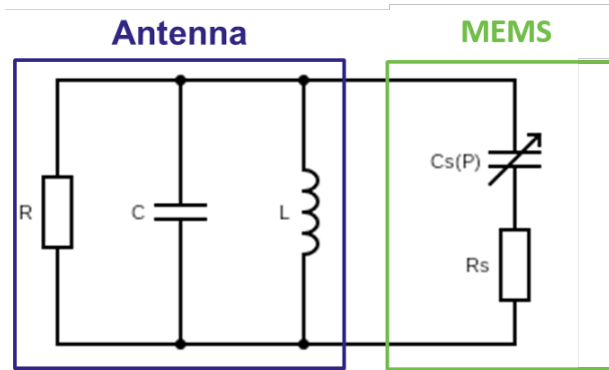


Figure 2.33: Representation by a simplified equivalent circuit of the antenna loaded by the MEMS.

In order to determine the value of the antenna lumped elements for a given value of the antenna quality factor  $Q_{ant}$ , the following methodology is used:

1. The resistance of the antenna  $R$  is determined as  $R = R_S + \frac{1}{R_S(C_S(0)\omega_e)^2}$  with  $\omega_e = 2\pi \times 868\text{MHz}$  and  $C_S$  the capacitance value at a theoretical pressure of 0 bar.
2.  $\omega_{ant}$  is determined with the formula  $\omega_{ant} = \frac{1 + \sqrt{1 + (2Q_{ant}C_S(0)R_S\omega_e)^2}}{2Q_{ant}C_S(0)R_S}$ .
3. The, the values of  $L$  and  $C$  can be deduced.

For example, with a value of  $Q_{ant} = 30$ , the MEMS impedance is defined as  $R_S = 100\Omega$ ,  $C_S(0) = 0.575\text{pF}$  and  $C_S(1) = 0.73\text{pF}$  as simulated in Ansys HFSS. The values of the antenna parameters are then  $R = 1116.87\Omega$ ,  $L = 6.47\text{nF}$  and  $C = 4.67\text{pF}$ .

By shifting the value of the antenna quality factor  $Q_{ant}$ , the variation of the sensitivity of the sensor with the quality factor of the antenna can be studied, as shown in Figure 2.34.

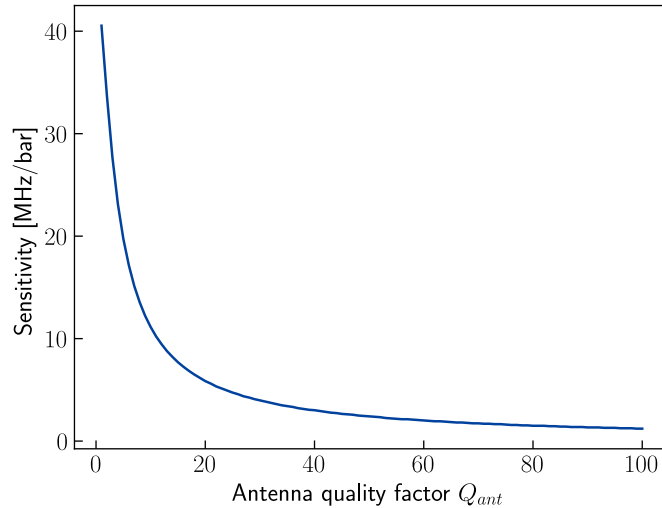


Figure 2.34: Variation of antenna sensitivity with its quality factor.

Again, the sensitivity decreases when the quality factor increases, as explained by the electrical size of the antenna in the previous analysis.

## Conclusion

Both analyses here show that the electrical size of the antenna has a strong impact on the variation of resonance frequency with the capacitance variation. Moreover, a decrease of the electrical size means an increase of the minimal quality factor of the antenna and, thus, narrower peaks in the antenna RCS response. In other words, the sensitivity decreases but also the bandwidth. If the size of the antenna is an important criterion, other parameters of the antenna can be tuned or, to a much greater extent, parameters of the MEMS.

### 2.7.3 Impact of the resistance of the MEMS on the sensitivity

The study here is focused on the impact of MEMS resistance, put as the load of the antenna, on the variation of resonance frequency and bandwidth of the antenna.

Using the same equivalent circuit of the antenna as in the previous section, the impact of the resistive part of the impedance of the MEMS  $R_S$  on the sensitivity is studied for different quality factors of the antenna. It allows to study the impact of the resistance of the MEMS on antennas with different electrical size. The antenna is impedance-matched to the MEMS and to simulate the sensitivity, each MEMS has the same relative variation of reactance  $X_S = 1/(jC_S\omega)$  between vacuum and 1 bar. Here, the relative variation of the imaginary part of the impedance of the MEMS is equal to 10 % (i.e.,  $X_S(1bar) = 0.9 \times X_S(0bar)$ ).

Figure 2.35 shows the impact of the real part of the impedance of the MEMS on the variation of resonance frequency for this two quality factors  $Q_{ant} = 30$  and  $Q_{ant} = 50$ , a capacitance under vacuum  $C_S(1mbar) = 0.575pF$ , and a relative variation of reactance of 10%. It shows that the resistance has an impact on the variation of resonance frequency: the higher the resistance is, the lower the sensitivity.

### 2.7.4 Impact of the wire-bonding

As the MEMS is wire-bonded to the antenna, it is convenient to study how it affects the impedance of the MEMS. The bondwire can be modelled as an inductance, with a value of [6]:

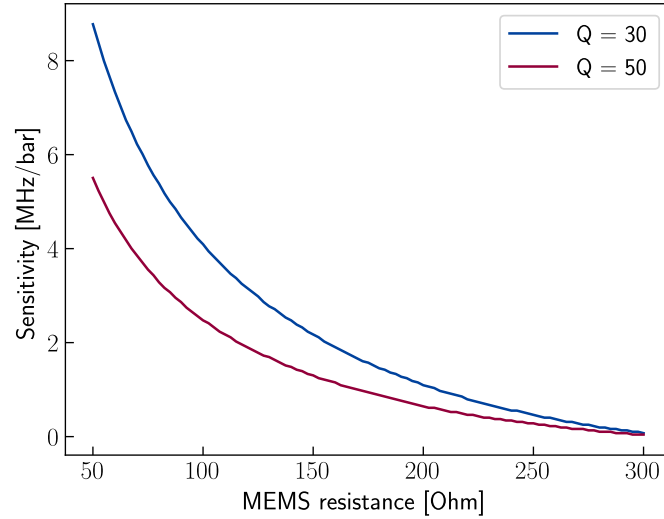


Figure 2.35: Variation of the sensitivity  $\Delta f$  with the resistive part of the impedance of the MEMS  $R_S$  for two values of the quality factor.

$$L = \frac{\mu_0}{2\pi} l \left[ \ln \left( \frac{2l}{r} \right) - 0.75 \right] \quad (2.12)$$

with  $r$  the radius of the bondwire,  $l$  its length and  $\mu_0$  the permeability of free space. The equation is valid for  $l \gg r$ .

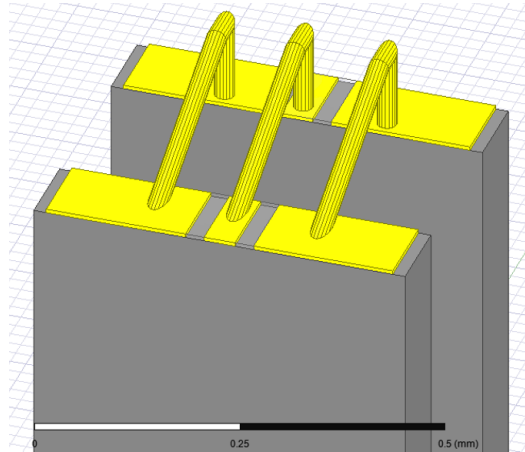


Figure 2.36: Simulated wire-bonding geometry on Ansys Q3D. The lines are the shortest possible in order to extract only the inductance of the wire-bonding.

To validate this formula in RF, a simulation as been made in Ansys Q3D which allows extracting lumped parameters from complex structures in RF. The simulated geometry is shown in Figure 2.36. The wire is  $25\mu\text{m}$  in diameter. The lines are as short as possible in order to extract only the inductance of the wire-bonding.

By varying the wire bond length in the simulation, we extract the value of the inductance and compare it with the value extracted from the theoretical formula. Figure 2.37 shows the comparison of both values of inductances obtained by simulation and by the analytical formula. The inductance of the wire-bonding is less than  $1\text{ nH/mm}$  of wire, which is equivalent to approximately equal to  $5\Omega$  of reactance at  $868\text{MHz}$ , a very low value compared to the order of magnitude of the reactance of the sensors (few hundreds of Ohms). Therefore, the effect of the wire-bonding can

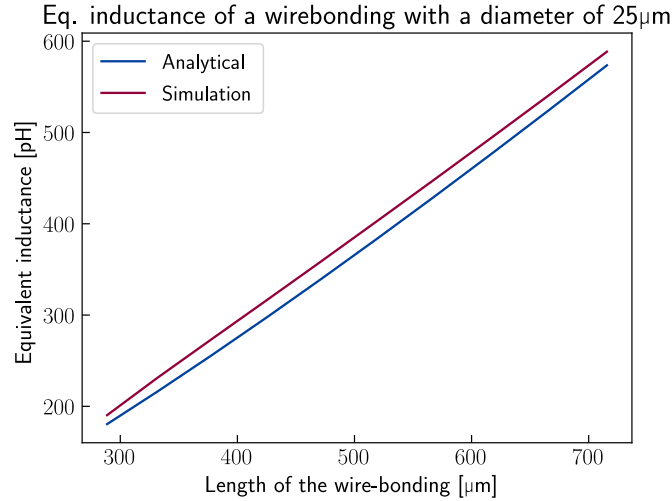


Figure 2.37: Variation of the inductance of a wire-bonding of 25 $\mu\text{m}$  of diameter as function of its length.

be neglected.

### 2.7.5 Analysis of an enhanced version of the sensor

The goal of this section is to study an example of sensor where the resistive part of the MEMS impedance is close to zero, and the antenna is a miniature antenna. The aim is to show the performance that sensors could achieve. To perform this study, the capacitance of the MEMS is kept as the standard one (i.e., from 0.44 pF to 0.61 pF between 1 mbar and 1 bar) and its resistive part is set to zero. The antenna geometry is a Split Ring Resonator (SRR) excited by a backside loop, with the MEMS as a lumped element of the external ring, and a 50 $\Omega$  load on the loop. The analysis was first performed based on the equivalent model developed in [7], and then simulated in Ansys HFSS. The overall structure is shown in Figure 2.38.

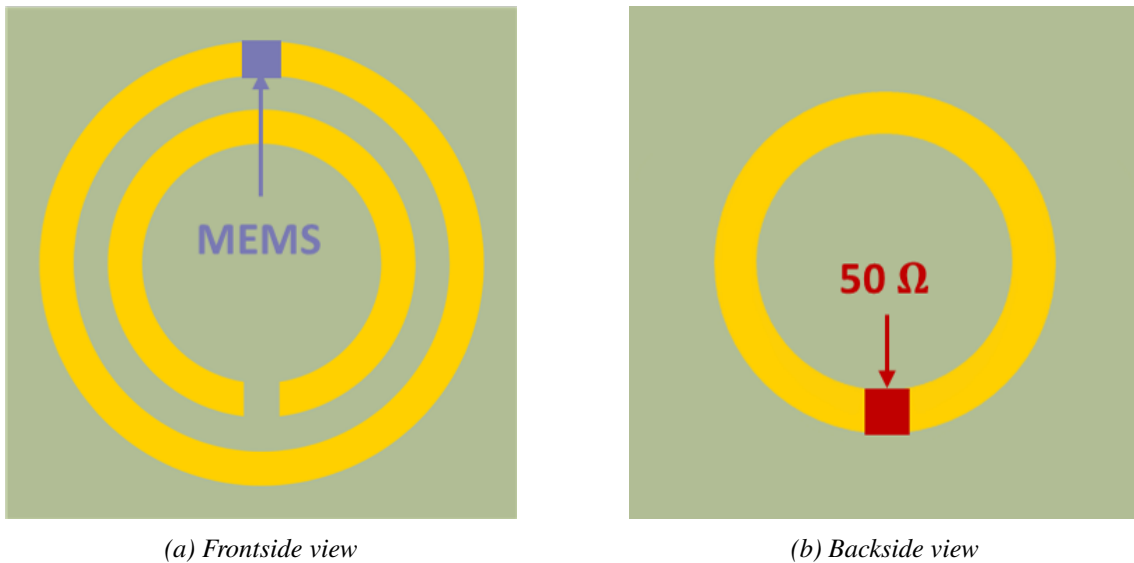


Figure 2.38: Geometry of the miniature antenna based on a SRR excited by a backside loop, with the positions of the load and the MEMS.

The antenna has an electrical size  $ka = 0.21$  at 868 MHz. The variation of its resonance

frequency due to the MEMS was then simulated on Ansys HFSS. Figure 2.39 shows that the resonance frequency of the SRR-based sensor varies from 858 MHz to 781 MHz, which is equivalent to a sensitivity of 77 MHz/bar. For comparison, the variation of the resonance frequency of a CLL-based sensor of section 2.7.2, with a MEMS resistance of  $100\Omega$  and an electrical size of 0.24 is shown. The CLL-based sensor has a sensitivity of 1.05 MHz/bar. This shows again the importance of reducing the MEMS resistance to increase the sensor sensitivity. Also, because of its small electrical size, this antenna has a low bandwidth, which increase the precision of the sensor.

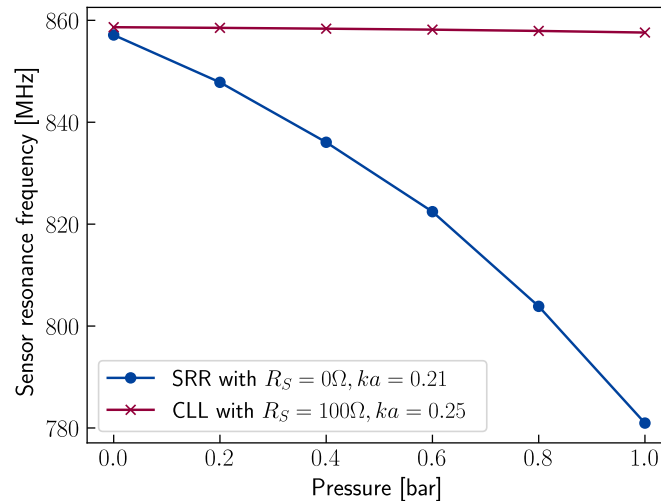


Figure 2.39: Variation of the resonance frequency of the SRR antenna with the MEMS as a perfect capacitance

## 2.7.6 Conclusion on the optimization of the performance of the sensor

All the studies described above allow extracting some conclusions on the properties the antenna and the MEMS must have in order to achieve the best possible resolution, that is high sensitivity and low antenna bandwidth. They are:

- A large capacitance variation of the MEMS with pressure. It is important to bear in mind that, for a membrane-based geometry, the variation becomes non-linear when the deflection is too high.
- The lowest possible MEMS resistance. If this resistive part is very low (less than few ohms), the MEMS can be placed on the radiative part of the antenna geometry, in order to change directly its electrical size. If it is not possible to lower it as much, the MEMS can only be put as the antenna load.
- A small antenna electrical size. Even if it lowers the sensitivity, it lowers also the bandwidth, which makes the sensor more precise. But also it reduces the radiation efficiency and the gain of the antenna, which tends to radiate more isotropically.
- The antenna should have a structural part as low as possible because it reduces the relative impact of the MEMS on the total amount of power backpropagated. But it also means less total amount of backpropagated power. For example, the use of a ground plane should be avoided.

All these criteria must also be taken into account in order to design antennas specifically for the MEMS, which was done after the characterization of the MEMS, in order to extract their equivalent impedance.

## 2.8 Conclusion

This chapter focuses on the MEMS design, the microfabrication process flow, and on the understanding of the MEMS behavior with pressure. Several studies were performed to understand the impact of each parameter of the design on the performance of the sensor, with a strong focus on the resolution. The conclusion of these studies is that the parameter to focus on to achieve the best possible performance is the reduction of the resistive part of the impedance of the MEMS. As a result, the MEMS has a great impact on the current distribution on the antenna. An example based on a miniature antenna, with a model of MEMS with no serial resistance is presented to determine the performance that this technology can achieve, which has a sensitivity of 77 MHz/bar for an electrical size of 0.24.

The electrical size of the antenna also has as a strong impact on performance: a smaller electrical size implies lower sensitivity but also a lower bandwidth. The variation of the frequency at which there is the maximal value of RCS is lower, but the peak is narrower. If the MEMS has a low resistive part of its impedance, a miniature antenna seems to be better, as it can achieve high sensitivity and low bandwidth.

## References

- [1] S. Timoshenko and S. Woinowsky-Krieger. *Theory of Plates and Shells*. Engineering mechanics series. McGraw-Hill, 1959. ISBN: 978-0-07-085820-6. URL: <https://books.google.fr/books?id=rTQFAAAAMAAJ>.
- [2] G. Ghione and C. Naldi. “Analytical formulas for coplanar lines in hybrid and monolithic MICs”. In: *Electronics Letters* 20.4 (Feb. 1984). Publisher: Institution of Engineering and Technology, 179–181(2). ISSN: 0013-5194. URL: [https://digital-library.theiet.org/content/journals/10.1049/el\\_19840120](https://digital-library.theiet.org/content/journals/10.1049/el_19840120).
- [3] George E. Ponchak, Linda P. B. Katehi, and Emmanouil M. Tentzeris. “Finite Ground Coplanar (FGC) Waveguide: It’s Characteristics and Advantages for Use in RF and Wireless Communication Circuits”. In: 1998.
- [4] J. Papapolymerou et al. “Crosstalk between finite ground coplanar waveguides over polyimide layers for 3-D MMICs on Si substrates”. In: *IEEE Transactions on Microwave Theory and Techniques* 52.4 (2004), pp. 1292–1301. DOI: [10.1109/TMTT.2004.825714](https://doi.org/10.1109/TMTT.2004.825714).
- [5] Marwan Jadid et al. “Parasitic-Based Electrically Small CLL Antenna”. In: *2021 IEEE 19th International Symposium on Antenna Technology and Applied Electromagnetics (ANTEM)*. 2021, pp. 1–2. DOI: [10.1109/ANTEM51107.2021.9519052](https://doi.org/10.1109/ANTEM51107.2021.9519052).
- [6] X. Qi and Stanford University. Department of Electrical Engineering. *High Frequency Characterization and Modeling of On-chip Interconnects and RF IC Wire Bonds*. Stanford University, 2001. URL: <https://books.google.fr/books?id=MFq0PAAACAAJ>.
- [7] Victor Engelhardt. “Contribution au développement d’antennes miniatures intégrant des fonctionnalités de capteurs”. PhD thesis. 2018. URL: <http://www.theses.fr/2018INPT0067/document>.



# 3

## MEMS characterization

---

*This chapter presents the characterization of the MEMS components designed to be integrated on an antenna and the comparison of their characteristics with the specifications. This characterization starts during the microfabrication in clean room, followed by the characterization of the properties of the materials and then the measurement of the RF behavior of the MEMS with the pressure. This procedure allows to have a deep understanding on the behavior of the MEMS in order to design antennas specifically for them.*

---

### Contents

---

<b>3.1</b>	<b>Introduction</b>	<b>66</b>
<b>3.2</b>	<b>In-line metrology</b>	<b>66</b>
3.2.1	Etching of the hole of the reference sensors	67
3.2.2	Surface defects of the deposited metal	69
3.2.3	Synthesis of the in-line metrology	69
<b>3.3</b>	<b>Electrical characterization of materials</b>	<b>70</b>
3.3.1	Sheet resistance of conductors (Van der Pauw)	70
3.3.2	Contact resistance between two conductors (CBKR)	72
3.3.3	Over-etching and continuity of the metal	73
3.3.4	Conclusion	74
<b>3.4</b>	<b>Changes made to the process flow</b>	<b>74</b>
3.4.1	Verification of the metal layer	74
3.4.2	Etching of membrane to create reference MEMS	75
<b>3.5</b>	<b>MEMS characterization procedure</b>	<b>76</b>
3.5.1	RF characterization at atmospheric pressure	76
3.5.2	RF characterization under vacuum	81
3.5.3	Measurement of the membrane deflection	83
<b>3.6</b>	<b>Conclusion</b>	<b>83</b>

---

### 3.1 Introduction

To ensure that the MEMS meet the specifications, i.e. the desired RF behavior and response with pressure, it is necessary to know their properties, from the properties of the materials to their functionality as sensors. This chapter presents each step of the characterization of the MEMS. This characterization procedure began during the fabrication process in clean room, as microfabrication is a complex process made of dozens or even hundreds of steps. The aim was then to check that each stage had been carried out correctly (for example, to ensure that each etch is at the desired depth, that the bonding between the wafer and the top silicon is good...). Then, the material were characterized to verify their properties, in particular their electrical properties. Finally, the MEMS were characterized with probe stations to verify their functionality and extract their impedance, which was used to design the antennas.

### 3.2 In-line metrology

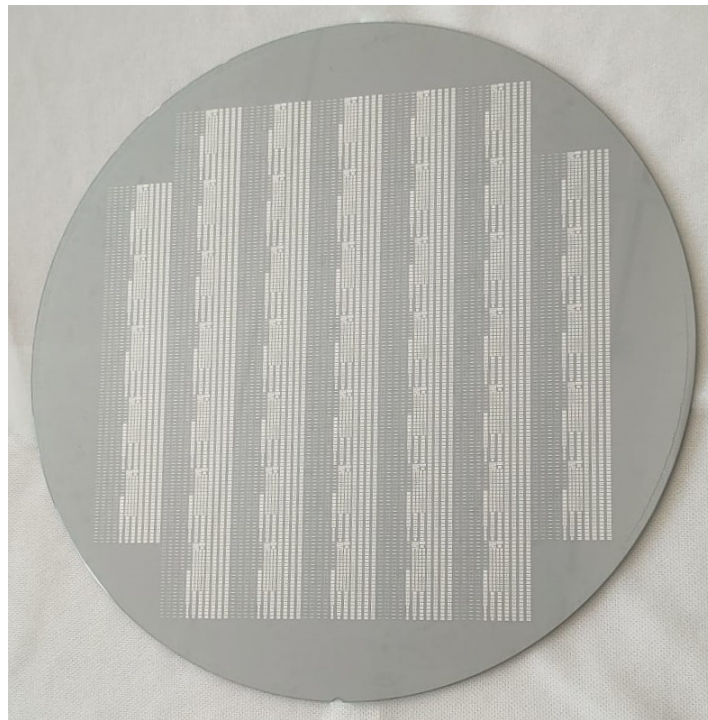


*Figure 3.1: Picture of one of the wafers*

This section focuses firstly on the characterization of the technological results of the fabrication process. In order to have the freedom to correct certain steps if problems were observed during fabrication, half the wafers (six over twelve) were set aside before the risky Si-top etching step (Figure 2.13 on the process flow). After the characterization of the six first wafers, it has been decided to modify some steps of the fabrication process to try to correct certain steps. As an illustration, Figure 3.1 shows a picture of one of the wafers at the end of the fabrication process. On each wafer, there is 45 fields, with 240 MEMS on each field, for a total of around 10800 MEMS per wafer.

During the fabrication of the MEMS, which occurred between the end of 2021 to the end of 2022 for the first half of the wafers, multiple steps of characterization were done at the end of

each critical step. This procedure is often referred to as in-line metrology. The goal is to ensure that each step is in accordance with the specifications, or if there is any difference, to evaluate if this difference impacts the following steps and the functionality of the MEMS. As an example, Figure 3.2 shows the topography of one of the MEMS, measured by a profilometer, which consists of a diamond tip running across the surface of the MEMS. On the left, the difference of height of -5000nm is perfectly in accordance with the requirements, as it represents the etching of the 4 $\mu$ m of thickness of the membrane (Figure 2.13 on the process flow), plus the 1000nm of etching made during the gap etching (Figure 2.9 on the process flow).

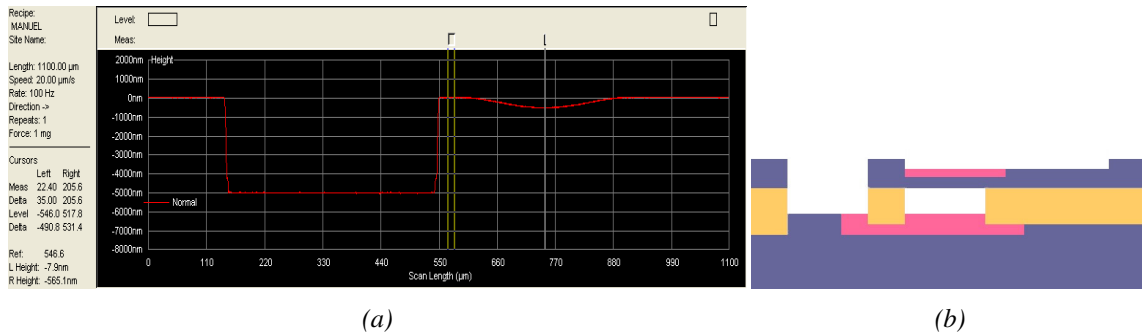


Figure 3.2: In-line characterization of the etching of the membrane. (a) Measurement of the topography of the MEMS using a profilometer after the etching of the membrane shown in Figure 2.13. (b) Side view of the MEMS at the corresponding step.

Another example of a crucial step characterized during the fabrication is the quality of the bonding between the two wafers, i.e. the quality of the clamping of the membrane. It is usually done using a Scanning Acoustic Microscope (SAM), which uses ultrasonic waves to image the internal structure of a material. An ultrasonic probe is placed close to the surface of the object to be inspected. The probe emits sound waves which propagate through the object. When the sound waves hit an interface between two materials of different densities, they are reflected. The time-of-flight can be used to evaluate, if necessary, the distance from the emitter to the interface between the two materials. The probe then receives the reflected sound waves and converts them into an electrical signal. This electrical signal is then used to create an image of the inside of the object.

Figure 3.3 shows an example of a full-wafer view of the quality of the bonding using SAM. Dark areas are well-sealed zones while the light peripheral areas represent areas where there is no bonding between Si and SiO<sub>2</sub>. This is due to a slight etching of the sealing oxide caused by the gap etching step, which should also have been carried out at the edge of the plate. On the center of the wafer, each dot represents the areas in white in Figure 3.3b, where there is no oxide below the top Si. It confirms the quality of the bonding, as the areas where there is MEMS are in black on the SAM view. On the edges of the wafer, the bonding defects occur in areas where there are no fields, which is due to a residual topology not taken into account during the definition of the process flow, which could have been corrected by slightly modifying the gap etching steps. However, these defects have no impact on the quality of the bonding in areas where MEMS are present.

### 3.2.1 Etching of the hole of the reference sensors

Firstly, in order to create reference MEMS, i.e., MEMS whose membrane does not deflect with pressure, a hole was etched at the center of the membrane during the top silicon etching (Figure 2.13 on the process flow). Figure 3.4 shows an example of a reference sensor with the hole at its center, and Figure 3.5a a zoomed-in view of one of the hole of the membrane. The images were taken using Secondary Electron Microscopy (SEM), a technique similar to classical optical

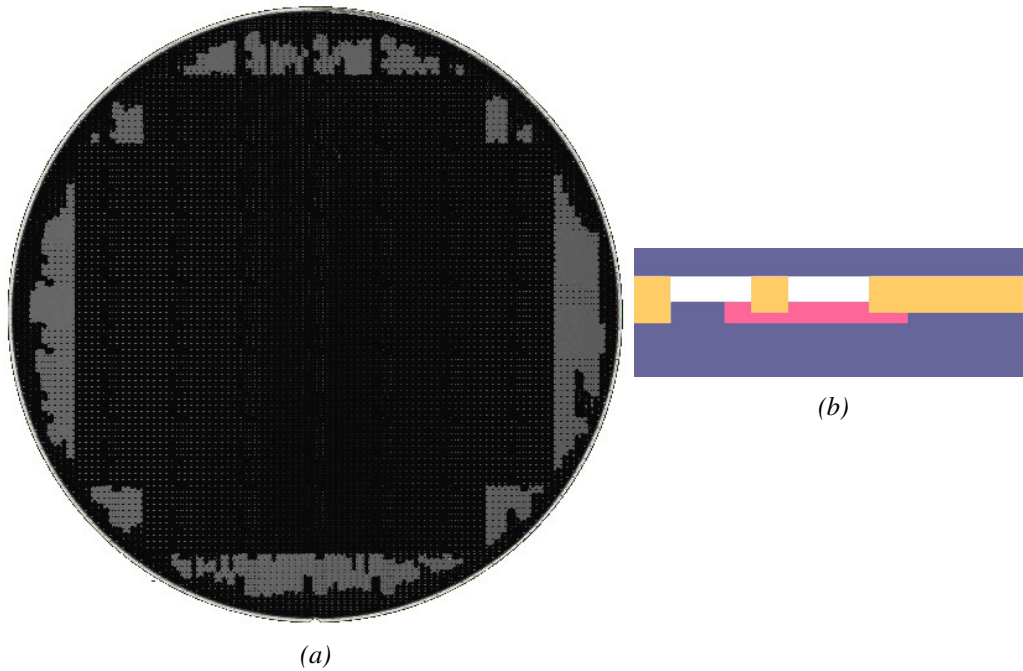


Figure 3.3: In-line characterization of the bonding of the wafers. (a) SAM full-wafer view after the bonding. The light areas show where the wafer is not correctly bonded to the SiO<sub>2</sub>. (b) Side view of the MEMS at the corresponding step.

microscopy. The scanning electron microscope (SEM) is an instrument that utilizes a beam of electrons to create high-resolution images of the surface of a sample. Electrons are emitted from a heated filament and then directed onto the sample through a series of electromagnetic lenses. Upon striking the sample, the electrons interact with surface atoms, generating various particles or signals such as secondary electrons, secondary ions, Auger electrons, and X-rays. Detectors collect these signals, which are then converted into a digital image.

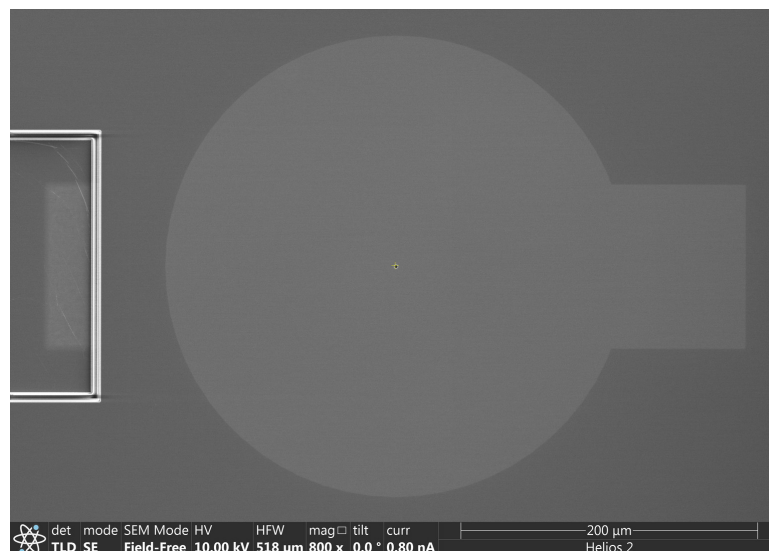


Figure 3.4: SEM view of one of the reference sensor centered on the hole.

After this etching it was observed that the membranes are still deflected under atmospheric pressure, which can be explained by holes that have not been completely etched. This assumption was confirmed by a Focused Ion Beam (FIB). This technique uses high-energy accelerated ions

(usually gallium) to pulverize the atoms on the surface of the sample. An image of the sample can be generated using a SEM. Figure 3.5b shows a SEM image of the hole after the FIB. It shows that the hole is not completely open. There is still about 1 $\mu\text{m}$  to etch.

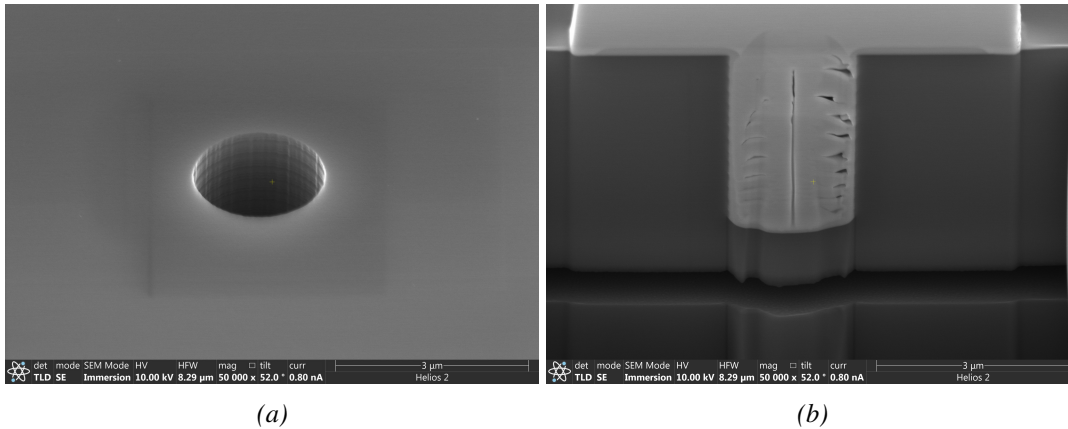


Figure 3.5: (a) Zoomed-in view of the hole in the membrane. (b) View of the depth of the etching of the hole. The hole is not fully etched.

This etching default can be explained by the fact that etching silicon creates a lot of heat, so the wafer is placed on a cooling surface during the etching. However, the presence of a vacuum under the membrane tends to make the cooling less effective at the level of the membrane. As the membrane is hotter than expected, etching is less efficient. This phenomenon is accentuated by the size of the hole: 2 $\mu\text{m}$  radius for a desired 4 $\mu\text{m}$  etch, and the smaller the aperture, the slower the etching process. However, these defects does not deteriorate the functionality of the sensors.

### 3.2.2 Surface defects of the deposited metal

Another defect was observed at the end of the fabrication, which is a surface defect of the metal deposited on the MEMS. Figure 3.6 shows some images of the metal on different wafers.

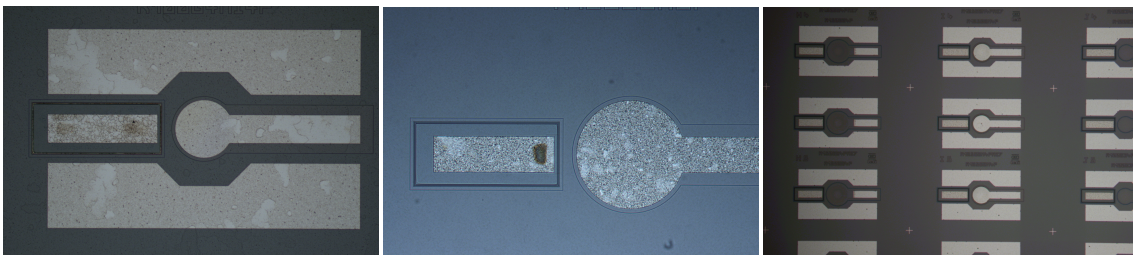


Figure 3.6: Visual defects observed on the metal after the forming gas annealing

The metal has a very rough appearance, with some blackened areas always in the same places on the wafer, some cracked areas and some lighter areas. As the high rugosity of the metal may create the cracked areas, no conclusion could be drawn as to the source of the problem of blackened areas, but a correction was made on the second half of the wafers, as explained in section 3.4. As will be shown later, the electrical properties of the metal were not affected.

### 3.2.3 Synthesis of the in-line metrology

As a conclusion, the in-line metrology does not highlight any problems that could affect the functionality of MEMS. Only the very last of the 105 steps of fabrication creates defects, which

are only aesthetic (appearance of the metal) or that does not have any impact at on the functionality (etching of the membranes). As a complement to these morphological analyses, electrical measurements are carried out on specific test patterns. The objective is to confirm other important parameters such as the resistivity of materials or the contact resistances between the metal and the doped areas.

### 3.3 Electrical characterization of materials

In order to make sure that the materials have the desired electrical behavior, A cell of electrical tests patterns was then designed. A semi-automatic characterization was performed to establish the mapping of the electrical properties of materials all over the wafer. This section focuses then on the results of these electrical tests.

#### 3.3.1 Sheet resistance of conductors (Van der Pauw)

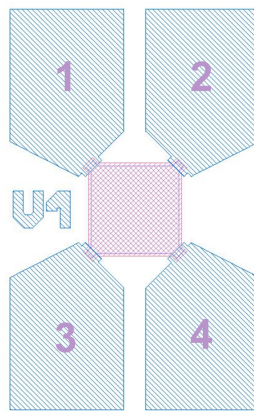


Figure 3.7: Van der Pauw structure for characterization of sheet resistance of materials.

The Van der Pauw method [1] is a commonly used method to determine the sheet resistance of thin-film materials. Figure 3.7 shows one of the geometry of a Van der Pauw structure: the electrical contacts are in blue, and the materials under test in purple. If the shape of the material to characterize is square, by applying a current  $I_{12}$  from contact 1 to contact 2, and measuring the voltage induced between contact 3 and contact 4  $V_{34}$ , the sheet resistance can be extracted using the formula:

$$R_{\square} = \frac{\pi}{\ln 2} \frac{V_{34}}{I_{12}} \quad (3.1)$$

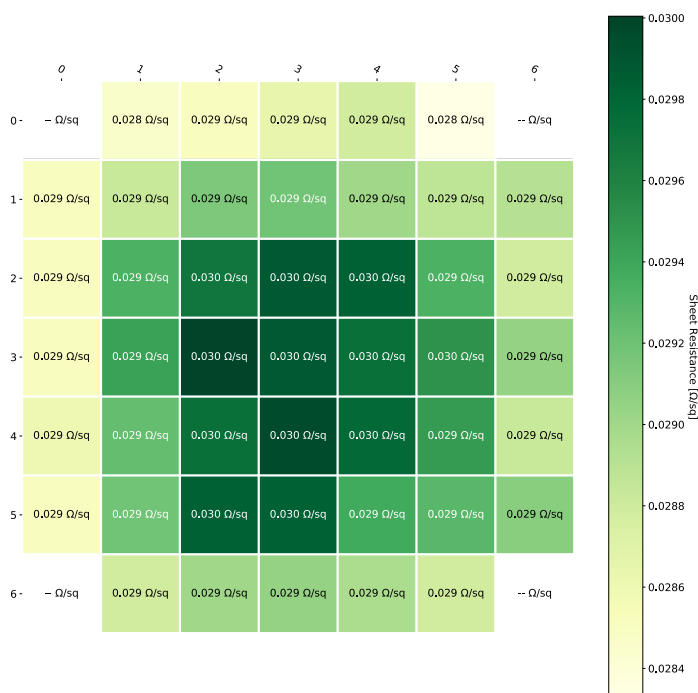


Figure 3.8: Mapping of the sheet resistance of AlCu over a wafer.

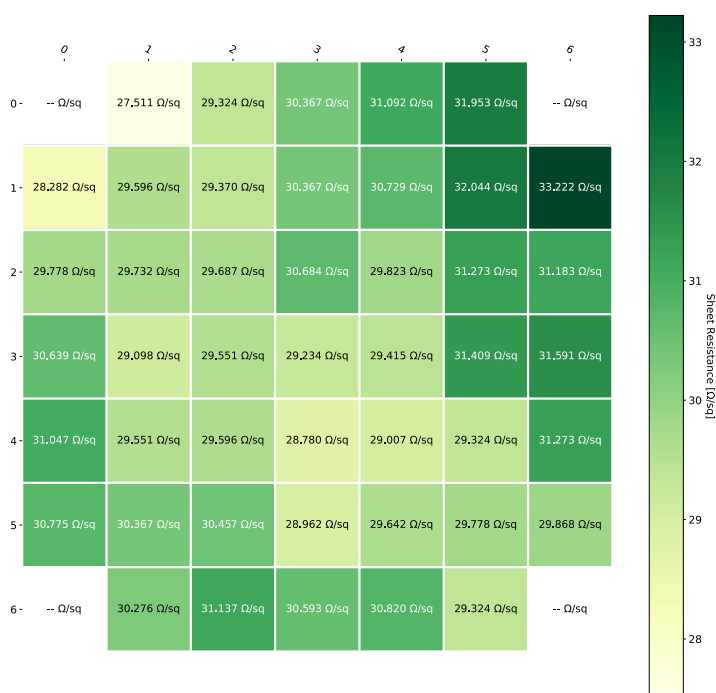


Figure 3.9: Mapping of the sheet resistance of the implant of the lower electrode over a wafer.

Figure 3.8 and 3.9 shows two examples of mapping of sheet resistances, respectively the resistivity of AlCu and the implant of the lower electrode after one of the two gap etching. Based on these mappings and the other ones not shown in this section, some conclusions can be extracted:

- The roughness of the metal does not impact the resistivity. Also, this resistivity is constant all over the wafers (for Figure 3.8,  $\overline{R}_{\square} = 0.0291\Omega/\square$ ,  $\sigma = 0.0004$ ) which is similar to the analytical value of  $0.03 - 0.035\Omega/\square$  [2].
- The sheet resistance of doped silicon is at the good order of magnitude, but higher than expected (from  $15.5\Omega/\square$  to  $24\Omega/\square$  depending on the etching,  $15.5\Omega/\square$  expected for the sheet resistance of Figure 3.9). It can be explained by a lateral diffusion of doping agents, a diffusion which can be different for HR silicon rather than non-HR silicon, or by the doping agent that tends to move to  $\text{SiO}_2$  with the successive annealings. However, this resistivity is also quite uniform on the wafer (for Figure 3.9,  $\overline{R}_{\square} = 29.89\Omega/\square$ ,  $\sigma = 1.06$ ). This is also the case for the other implants.
- Both the bulk of the wafer and the top silicon seems to still be HR, moreover, there is a lack of precision on the value of resistivity due to the low current applied compared to the resistivity.

Finally, the different materials present good behavior in terms of resistivity, and the defects of the metal seems to be only aesthetic and do not seem to impact the electrical performance in DC.

### 3.3.2 Contact resistance between two conductors (CBKR)

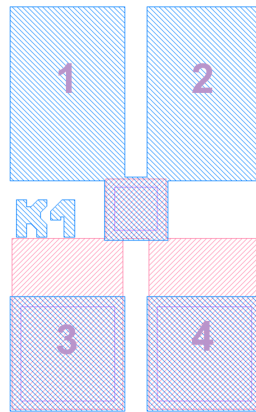


Figure 3.10: CBKR structure for the characterization of the contact resistance between a metal and a semi-conductor.

The Cross-Bridge Kelvin Resistor (CBKR) test structure is a very classical way to perform a characterization of the contact resistance between a metal and a semi-conductor. Figure 3.10 shows the geometry of one CBKR structures. By applying a current  $I_{14}$  from contact 1 to contact 4, and measuring the voltage induced  $V_{23}$  between contact 2 and contact 3, the contact resistance  $R_C$  can be extracted using the formula [3]:

$$R_C = \frac{V_{23}}{I_{14}} \quad (3.2)$$

By shifting the applied current  $I_{14}$ , an Intensity-Voltage (IV) curve can be plotted for each CBKR structure. If the curve is a straight line, the contact is purely resistive and the contact resistance can be extracted thanks to the slope. However, as shown in Figure 3.11, the IV curve is

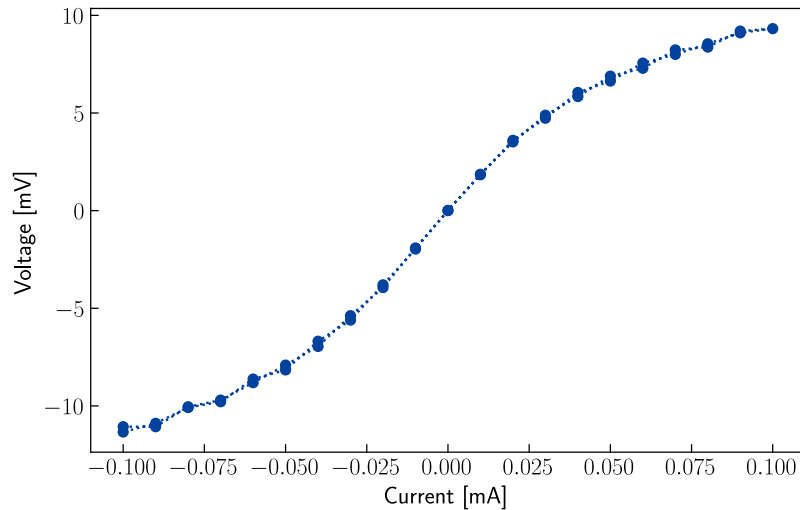


Figure 3.11: Intensity-Voltage (IV) curve for one contact between the metal and the lower implant.

not linear. This phenomenon is present on all the structures for the contact between the metal and the lower electrode.

A number of explanations can be put forward to explain this non-linearity: doping agents that tend to migrate to the oxide near the contact, which create a depletion zone at the surface of silicon; a thin oxide at the interface between the metal and the silicon; or a difference in the profile of the implantation due to the high-resistivity nature of the wafer. This non-linear contact resistance can create distortion of the signal, as the amplitude of the signal voltage at any instant is no longer proportional to the amplitude of the current. However, the source of this phenomenon has not been clearly identified.

### 3.3.3 Over-etching and continuity of the metal

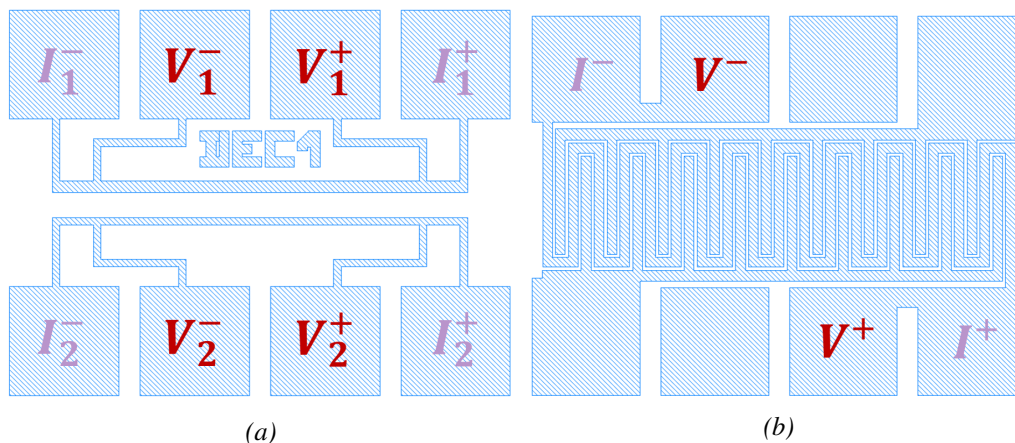


Figure 3.12: Test structures to characterize the quality of etching of AlCu. (a) Test structure to characterize the over-etching and the sheet resistance. (b) Test structure to characterize isolation and continuity.

The last structures, shown in Figure 3.12 are used to characterize the quality of the metal etching. It is a crucial parameter as, for example, the characteristic impedance of the lines are highly dependent on the width of the lines and the distance to the ground planes.

On one hand, the structure shown in Figure 3.12a is used to characterize the overetching of the

metal. By measuring the resistance of the top line  $R_1$  and the resistance of the bottom line  $R_2$ , the overetching  $o$  can be calculated using:

$$o = \frac{R_1 w_1 - R_2 w_2}{R_1 - R_2} \quad (3.3)$$

With  $w_1$  and  $w_2$  the expected width of the top and bottom lines. For all the wafers characterized, no overetching has been measured.

On the other hand, the structure shown in Figure 3.12b is used to characterize the metal continuity and electrical insulation. It consists in a long serpentine line and a comb forming a capacity. Again, no problems of continuity or insulation were highlighted.

### 3.3.4 Conclusion

As a conclusion, the electrical characterization of the materials have shown good results overall: the appearance of the metal had no impact on its electrical properties, and the resistivity of the doped silicon zones was only slightly higher than expected. Both for the metal and the implanted areas, the values for the resistivity are uniform on each wafer.

However, a non-linearity of the IV curves for CBKR of the contact resistances of metal over implants of lower electrodes has been shown. These contacts are then not fully resistive. The next section will be focused on the modifications bring to the fabrication process applied in order to try to correct this issue.

## 3.4 Changes made to the process flow

As mentioned at the beginning of this chapter, half of the wafers were set aside before the Si top etching (Figure 2.13). In order to correct the steps that do not comply with the specifications, some changes on the steps that follow the Si top etching have been done on the second part of the wafers:

- The metal is changed from AlCu to AlSi. Although this is highly unlikely, it can confirm that the metal is not the cause of the contact resistance problem.
- In order to prevent any oxide between the metal and the implanted area, the deoxidation will be longer, with a higher concentration of HF. In fact, the deoxidation on HR silicon is more difficult than deoxidation on less resistive silicon.
- To correct a possible depletion zone on the contact of the lower electrode, another implantation was performed just after the etching of the top silicon. It will consequently add more doping agents at the surface of the silicon.
- The hole on the membrane of reference MEMS are done on individual chip using FIB, as it will not impact the functionality of the other MEMS.

### 3.4.1 Verification of the metal layer

The modifications listed on the previous section were applied on the second half of the wafers. Figure 3.13 shows the comparison between the appearance of the two metals: the change from AlCu to AlSi has significantly reduced roughness and removed any blackened appearance.

However, the applied changes does not improve the contact resistance between the lower electrode and the metal. Figure 3.14 shows the IV curves for a contact resistance on one of the wafers

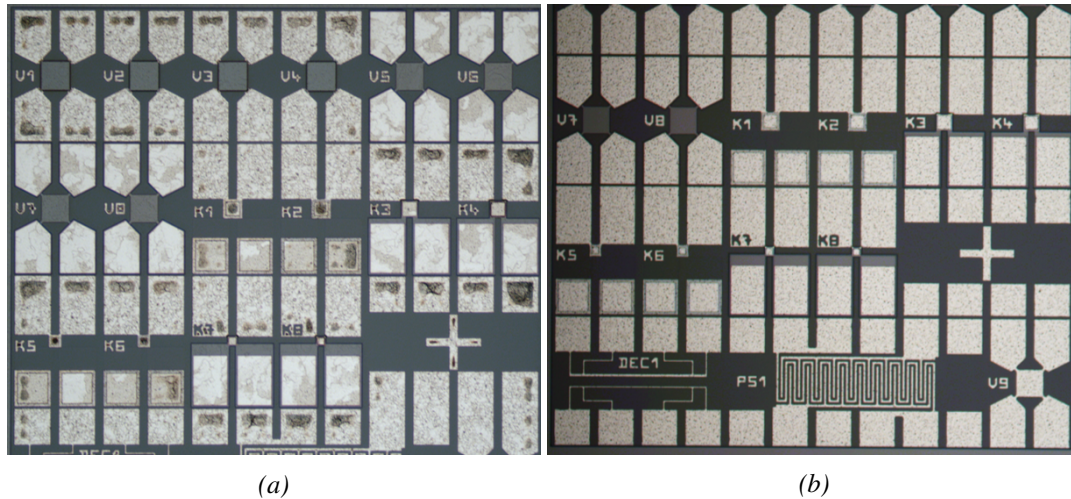


Figure 3.13: Comparison between the appearance of the two metals used AlCu and AlSi. (a) Cell of technological tests with AlCu. (b) Cell of technological tests with AlSi.

with the changes applied on it. The contact resistance is still non-linear and also not symmetrical about the  $I = 0$  axis.

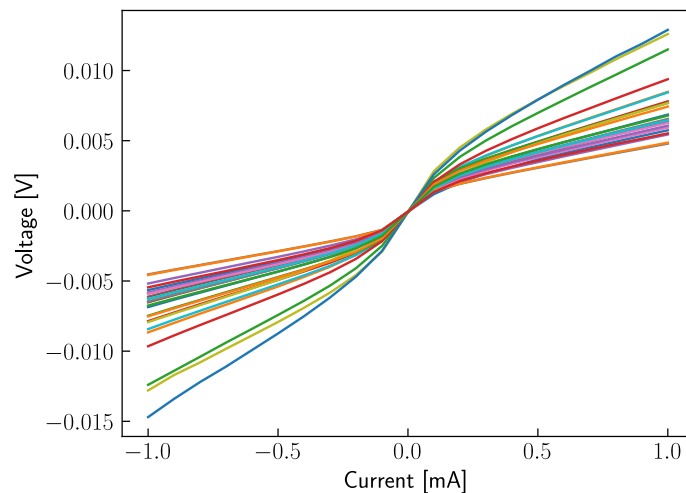


Figure 3.14: IV curves for all the contact resistances of a wafer with the correction steps.

The contact resistance problem does not therefore appear to be due to the presence of oxide at the interface between the metal and the silicon, or to a depletion zone on the surface of the doped zone. The change of metal also had no effect on the shape of the IV curve. It would be useful to measure the profile of doping agents in order to gain a better understanding of this phenomenon.

### 3.4.2 Etching of membrane to create reference MEMS

As highlighted in part 3.4, the holes on the center of the membranes were not fully etched during the fabrication. A first test, shown in Figure 3.15a, aimed at finishing the etching directly on the hole which was done during the fabrication by using FIB. However, a deposit forms at the bottom of the hole, which tends to obstruct the hole, as it is not large enough.

To prevent this, it was decided to etch the membrane next to the hole created during the fabrication, as shown in Figure 3.15b. The shape of the hole is made to prevent the formation of material deposition during FIB. This result shows the possibility of using this technique to create

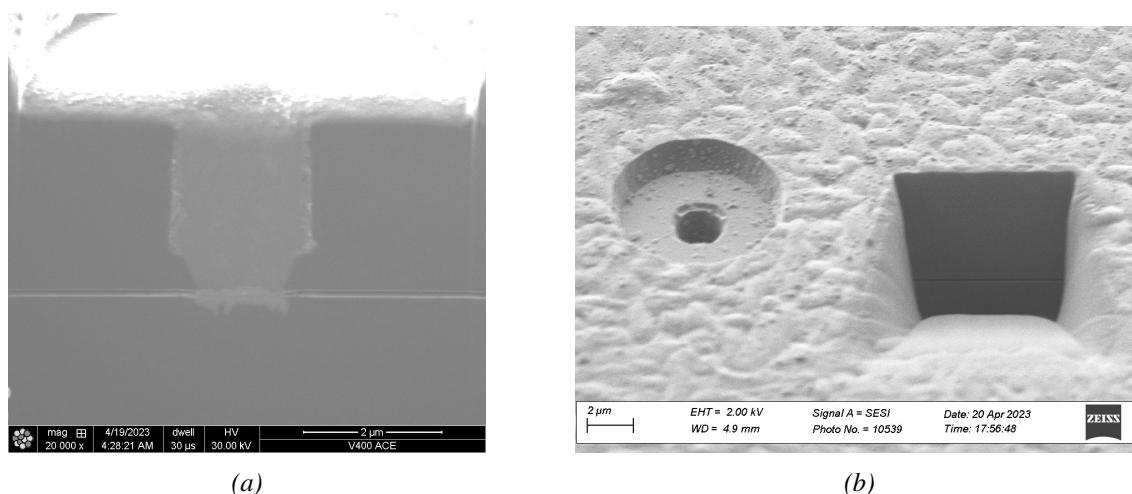


Figure 3.15: Observations after etching holes using FIB to create a reference MEMS. (a) FIB image of the first etching test. It creates deposition of materials at the bottom of the hole. (b) SEM image of a hole etched using FIB next to the hole created during the microfabrication.

reference MEMS in order to have reference sensors for a differential measurement.

### 3.5 MEMS characterization procedure

After the characterization of the material properties, which has shown that the specifications are generally respected, apart from the issue of the contact resistance, the MEMS were then characterized in order to extract their RF behavior and with the variation of pressure. Firstly, the MEMS on the wafer were entirely characterized at atmospheric pressure to extract their impedance. Then, some MEMS were characterized under vacuum to extract the change of impedance between the atmospheric pressure and the vacuum. To link the change of impedance with a deflection of the membranes, and to evaluate the static deflection of the membranes, their profile was measured with a Digital Holographic Microscope (DHM). Finally, in order to create reference MEMS, some samples were etched using FIB to create a hole on the membranes. This characterization phase served as the basis for selecting the MEMS and designing the associated antennas.

#### 3.5.1 RF characterization at atmospheric pressure

##### Characterization setup and objectives

The objective of this section is to characterize the RF behavior of the MEMS under atmospheric pressure, in order to compare the results with the simulations, and also to make a comparison between MEMS devices with a specific geometry on the same wafer and between different wafers. This was performed using a semi-automatic prober, which measured each MEMS and characterization lines on the wafer. The prober, shown in Figure 3.16, was a PA300 connected to a Virtual Network Analyzer (VNA) in order to extract the S-parameters of each structure, and those S-parameters were later converted into ABCD parameters to extract the MEMS impedance.

The impedances of the MEMS were plotted on mappings similar to those used for the measurement of resistivity of materials. The statistical analysis of the impedances was automatically performed using a Python script, in order to study, for example, the variation of the equivalent series resistance of the MEMS over a wafer, to study how close the MEMS reactance is to the

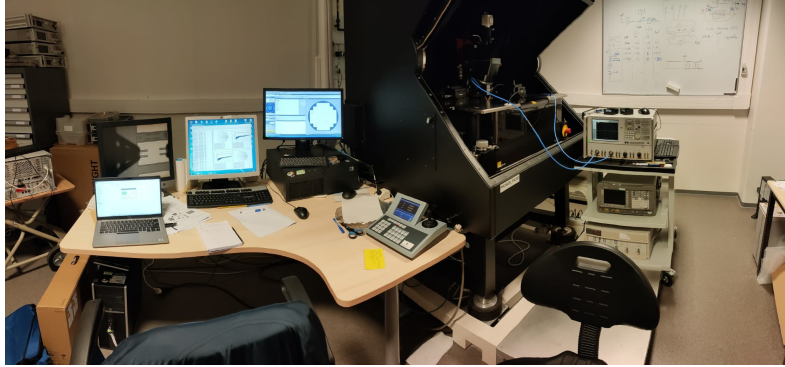


Figure 3.16: RF semi-automatic prober used for  $S$ -parameters measurement at atmospheric pressure.

reactance of a perfect capacitor and also to compare the impedance of the same MEMS all over the wafer.

### Calibration

As explained in section 2.6.1, the measured  $S$ -parameters on the prober are not directly the  $S$ -parameters of the MEMS itself, even after the calibration procedure of the VNA. It is because the calibration of the VNA puts the reference plane at the end of the probes. A similar approach as that done in section 2.6.1 should be performed in order to compensate the influence of the lines, and extract only the impedance of the MEMS.

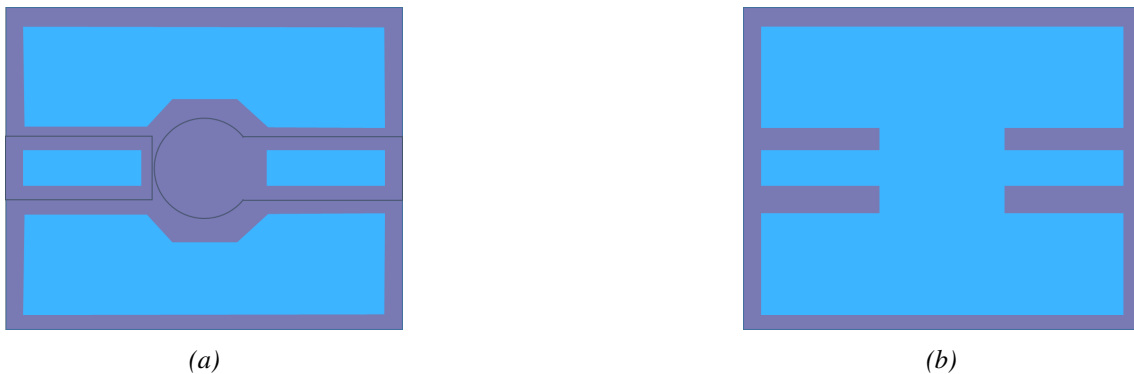


Figure 3.17: Open (a) and short (b) geometries used for de-embedding

The de-embedding method used here is based on the measurement of two lines: a short-circuit and an open-circuit (Figure 3.17). The Open-Short calibration is the easiest de-embedding method [4]. By considering the lines using the classical transmission line model, the Open lines allow calculating the sum of the parallel and series impedance of the line, and the Short the series impedance of the line.

### MEMS impedance and impact of de-embedding.

On this section, the MEMS are identified using the triplet of dimensions  $(R, h, g_0)$  presented in section 2.4.3. The MEMS chosen here has dimensions of  $R = 100\mu m$ ,  $h = 3.5\mu m$  and  $g_0 = 0.3\mu m$ . The goal here is to compare the measured impedance with the RC circuit obtained by simulation and to verify the quality of the de-embedding. The ABCD matrixes of this particular MEMS was plot in order to compare it with the ABCD matrix of a RC series circuit and to study the impact of the de-embedding on the matrix, which allows to verify the quality of the de-embedding, and then

to study more precisely its impedance. As a reminder, the ABCD matrix of a RC series circuit is equal to:

$$[ABCD] = \begin{pmatrix} 1 & R_S + \frac{1}{jC_S\omega} \\ 0 & 1 \end{pmatrix} \quad (3.4)$$

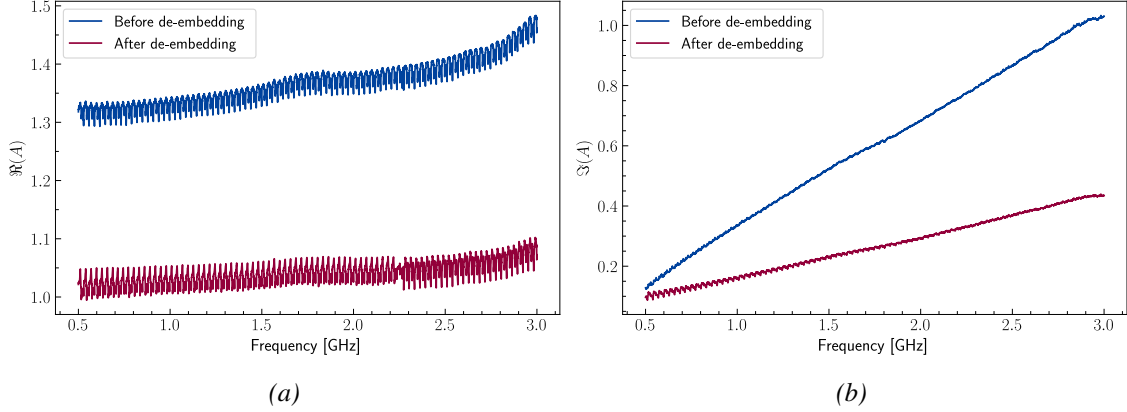


Figure 3.18: Impact of the de-embedding on the real (a) and imaginary parts (b) of the A parameter of the ABCD matrix for the MEMS with dimensions of  $R = 100\mu\text{m}$ ,  $h = 3.5\mu\text{m}$  and  $g_0 = 0.3\mu\text{m}$ .

As an example, the evolution of the A parameter of the ABCD matrix is shown in Figure 3.18. After the de-embedding, the measured ABCD matrix of this MEMS over the 0.5-3 GHz band is equal to:

$$[ABCD]_{dm} = \begin{pmatrix} 1.05 \pm 0.05 + j(0.25 \pm 0.15) & Z_S \\ 4 \times 10^{-3} \pm 1 \times 10^{-3} + j(7 \times 10^{-4} \pm 3 \times 10^{-4}) & 1.27 \pm 0.02 - j(0.055 \pm 0.025) \end{pmatrix} \quad (3.5)$$

After the de-embedding, the matrix became very close to the matrix of a series impedance. The de-embedding does not have a strong impact on the value of the impedance other than a small impact between 1.5 and 2 GHz. This can be explained by the length of the lines (around 400  $\mu\text{m}$  long) compared to the wavelength of the signal (3 cm on the silicon at 3 GHz), so there is no real propagation as such. The impedance does not change significantly with the deembedding.

To study how close the MEMS impedance  $Z_S$  is close to a series RC circuit, the concept of equivalent resistance and capacitance was introduced, with  $R_{eq} = \Re(Z_S)$  the equivalent resistance and  $C_{eq} = 1/(j\Im(Z_S)\omega)$  the equivalent capacitance.

Figure 3.19 shows the curves of resistance and equivalent capacitance of this MEMS between 0.7 GHz and 1 GHz. It appears that both the equivalent resistance and the equivalent capacitance decreases with frequency. The impedance of the MEMS cannot be then approximated only by a RC series circuit, as it seems to have parasitic element in parallel. Also, a parasitic periodic effect can be shown in both real and imaginary part, but which is not present on the other measurements, as for example during the characterization of section 3.5.2.

As no representation with localized elements was found which fits the curves, the MEMS impedance is, for the rest of this manuscript, analyzed using its real and imaginary part directly. Moreover, the real part of the impedance is much higher than expected, with a value around 550  $\Omega$  much higher than the 100  $\Omega$  obtained by simulation. The presence of the parasitic element makes difficult to conclude on the measured imaginary part of impedance compared to the simulated one. It seems then convenient to study if these behaviors are present on all the MEMS on a wafer.

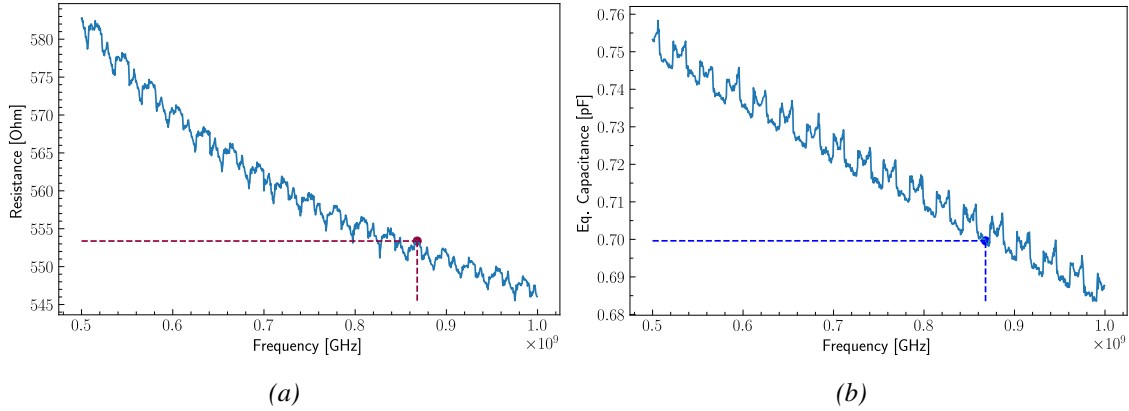


Figure 3.19: Equivalent resistance (a) and capacitance (b) of a MEMS with ( $R = 100\mu\text{m}, h = 3.5\mu\text{m}, g_0 = 0.3\mu\text{m}$ ). The dotted lines highlight the extracted equivalent resistance and capacitance of the MEMS at 868 MHz.

### Full-wafer analysis

In order to optimize the analysis of the more than 2500 characterized MEMS per wafer, different representations of the data were extracted. Because the impedance is not equivalent to a RC series circuit, mappings of value of resistance and reactance of the MEMS impedance at 868 MHz were done for each MEMS over the wafer. Figure 3.20 shows an example of a mapping for a MEMS with dimensions of ( $R = 100\mu\text{m}, h = 3.5\mu\text{m}, g_0 = 0.3\mu\text{m}$ ).

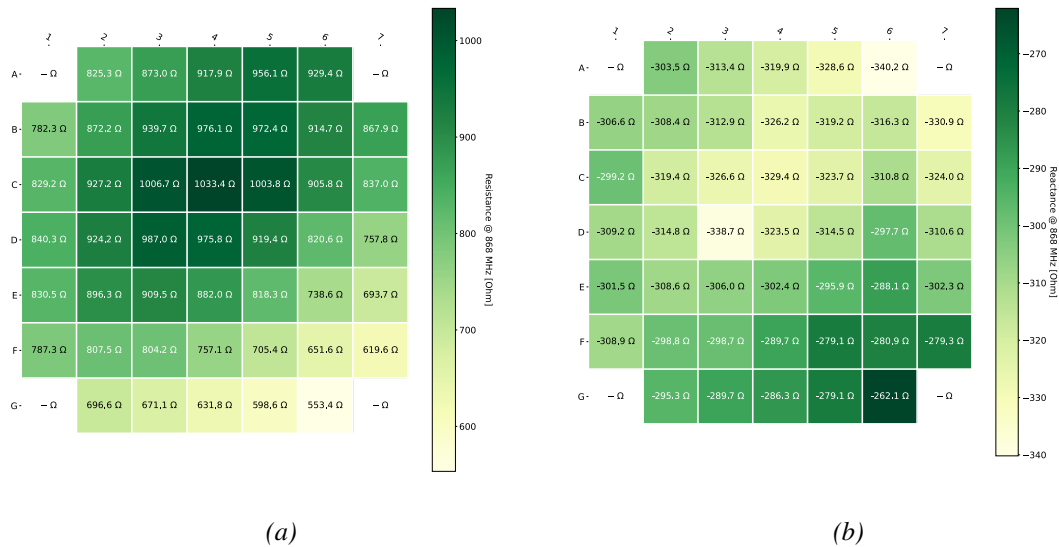


Figure 3.20: Mappings of resistance (a) and reactance (b) at 868 MHz of a MEMS with  $R = 100\mu\text{m}, h = 3.5\mu\text{m}$  and  $g_0 = 0.3\mu\text{m}$

These mappings highlight some results about the impedance of the MEMS : the resistance at 868 MHz is 5 to 10 times higher than simulated, depending on the location of the MEMS on the wafer (from 553Ω to 1033Ω at 868 MHz compared to 110Ω expected). Moreover, the MEMS has a reactance at 868 MHz slightly higher than expected the expected (around  $-333\Omega$  compared to  $-270\Omega$  expected), a correlation seems to appear between the value of the resistance and the reactance.

Figure 3.21 shows the plot for the 4 MEMS with the same geometries than the MEMS pre-

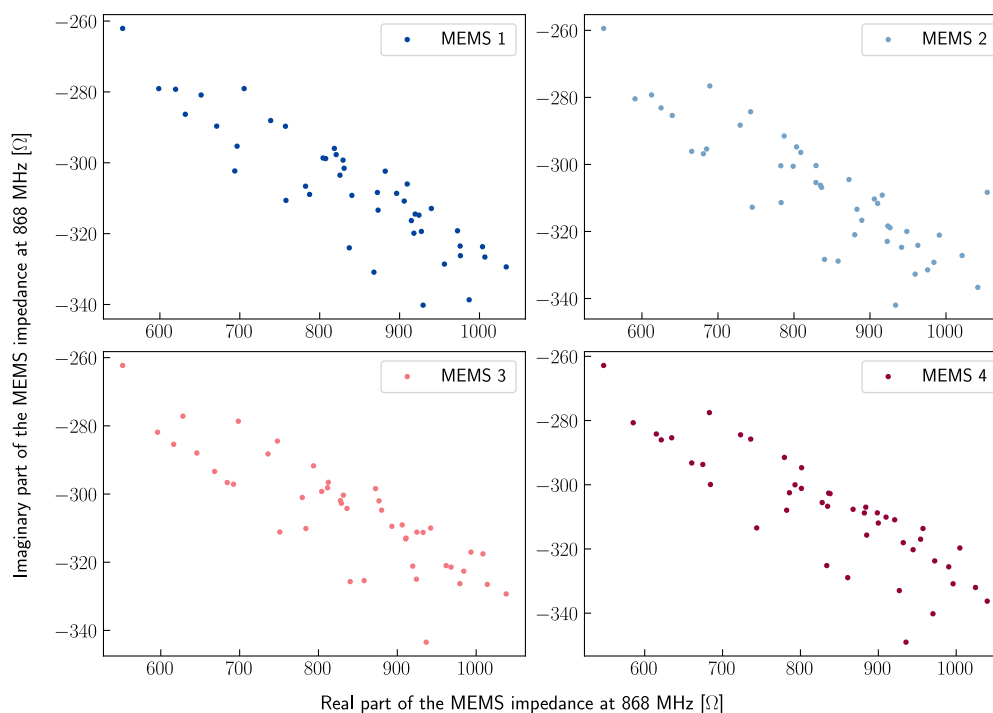


Figure 3.21: Plot of the relationship between the resistance and the reactance at 868 MHz of 4 MEMS with the same geometries over the wafer. A correlation between the value of the resistance and the reactance is observed.

sented in the mappings above. Each plot represents one geometry of MEMS placed at a certain location in the field (i.e. a mapping of resistance and a mapping of reactance) and each dot represent one measurement of impedance (i.e. one value of resistance and one value of reactance in the mappings). This figure confirms the correlation, and this phenomenon is present for all the geometries of sensors and all the wafers. It confirms that there is a parasitic element on the MEMS impedance which modify it both in real and imaginary part.

### Analysis of the results and conclusion

The RF characterization of the MEMS shows that it cannot be modelled as a RC series circuit, as both the resistance and the equivalent capacitance of the MEMS tend to decrease with the frequency and their resistance and reactance seem to be correlated. Also, the value of the resistance is much higher than expected.

As all these phenomena are present on all the MEMS, no matter if the membrane is only doped or if the membrane is only metallized, it can be caused only by a phenomenon which occurs at the lower electrode.

The first hypothesis put forward to explain this correlation was that the etching of the gap was not uniform on the wafer. Indeed, if the gap is overetched, the reactance will increase, and there will be less doping agents at the lower electrode, which will induce an increase of this electrode resistivity. However, a measurement using a mechanical profilometer was done during the fabrication after this etching, by measuring the depth of etching at different locations on the wafer. It shows that this etching is quite uniform all over the wafer, and the slight differences of depth could not be the source of this correlation.

Another way to explain at the same time the correlation and the high value of resistance together is by looking at a profile of the implantation of doping agents of the lower electrode obtained by SIMS. However, this could not be done before the end of the thesis.

Finally, the non-resistive contact between the line and the lower electrode could also influence the RF behavior of the MEMS. However, as the changes made to the manufacturing process did not correct the contact, this hypothesis could not be verified.

### 3.5.2 RF characterization under vacuum

Now that the RF behavior of the MEMS has been characterized under atmospheric pressure, it is necessary to determine the variation of this electrical response under vacuum. Both of the impedances curves extracted at atmospheric pressure and under vacuum were used to design the antenna, and to link the RCS variation of the antenna with the variation of the MEMS impedance.



Figure 3.22: View of the inside of the vacuum chamber of the PAV2000 prober.

This characterization was done at a pressure of  $10^{-3} \text{ mbar}$  on a PAV2000 prober connected to a VNA. The view of the inside of this prober is shown on Figure 3.22. After the calibration of the VNA, the measurement of the MEMS were done in three steps :

- Validation of the measurement under atmospheric pressure by comparing the measurement of this prober with the measurement made previously.
- Measurement of a potential temporal drift of the capacitance value. To achieve this, two measurements of the same MEMS were done 16 hours apart.
- Measurement of the MEMS under vacuum and comparison with the measurement at atmospheric pressure.

#### Validation of the measurement

Firstly, a MEMS was measured at atmospheric pressure with the PAV2000 prober in order to validate the measurement with this measurement done with the prober used for the semi-automatic characterization at atmospheric pressure (Cascade prober). Figure 3.23 shows both ABCD matrixes of the two measurements.

By comparing the two measured impedances, it can be seen that both measurements are very similar, with a slight difference in terms of real part which can be linked to difference in terms of contact resistance of the probes on the CPW lines.

This results shows also the stability of the measurement over time, as there was multiple days between both measurements. As the imaginary part of the impedance of the MEMS remains constant between the two measurements, but the real part changes a little bit, this may be caused by a difference in contact between the probes and the metal of the lines, as the probes deteriorates a little bit the metal. However, this drift is very small in relative value (less than 0.5% of the value of the resistance).

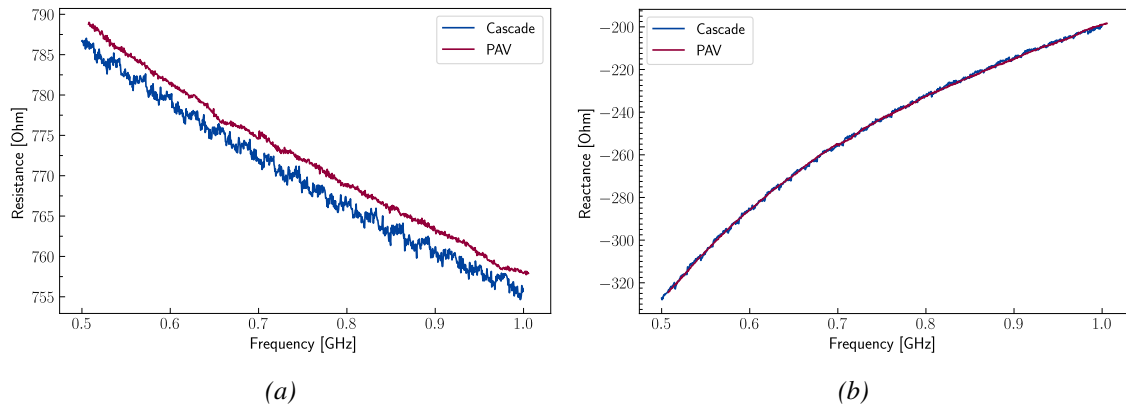


Figure 3.23: Comparison of the measurements made by the two probers of the real (a) and imaginary part (b) of the impedance after de-embedding.

### Response of the MEMS as a function of pressure

Now that it has been shown that the measurement of the impedance of the MEMS does not vary with the prober and over time, the measurement of the impedance of some MEMS was done at atmospheric pressure and under a pressure of  $10^{-3}$  mbar.

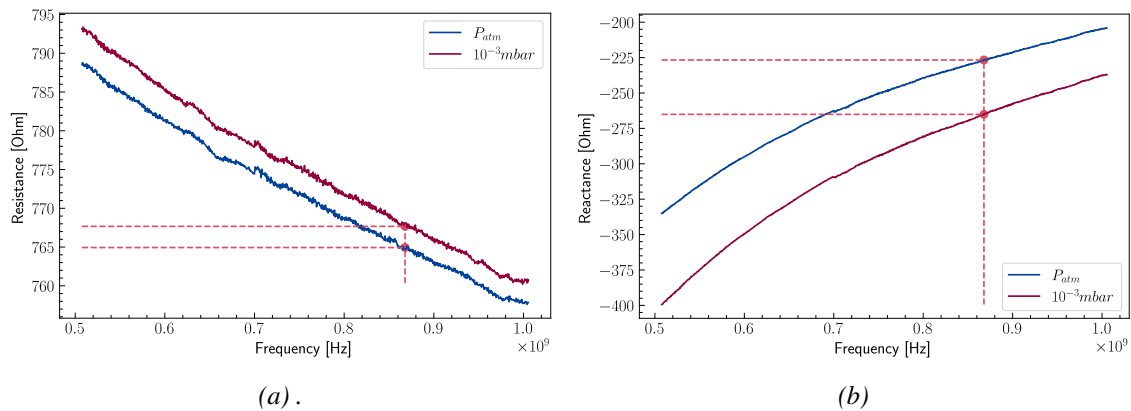


Figure 3.24: Resistance (a) and reactance (b) of a MEMS with  $R = 100\mu m$ ,  $h = 3.5\mu m$  and  $g_0 = 0.3\mu m$  as function of pressure. The dotted line highlights the resistance and reactance of the MEMS at 868 MHz.

Figure 3.24 shows an example of impedance variation with pressure of a MEMS with dimensions of  $R = 100\mu m$ ,  $h = 3.5\mu m$  and  $g_0 = 0.3\mu m$ . At 868 MHz (dotted line), the equivalent reactance goes from approximately  $-225\Omega$  at atmospheric pressure to  $-265\Omega$  at  $10^{-3}$  mbar, which represents a sensitivity of 17%/bar of the reactance. The simulated reactance variation at 868 MHz runs from  $-269\Omega$  at atmospheric pressure to  $-316\Omega$  at  $10^{-3}$  mbar which represents a sensitivity of 17.4%/bar of the reactance. The functionality of the MEMS is therefore confirmed, with similar absolute variations in reactance between the simulated and measured values.

The difference between the expected and the measured reactance can be explained firstly by the fact that the equivalent circuit of the MEMS is not a pure RC circuit. The parasitic element on the MEMS then modify the reactance. Another explanation could be the presence of a residual stress on the membrane, typically caused by various manufacturing processes used to fabricate MEMS devices, including deposition, etching, bonding, and thermal treatments. The membrane may not be flat under vacuum, which causes the increase of the global value of the reactance.

### 3.5.3 Measurement of the membrane deflection

In order to link the reactance variation of the MEMS with the pressure, and to evaluate the static deflection of the membrane under vacuum, the measurement of the profile of membranes were done using Digital Holographic Microscopy (DHM). This method uses light to create an interference pattern between a reference wave and a wave emanating from the sample. Thanks to a reconstruction algorithm of the amplitude and the phase of the light signal received, a 3D image of the sample can be created.

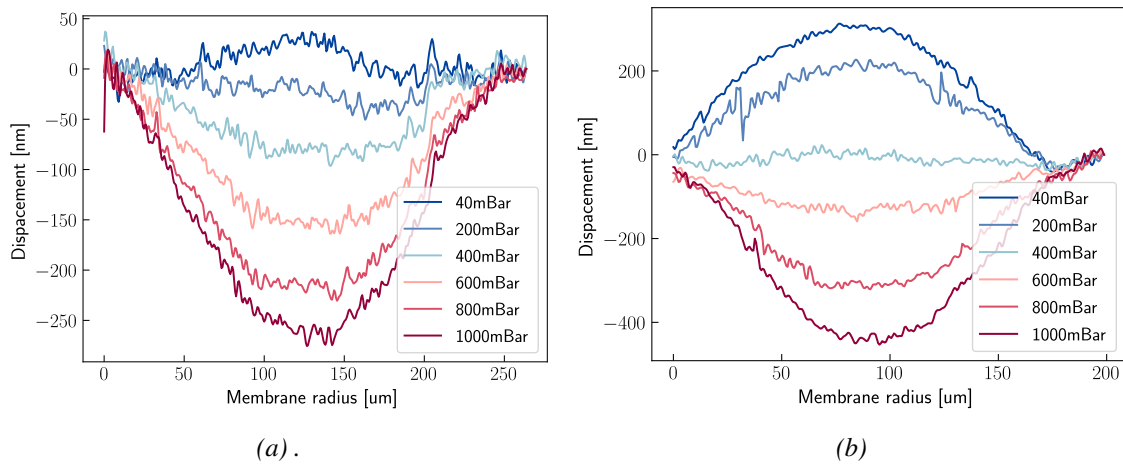


Figure 3.25: Measurement of the profile of MEMS with a metallized membrane (a) and a non-metallized membrane (b), at different level of pressure.

Figure 3.25 shows the profile of two different membranes: one metallized and the other one non-metallized. The non-metallized membrane is not flat at 40 mBar, but it is at a pressure of 400 mBar, while the metallized membrane is relatively flat at 40 mBar. The total displacement of both membrane is however coherent with the values expected. This phenomenon of curved membrane under vacuum is present at different level for all the non-metallized membranes measured, while the metallized membrane are less impacted by this issue.

This curvature of the membranes under vacuum can be explained either by a mechanical stress in the membrane that opposes the pressure or a much higher than expected pressure inside the cavity, or a combination of both hypothesis.

One method of determining the source of this curvature would be to etch the center of one of the membrane with FIB, then remeasure the membrane curvature with a DHM. If it has the same curvature as before etching, the problem is induced by a stress. If the membrane is flat, the cavity was not fully vacuum sealed. If it is less curved, both phenomena were present.

## 3.6 Conclusion

To conclude, this chapter focused on the characterization on the MEMS, from the properties of the materials to the verification of the functionality of the MEMS and their response with the pressure. This enabled to validate the correct execution of manufacturing steps, such as sealing the Si top or the etching of the metal. The electrical properties of the metal were also validated, such as the conductivity of the metal. The functionality of the MEMS, i.e. the variation of its impedance with pressure has been shown. However, some characterizations showed differences from what was expected, such as the non-resistive nature of the contact between the metal and

the doped silicon. Other characterizations remain to be carried out, such as a measurement of the doping profile by SIMS or an FIB to study the non-planarity of membranes in vacuum.

This enables to identify areas for improvement in the manufacturing process to enhance the performance of the MEMS. The priority for improvement is to reduce the resistivity of the MEMS. The problem of contact resistance between the silicon and the metal also needs to be resolved in order to optimize the behavior of the MEMS.

The variation of impedance of the MEMS were then extracted and imported on to Ansys HFSS in order to design the antennas. The following chapter focus on this design considering the RF performances of the MEMS, on the fabrication of the antennas as well as the characterization of the sensor in the anechoic chamber.

## Bibliography

- [1] L. J. van der Pauw. “A METHOD OF MEASURING SPECIFIC RESISTIVITY AND HALL EFFECT OF DISCS OF ARBITRARY SHAPE”. In: 1991. URL: <https://api.semanticscholar.org/CorpusID:123851079>.
- [2] P. Ólafsson and R. Sandström. “Calculations of electrical resistivity for Al–Cu and Al–Mg–Si alloys”. In: *Materials Science and Technology* 17.6 (2001), pp. 655–662. DOI: [10.1179/026708301101510528](https://doi.org/10.1179/026708301101510528). eprint: <https://doi.org/10.1179/026708301101510528>. URL: <https://doi.org/10.1179/026708301101510528>.
- [3] S.J. Proctor, L.W. Linholm, and J.A. Mazer. “Direct measurements of interfacial contact resistance, end contact resistance, and interfacial contact layer uniformity”. In: *IEEE Transactions on Electron Devices* 30.11 (1983), pp. 1535–1542. DOI: [10.1109/T-ED.1983.21334](https://doi.org/10.1109/T-ED.1983.21334).
- [4] M.C.A.M. Koolen, J.A.M. Geelen, and M.P.J.G. Versleijen. “An improved de-embedding technique for on-wafer high-frequency characterization”. In: *Proceedings of the 1991 Bipolar Circuits and Technology Meeting*. 1991, pp. 188–191. DOI: [10.1109/BIPOL.1991.160985](https://doi.org/10.1109/BIPOL.1991.160985).



# 4

## Antenna design and sensor characterization

---

*This chapter presents the designs of the pressure sensors in a co-design approach. The antenna geometries are chosen based on the characterization of the MEMS presented in Chapter 3. The sensors are then characterized in an anechoic chamber, using a measurement setup specifically designed for this thesis. The signal processing algorithm is presented in order to extract the response of the sensors versus the pressure.*

---

### Contents

---

<b>4.1</b>	<b>Introduction</b>	<b>88</b>
<b>4.2</b>	<b>Sensor design</b>	<b>88</b>
4.2.1	MEMS selection criteria	88
4.2.2	Antenna design and simulations	89
4.2.3	Summary of the properties of the antennas	95
<b>4.3</b>	<b>Frequency response of the sensors in anechoic chamber</b>	<b>96</b>
4.3.1	Generalities about characterization in anechoic chamber	96
4.3.2	Algorithm of signal processing	97
4.3.3	Frequency response of the sensors	98
<b>4.4</b>	<b>Pressure response of the sensors in anechoic chamber</b>	<b>100</b>
4.4.1	Measurement setup in anechoic chamber	100
4.4.2	Frequency response of the vacuum chamber	100
4.4.3	Modification of the time-gating algorithm to extract the pressure response	101
4.4.4	Analysis of the raw measurements	102
4.4.5	Pressure response of the sensors	104
4.4.6	Estimation of the reading range	108
4.4.7	Estimation of the resolution	109
<b>4.5</b>	<b>Conclusion</b>	<b>109</b>

---

## 4.1 Introduction

On this chapter, the design of the wireless pressure sensors is presented, based on the characterization of the wafers, presented in Chapter 3, which provided a precise understanding of the mechanical and electrical behavior of the capacitive MEMS pressure sensors. Among the 10 wafers fabricated, a wafer was selected and cut to extract individual chips. The two main selection criteria relate to MEMS impedance: the real part of the MEMS impedance must be as low as possible, and as constant as possible over the 0.7-1 GHz range. Based on the results of the characterization of the MEMS on these chips, antennas were designed. These antennas were laser printed on a copper clad FR4 substrate. The MEMS were then wire-bonded to the antennas.

These sensors are characterized in an anechoic chamber, where the aim is to determine the response of the antenna to an incident EM wave and to compare it with the results of simulation. This first part of the characterization aims to verify that the sensor has the desired response at atmospheric pressure and to implement the signal processing algorithms. The focus is on characterizing their properties as an antenna (i.e., mainly its RCS).

This is followed by the characterization of the functionality of the sensor, i.e., in the context of this thesis, if it is possible to extract the pressure value from the responses of the sensors. A measurement setup has been specifically designed for this thesis, taking into account measurement constraints in anechoic chambers. By slightly modifying the signal processing algorithm, the evolution of the frequency response of the sensor with the pressure is shown, and then the pressure responses of the sensors.

## 4.2 Sensor design

This section focuses on the design of the sensors, starting with the choice of MEMS to be placed on the antennas. To make these choices, some criteria were defined to obtain the best performances possible. On the one hand, the real part of the MEMS impedance must be as low as possible, in order to increase the sensitivity. On the other hand, the MEMS resistance must be as constant as possible over the 0.5-1 GHz range: its variation in frequency could be related to a parasitic effect which can reduce the MEMS sensitivity. Then, three antennas were designed and simulated on Ansys HFSS and impedance-matched to their MEMS around 868 MHz. The choice of these geometries among others studied (patch antenna, monopole wire-patch antenna [1]...) is motivated by several reasons, such as the desire to study two different interrogation methods, based on frequency variation and backpropagated power, or the need to adapt to the high resistance of MEMS. Their electrical and electromagnetic behavior were extracted from these simulations.

### 4.2.1 MEMS selection criteria

As described in the last chapter, the MEMS presents a characteristic that strongly impact the sensitivity of the antenna : the high value of serial resistance, which is around 500 to 1000  $\Omega$ . To overcome this issue, it as been decided to parallelize multiple MEMS on the same antenna, i.e., 2 or 4 MEMS to reduce the equivalent resistive part of the MEMS. On each chip, the two MEMS on the same chip are sensitive to pressure as the membrane of the reference MEMS are not fully etched. Bearing this in mind, the criteria for selecting MEMS are :

- The MEMS must have their resistance as low as possible, in order to increase the sensitivity, as shown in section [2.7.3](#).
- All the MEMS selected for a particular antenna must have the same impedance. This makes

it possible to determine the total impedance by dividing the impedance of a single MEMS by the number of MEMS connected in parallel.

- The MEMS must have their resistance as constant as possible in the 0.7-1 GHz band. This is to avoid parasitic effects that could lower the sensitivity at 868 MHz.

Based on these criteria, a wafer was chosen, and cut in order to have chips of  $2 \times 2$  mm with two MEMS on each chip, which were wire-bonded on the antennas. At 868 MHz, the resistance of the MEMS can be reduced to around  $300\Omega$  if two MEMS are put in parallel, or around  $150\Omega$  if four MEMS are put in parallel.

#### 4.2.2 Antenna design and simulations

Based on the MEMS chosen, it was decided to design three antennas with three different geometries. One is a miniature antenna designed to be interrogated on the variation of backpropagated power. The two other ones are based on the variation of resonance frequency. One has two MEMS in parallel as a load and the other one has four MEMS in parallel. These geometries are shown in Figure 4.1. All the antennas are designed with a  $35\ \mu\text{m}$  thick copper over a 0.8 mm thick FR4 substrate.

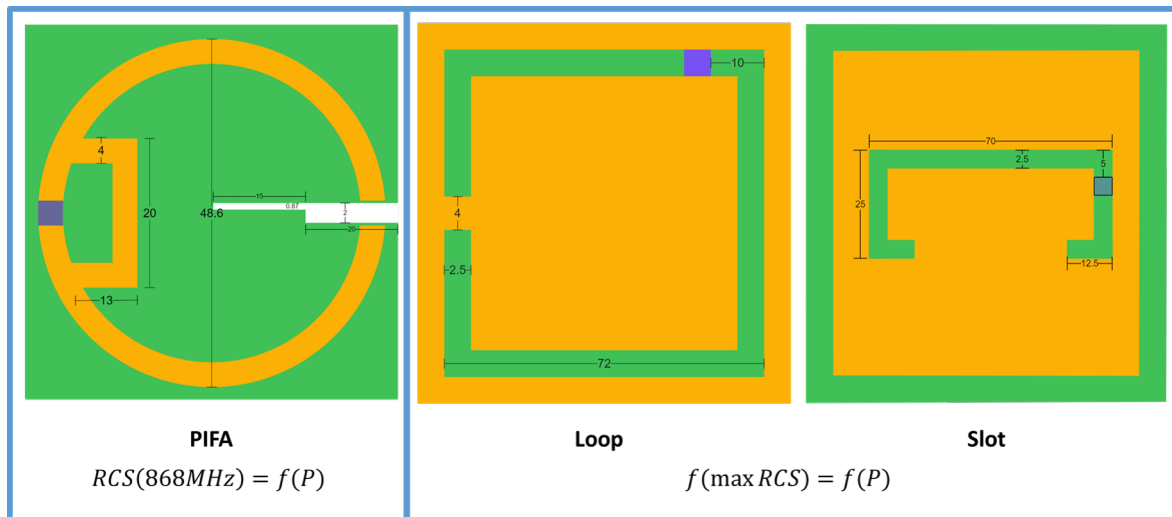


Figure 4.1: Geometries of the antennas, where the yellow part is the copper, the green part the substrate and the blue part the position of the MEMS. The PIFA is designed to study the variation of RCS at 868 MHz and the two others ones the variation of the frequency of maximum of RCS.

The following sections present the simulations of each antenna and the impedances of the MEMS associated. The impedances of the MEMS at 1 bar obtained by measurement under probes, while the impedances under vacuum were interpolated based on the measurement of another wafer at  $10^{-3}$  mbar and on the analytical model of the capacitance (Eq. 2.3). The objective is to extract the electrical behavior of the sensors (input impedance of the antenna, reflection coefficient at the load) and their electromagnetic behavior (RCS, gain diagram).

##### PIFA antenna

The first antenna is based on a PIFA (Planar Inverted F-shaped Antenna) [2], a geometry of miniature antenna inspired by a F-shaped antenna. Miniature antennas with low structural mode like the PIFA are very suitable for a measurement based on the variation of RCS at a fixed frequency (in our case, 868 MHz), because the variation of the antenna mode of the RCS has a relative greater impact on the total RCS. The resonance frequency of the antenna is mainly fixed

by the size of the loop, while the short-circuit around the MEMS is used for impedance adaptation. It has an electrical length  $ka = 0.44$  at 868 MHz. This sensor has a radiation efficiency  $e_0 = 0.76$ . On this chapter, this antenna (and the sensor associated) is called "PIFA".

4 MEMS with the same impedances were put in parallel on this structure, with the impedance of one of the MEMS at 1 bar shown in Figure 4.2. The small oscillations on the curves are due to the prober, as shown in section 3.5.2. Those impedances were firstly imported to Ansys HFSS as a lumped port in order to impedance-match the MEMS and the antenna around 868 MHz.

The input impedance and the reflection coefficient were extracted as shown in Figure 4.3. In order to evaluate the variation of the sensor behavior with the pressure, the MEMS impedance at atmospheric pressure and under vacuum was set on Ansys HFSS. The reflection coefficient shows nearly no variation of resonance frequency between vacuum and the atmospheric pressure, but a difference of 15 dB in the amplitude of the peak, and a very narrow bandwidth. All this phenomena are due to the small electrical size of the antenna, as it impacts the bandwidth but also the sensitivity as shown in section 2.7.2. This antenna shows a radiation pattern close to an unidirectional pattern in the gain diagram of Figure 4.4a, with a maximal gain of 0.51 dB.

To study the field backpropagated by the sensor, the lumped port were replaced on Ansys HFSS by a circuit port with the 4 impedances of the MEMS in parallel. A plane wave was used to excite the sensor. Its direction of propagation is along the symmetry axis of the antenna, while the electric field is in the plane of the antenna. The sensor does not modify the polarization of the signal. The simulated RCS is plotted in Figure 4.4b. It shows a narrow peak around the resonance frequency, as expected for a miniature antenna.

The variation of RCS extracted from simulations, shown in Figure 4.5, is from 2895 mm<sup>2</sup> to 3142 mm<sup>2</sup> when the pressure varies from 10<sup>-3</sup> mbar to 1 bar. It is equivalent to a sensitivity of 8%/bar of backpropagated power.

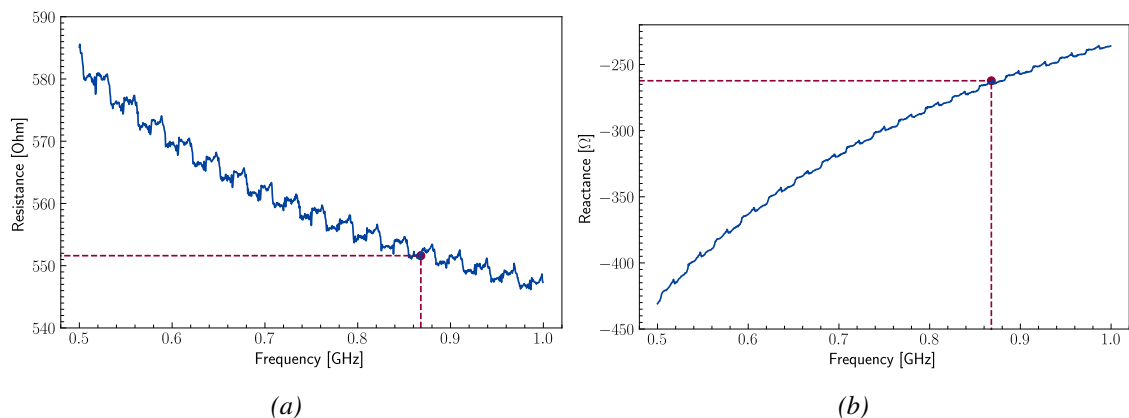


Figure 4.2: Real (a) and imaginary parts (b) of the impedance of one of the 4 MEMS put in parallel as the load of the PIFA antenna at 1 bar. The points with the dotted lines correspond to the value of the impedance at 868 MHz. The small periodic variations in the curves are due to the prober used for the characterization of the MEMS. At 868 MHz and 1 bar, the 4 MEMS in parallel have an equivalent impedance of  $137.9 - j65.57\Omega$ .

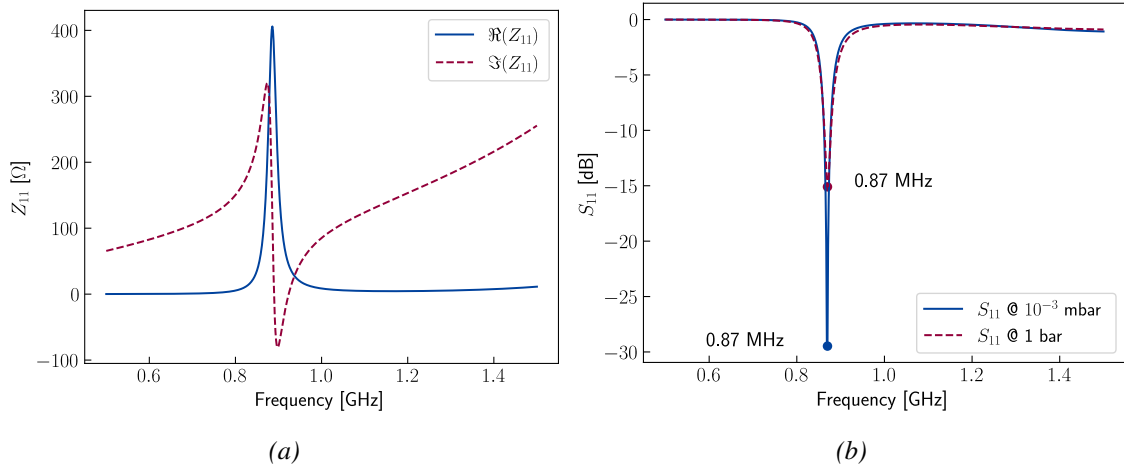


Figure 4.3: Electrical properties of the PIFA sensor. (a) Input impedance of the PIFA antenna at the location of the MEMS. (b) Reflection coefficient of the antenna loaded by the MEMS.

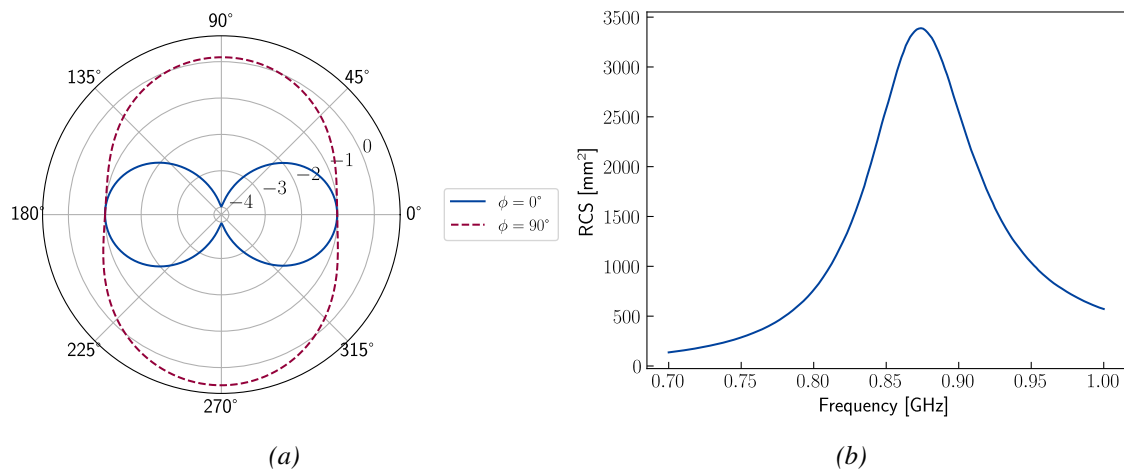


Figure 4.4: Electromagnetic behavior of the PIFA. (a) Realized gain of the PIFA sensor at 1 bar and 868 MHz. (b) RCS of the PIFA sensor at 1 bar.

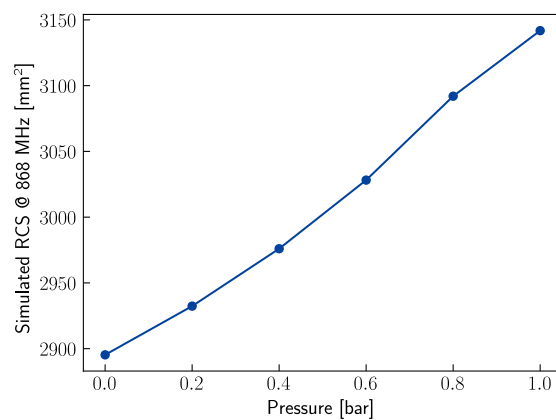


Figure 4.5: Simulated RCS at 868 MHz versus pressure for the PIFA sensor.

## Loop antenna

The second antenna is based on the complementary structure of a loop antenna. It is designed using the Babinet principle, which claims that an antenna and its complementary have the same radiation pattern when they are excited with equivalent currents of the same magnitude but opposite phases. H.G. Booker [3] extends this principle for the polarization. It allows to increase the input impedance of an antenna for the same size, which is very suitable as the MEMS resistance is higher than expected. On this geometry, the resonant element is the loop itself (i.e., the part of the antenna without copper). By modifying the size of this loop, the resonance frequency of the antenna is changed, while the position of the MEMS on the loop modifies the impedance matching. The minimal width of the loop is fixed by the size of the chips. This antenna has an electrical size  $ka = 0.92$  at 868 MHz. On this manuscript, this antenna (and the associated sensor) is called "Loop".

As it has a lower quality factor than the PIFA, this geometry can be used to have a sensor which working principle is based on the variation of the frequency of the maximum RCS, as a higher electrical size means higher sensitivity. 4 MEMS with the same impedances were put in parallel on this structure, with the impedance of one of the MEMS shown in Figure 4.6.

Using the same procedure as for PIFA, the input impedance of the antenna (Figure 4.7a) and the reflection coefficient (Figure 4.7b) were extracted using a lumped port. The resonance frequency, as a function of the pressure, shifts from 863.625 MHz to 868.25 MHz (sensitivity of 4.625 MHz/bar), which is much higher than the shift of resonance frequency of the PIFA, as expected because this antenna has an higher electrical size. The resonance frequency increases with the pressure, which is because the adaptation occurs at the anti-resonance of the antenna (i.e., in the frequency band where  $\Im(Z_{11})$  decreases). This sensor has a radiation efficiency  $e_0 = 0.97$ .

Figure 4.8a shows the radiation pattern of the sensor in the  $\phi = 0^\circ$  and  $\phi = 90^\circ$  planes at 868 MHz and 1 bar. The maximal gain of the sensor is 3.35 dB at  $\theta = 0^\circ$  and  $\theta = 180^\circ$  (i.e. in the out-of-plane axis), which is as expected higher than the PIFA.

Finally, Figure 4.8b shows the RCS of the antenna at 1 bar. The slight difference between the maximum of RCS and the resonance frequency may be due to a difference in how the plane wave and the lumped port excites the antenna, as the sensor is not placed at the center of the loop. The value of the RCS is much higher than the PIFA, as the antenna has a larger electrical size and a larger structural mode.

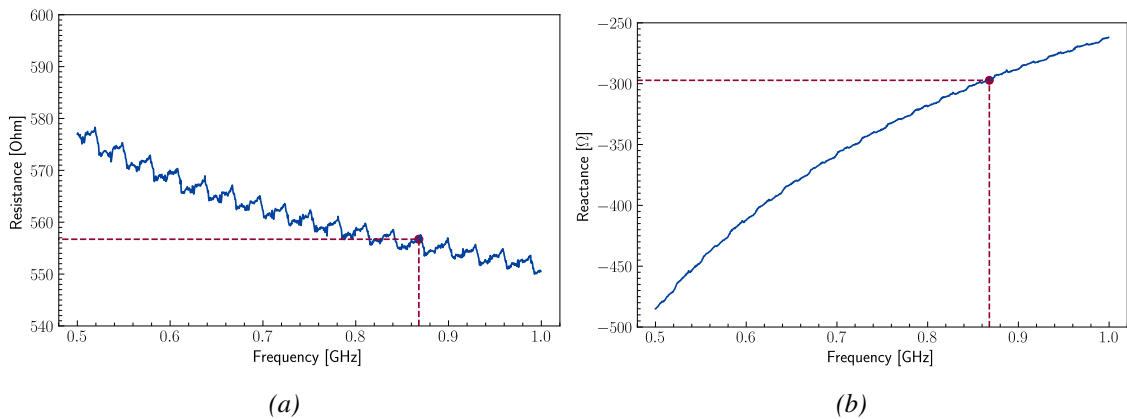


Figure 4.6: Real (a) and imaginary parts (b) of the impedance of one of the 4 MEMS put in parallel as the load of the Loop antenna. The points with the dotted lines correspond to the value of the impedance at 868 MHz. The small periodic variations in the curves are due to the prober used for the characterization of the MEMS. At 868 MHz and 1 bar, the 4 MEMS in parallel have an equivalent impedance of  $139.18 - j74.31\Omega$ .

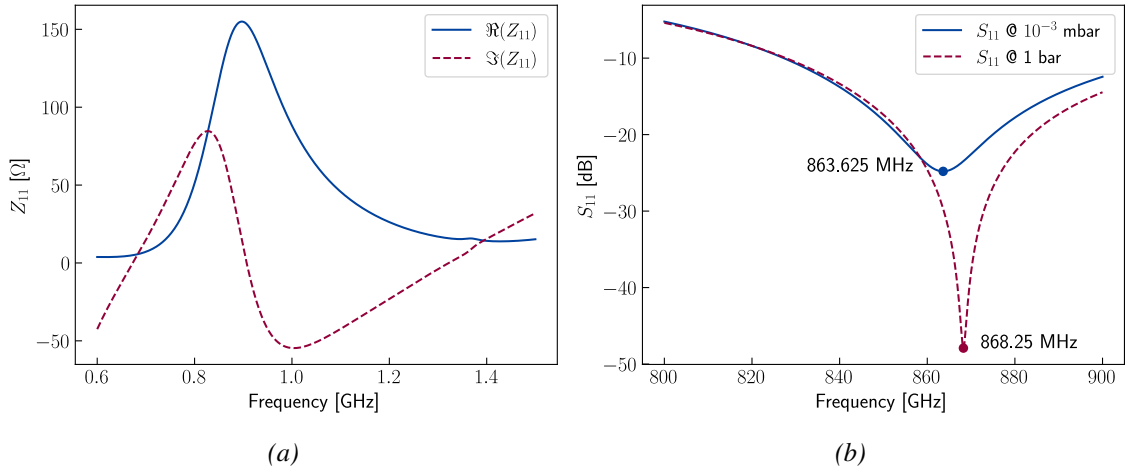


Figure 4.7: Electrical properties of the Loop sensor. (a) Input impedance of the Loop antenna at the location of the MEMS. (b) Reflection coefficient of the antenna loaded by the MEMS.

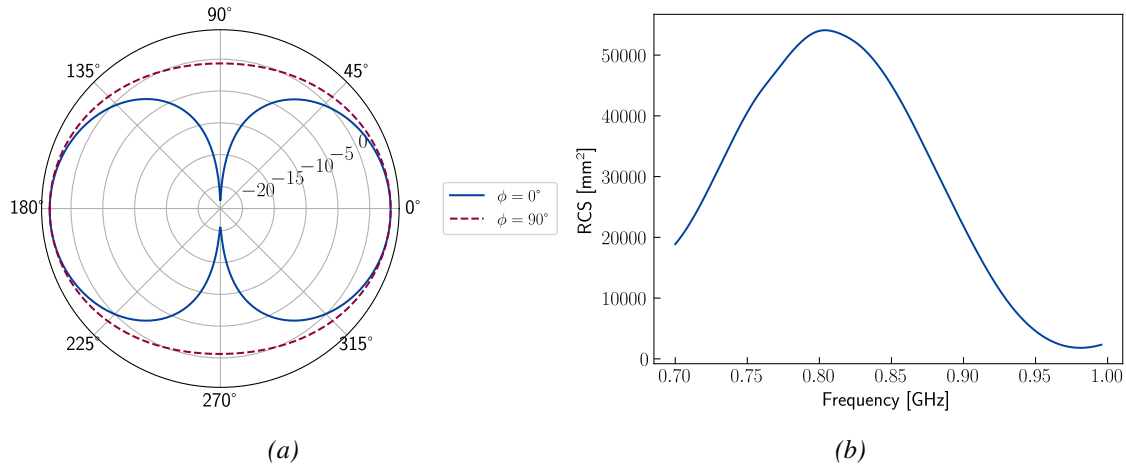


Figure 4.8: Electromagnetic behavior of the Loop. (a) Realized gain of the Loop sensor (in dB) at 1 bar and 868 MHz. (b) RCS of the Loop sensor at 1 bar.

### Slot antenna

Finally, the third antenna is the complementary of a dipole, with a similar design approach as the Loop: the geometry allows to have a higher input impedance than a dipole. It allows to have a different geometry of sensor with a measurement based on the variation of resonance frequency. The slot is the radiating element on this antenna. By modifying the length of the slot, the resonance frequency changes, while the position of the MEMS fixes the impedance matching. The width of the loop is fixed by the size of the chips. The slot has been folded at its ends to reduce its size. 2 MEMS were put in parallel on this antenna, the impedance of an individual MEMS is shown in Figure 4.9. This choice was motivated by the desire to have a sensor with 2 MEMS in parallel. It has an electrical size  $ka = 0.67$  at 868 MHz. This sensor has a radiation efficiency  $e_0 = 0.92$ . On this chapter, this antenna (and the sensor associated) is called "Slot".

Figure 4.10 shows the input impedance and the reflection coefficient of the Slot antenna. The resonant frequency shift from 867.875 MHz to 873 MHz (sensitivity of 5.125 MHz/bar). Figure 4.11a shows the realized gain of the antenna, with a maximum gain of 2.80 dB in the out-of-plane direction.

Finally, the RCS of the antenna under a plane wave excitation is plotted in Figure 4.11b. By

looking at the RCS, it can be seen that the frequency of maximum RCS is slightly different than the resonance frequency (i.e., the frequency of minimum of  $S_{11}$ ). It is because the excitation is different: for the calculation of the  $S_{11}$  the excitation is done at the position of the MEMS, while for the RCS it is by an incident wave. Even the excitation under an incident wave is different depending on whether the plane wave arrives on the side of the antenna where the MEMS is located or on the opposite side. In this case, the plane wave is on the side of the MEMS.

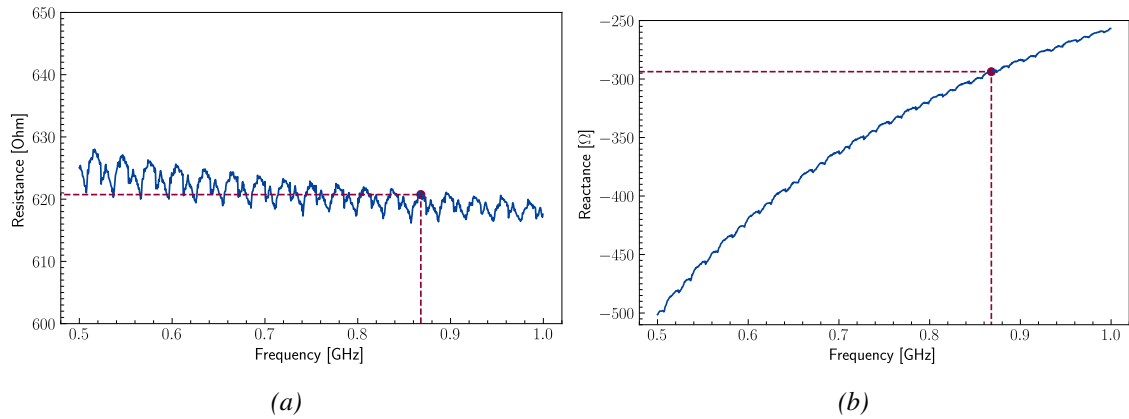


Figure 4.9: Real (a) and imaginary parts (b) of the impedance of one of the 2 MEMS put in parallel as the load of the Slot antenna. The points with the dotted lines correspond to the value of the impedance at 868 MHz. The small periodic variations in the curves are due to the prober used for the characterization of the MEMS. At 868 MHz and 1 bar, the 2 MEMS in parallel have an equivalent impedance of  $310.37 - j146.86\Omega$ .

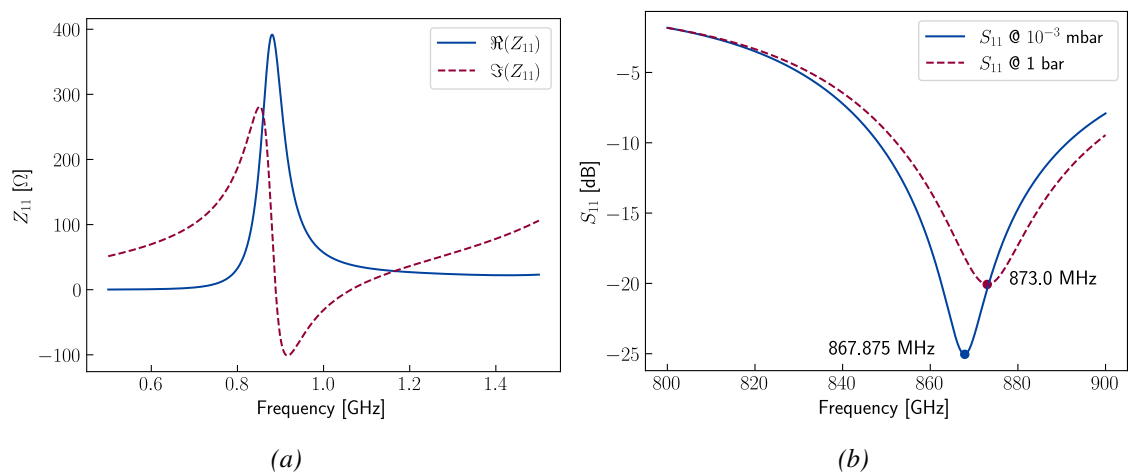


Figure 4.10: Electrical properties of the Slot sensor: (a) Input impedance of the Slot antenna at the location of the MEMS. (b) Reflection coefficient between the antenna and the MEMS.

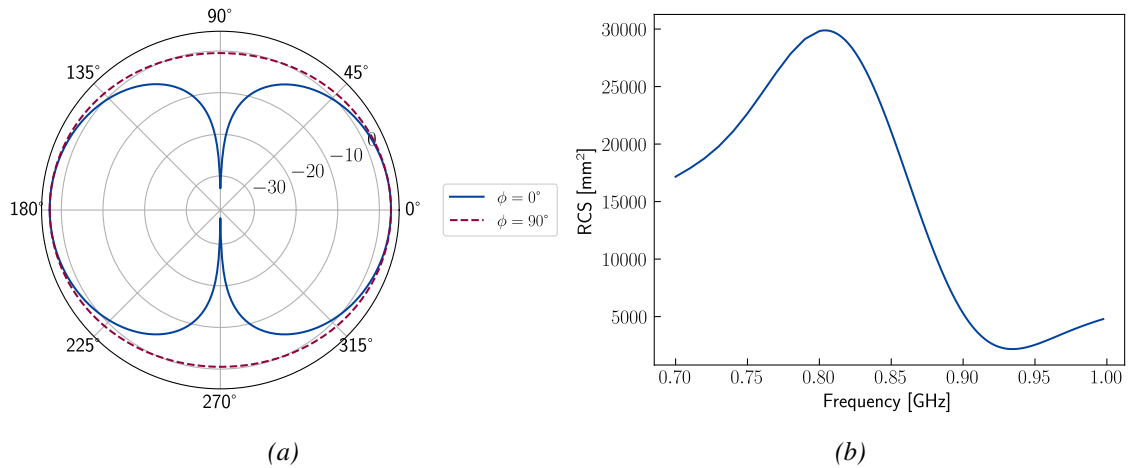


Figure 4.11: Electromagnetic behavior of the Slot. (a) Realized gain of the Slot sensor at 1 bar and 868 MHz. (b) RCS of the Slot sensor at 1 bar.

### 4.2.3 Summary of the properties of the antennas

As a conclusion, three antennas were designed specifically for particular MEMS, that meet the requirements in terms of sensitivity and high MEMS input impedance. One of them is a miniature antenna (the PIFA), with a working principle based on the variation of amplitude of RCS at 868 MHz. The two others (the Loop and the Slot) are based on the variation of the frequency of maximum RCS. Table 4.1 summarizes the important parameters of these sensors.

Antenna	Electrical size $ka$	Efficiency $e_0$	Max Gain	Max RCS	Sensitivity
PIFA	0.44	76%	0.51 dB	3390 mm <sup>2</sup>	8% RCS/bar
Loop	0.92	97%	3.35 dB	54091 mm <sup>2</sup>	4.6 MHz/bar
Slot	0.67	92%	2.80 dB	29885 mm <sup>2</sup>	5 MHz/bar

Table 4.1: Summary of the properties of the sensors.

It seems interesting to point out that, as the Loop sensor have the highest RCS, it will have the highest reading range. It this mainly because the Loop is the less miniaturized sensor among the three. However, the resolution is also dependent of the interrogation distance. These parameters will be studied during the characterization of the three sensors in anechoic chamber, presented in the following sections.

### 4.3 Frequency response of the sensors in anechoic chamber

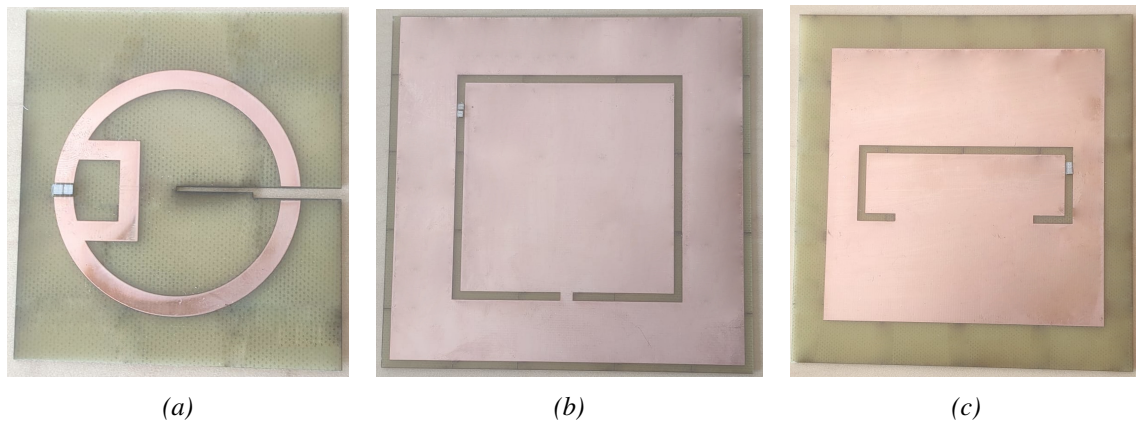


Figure 4.12: Pictures of the sensors, where the antenna is made of copper over FR4. The MEMS are wire-bonded to the antennas. (a) PIFA sensor (b) Loop sensor (c) Slot sensor.

After the simulations, the antennas were printed using a laser etching of a 30 $\mu\text{m}$ -thick copper over a 0.8mm-thick FR4 sheet. The wafer chosen was diced, and the chips were put on the PCB using UV glue. Then, they were wire-bonded to the antennas, as shown in Figure 4.12.

The characterization of the sensors is done in two times: firstly, the sensors are characterized at atmospheric pressure to extract their response in frequency, and to compare them with the simulations. This is presented in this section. Then, using a setup specifically designed for this thesis, the sensors are characterized in pressure, to extract the variation of the frequency of maximum RCS or the backpropagated power. This is presented in section 4.4.

#### 4.3.1 Generalities about characterization in anechoic chamber

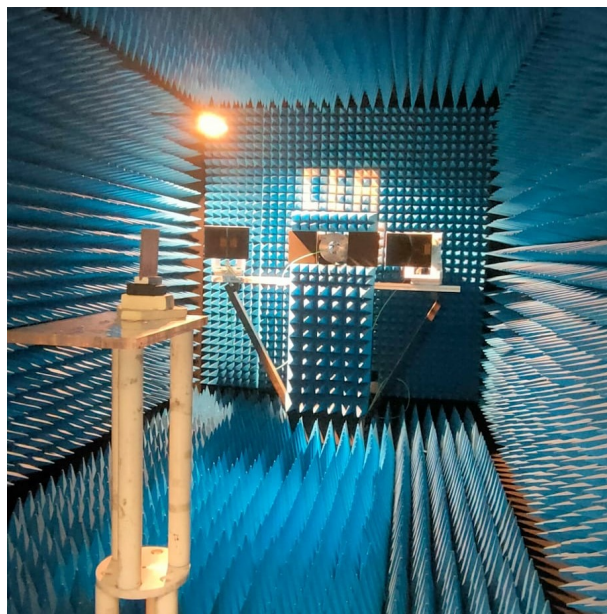


Figure 4.13: CEA-Leti anechoic chamber, for measurements up to 40 GHz, with the sensor to characterize in frequency placed on the support.

An anechoic chamber is a specialized testing environment which provides a controlled electromagnetic environment, free from any outside signals and reflections, thanks to absorbers which cover the walls of the chamber. The most common absorber is the carbon-loaded foam pyramid. As an example, one of the CEA-Leti's anechoic chambers is shown in Figure 4.13.

The classical antenna characterization includes the measurement of its input impedance  $Z_{11}$ , its reflection coefficient  $S_{11}$  and its gain diagram. This is done by feeding the antenna at the load position, and for the gain pattern measurement, by placing the antenna on a rotating support. However, the characterization of the sensors done in this thesis is different. The main parameter to measure for the sensors is their RCS in a particular direction, done by measuring the signal backpropagated by the sensor. This measurement was confirmed by the measurement of a metallic sphere.

There are two main ways to characterize a sensor: monostatic characterization, where the same antenna is used for both transmission and reception, and bistatic characterization, where there is one antenna for transmission and a different one for reception. In order to characterize the sensors in anechoic chamber, it was chosen to do a bistatic interrogation. In bistatic case, the emitter (Tx) and the receiver (Rx) are separated. Measurement in a bistatic configuration allows to obtain a better isolation between the signal sent and received, but at the cost of using two antennas for interrogation.

### 4.3.2 Algorithm of signal processing

The goal of the characterization is to extract only the response of the sensor from all the signal received. Indeed, even if the anechoic chamber is an environment with very few reflections, there are always parasitic signals received during the characterization. This includes reflections by the support of the antenna, coupling between the two antennas in case of a bistatic interrogation (signal emitted by one antenna which propagates directly to the other one) or small oscillations which, added together over the entire interrogation time, can strongly modify the received signal.

In order to mitigate this, the characterization is done in two times: firstly, the measurement of the anechoic chamber without the sensor is done, in order to extract the frequency response of the background  $S_{21}^{bg}$ . Then, one measurement is done for each sensor  $S_{21}^{raw}$  to determine their frequency response. By subtracting the background  $S_{21}^{bg}$  to the measurement of the sensor  $S_{21}^{raw}$ , the calibrated response is obtained  $S_{21}^{cal}$ . The RCS of the sensor can be extracted using the radar equation:

$$\sigma(f) = \left(S_{21}^{cal}\right)^2 \frac{(4\pi)^3 (R_1 R_2)^2}{G^2 \lambda^2} \quad (4.1)$$

The VNA is first calibrated using a Short-Load-Open-Thru calibration. Only the sensor and the support are present in the anechoic chamber to characterize the frequency response of the sensors under atmospheric pressure without any perturbation from any kind. The background is then considered as the anechoic chamber with the support for the sensor. Then, the signal processing is done in Python and the algorithm in pseudo-code is shown in Algorithm 1.

The steps of this algorithm are :

- Firstly, the measurement of the background  $S_{21}^{bg}$  is subtracted from the raw frequency response of the sensor  $S_{21}^{raw}$ . The background measurement is the measurement of the anechoic chamber without the object to be characterized, here, without the sensor. It allows to cancel every signal which come from reflections in the anechoic chamber.
- The calibrated response  $S_{21}^{cal}$  is then converted into the square root of the RCS  $\sqrt{\sigma(f)}$ . The usage of the square root of the RCS rather than the RCS was motivated by the visualization of the signal in time domain (or equivalently, in distance domain, by multiplying time by the celerity  $c$ ). By plotting  $S_{21}^{cal}$  in time domain, the response of the sensor will be seen in time

**Algorithm 1** RCS calculation

---

$S_{21}^{scal} \leftarrow S_{21}^{raw} - S_{21}^{bg}$	▷ Background cancellation
$\sqrt{\sigma(f)} \leftarrow S_{21}^{scal} \frac{(4\pi)^{3/2} R_1 R_2}{G\lambda}$	▷ Convert into square root of RCS
$\sqrt{\sigma(f)} \leftarrow [0, 0, 0, 0 \dots \sqrt{\sigma(f)} \dots, 0, 0, 0]$	▷ Zero padding
$\sqrt{\sigma(t)} \leftarrow \text{iFFT}(\sqrt{\sigma(f)})$	▷ Inverse FFT
$w(n) \leftarrow \text{Hann}(N_{min}, N_{max})$	▷ Hann window
$\sqrt{\sigma(t)} \leftarrow \sqrt{\sigma(t)} \times w(n)$	▷ Time gating between $N_{min}$ and $N_{max}$
$\sigma(f) \leftarrow (\text{FFT}(\sqrt{\sigma(t)}))^2$	▷ FFT of the time-gated signal
<b>return</b> $\sigma(f)$	

---

domain after 20ns, which is equivalent to a 6 meters distance, i.e. the round trip between the interrogators and the sensor. Because the RCS is proportional to  $(S_{21}^{scal})^2$ , the response would appear after 40ns, so 12 meters.

- Then, a zero-padding is done on the signal, in order to add points from 0 Hz to the minimum frequency of  $\sqrt{\sigma(f)}$  and to smoothen the curve in time domain.
- This zero-padded signal is then converted into time domain after an anti-symmetry (to keep the signal real). Because it is easier to link the response in time domain to the measurement set-up, this time-domain signal will be expressed equivalently in terms of distance.
- Then, the response is windowed around 6 meters, in order to extract only the response of the sensor and filter the other signals. The choice of the size of the window is a crucial parameter, as the goal is to match the response of the sensor with the response obtained by simulation.
- This filtered signal is then converted back into frequency domain and squared to retrieve the RCS, which is then compared to the response obtained by simulation.

This algorithm was applied for each sensor, with a size of window manually set as the choice of this window depends on the geometry of the antenna. The Python code used is shown in Appendix A.1.

### 4.3.3 Frequency response of the sensors

Subfigures (a) of 4.14, 4.15 and 4.16 shows the time-domain response of the sensors at 1 bar before and after time-gating for the three different sensors. The direct coupling between the two antennas can be seen in Figure 4.14a: as the PIFA sensor has a lower RCS, it sends back a lower amount of power, which makes this coupling appear more clearly on the time-domain signal. It is also present on the time-domain response of the two other sensors, but it is less noticeable.

As the distance between the interrogators and the sensor is 3 meters, the signals were filtered around 6 meters to extract only the response of the sensors. These time-gated signals were then converted back into frequency domain to extract the RCS in frequency domain, plotted in subfigures (b) of 4.14, 4.15 and 4.16.

The PIFA and the Slot sensors shows a good correlation between the measured signal and the simulations, while the Loop sensor shows a slight difference in terms of frequency of maximum RCS. It may be caused by a slight difference in the MEMS impedances or a misplacement of the MEMS on the antenna which changes its input impedance. For the three sensors, the amplitudes of the peaks match with the simulations. These results validates the frequency response of the sensors at atmospheric pressure obtained by simulation, and so their good design.

### 4.3. Frequency response of the sensors in anechoic chamber

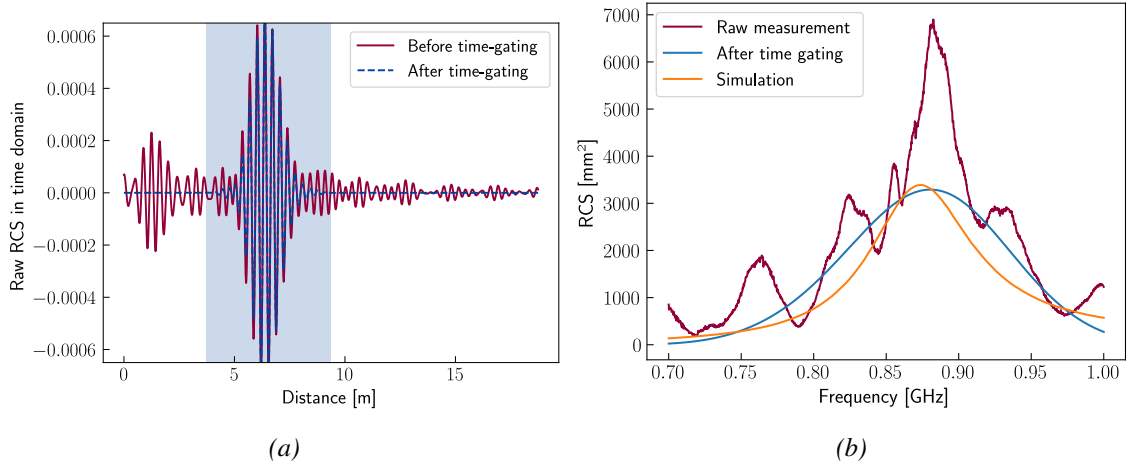


Figure 4.14: Time-domain (a) and frequency (b) response of the PIFA and comparison with the simulation. The colored area correspond to the window applied.

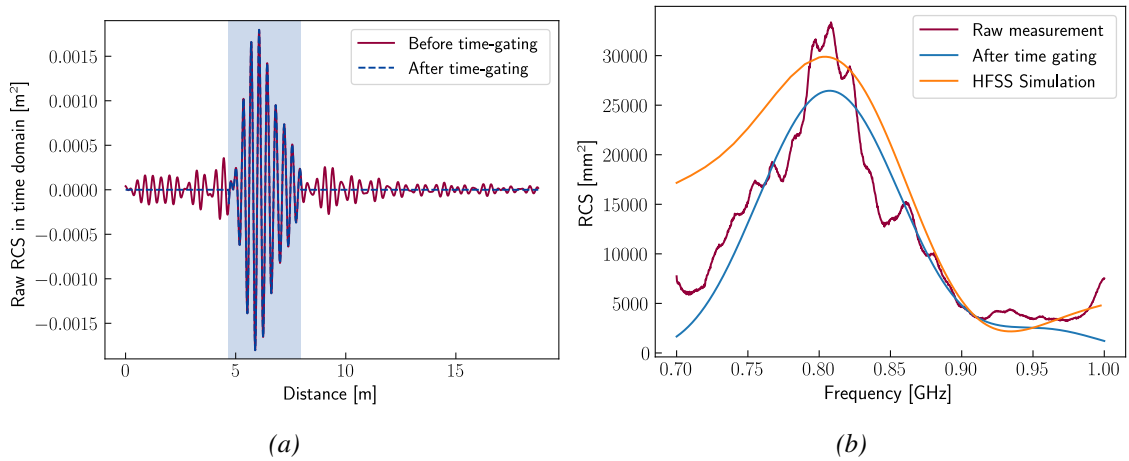


Figure 4.15: Time-domain (a) and frequency (b) response of the Slot and comparison with the simulation. The colored area correspond to the window applied.

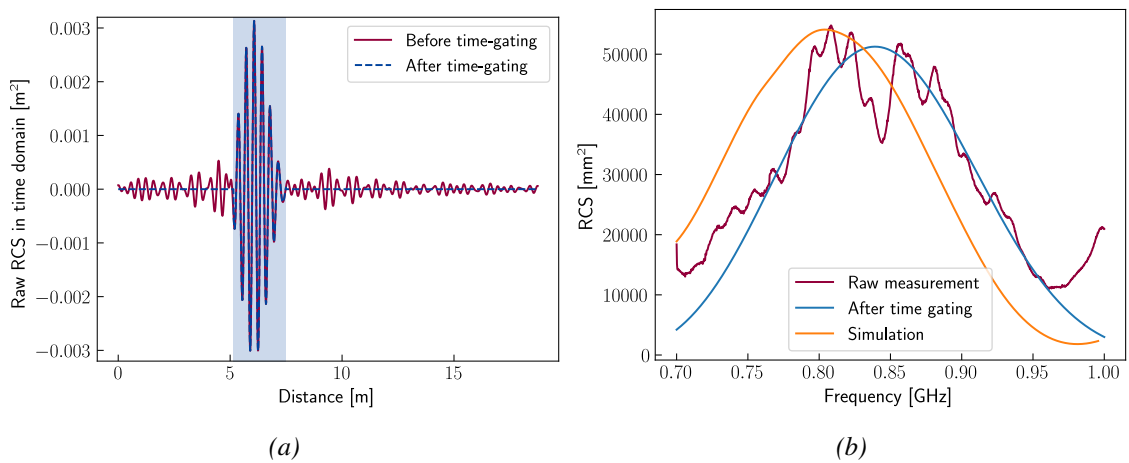


Figure 4.16: Time-domain (a) and frequency (b) response of the Loop and comparison with the simulation. The colored area correspond to the window applied.

## 4.4 Pressure response of the sensors in anechoic chamber

### 4.4.1 Measurement setup in anechoic chamber

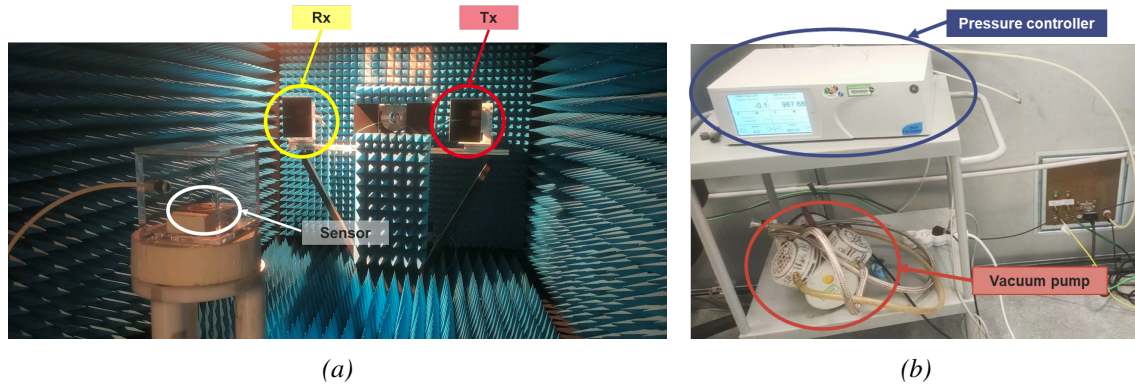


Figure 4.17: Measurement setup of the sensors in anechoic chamber. The sensor are placed inside a vacuum chamber. The pressure controller, connected to a vacuum pump, is used to change the pressure inside the vacuum chamber. The two antennas in Rx and Tx are used for the interrogation of the sensor. (a) Interior of the anechoic chamber (b) Vacuum pump and pressure controller outside the anechoic chamber.

Now that it has been shown that measured responses match those obtained by simulation, the sensors need to be characterized in pressure in order to validate their functionality. To look at the impact of pressure on the response of the sensors, a specific measurement setup was designed during this thesis. It is shown in Figure 4.17. The sensor to characterize is placed inside a vacuum chamber in plexiglass ( $\epsilon_r = 3.4$ ), manufactured for this project, over a support in Styrofoam ( $\epsilon_r = 1.1$ ). The Styrofoam is used because of its low permittivity and to align in height the antenna with the interrogators. Two antennas are used to characterize the sensor, one for the transmission (Tx) and one for the reception (Rx). The distance from each interrogator to the vacuum chamber is 3m.

A tube connects the vacuum chamber to a pressure controller outside of the anechoic chamber, which sets the pressure inside the vacuum chamber thanks to a vacuum pump. With this setup, the pressure can be set from the atmospheric pressure to 40 mbar due to limitations of the vacuum pump. The pressure controller and the vacuum pump were placed outside the anechoic chamber in order to not affect the response of the sensor.

### 4.4.2 Frequency response of the vacuum chamber

First, it is necessary to determine the response in frequency of the vacuum chamber, in order to estimate which amount of power it backpropagates. Algorithm 1 is then used again.

Figure 4.18 shows the raw signal received, the signal after data treatment and the signal obtained by simulation. At 868 MHz, there is nearly no reflection from the vacuum chamber as the RCS is very low. A peak at the response occurs at around 3 GHz. Even if its does not affect our measurements, it is interesting to understand its cause.

By plotting the electric field at 3 GHz on Ansys HFSS (Figure 4.19), under an EM wave which propagates through the z axis, it can be seen that there are two maxima of E-field at the surface orthogonal to the propagation. It can be correlated to the presence of a full wavelength on the surface. This may seem coherent because the wavelength at this frequency (10cm) is close to the dimensions of the chamber. This should be taken into account if the antenna resonates around this frequency, but it does not have an impact at 868 MHz as the RCS is much lower.

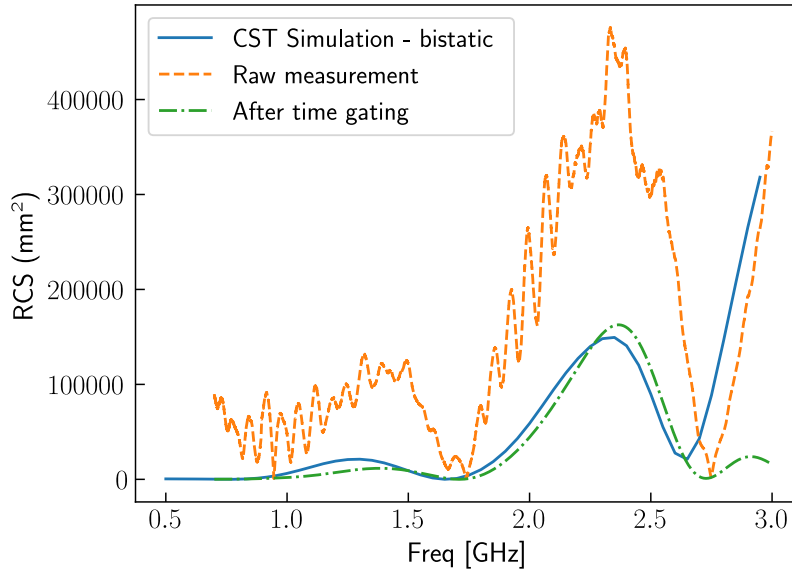


Figure 4.18: RCS of the vacuum chamber. At 868 MHz, the vacuum chamber does not reflect a lot of power, as its RCS is 573.86 mm<sup>2</sup>.

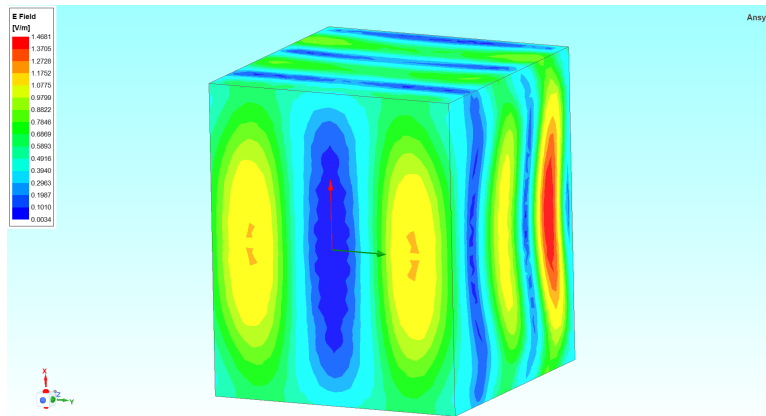


Figure 4.19: Magnitude of the electric field at the surface of the vacuum chamber at 3 GHz.

#### 4.4.3 Modification of the time-gating algorithm to extract the pressure response

During the characterization of the frequency response of the sensors at atmospheric pressure, the window of time-gating was chosen manually by looking at the time-domain response and tuning the bounds of the window to match the response in frequency domain with the simulations. However, in order to characterize the sensors in pressure, the goal is to determine the variation of the physical quantity of interest with the pressure (i.e., the frequency of maximum RCS for the Loop and the Slot sensor or the RCS at 868 MHz for the PIFA).

Algorithm 1 needs to be slightly modified. The pseudo-code is shown in Algorithm 2, applied on the variation of the frequency of maximal RCS as an example.

This function has two input parameters, which are the lower and the upper bond of the window  $N_{min}$  and  $N_{max}$ . As the environment of measurement does not changes between the measurements, this window will be applied for every pressure measured, so every measurement will have the same signal processing. It is quite similar to Algorithm 1, with some steps added at the end:

- After the FFT of the time-gated signal, the algorithm finds the frequency where the RCS is maximal, and it adds it to a list. At the end, that list will contain the frequency of maximal

**Algorithm 2** RCS time-gating in pressure**Require:**  $N_{min}, N_{max} \in \mathbb{N}^2$ **Ensure:**  $N_{min} < N_{max}$ **for all**  $P \in [0.1 - 1]$  **bar do** $S_{21}^{scal} \leftarrow S_{21}^{raw}(P) - S_{21}^{bg}$  ▷ Background cancellation $\sqrt{\sigma(f)} \leftarrow S_{21}^{scal} \frac{(4\pi)^{3/2} R_1 R_2}{G\lambda}$  ▷ Convert into square root of RCS $\sqrt{\sigma(f)} \leftarrow [0, 0, 0, 0 \dots \sqrt{\sigma(f)} \dots 0, 0, 0, 0]$  ▷ Zero padding $\sqrt{\sigma(t)} \leftarrow \text{iFFT}(\sqrt{\sigma(f)})$  ▷ Inverse FFT $w(n) \leftarrow \text{Hann}(N_{min}, N_{max})$  ▷ Hann window $\sqrt{\sigma(t)} \leftarrow \sqrt{\sigma(t)} \times w(n)$  ▷ Time gating between  $N_{min}$  and  $N_{max}$  $\sigma(f) \leftarrow (\text{FFT}(\sqrt{\sigma(t)}))^2$  ▷ FFT of the time-gated signal $f(P) \leftarrow f(\max |\sigma(f)|)$  ▷ Add the frequency of max RCS to the list $\Sigma(f, P) \leftarrow \Sigma(f) \cup \sigma(f)$  ▷ Add the RCS to the list**end for** $a, b, R^2 \leftarrow \text{linreg}(f(P))$  ▷ Linear regression  $f = aP + b$  with a determination coefficient  $R^2$ **return**  $\Sigma(f, P), f(P), a, b, R^2$ 

RCS for each value of pressure. For a sensor based on the variation of RCS at a fixed frequency, the algorithm adds the value of the RCS to the list. It allows to determine the sensor linearity.

- Then, a linear regression is done on the points of the list to find the value of the determination coefficient  $R^2$ , which quantify how close the points of the list are close to a linear function.
- Finally, it returns the list of the curves of RCS in frequency domain  $\Sigma(f, P)$ , the list of frequencies of maximum RCS  $f(P)$  (or equivalently the values of RCS at a fixed frequency), the coefficients of the equation of linear regression  $a$  and  $b$  and the determination coefficient  $R^2$ .

The equivalent Python code used is shown in Appendix [A.2](#).

#### 4.4.4 Analysis of the raw measurements

The sensors were then placed inside the vacuum chamber and their response measured from 0.1 to 1 bar with a step of 0.1 bar. Before any signal processing, it seems interesting to look at the impact of the pressure on the raw RCS of the sensor, i.e. the spectrum before the time-gating. It allows to have an overview on the sensitivity of the sensor and the value of the frequencies of the peaks, which is used later to validate the pressure response curves of the sensors.

#### 4.4. Pressure response of the sensors in anechoic chamber

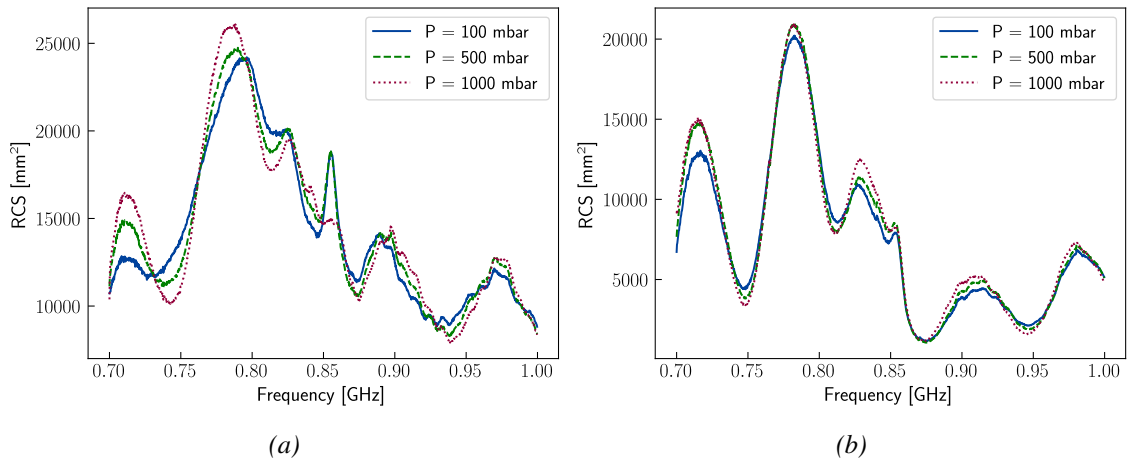


Figure 4.20: Comparison of the raw RCS measurements of the Loop (a) and Slot (b) sensors at 100 mbar, 500 mbar and 1 bar.

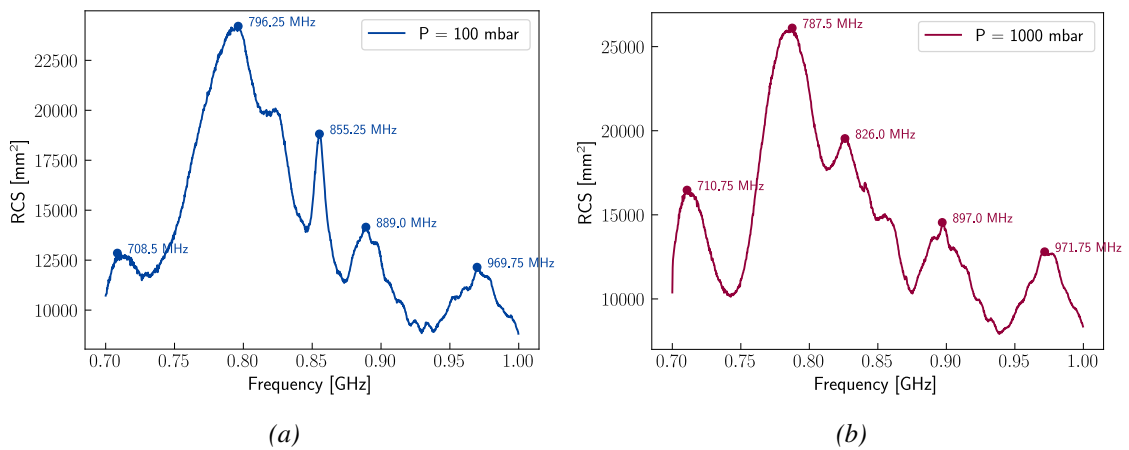


Figure 4.21: Raw measurement of the Loop sensor before the time gating, at 100 mbar (a) and 1 bar (b) with the frequencies of the main peaks.

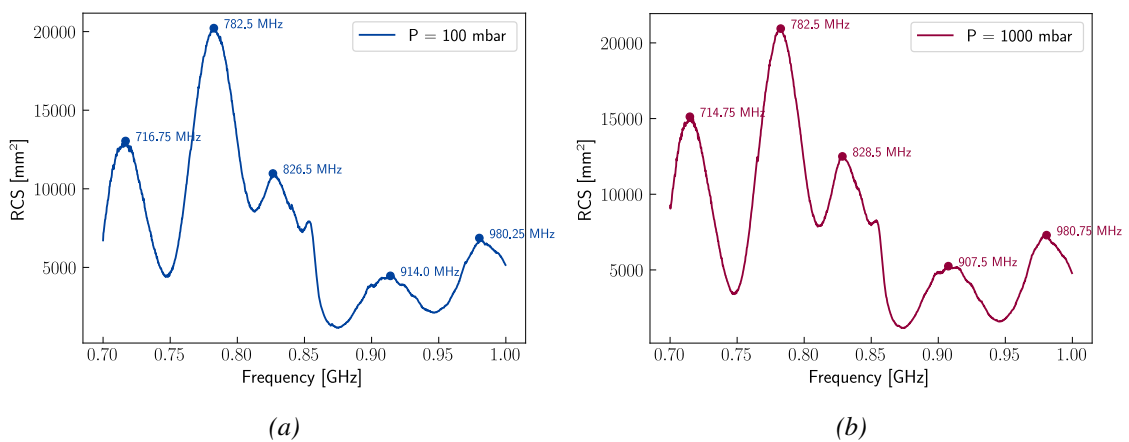


Figure 4.22: Raw measurement of the Slot sensor before the time gating, at 100 mbar (a) and 1 bar (b) with the frequencies of the main peaks.

Figure 4.20 shows the raw measurements of the RCS of the Loop and the Slot sensors, at 100

mbar, 500 mbar and 1 bar. It confirms that the MEMS have an impact on the measurement, and more specifically on its peaks, in order to compare them to the results of the characterization in frequency. It is then interesting to study the variation of the frequency of those peaks:

- For the Loop, among the 5 peaks plotted in Figure 4.21, the peak between 710.75 MHz and 708.5 MHz significantly change with the pressure, a similar variation of frequency is seen at 796.5 MHz, 889 MHz and 969.75 MHz. The frequency of the peak at 796.5 MHz is slightly lower than the frequency of the peak observed in simulation (803.7 MHz) but much lower than value obtained during the characterization under atmospheric pressure (839.25 MHz).
- For the Slot the variation of the frequency of the peaks in Figure 4.22 is less clear: a peak at 826.5 MHz shows a variation of 2 MHz of its frequency. This peak is comparable to the peak observed during the frequency characterization and in simulation, which was respectively at 807.25 MHz and 805 MHz. Another variation occurs between 914 and 907.5 MHz but it needs to be validated. The two other peaks does not seem to be impacted significantly by the MEMS.
- For the PIFA, as shown in Figure 4.23, a variation of the amplitude of the peak around 900 MHz can be seen. It is slightly higher than the frequency of the peak observed during the characterization of this sensor without the vacuum chamber, which was 880.5 MHz, and in simulation (874 MHz).

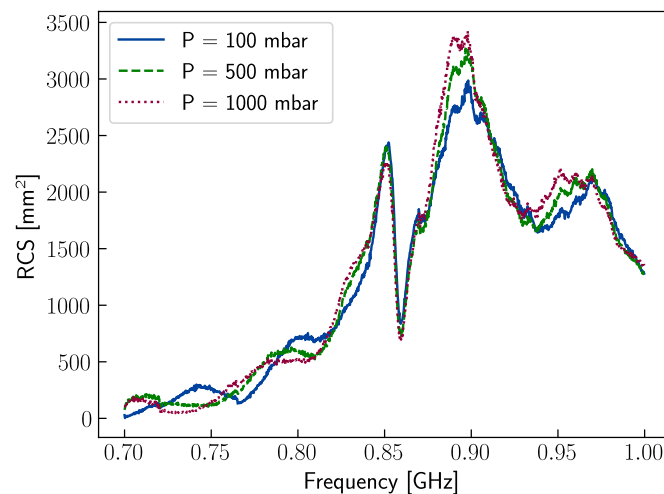


Figure 4.23: Comparison of the raw RCS measurements of the PIFA sensor at 100 mbar, 500 mbar and 1 bar.

The differences between the frequencies of the characterization in frequency and in pressure can be attributed to the presence of the vacuum chamber, in addition to the impact of other parameters such as temperature (the measurements in section 4.3.3 and this section were not carried out on the same day). These variation of the frequencies of the peaks are now validated thanks to the time-gating algorithm, which extracts only the response from the sensor, to ensure that those variations came from them.

#### 4.4.5 Pressure response of the sensors

The algorithm of section 4.4.3 was then applied on the measurements of each sensor. For each sensor, a unique time-gating window is applied for each value of pressure. The VNA was calibrated using a Short-Load-Open-Thru calibration. The background is considered as the anechoic chamber with the vacuum chamber, in order to cancel direct reflections of the EM signal due to the vacuum chamber.

### Loop sensor

The algorithm applied on the Loop sensor confirms that the peaks observed at around 826 MHz in the raw measurement is the peak which corresponds to the response of the sensor. Figure 4.24 shows the response extracted from the algorithm both in time-domain and frequency domain. The amplitude of the peaks are lower than the measurement without the vacuum chamber, as this chamber reflect a part of the backpropagated power by the sensor.

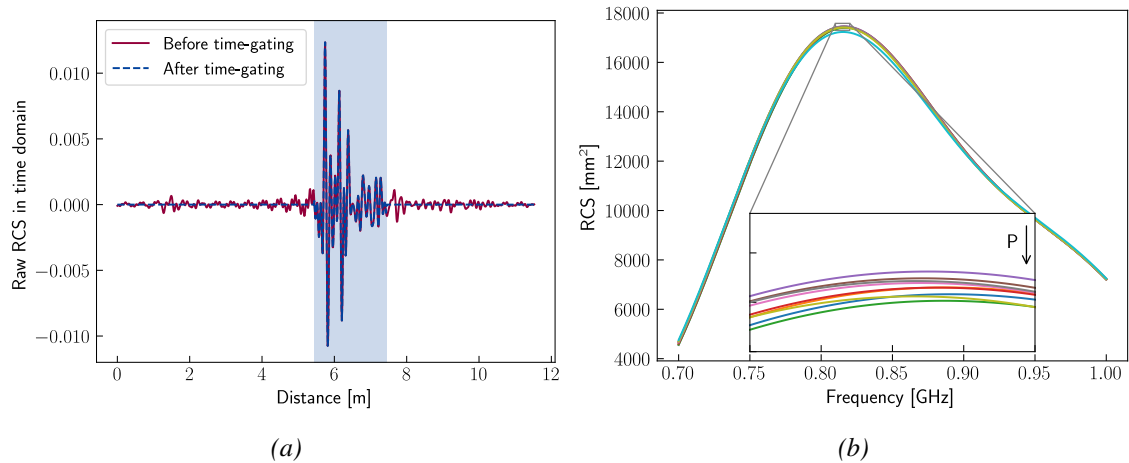


Figure 4.24: RCS of the Loop sensor extracted from the algorithm in time-domain (a) and frequency domain (b). The colored area in time-domain correspond to the window applied. The arrow indicates the reading direction for increasing pressure. 10 measurements are taken between 100 and 1000 mbar, in 100 mbar steps.

Figure 4.25 shows the variation of the frequency of the maximum RCS with pressure, extracted from the algorithm. The sensitivity obtained by simulation is 4.8 MHz/bar at 835 MHz and the measured sensitivity is 2 MHz/bar at 826 MHz. This difference in sensitivity can be explained by the way the impedance of the MEMS under vacuum is estimated (based on the measurement of other MEMS), combined to the presence of the parasitic element seen on the MEMS impedance which can limit the relative variation of the impedance of the MEMS.

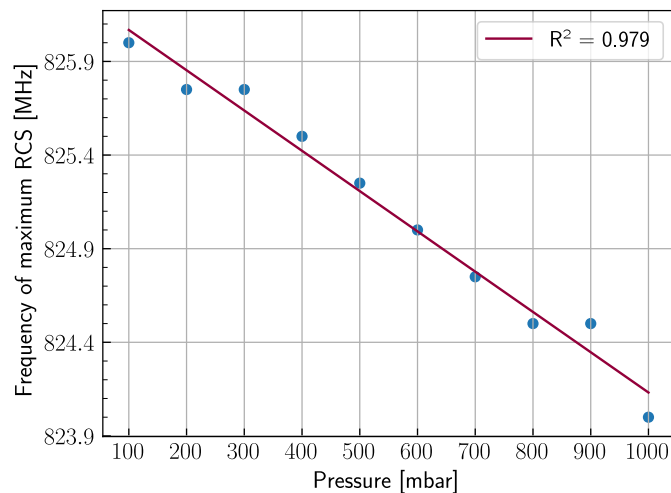


Figure 4.25: Variation of the frequency of maximum RCS of the Loop sensor with pressure. The points at 300 and 900 mbar are at the same frequencies at the previous ones due to the frequency resolution of the interrogation.

### Slot sensor

The analysis of the raw RCS of the Slot sensors shows multiple peaks which varies with the pressure: one around 828.5 MHz, which can be correlated to the peak measured during the characterization of the sensor at atmospheric pressure, one around 910 MHz, and finally one at 716 MHz. A peak at around 803 MHz is found by the algorithm, which corresponds to the peak obtained both in simulation (805 MHz) and measurement (807.25 MHz). This response is shown in time and frequency domains in Figure 4.26. The time-domain response shows that the algorithm takes the main peak at 6 meters and the lower peaks just after to extract the response at 803 MHz.

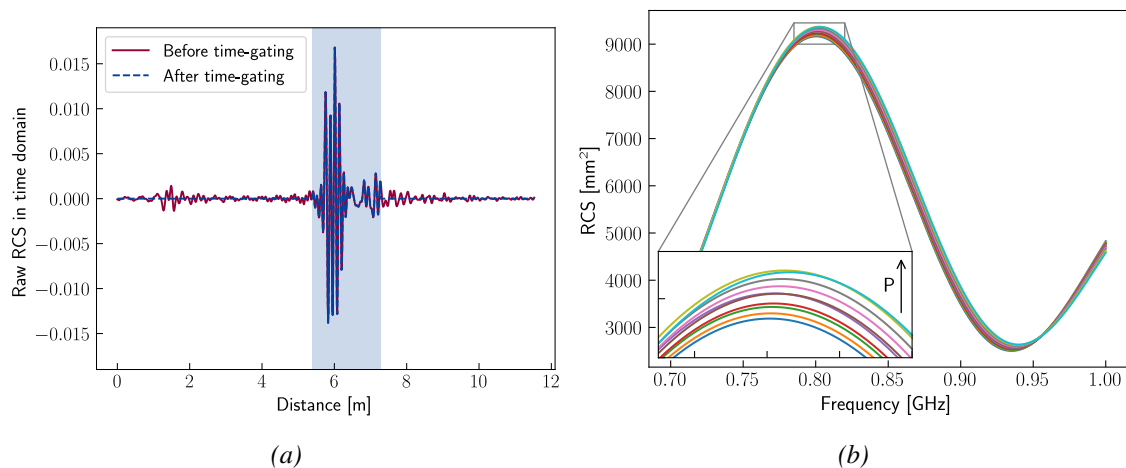


Figure 4.26: RCS of the Slot sensor with a maximum at 803MHz extracted from the algorithm in time-domain (a) and frequency domain (b). The colored area in time-domain correspond to the window applied. The arrow indicates the reading direction for increasing pressure. 10 measurements are taken between 100 and 1000 mbar, in 100 mbar steps.

The variation of the maximum RCS corresponding to that window is then shown in Figure 4.27. The measured sensitivity is 3 MHz/bar, which is lower than the 5MHz/bar obtained by simulation. As for the loop, the combination of the way the impedance of the MEMS under vacuum and the parasitic element on the impedance can explain this differences. Moreover, the frequency of maximum RCS increases with pressure, which was already observed in simulation, as the adaptation is made at the anti-resonance of the antenna.

### PIFA sensor

Finally, the algorithm was applied to extract the response of the PIFA sensor. The time and frequency domain response are shown in Figure 4.28. The peak occurs at 896.75 MHz, which is slightly higher than in the frequency response characterization (880.5 MHz) and simulation (874 MHz). As the two other sensors, there is a main peak at 6 meters followed by a lower peak just after. As it is present on the time-domain responses of all three sensors with the vacuum chamber, but not present on the characterization without the vacuum chamber, it can be attributed to the presence of the vacuum chamber.

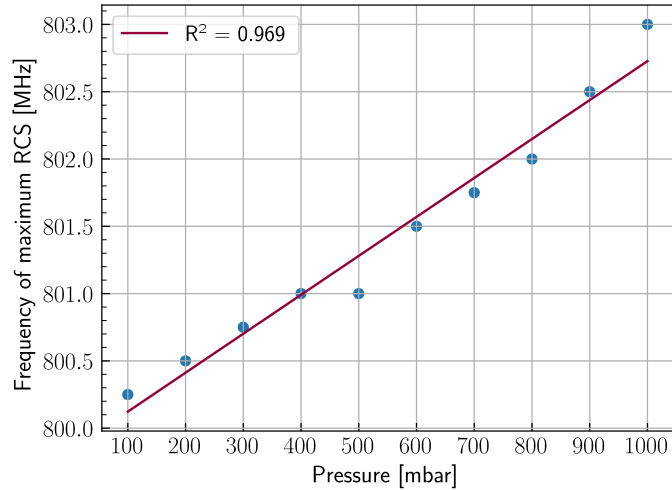


Figure 4.27: Variation of the frequency of the maximum RCS of the Slot sensor at 800MHz with pressure. The point at 500 mbar is at the same value of frequency than 400 mbar due to the frequency resolution of the interrogation.

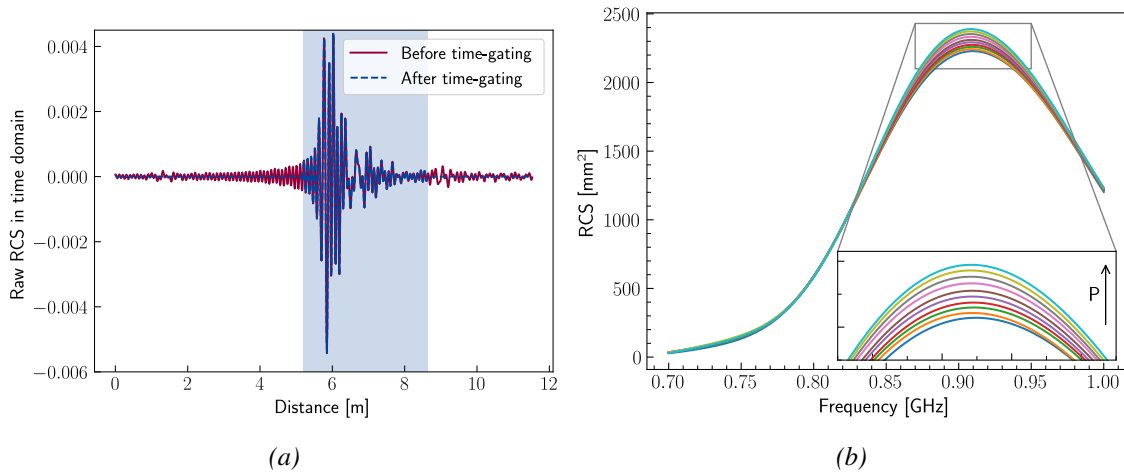


Figure 4.28: RCS of the PIFA sensor extracted from the algorithm in time-domain (a) and frequency domain (b). The colored area in time-domain correspond to the window applied. The arrow indicates the reading direction for increasing pressure. 10 measurements are taken between 100 and 1000 mbar, in 100 mbar steps.

The value of the RCS is then plot at 868 MHz and at 896.75 MHz, i.e. at the peak of the frequency response, in Figure 4.29. Compared to the variation of RCS obtained by simulation, which varies from 2895 mm<sup>2</sup> to 3142 mm<sup>2</sup> when the pressure varies from 10<sup>-3</sup> mbar to 1 bar (sensitivity of 8%/bar), it has a similar relative sensitivity at 868 MHz (6.7%/bar) while at 896.75 MHz it has a sensitivity of 8.9%/bar. Both curves present an excellent linearity with value of  $R^2$  of 0.996 and 0.997.

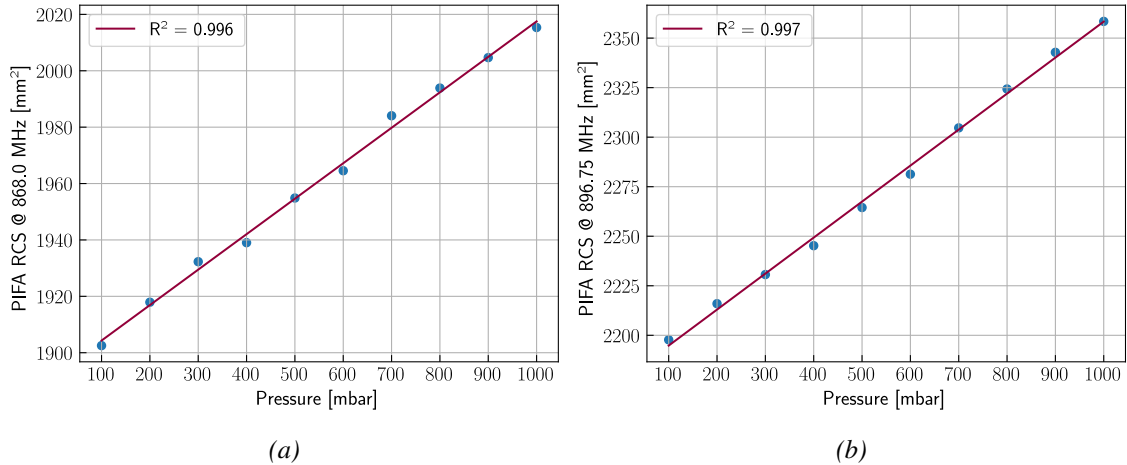


Figure 4.29: Variation of the RCS of the PIFA sensor at 868 MHz (a) and at 896.75 MHz, the peak of the frequency response (b).

However, the value of the RCS is different due to the presence of the vacuum chamber which modifies the response of the antenna. This sensor was presented in an oral presentation for the Eurosensors 2023 conference.

A differential measurement, done with a reference MEMS (i.e. etched at the center of the membrane) placed on another PIFA is necessary to have a good accuracy of the measurement in case the environment around the sensor changes over time.

## Conclusion

To conclude, the functionality of the sensors has been proved, either for the sensors based on the variation of frequency of maximum RCS or the variation of RCS at a single frequency. The algorithm presented here successfully find a window which, when applied on each measurement in pressure, allows to have a linear response. The measurements showed a sensitivity of 3 MHz/bar or 9%/bar of back-propagated power. Two other parameters seem to be interesting to study on: the reading range, i.e., at which distance the sensor can be detected by the interrogators and the maximal resolution achievable.

### 4.4.6 Estimation of the reading range

In order to estimate the reading range of the sensors in an ideal case, i.e. without any clutter, multi-path or polarization mismatch, the form of the radar equation expressed in Eq. 1.12 is used. We assume a power sent  $P_t$  by the interrogator of 400 mW to respect the French regulations on the usage of frequency bands [4]. The gain on reception  $G_r$  and in transmission  $G_t$  are set to be 7.7 (the same gain as the antenna which are used to characterize the sensors) and a reader sensitivity  $S_r$  is fixed at -80dBm ( $10^{-8}$  mW). The reading range can be estimated with:

$$R_{max} = \sqrt[4]{\frac{\sigma \lambda^2 P_t G_t G_r}{S_r (4\pi)^3}} \quad (4.2)$$

For the Slot and the Loop sensor, the maximum RCS are respectively around 30000 mm<sup>2</sup> at 806.7 MHz and 54000 mm<sup>2</sup> at 837 MHz. It allows to calculate the maximal reading range of both antennas, which are 47.2 m for the Slot sensor and 53.6 m for the Loop sensor. For the PIFA sensor, the reading range is 26.37 m. This is the distance at which we can read the response of the sensor, but not necessarily read the value of the pressure. This expresses the maximum distance at which the presence of the sensor response can be detected, while pressure causes a smaller

variation in this antenna response. To study the extent to which the pressure reading is influenced by distance, it is worth looking at the resolution of the sensor.

#### 4.4.7 Estimation of the resolution

The resolution of a sensor, defined as the smallest variation in the physical quantity that can be measured, is strongly dependent of the setup of measurement. It is even more the case for our sensor as it is also dependent of the quality of the measurement of the clutter. The goal of this section is then to find the maximal resolution that can be achieved, i.e. using a theoretical perfect measurement setup. The definition of the maximal theoretical resolution is quite different between the sensors based on the maximum RCS frequency variation (the Loop and the Slot sensors) and on the RCS at a given frequency (the PIFA sensor). For the PIFA sensor, it is defined as the minimum variation of power received that can be detected, while for the two others it is the minimum variation of frequency which can be detected. In both case, it is dependent on the distance between the interrogators and the sensor, and related to the lowest variation of RCS  $\Delta\sigma$  which is detectable by the reading system. It can be calculated using the radar equation:

$$\Delta\sigma = \frac{S_r (4\pi)^3 d^2}{P_t G_t G_r \lambda^2} \quad (4.3)$$

This variation of RCS can be then linked to the resolution using the response curves of the sensors obtained in Section 4.4.5. The interrogation conditions are assumed to be the same than for the determination of the reading range.

Assuming a distance of 3 meters, and by applying the radar equation, the minimum variation of RCS that can be detected is 0.586 mm<sup>2</sup>. By taking the response curve of the PIFA of Figure 4.29b, it corresponds to a maximal resolution of 3.12 mbar.

For the two other sensors, the resolution is lower: for the same minimum variation of RCS, and by looking at the frequency spectrum of the RCS, the maximal resolution of the Loop is 146.56 mbar at 3m, while the maximal resolution of the Slot is 78 mbar at this distance. The evolution of the maximal resolution achievable of the sensors with distance is shown in Figure 4.30.

It could be interesting to evaluate the resolution for a precise measurement setup, which includes the knowledge of the noise or the measurement of the Allan variance of the sensor as an example.

## 4.5 Conclusion

As a conclusion, this chapter presented the design of antennas specifically for specific MEMS. One geometry (the PIFA) is a miniature antenna designed to create a sensor based on the variation of the RCS at 868 MHz, while two other geometries (the Loop and the Slot) were designed with a larger electrical size to work on the variation of frequency of maximum RCS. Those antenna were printed on a FR4 substrate and characterized in anechoic chamber, with a set-up of characterization under vacuum specifically designed for this thesis. It allows to control the pressure inside a vacuum chamber made in plexiglass at the outside of the chamber, and to have a limited (but non negligible) impact on the response of the sensors. The signal processing algorithm was then modified to measure the responses of the sensors in pressure. Experimental data shows good agreement with simulations. The functionality has been proven for the three sensors and the two interrogation methods.

The characterization allows also to identify three different cases for the conditions of measurement of the sensor:

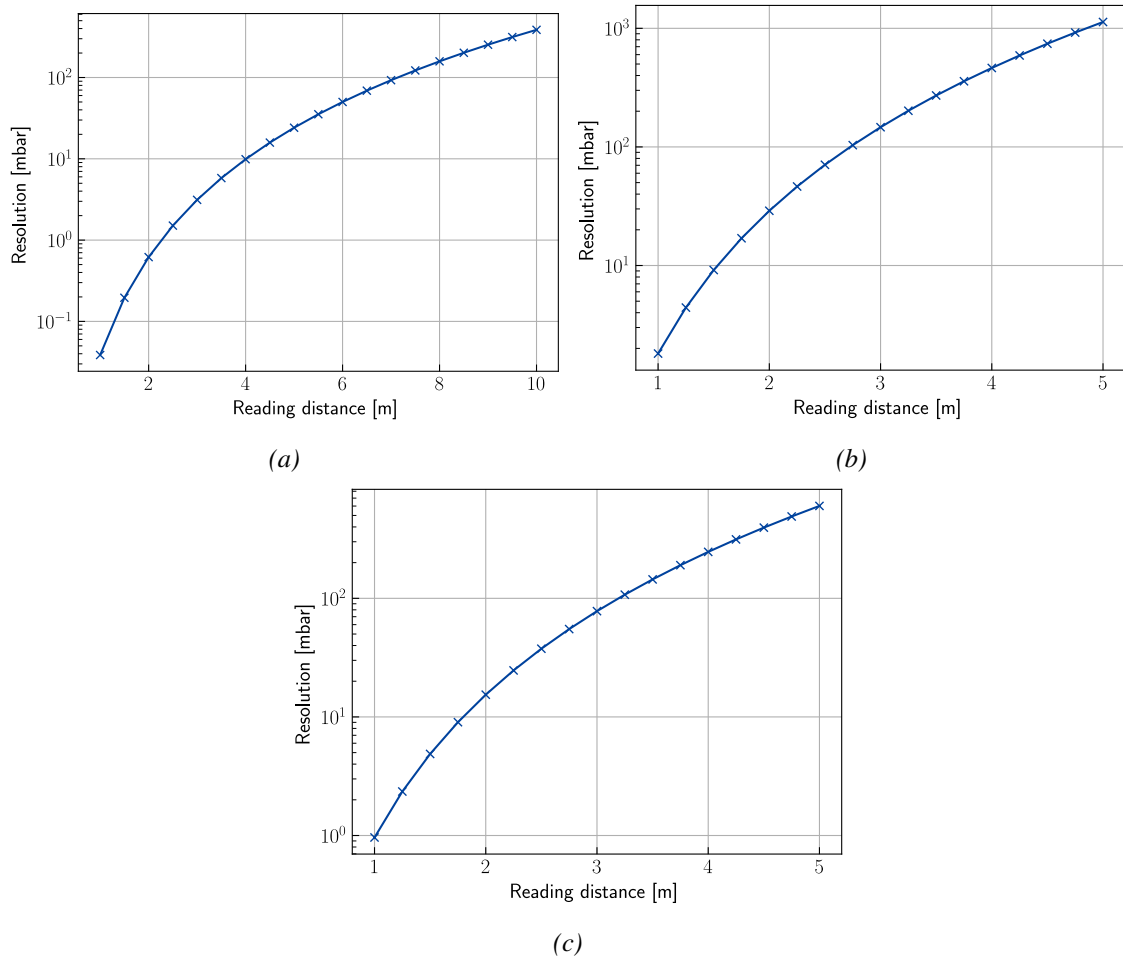


Figure 4.30: Evolution of the maximal resolution achievable in function of the distance for the PIFA sensor (a), the Loop sensor (b) and the Slot sensor (c).

- If the signature of the background does not change over time, which means the background measurement is the same and other physical parameters does not vary, such as the temperature, a pressure characterization of the sensor seems to be enough to ensure accuracy of measurement.
- If the signature of the background does not change over time, but other physical parameters change, a differential measurement is an interesting solution by, for example, using an antenna with the same geometry as the sensor, loaded by a MEMS with a perforated membrane. To differentiate the sensor and the reference, they can have a different polarization.
- If both the signature of the background and the other physical parameters changes, an accurate measurement becomes very difficult. The background would not be totally canceled at the beginning of the signal processing, which reduces the accuracy of the measurement even if a reference is present.

To enhance the accuracy, another method of interrogation is presented on the next chapter, based on the remote measurement mechanical resonance of the MEMS. It allows to enhance the accuracy of the measurement, increase the reading range and to have a MEMS and their reference on the same antenna.

# Bibliography

- [1] B. Jecko. “Small-sized low-profile antenna to replace monopole antennas”. English. In: *Electronics Letters* 34 (8 Apr. 1998), 716–717(1). ISSN: 0013-5194. URL: [https://digital-library.theiet.org/content/journals/10.1049/el\\_19980550](https://digital-library.theiet.org/content/journals/10.1049/el_19980550).
- [2] F. Sarrazin, S. Pflaum, and C. Delaveaud. “Radiation efficiency measurement of a balanced miniature IFA-inspired circular antenna using a differential Wheeler cap setup”. In: *2016 International Workshop on Antenna Technology (iWAT)*. 2016, pp. 64–7. DOI: [10.1109/IWAT.2016.7434802](https://doi.org/10.1109/IWAT.2016.7434802).
- [3] H.G. Booker. “Slot aerials and their relation to complementary wire aerials (Babinet principle)”. English. In: *Journal of the Institution of Electrical Engineers - Part IIIA: Radiolocation* 93 (4 Jan. 1946), 620–626(6). ISSN: 2050-5485. URL: <https://digital-library.theiet.org/content/journals/10.1049/ji-3a-1.1946.0150>.
- [4] Agence Nationale des Fréquences Radio (ANFR). *Tableau national de répartition des bandes de fréquences (TNRBF)*. Feb. 16, 2023. URL: [https://www.anfr.fr/fileadmin/mediatheque/documents/tnrbf/20230216\\_TNRBF/TNRBF\\_2023-02-16t.pdf](https://www.anfr.fr/fileadmin/mediatheque/documents/tnrbf/20230216_TNRBF/TNRBF_2023-02-16t.pdf) (visited on 09/14/2023).



# 5

## Wireless interrogation of resonant MEMS

---

*In this chapter, a new method of interrogation of the sensor is presented, based on the sending of two signals of close frequencies. The membrane of the MEMS is then put in mechanical resonance, which modulates the backpropagated signal, which creating intermodulation peaks in the received signal. These peaks contains only the information of the measurement. This technique allows having better clutter isolation in real environments, a greater accuracy and the possibility to interrogate different MEMS on the same antenna.*

---

### Contents

---

<b>5.1</b>	<b>Introduction</b>	<b>115</b>
<b>5.2</b>	<b>General principle and interest for wireless measurement</b>	<b>115</b>
5.2.1	Reading in real environment and clutter isolation issue	115
5.2.2	General principle	116
<b>5.3</b>	<b>Complete theoretical model</b>	<b>117</b>
5.3.1	Incident signal and voltage at the MEMS terminals	118
5.3.2	Membrane mechanical resonance and actuation	120
5.3.3	Equivalent capacitance of the MEMS and reflection coefficient	124
5.3.4	Variation of Radar Cross Section	125
5.3.5	Shape of the backpropagated signal	126
5.3.6	On the necessity to calculate by recurrence	126
5.3.7	Conclusion on the complete model	127
<b>5.4</b>	<b>Linearized model for the co-design</b>	<b>127</b>
5.4.1	Approximations used	127
5.4.2	Simplification and linearization of the model	128
<b>5.5</b>	<b>Analysis of the models</b>	<b>130</b>
5.5.1	Analysis of the equation of the signal received	130
5.5.2	Interrogation of multiple MEMS on one antenna	131
5.5.3	Amplitude of the peaks in the frequency spectrum	132

<b>5.6</b>	<b>Example of numerical applications of the models</b>	<b>132</b>
5.6.1	Geometries used for this analysis	132
5.6.2	Validation of the voltage on the antenna	134
5.6.3	Validation of the linear model	134
5.6.4	Example of a received signal	135
5.6.5	Choice of the interrogation frequency	135
<b>5.7</b>	<b>Measurement of the resonance of the MEMS</b>	<b>137</b>
5.7.1	Resonance frequency and pressure	137
5.7.2	Quality factor of the MEMS	138
5.7.3	MEMS resonance and intermodulation	140
5.7.4	Conclusion on the measurements	140
<b>5.8</b>	<b>Conclusion</b>	<b>142</b>

---

## 5.1 Introduction

This final section focuses on the presentation of a new method of operation for our wireless MEMS capacitive pressure sensor. This approach is based on the determination of the pressure-dependent mechanical resonance frequency of the membrane of the MEMS, and it allows obtaining a theoretically better reading range in real environments, a better accuracy of the measurement or the possibility to have multiple MEMS on the same antenna.

The new approach is based on a modulation technique, in which the MEMS is operated at resonance, and the pressure is measured through its resonance frequency. In this configuration the resonance of the MEMS modulates the signals sent to the antenna, so the back-propagated frequencies are different from the interrogation ones: this is a major advantage, allowing to separate the measurement signal coming from the MEMS from reflections from the environment and the antenna (clutter). As this interrogation is based on both electromagnetic and non-linear mechanical phenomena, it cannot be simulated on Ansys HFSS. An analytical model must then be developed one to predict the behavior of the sensor, and to allow a co-design between a MEMS and an antenna specifically for this interrogation.

Firstly, the motivations and the general principle of this method of interrogation technique are presented. Then, based on the understanding of each physical phenomenon involved, a complete theoretical model is established. This model is then linearized to highlight the key parameters of the design of an antenna and a MEMS for this interrogation technique, in order to better understand which aspect to prioritize for a co-design approach. Then, preliminary measurements of the MEMS conceived in this thesis using this new approach are presented.

## 5.2 General principle and interest for wireless measurement

### 5.2.1 Reading in real environment and clutter isolation issue

The interrogation methods presented previously, based either on the variation of RCS at a fixed frequency, or on variation of the frequency of maximum RCS are based on a type of reading where the signal backpropagated by the sensor is at the same frequency that the signal which was sent by the reader. The sensor can be seen here as a linear time invariant (LTI) system.

A common issue in antenna reading is the necessity to isolate the information (here, the signal backpropagated by the sensor) from the residual environment, or, as it is also called, the clutter. The clutter can also be modelled as a LTI system, so the response of the clutter is at the same frequency as the interrogation signal. To overcome this issue, the clutter is usually estimated by characterizing the environment without the sensor, and then subtracting this measurement of the clutter to the measurement of the sensor. In real environments (REs), it is sometimes difficult to characterize it (for example, if the environment is changing or if the sensor cannot be removed). This issue can reduce the accuracy of the reading procedure: it adds uncertainties on the value of the physical quantity or, even worse, produces a false measurement.

Barbot et al [1] has shown that, for LTI systems, the maximal reading distance in REs cannot be estimated using the classical radar equation, because it does not depend on power sent nor reader sensitivity, but on the relationship between the RCS of the sensor and the clutter: if more power is sent by the reader, the sensor will sent more power, but the clutter also. As they are both LTI systems, the ratio signal over background is still the same. It means than, in practice, the maximal reading range is much lower in REs than one estimated with the radar equation. They have demonstrated that using a non-linear phenomenon can increase the reading range in REs by reading at frequency which is different from the frequency sent. For example, they use

Micro-Doppler effect on chipless RFID tag [2] to create this signal at a different frequency.

### 5.2.2 General principle

The main issue for us is to use a non-linear phenomenon to create that harmonic, as the sensor is totally passive. Some common techniques include the addition of a mixing diode as a way to create a response signal at twice the frequency of the reading signal. However, in order to work in harsh environments, the use of mixing diodes or any CMOS component other than the MEMS and the antenna must be avoided.

For this, we propose a concept based on a MEMS placed on an antenna, putted in mechanical resonance by two signals at close frequencies sent to this antenna (i.e., at two frequencies  $f_0$  and  $f_0 + f_\Delta$  with  $f_\Delta \ll f_0$ ). During our studies, we saw that this concept was already demonstrated by Viikari et al. [3] [4]. The general principle of the reading procedure is shown Figure 5.1.

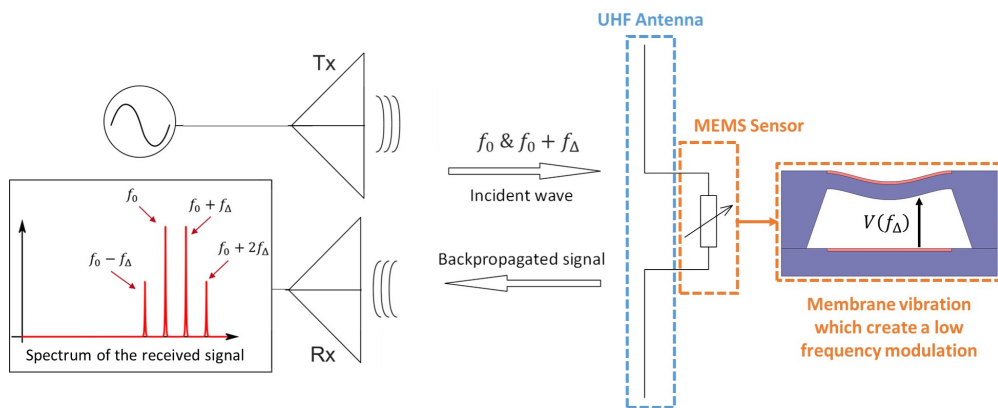


Figure 5.1: Principle of wireless reading method using the MEMS mechanical resonance by intermodulation.

The goal of using two signals at close frequencies to put the MEMS in mechanical resonance is to be able to counter the problem created by the difference between the electrical resonance of the antenna (here, at 868 MHz) and the mechanical resonance of the MEMS membrane (usually less than few MHz). It generates a low-frequency harmonic in the electrical force created on the MEMS, which puts the membrane of the MEMS in vibration. This periodically shifts the impedance of the MEMS, and thus the reflection coefficient between the MEMS and the antenna, creating a modulation of the backpropagated signal.

We couple this interrogation method with a resonant operation of the MEMS sensor. In this configuration, the MEMS vibrates at its resonance frequency, which is dependent on the measured variable (in this case, pressure). The pressure can be then deduced from an accurate measurement of the resonance frequency of the MEMS.

The combination of the interrogation method with the resonant operation of the MEMS produce an operating principle where the measured pressure is deduced via the maximum of the amplitude of the modulation. This is done by shifting one of the two frequencies sent to the sensor.

This method has the advantage of being more robust than a static measurement (as frequency drifts in instrumentation are rarer than amplitude drifts) and generally more sensitive.

Viikari et al. [3] demonstrated a model to predict the variation of reflection coefficient of a MEMS resonator impedance-matched to an antenna illuminated by two close frequencies. In their model, the antenna is represented as a RL circuit, which cannot represent precisely the electrical behavior of all antenna geometries. A more general theoretical model was then developed in this thesis, presented in section 5.3, to be able to study precisely the behavior of the MEMS for different antennas, with different electrical size, structural part or gain for example. Based on this

model, and a linearized model shown in section 5.4 was deduced to be able to make conclusions on which parameters to optimize on the sensor co-design. This model is also necessary because it is not possible to do the study by simulation using the ANSYS HFSS software, as it is not yet a multiphysics software.

### 5.3 Complete theoretical model

In order to predict the behavior of the sensor subjected to two signals of close frequencies, a theoretical model has been developed. The objective is to deduce the time course of the power backpropagated by the antenna as a function of the pressure and the two sent signals. This backpropagated power is dependent on the electrical parameters of the antenna and the MEMS, but also on the mechanical parameters of the MEMS. In this part, the key equations to set up this theoretical model are presented. Figure 5.2 shows the block diagram used to establish the model.

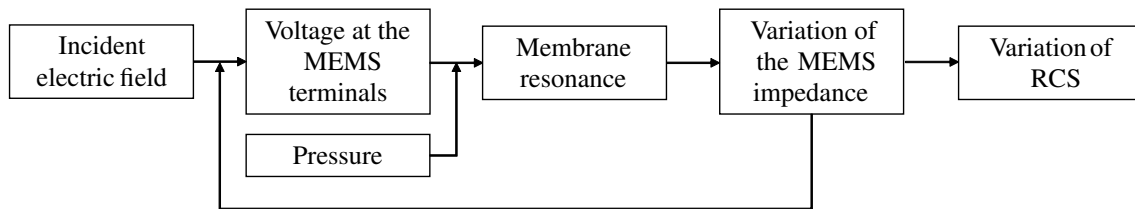


Figure 5.2: Block diagram of the interrogation of resonant MEMS using intermodulation. Two signals at  $f_0$  and  $f_0 + f_\Delta$  with  $f_\Delta \ll f_0$  are sent to the sensor. Due to the non-linear aspect of the electrostatic force, the MEMS is put in mechanical resonance at  $f_\Delta$ . This resonance modulates the backpropagated signal by adding peaks in the spectrum received back by the reader. Only the two first intermodulation peaks are considered here.

The methodology used to set up the model is to explain each phenomenon involved in the interrogation, and write down the equations which link these physical phenomena:

- An incident electromagnetic field will come on the sensor, which induce a current on the antenna. It will create a voltage at the MEMS terminal. Section 5.3.1 shows a method to determine the voltage using the antenna effective length combined to either the equivalent circuit of the sensor or FEM simulations. In our work, FEM simulations are used to determine the voltage. The propagation of the signal in free-space is also considered in this analysis.
- That voltage will create an electrical force between the two electrodes of the MEMS that will put its membrane in resonance. Section 5.3.2 presents the equation used to determine the pressure-dependent resonant frequency of the membrane, the differential equation of the displacement of the center of the membrane (including the static displacement due to the pressure), and its solution.
- The displacement of the membrane will periodically change the equivalent capacitance of the MEMS. Section 5.3.3 shows a formula used to calculate it. FEM simulations can be used for different values of maximal deflection and linear regression between the points for a better accuracy. That change in the MEMS impedance will change how the sensor reacts to an incident field, and thus the voltage at the MEMS terminal (hence the feedback loop in

the block diagram). Section 5.3.6 shows why it is necessary to calculate the key parameters of the model by recurrence.

- The capacitance change will affect the antenna RCS by varying the loaded impedance and, thus, the backpropagated signal. Section 5.3.4 shows how to calculate the modification of the RCS and the structural part of the RCS.
- That change in the RCS will create an modulation on the backpropagated signal. The equation of that signal is presented in section 5.3.5.

### 5.3.1 Incident signal and voltage at the MEMS terminals

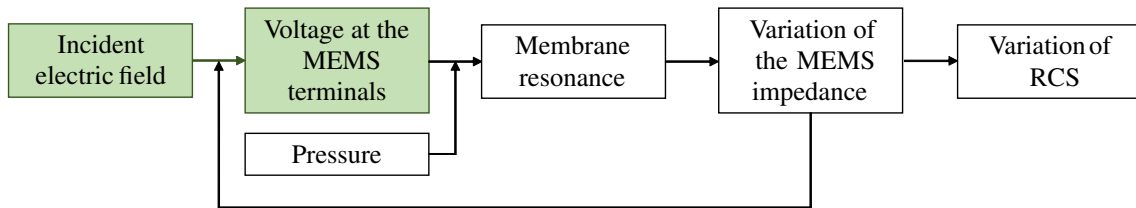


Figure 5.3: Block diagram of the interrogation of resonant MEMS using intermodulation, with the current step of the calculation highlighted. This section focuses on determining the voltage across the MEMS based on the incident electric field.

The MEMS is here considered as the load of the antenna. To determine the amplitude of the vibration of the membrane, it is necessary to determine the voltage at the terminals of the MEMS. This voltage depends on the incident power on the antenna. In this section, the voltage is calculated using the effective length of the antenna, a parameter which links the incident electric field to the open-circuit voltage created at the load of the antenna.

Taking the general case of a receiving antenna, Balanis defines it as a  $R_A L_A C_A$  series circuit [5]. This assumption is taken in this analysis in order to have a general representation of an antenna. This antenna is loaded by the MEMS, which is assimilated in this model to a series  $R_S C_S$ , with a variable capacity as simulated on Ansys HFSS. This circuit is shown in Figure 5.4. Here, the MEMS is considered as a load of the antenna. This method can also be applied if the MEMS is placed on the antenna loaded by an other impedance if there is an equivalent circuit of the sensor.

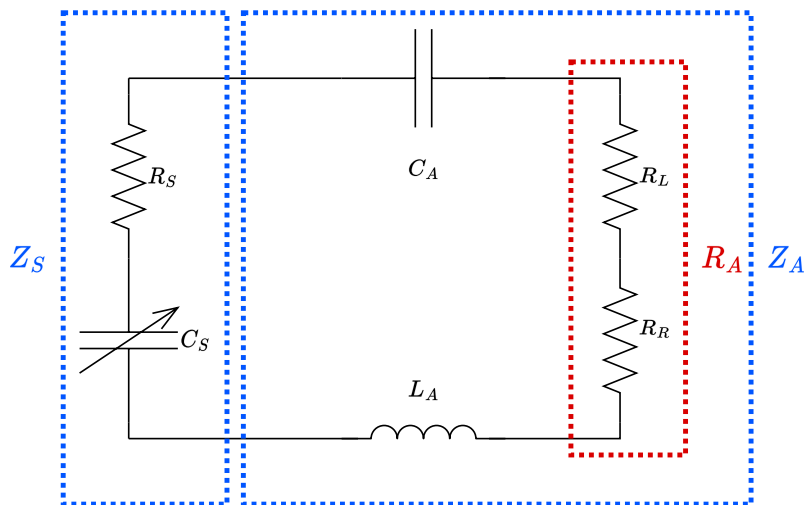


Figure 5.4: General equivalent circuit of a receiving antenna loaded by a MEMS.

The lumped elements of the electrical circuit are denoted by  $R_A = R_R + R_L$  the antenna resistance, with  $R_R$  the radiation resistance and  $R_L$  the loss resistance, and  $X_A = \frac{1}{jC_A\omega} + jL_A\omega$  the antenna reactance,  $Z_A = R_A + jX_A$  the antenna impedance and  $Z_S(P, t) = R_S + \frac{1}{jC_S(P, t)\omega}$  the MEMS impedance. The MEMS impedance is both dependent of the time  $t$  and the pressure  $P$ .

The sensor is interrogated using a reader with two signals of close frequencies. The expression of the incoming signal is then:

$$X(t) = \sqrt{2P_t} (\sin(\omega_e t) + \sin([\omega_e + \omega_\Delta] t)) \quad (5.1)$$

with  $P_t$  the power received by the sensor, which includes the free-space attenuation,  $\omega_e = 2\pi f_e$  the antenna interrogation frequency, and  $\omega_\Delta = 2\pi f_\Delta$  the low difference frequency, with  $\omega_\Delta \ll \omega_e$ . This signal will create a time-varying current on the antenna, and then, a voltage at the terminal of the MEMS.

To determine the voltage at the terminals of the MEMS, the effective length of the antenna can be used. The effective length  $h_e$  is defined as the ratio of the incident electric field  $E^i$  to the open-circuit voltage  $V_{OC}$  [6]:

$$V_{OC} = h_e E^i \quad (5.2)$$

By simulation, the effective height of the antenna can be determined by multiplying the actual physical length of the antenna  $h_p$  (e.g. for a dipole antenna, its length) by the average normalized current:

$$h_e = \frac{1}{I_0} \int_0^{h_p} I(z) dz = \frac{I_{moy}}{I_0} h_p \quad (5.3)$$

with  $I_0$  the maximum current on the antenna and  $I(z)$  the function determining the current distribution on the antenna as function of the position on the conducting part  $z$ . Another method to determine the effective height of the antenna is to use the input impedance of the antenna and the effective area of the antenna. The power sent to the load (and so to the MEMS) can be expressed as:

$$P_S = \frac{V_{OC}^2 R_S}{|Z_S(P, t) + Z_A|^2} \quad (5.4)$$

This power can be written using the effective area of the antenna  $A_e$ :

$$P_S = S A_e = \frac{(E^i)^2 A_e}{Z_0} \quad (5.5)$$

with  $Z_0 \approx 120\pi$  the vacuum characteristic impedance, and  $S$  the incident power density. The effective area can be written as:

$$A_e = \frac{\lambda^2}{4\pi} G_A \quad (5.6)$$

with  $G_A$  the antenna realized gain, which is frequency dependent. By combining equations (5.2), (5.4), (5.5) and (5.6) the effective length becomes:

$$h_e = \sqrt{\frac{G_A (|Z_S(P, t) + Z_A| \lambda)^2}{4\pi Z_0 R_S}} \quad (5.7)$$

By taking the realized gain as  $G_A = G_A^{IEEE} (1 - |\Gamma|^2)$ , with  $\eta$  the radiation efficiency, and  $G_A^{IEEE} = \eta D$  the IEEE gain with  $D$  the directivity, there is, after simplification:

$$h_e = \sqrt{\frac{G_A^{IEEE} re(Z_A) \lambda^2}{\pi Z_0}} \quad (5.8)$$

The effective height is thus only dependent of the antenna parameters, which is physically explainable because the open-circuit voltage and the incident electric field does not depend on the antenna load, and the power is received by the antenna resistance. The effective height can be calculated in simulation thanks to the input impedance of the antenna at the load and the gain of the antenna. Therefore, to determine the open-circuit voltage, the electric field incident on the antenna through the radar equation and the Poynting's equation is expressed as:

$$E^i = \sqrt{|P_i| Z_0} \frac{\sqrt{\frac{Z_0}{4\pi} P_T G_T}}{d} \quad (5.9)$$

with  $P_i = (P_T G_T)/(4\pi d^2)$  the incident power on the antenna. Therefore, by combining equations (5.8) and (5.9) the open-circuit voltage can be expressed as:

$$V_{OC} = \sqrt{G_A^{IEEE} re(Z_A)} \frac{\lambda}{2\pi d} P_T G_T \quad (5.10)$$

Finally, the expression of the voltage at the load can be expressed thanks to a voltage divider:

$$V = V_{OC} \frac{|Z_S(P,t)|}{|Z_A + Z_S(P,t)|} = E^i h_e \frac{|Z_S|}{|Z_A + Z_S|} = |Z_S(P,t)| \frac{\lambda P_T G_T}{4\pi d} \sqrt{\frac{G_A}{R_S}} \quad (5.11)$$

An equivalent circuit of the antenna can be used to calculate the voltage no matter the position of the MEMS (at the load of the antenna or not). If one does not have an equivalent circuit for the antenna one wishes to use, and if the antenna is loaded by the MEMS, the voltage at the MEMS terminals can be determined by extracting the input impedance of the antenna from a FEM simulation.

The first method, the use of an equivalent circuit, can be useful for antenna geometries that are well known from the literature or those for which an accurate equivalent circuit which links the localized elements and the antenna dimensions can be determined. The model must accurately determine the impedance of the antenna in order to have information about the resonant frequency and sensitivity of the sensor. In this case, the performance of the sensor by intermodulation can be determined by varying the dimensions of the antenna or the MEMS without the need for additional simulations. Therefore, the study can be done with the MEMS not necessarily as the antenna load, if the model is well defined. If one does not have an accurate equivalent pattern for the antenna, a modification of the antenna dimensions will involve new simulations to determine the antenna impedance, its gain, and also the evolution of its RCS with the load capacitance.

### 5.3.2 Membrane mechanical resonance and actuation

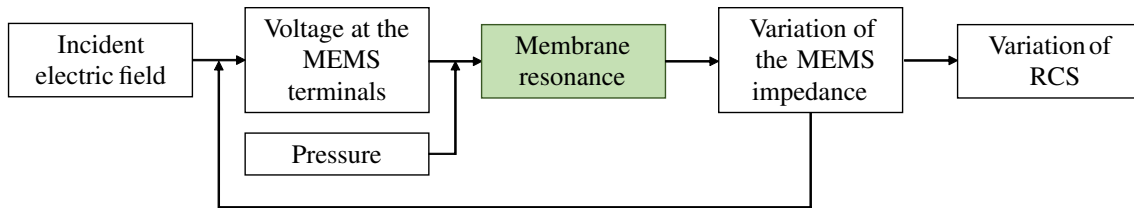


Figure 5.5: Block diagram of the interrogation of resonant MEMS using intermodulation, with the current step of the calculation highlighted. This section focuses on determining an expression for the pressure-dependent mechanical resonance frequency of the membrane, and establishing the equation of motion of the membrane under the application of a pressure and an electrostatic force.

This section focuses on the determination of the equation of displacement of the membrane. When a voltage is applied between the fixed electrode and the membrane, it creates an electrostatic force on the membrane which puts it in resonance if the voltage frequencies are well chosen. Based on the calculation of the voltage of the previous section, the equation of motion of the membrane is expressed. It allows predicting the behavior of the membrane and to understand how the choice of the frequencies of the signal sent to the sensor impacts the membrane resonance.

### Mechanical modeling of the displacement of the membrane

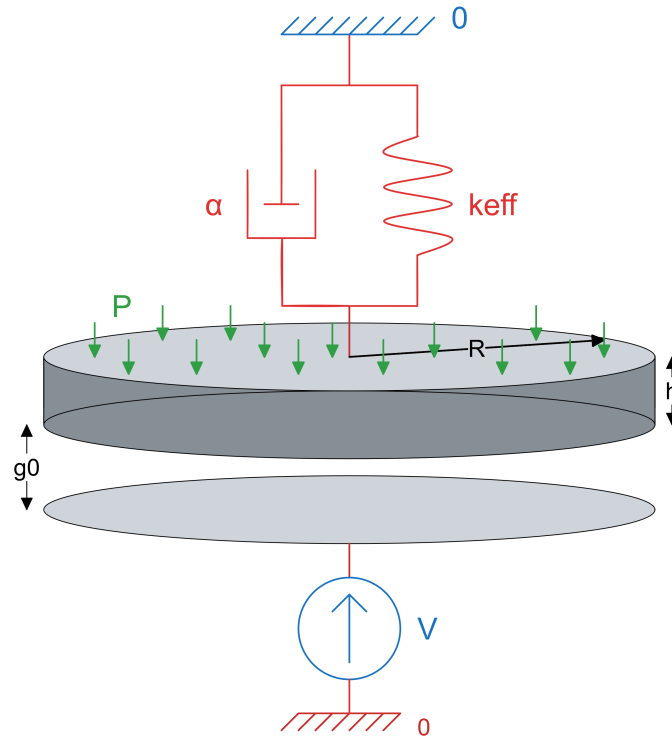


Figure 5.6: Representation of a circular parallel plate capacitor with a membrane and a fixed electrode under a voltage  $V$  and a uniform pressure  $P$ .

In order to establish the equation governing the displacement of the membrane, some assumptions are made to make it easier to resolve:

- The external forces are applied uniformly on the surface of the membrane;
- The out-of-plane deformation is assumed to be small regarding to the thickness of the membrane and there is no lateral displacement. It allows to keep the displacement without electrical force applied proportional to the pressure;
- The pressure is supposed to be constant since a long time compared to the interrogation time;
- The gravitational force due to the mass of the membrane is assumed to be small compared to the forces due to the pressure and the electrostatic force. It can therefore be neglected;
- The analysis is done only on the center of the membrane. Its out-of-plane displacement is denoted by  $x$ . Only the first mode of resonance of the membrane is analyzed. Knowing the displacement of the center, the displacement  $w$  of any point  $r$  of the radius  $R$  of the membrane can be then known using  $w(r) = x \left(1 - \frac{r^2}{R^2}\right)$ .

The out-of-plane deformation  $x$  of its center can be then modeled as a mass-spring system. This representation is shown in Figure 5.6. By adding the forces applied on the center of the membrane, the equation of its deformation is:

$$m_{eff}\ddot{x} + \alpha\dot{x} + k_{eff}x = \Sigma F_{ext} \quad (5.12)$$

With  $m_{eff}$  the effective mass of the center, it refers to the apparent mass that the resonator presents to an applied force or excitation, and so its inertial properties.  $\alpha$  is the air damping and  $k_{eff}$  the effective stiffness of the center.  $\Sigma F_{ext}$  represents the sum of the forces applied to the membrane at its center. By introducing  $Q_m = \frac{\omega_m m}{\alpha}$  the quality factor of the membrane, and  $\omega_m = \sqrt{\frac{k_{eff}}{m_{eff}}}$  its pulsation frequency, the differential equation becomes:

$$\ddot{x} + \frac{\omega_m}{Q_m}\dot{x} + \omega_m^2 x = \frac{1}{m_{eff}}\Sigma F_{ext} \quad (5.13)$$

The quality factor  $Q_m$  reflects in particular the energy loss of the system linked for example to friction with the air, clamping losses etc. It is therefore difficult to estimate theoretically.

### External forces applied on the membrane

In this analysis, we assume that two forces are applied to the membrane: the electrical force due to the voltage and the force due to the pressure. The gravitational force is neglected in this analysis.

Firstly, in case of a pressure sensor, the force applied on the center of the membrane due to the pressure is  $S_{eff}P$ . Here, the term  $S_{eff}$  represents the effective surface, and is equal to a quarter of the real surface of the membrane. In practice, only a quarter of the membrane surface area harvests the pressure. Beyond half the radius, the pressure work is transmitted to the anchor. It has been shown by Timoshenko in [7].

Then, the expression of the electrostatic force in a parallel-plate capacitor system is well known. When a voltage is applied between the electrodes of a parallel plate capacitor, due to the Coulombic forces between the charges on each electrode, an electrostatic attractive force is created between each plate, which is equal to, in case of circular electrodes:

$$F_{el} = -\frac{1}{2}V^2 \frac{\epsilon_0 \pi R^2}{g_0^2} \quad (5.14)$$

with:

- $V$ : the voltage applied on the capacitor;
- $R$ : the radius of the membrane ;
- $\epsilon_0$ : the vacuum permittivity ;
- $g_0$ : the gap between the electrodes.

This force is quadratic with the gap, so larges forces are created for small values of the gap. It is also quadratic with the voltage and so is inherently non-linear. In the small motion approximation, the electrical force can be expressed as  $F_{el}(t) \approx \frac{(C_0 V^2)}{2g_0} (1 + \sin \omega_\Delta t)$  for the case of an interrogation using two close signals of pulsations  $\omega_e$  and  $\omega_e + \omega_\Delta$  close to the resonance pulsation of the antenna and  $\omega_\Delta \ll \omega_e$ . For an amplitude modulation of pulsation  $\omega_\Delta$  and a carrier pulsation  $\omega_e$ , the electric force is  $F_{AM}(t) = \frac{C_0 V^2}{2g_0} \left( \frac{1}{2} + \frac{M^2}{4} + M \sin \omega_\Delta t \right)$ , with  $M$  the modulation index of the signal.

### Resolution of the differential equation

By injecting the expression of the external forces applied to the membrane, the differential equation describing the displacement of the center of the membrane becomes:

$$\ddot{x} + \frac{\omega_m}{Q_m} \dot{x} + \omega_m^2 x = \frac{1}{m_{eff}} (S_{eff} P + F_{el}(t)) \quad (5.15)$$

Here, the calculation is done using the example of sending two signals at close frequencies. The voltage can be expressed as  $V = V_0(\sin \omega_e t + \sin(\omega_e + \omega_\Delta)t)$  with  $\omega_e$  a pulsation close to the electrical resonance pulsation of the antenna and  $\omega_\Delta \ll \omega_e$ .

In order to solve the equation, the displacement is separated into a displacement due to the pressure  $x_p$ , which is supposed to be constant since the beginning to the interrogation time, and a displacement due to the electric force  $x_{el}$ , which varies sinusoidally. There is then a system of two differential equations:

$$\begin{cases} \ddot{x}_{el} + \frac{\omega_m}{Q_m} \dot{x}_{el} + \omega_m^2 x_{el} = \frac{1}{m_{eff}} \frac{(C_0 V^2)}{2g_0} (1 + \sin \omega_\Delta t) \\ x_p = \frac{S_{eff}}{k_{eff}} P \end{cases} \quad (5.16)$$

This assumption allows to keep the model linear: the electrical force is dependent of the static deflection of the membrane, and, as shown in [8], the resonance frequency of the membrane is also dependent on the static deflection of the membrane:

$$f_m = \frac{10.21}{\pi R^2} \sqrt{\frac{D}{\rho h}} \sqrt{1 + 1.464 \frac{x_p^2}{h^2}} \quad (5.17)$$

with:

- $h$ : the thickness of the membrane ;
- $E$ : the Young's modulus of the membrane material ;
- $\nu$ : the Poisson's ratio of the membrane material;
- $D$ : the bending stiffness:  $D = \frac{Eh^3}{12(1-\nu^2)}$  ;
- $\rho$ : the density of the membrane material;
- $x_p$ : the deflection at the center of the membrane due to the pressure.

Moreover, the electrical force is also dependent on the pressure, as the deflection due to the pressure change the value of the gap. This gap is also non-constant over all the surface of the electrodes. In order to estimate the electrical force, the gap is set equal to the mean gap between the membrane and the lower electrode, i.e.  $g_0 = \bar{g}(P)$ .

The differential equation of variable  $x_{el}$  is then a homogeneous constant coefficient second order linear differential equation, and can be easily solved using the limit conditions  $x_{el}(0) = 0$  and  $\dot{x}_{el}(0) = 0$ . The solution of that system is:

$$\begin{aligned} x(t) = & \frac{S_{eff} P}{k_{eff}} + \frac{F_0}{k_{eff}} + \frac{F_0 Q_m}{k_{eff}} \sin(\omega_\Delta t + \Phi) g_m(\omega_\Delta, \omega_m, Q_m) \\ & + e^{-\frac{\omega_m}{2Q_m} t} (x_0(\omega_\Delta) \cos(\Omega t) + x_1(\omega_\Delta) \sin(\Omega t)) \end{aligned} \quad (5.18)$$

with:

- $F_0 = \frac{C_0 V^2}{2\bar{g}(P)}$ , the amplitude of the electric force created in the capacitor due to the intermodulation of the two signals, with  $\bar{g}(P)$  the average gap between the two plates;

- $\Omega = \omega_m \sqrt{1 - \frac{1}{4Q_m^2}}$  the pulsation of the oscillations in the transient state;
- $\Phi = -\arctan \frac{\omega_\Delta \omega_m}{Q_m(\omega_m^2 - \omega_\Delta^2)}$  the phase shift related to the difference between the sent frequency and the resonance frequency of the membrane;
- $g_m(\omega_\Delta, \omega_m, Q_m) = \frac{\omega_m}{\omega_\Delta \sqrt{1 + \left(\frac{Q_m(\omega_\Delta^2 - \omega_m^2)}{\omega_\Delta \omega_m}\right)^2}}$  the mismatch factor between the sent difference frequency  $f_\Delta$  and the mechanical resonance frequency of the MEMS  $f_m$ . It shows a band-pass behavior of the displacement of the center of the membrane around the resonance frequency;
- $x_0 = -F_0 \left( \frac{1}{k_{eff}} + \frac{Q_m}{k_{eff}} g_m(\omega_\Delta, \omega_m, Q_m) \sin \Phi \right)$  and  $x_1 = \frac{1}{\Omega} \left( \frac{\omega_m}{2Q_m} x_0 + \frac{F_0 Q_m}{k_{eff}} \omega g_m(\omega_\Delta, \omega_m, Q_m) \cos \Phi \right)$ , the frequency dependent amplitude of the transient signal.

Equation (5.18) can be analyzed to understand the phenomena behind each term of the equation:

- $\frac{S_{eff} P}{k_{eff}}$  is the expression of the static deflection due to the pressure applied on the membrane;
- $\frac{F_0}{k_{eff}}$  is the expression of the static deflection of the membrane due to the electrostatic force;
- $\frac{F_0 Q_m}{k_{eff}} \sin(\omega_\Delta t + \Phi) g_m(\omega_\Delta, \omega_m, Q_m)$  is the expression of the vibration of the membrane in steady state;
- $e^{-\frac{\omega_m}{2Q_m} t} (x_0(\omega_\Delta) \cos(\Omega t) + x_1(\omega_\Delta) \sin(\Omega t))$  is the expression of the vibration of the membrane in transient state.

This equation allows to determine the profile of the membrane at any instant, using the equation  $w(r) = x \left(1 - \frac{r^2}{R^2}\right)$  which allows to determine the displacement of any point  $r$  of the radius  $R$  of the membrane. Based on this profile, the capacitance of the MEMS can be calculated.

### 5.3.3 Equivalent capacitance of the MEMS and reflection coefficient

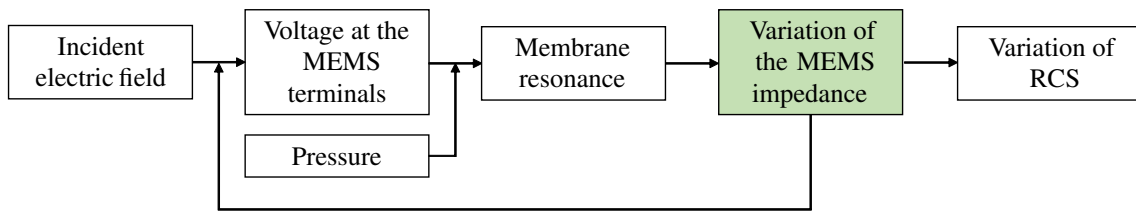


Figure 5.7: Block diagram of the interrogation of resonant MEMS using intermodulation, with the current step of the calculation highlighted. This section focuses on determining the expression of the capacitance variation and the impedance mismatch between the MEMS and the antenna.

As described in the previous section, the deflection of the membrane will change the value of the capacitance of the MEMS. By analogy with section 2.4.2, the value of the deflection for each point  $r$  of the radius  $R$  of the membrane can be calculated thanks to the equation  $w(P, r, t) = x(t) \left(1 - \frac{r^2}{R^2}\right)$  with  $x(t)$  the displacement of the center of the membrane calculated using the unidimensional differential equation of the previous section. The value of the capacitance of the MEMS at each time  $t$  is then:

$$C_S(P, t) = \int_0^R \frac{2\pi\epsilon_0 r}{g_0 + \frac{h}{\epsilon_r} - w(P, r, t)} dr \quad (5.19)$$

with  $\epsilon_r$  the relative permittivity of silicon.

Section 2.6.2 showed a difference between the values of the capacitance simulated and calculated analytically, for a static deflection due to the pressure. If the choice made is to use the results obtained by simulation, the values of the MEMS impedance can be calculated for different values of  $x(t)$  using the methodology presented in section 2.6.1. Then, a regression can be applied to obtain the value of the capacitance for all the values of  $x(t)$ .

Then, as seen in part 1.3.2, the reflection coefficient between the antenna and the loaded MEMS is defined as:

$$\Gamma = \frac{Z_A - Z_S^*(P, t)}{Z_A + Z_S(P, t)} \quad (5.20)$$

It is this periodic change of the impedance mismatch that will modulate the backpropagated power.

### 5.3.4 Variation of Radar Cross Section

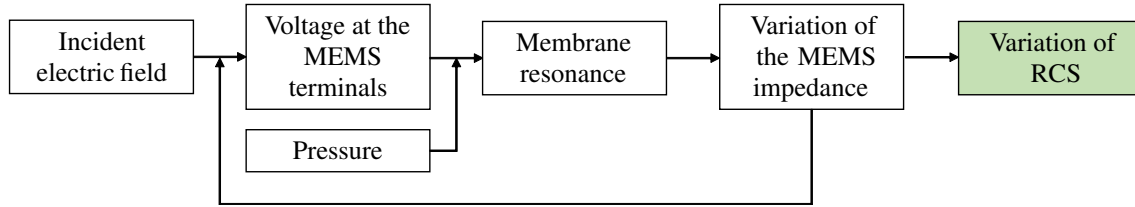


Figure 5.8: Block diagram of the interrogation of resonant MEMS using intermodulation, with the current step of the calculation highlighted. This section focuses on determining the expression of the RCS of the antenna based on the reflection coefficient. Then, the expression of the electric signal received can be expressed.

As the RCS of a loaded antenna is dependent of the reflection coefficient between the antenna and the load (i.e., the MEMS), the variation of impedance of the MEMS modify its RCS. The two previous sections show that the membrane of the MEMS vibrates periodically, which changes the MEMS impedance periodically. This section focuses on the impact of the impedance on the RCS. The RCS of a loaded antenna can be written as follows [9]:

$$\sigma = \frac{\lambda^2 G_A^2}{4\pi} |\Gamma - A_s|^2 \quad (5.21)$$

with  $A_s$  the structural mode of the antenna, which means the part of the RCS which does not vary with the load. To calculate this value for a specific antenna, Victor Engelhardt developed a methodology in his thesis [10]. Firstly, the modulus of  $A_s$  can be determined by loading the antenna by his conjugate impedance at the frequency  $f_e$ , i.e.  $Z_A^*(f_e)$ , and calculate (by simulation or measurement) the value of the RCS  $\sigma_1$ :

$$|A_s| = \sqrt{\frac{4\pi\sigma_1}{G_A^2 \lambda_e^2}} \quad (5.22)$$

Then, by loading the antenna with an impedance  $Z_\theta = \frac{Z_A^*(f_e) + |A_s| Z_A(f_e)}{1 - |A_s|}$ , the value of the phase of the structural mode can be deduced:

$$|\theta_A| = \pm \arccos \left( 1 - \frac{2\pi\sigma_2}{G_A^2 \lambda_e^2 |A|^2} \right) \quad (5.23)$$

This structural mode, as a part of the RCS that does not vary with the load, will impact only the harmonics created at the interrogation frequencies. However, its determination is important to determine precisely the shape of the backpropagated signal, which impacts the performances of the sensor such as the reading range or the resolution. The following section focuses on this analysis of the backpropagated signal.

### 5.3.5 Shape of the backpropagated signal

As shown in section 5.3.1, the signal sent by the reader, in the case where two sinusoidal signals are sent is of the form:

$$X(t) = \sqrt{2P_t} (\sin(\omega_e t) + \sin([\omega_e + \omega_\Delta]t)) \quad (5.24)$$

with  $\omega_e = 2\pi f_e$  the high electrical resonance frequency of the antenna, and  $\omega_\Delta = 2\pi f_\Delta$  the low difference frequency, related to the mechanical resonance of the MEMS. The goal is to find  $\omega_\Delta = \omega_m$ . As seen previously, the signal will be modulated by the vibration of the MEMS. In return, the signal received by the interrogation antenna will be, in steady state, of the form:

$$Y(t) = \sqrt{2\gamma P_t [\beta + \alpha g_m(\omega_\Delta, \omega_m, Q_m) \sin(\omega_\Delta t + \phi)]} (\sin(\omega_e t) + \sin([\omega_e + \omega_\Delta]t)) \quad (5.25)$$

with  $\beta$  the response of both the environment and the structural part of the antenna,  $\gamma$  the signal attenuation related to free-field propagation,  $\alpha$  the amplitude of the signal modulation related to vibration, and  $g_m$  the transfer function as defined in section 5.3.2.

Analyzing this equation allows to understand that four peaks are in the frequency spectrum of  $Y(t)$ : two peaks at  $f_m$  and  $f_m + f_\Delta$  which correspond to the received signal due to environment and the structural part of the antenna, and two peaks at  $f_m - f_\Delta$  and  $f_m + 2f_\Delta$  due to the modulation of the signal, which is the quantity of interest.

The determination of expressions for both  $\alpha$  and  $\beta$  is very important to evaluate the performances of the sensor. For example, if the received power at the interrogation frequencies set by  $\beta$  is much higher than the received power at the intermodulation frequencies set by  $\alpha$ , the difference of both powers can be higher than the dynamic range of the measuring instrument (such as a lock-in amplifier). Consequently, the intermodulation peaks would not be seen by the measuring instrument. However, precise formulations for  $\alpha$  and  $\beta$  can be difficult to put in equations without approximations to linearize the model. The following section explains why it is necessary to calculate the behavior of the sensor by recurrence, which makes it impossible to determine expressions for  $\alpha$  and  $\beta$ .

### 5.3.6 On the necessity to calculate by recurrence

Here, the time-varying force which cause the vibration of the membrane will change the value of the MEMS impedance, thus will modify the impedance mismatch between the MEMS and the antenna, i.e. changes the value of the reflection coefficient  $\Gamma$ . But, the MEMS voltage, defined by equation (5.10) is also impedance dependent. So a change in the MEMS impedance will change the voltage applied on the MEMS, therefore will change the amplitude of the force applied on the membrane. There is here a loop: the MEMS impedance-dependant voltage will change the MEMS impedance.

To resolve that issue, each value of the MEMS impedance needs to be calculated by recurrence. Let  $t$  and  $t + \Delta t$  two instants with  $\Delta t \ll t$  and  $\Delta t \ll 1/f_\Delta$ . The MEMS has an impedance  $Z_S(t)$  which will be used to calculate the value of the voltage  $V(t + \Delta t)$ , then the force and finally the value of the impedance  $Z_S(t + \Delta t)$ . This impedance will be used to calculate the value of the voltage at the next instant, i.e.  $V(t + 2\Delta t)$ . It is this phenomenon that is at the origin of the feedback loop in Figure 5.2.

### 5.3.7 Conclusion on the complete model

To conclude, a complete model was presented in order to predict the behavior of a sensor illuminated by an EM signal consisting of two sinusoidal signals of close frequencies. This model can be used to predict the signal backpropagated by the sensor using the parameters of the MEMS, the antenna and the measurement setup, as it is not possible to predict this behavior using simulation software like Ansys HFSS or CST. The main strength of this model is it uses only few approximations, but it is also its main limitation, as it is a complex model which can be calculated only using recurrence.

The interrogation is done by sending two signals of close frequencies  $f_e$  and  $f_e + f_\Delta$  (Eq. (5.1)). It creates a two-tones voltage at the terminal of the MEMS, and then a sinusoidal electrostatic force at  $f_\Delta$  which puts the membrane of the MEMS in vibration. This vibration changes periodically the impedance mismatch between the antenna and the MEMS, which modulates the backpropagated signal. The frequency spectrum of this signal is composed of four peaks, as shown in Eq. (5.25): two at the interrogations frequencies  $f_e$  and  $f_e + f_\Delta$ , which are polluted by the clutter, and two other peaks at the intermodulation frequencies  $f_e - f_\Delta$  and  $f_e + 2f_\Delta$  which contain only the information of the amplitude of the MEMS vibration. By shifting the difference frequency  $f_\Delta$  and studying at which frequency the modulation of the backpropagated signal is the highest, the mechanical resonance frequency of the MEMS is deduced. As this frequency is pressure-dependent (Eq. (5.17)), the reading of the pressure is then possible.

The model presented here is then interesting to predict the behavior of a given sensor, but the co-design of a sensor specifically for this method of interrogation can be difficult. To overcome this issue, a linearized version of this model is shown in the following sections, in order to obtain a single equation which links all the important parameters of the design and the backpropagated signal.

## 5.4 Linearized model for the co-design

The complete theoretical model presented above is useful if the goal is to predict precisely the behavior of a specific sensor. But, it is difficult to make any conclusion in order to achieve a co-design between the antenna and the MEMS because of the complexity of this model. It is thus necessary to establish a linearized model in order to have a single equation which links important parameters of the system (impedances, quality factors, antenna gain etc.) and RCS variation. To achieve it, some approximations are applied on the complete model to linearize it. In this section, the methodology and results based on this model are presented. The values of the parameters out of mechanical resonance will be expressed with an index 0, for example  $Z_{S0}$  will be the impedance of the MEMS out of mechanical resonance.

### 5.4.1 Approximations used

In order to linearize and simplify the complete model, some approximations must be used:

1. The antenna is modelled as a parallel RLC circuit, as shown in Figure 5.9. It allows to take into account the quality factor of the antenna.
2. The displacement of the vibrating membrane is taken as small compared to the average gap between the membrane and the lower electrode (ie when it is at rest).
3. The small displacements approximation implies that the capacitance (and thus, the impedance) variation of the MEMS is small compared to the static capacitance (respectively impedance)

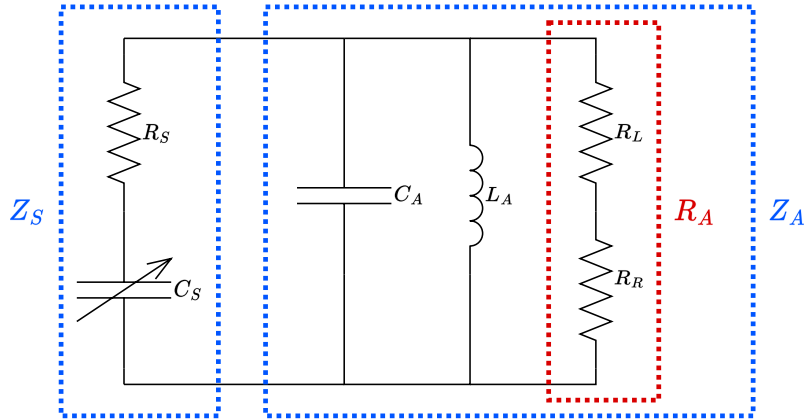


Figure 5.9: Equivalent circuit of a sensor used for the simplified model. The parallel RLC representation is used to represent the input impedance of the antenna around the antiresonance.

without any actuation.

4. The voltage at the MEMS terminals is taken as constant, as a consequence of the approximations presented above, and in order to remove the feedback loop in the Figure 5.2 block diagram.
5. The MEMS is considered to be put in vibration at its mechanical resonant frequency.

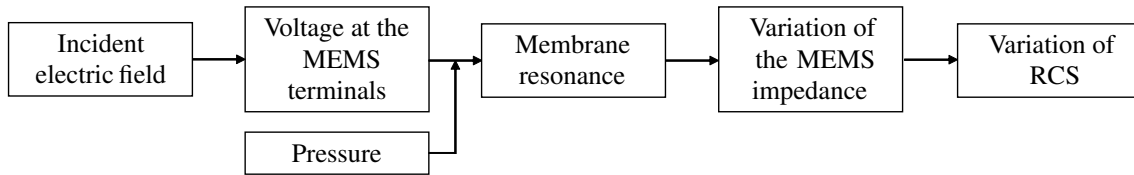


Figure 5.10: Simplified block diagram of the interrogation of resonant MEMS using intermodulation. The feedback loop is no longer present due to the approximation of constant voltage.

The impact and selection criteria of each of the approximations are shown during the development of the linearized model. These approximations were validated using both FEM simulations and the complete model using a precise geometry of antenna and one of the MEMS conceived in this thesis. The simplified block diagram is shown in Figure 5.10. For this calculation, the MEMS is considered as the load of the antenna. For each step of the calculation, each approximation used will be referred using expressions like "Approximation 4" for the constant voltage approximation, as described in the list above.

## 5.4.2 Simplification and linearization of the model

### Voltage at the MEMS terminal

Using Approximation 4 and equation (5.11), the voltage can now be considered as constant. The complete expression of the incident electric field  $E^i$  will not be explicitly written because the goal here is to focus on the sensor parameters. The voltage can now be expressed as:

$$V_S = |Z_{S0}| E^i \lambda \sqrt{\frac{G_A}{4\pi Z_0 R_S}} \quad (5.26)$$

with  $Z_{S0}$  the impedance of the MEMS out of mechanical resonance. The amplitude of the voltage is no longer time-dependent, as the modulus of the impedance of the sensor in the expression is no longer time-dependent.

### Membrane resonance

Here, the MEMS vibration is considered as in steady state. Using Approximation 2, the static displacement due to the electric force can be neglected regarding to the displacement due to the pressure and the gap. Also, thanks to Approximation 5, the assumption  $g_m(\omega_\Delta, \omega_m, Q_m) = 1$  can be made. Using equation (5.18), the displacement of the center of the membrane becomes:

$$x(P, t) = \frac{S_{eff}P}{k_{eff}} + \Delta x(P, t) = \frac{S_{eff}P}{k_{eff}} + \frac{C_0 V_S^2}{2\bar{g}(P)} \frac{Q_m}{k_{eff}} \sin \omega_m t \quad (5.27)$$

Then, by combining equations (5.26) and (5.27):

$$x(P, t) = \frac{S_{eff}P}{k_{eff}} + \frac{C_0}{2\bar{g}(P)} |Z_{S0}|^2 (E^i)^2 \lambda^2 \frac{G_A}{4\pi Z_0 R_S} \frac{Q_m}{k_{eff}} \sin \omega_m t \quad (5.28)$$

with  $\bar{g}(P)$  the modified value of the gap. The modified gap due to the deformation can be calculated using methods such as presented in [11]. The linearized displacement contains only two terms, one represents the static deflection due to the pressure, and the other one the vibration of the membrane, which has a constant amplitude.

### Variation of the MEMS impedance

In order to simplify the equation, the deflection of each point of the membrane can be approximated as the modified value of the total deflection. Equation (5.19) can be written:

$$C_S(P, t) = \frac{\epsilon_0 S}{\bar{g}(P) - \Delta x(P, t)} \quad (5.29)$$

with  $\Delta x(P, t)$  as in Equation (5.28). Using Approximation 3, the equation can be linearized as:

$$C_S(P, t) \approx \frac{\epsilon_0 S}{\bar{g}(P)} \left( 1 + \frac{\Delta x(P, t)}{\bar{g}(P)} \right) \approx C_{S0}(P) + \Delta C(P, t) \quad (5.30)$$

with  $\Delta C(P, t) = \frac{C_{S0} \Delta x(t)}{\bar{g}(P)}$  the variation of capacitance due to the vibration and  $C_{S0}(P) = \frac{\epsilon_0 S}{\bar{g}(P)}$  the static value of the capacitance.

### Equivalent impedance of the MEMS

Using again Approximation 3, the MEMS impedance expression can be linearized:

$$Z_S(P, t) = R_S + \frac{1}{j[C_{S0}(P) + \Delta C(P, t)]\omega_e} = R_S + \frac{1}{jC_{S0}(P)\omega_e} \left( \frac{1}{1 + \frac{\Delta C(P, t)}{C_{S0}(P)}} \right) \approx Z_{S0}(P) - \Delta Z(P, t) \quad (5.31)$$

with  $\Delta Z(P, t) = \frac{\Delta C(P, t)}{jC_{S0}(P)^2 \omega_e}$  the variation of impedance due to the vibration of the MEMS.

### Reflection coefficient

By using  $\Gamma = \frac{Z_A - Z_S^*}{Z_A + Z_S}$ , and combining equations (5.28), (5.30) and (5.31), the reflection coefficient becomes:

$$\Gamma(t) = \frac{Z_A - Z_{S0}^*(P) - \Delta Z(P, t)}{Z_A + Z_{S0}(P) - \Delta Z(P, t)} \approx \frac{Z_A - Z_{S0}^*(P)}{Z_A + Z_{S0}(P)} - \frac{\Delta Z(P, t)}{Z_A + Z_{S0}(P)} \quad (5.32)$$

which becomes after using the expression of  $\Delta Z(P, t)$ :

$$\Gamma(P,t) = \Gamma_0(P) + j \frac{G_A(E^i)^2 \lambda^2}{4\pi Z_0 \omega_e} \frac{|Z_{S0}(P)|^2}{R_S(Z_A + Z_{S0}(P))} \frac{Q_m}{k_{eff}} \sin \omega_m t \quad (5.33)$$

with  $\Gamma_0(P) = \frac{Z_A - Z_{S0}^*(P)}{Z_A + Z_{S0}(P)}$  the out-of-vibration reflection coefficient at the load.

### Variation of RCS

Combining equations (5.21) and (5.33) the expression of the time-varying antenna RCS is:

$$\sigma(P,t) = \frac{\lambda^2 G_A^2}{4\pi} \left| \Gamma_0(P) - A_s + j \frac{G_A(E^i)^2 \lambda^2}{4\pi Z_0 \omega_e} \frac{|Z_{S0}(P)|^2}{R_S(Z_A + Z_{S0}(P))} \frac{Q_m}{k_{eff}} \sin \omega_m t \right|^2 \quad (5.34)$$

### Signal received by the reader

The radar equation can be used to express the power received by the reader  $P_R$ :

$$P_R = \sigma(t) \frac{\lambda^2}{(4\pi)^3 d^4} G_T G_R P_T \quad (5.35)$$

with  $G_R$  the gain of the reader in reception. By combining Eq. (5.25), (5.34) and (5.35), and by omitting the response of the environment (i.e.  $\beta = 0$  in (5.25)), the received signal due to the sensor is:

$$Y(t) = \frac{\lambda^2 G_A}{(4\pi d)^2} \sqrt{2G_T G_R P_T} \left| \Gamma_0 - A_s + j \frac{G_A(E^i)^2 \lambda^2}{4\pi Z_0 \omega_e} \frac{|Z_{S0}|^2}{R_S(Z_A + Z_{S0})} \frac{Q_m}{k_{eff}} \sin \omega_m t \right| (\sin(\omega_e t) + \sin([\omega_e + \omega_m]t)) \quad (5.36)$$

These equations clearly show the modulation created by the resonance of the MEMS through the term before the  $\sin \omega_m t$ . This term should be maximized in a co-design approach to have the highest modulation possible.

## 5.5 Analysis of the models

In previous sections, the complete model, which can be used for a precise estimation of the signal received by the interrogator, and the linearized model, to understand precisely which parameters are important in a co-design approach, have been presented. This section focuses on analyzing these models to understand the advantages of this interrogation technique and the important parameters in a co-design approach.

### 5.5.1 Analysis of the equation of the signal received

The final equation of the linearized model, expressed in Eq. (5.36) can be analyzed to understand which parameters are important in a co-design approach:

- The term  $\frac{\lambda^2 G_A}{(4\pi d)^2} \sqrt{2G_T G_R P_T}$  before the absolute value represents parameters of the interrogation. The gain of the antenna  $G_A$  and the working frequency of the antenna can be tuned to increase the amount of power received.

- The term  $\Gamma_0 - A_s$  represents the static behavior of the sensor, i.e., the out-of-resonance response of the sensor. It is related to the geometry of the antenna and the impedance matching between the antenna and the MEMS. If the objective is to increase the amplitude of the peaks at the intermodulation frequencies and to reduce the peaks at the interrogation frequencies, these parameters must be reduced.
- The term before the  $\sin \omega_m t$  represents the amplitude of the modulation of the backpropagated signal. It must be then maximized. It can be divided into three parts:
  - The term  $\frac{G_A(E^i)^2 \lambda^2}{4\pi Z_0 \omega_e}$  represents the electromagnetic properties of the sensor, mainly related to the gain of the antenna and the choice of its resonance frequency.
  - The term  $\frac{|Z_{S0}|^2}{R_S(Z_A + Z_{S0})}$  represents the electrical properties of the sensor. It includes the choice of the impedance of the sensor and the antenna, but also the quality factor of the antenna (included in its impedance  $Z_A$ ). A study of the impact of the electrical size of the antenna on the modulation of the RCS could be interesting to perform.
  - Finally, the term  $\frac{Q_m}{k_{eff}}$  represents the mechanical properties of the membrane of the MEMS. In order to increase the amplitude of the modulation, the mechanical quality factor  $Q_m$  should be increased and/or the effective stiffness  $k_{eff}$  reduced.

This equation shows more clearly the importance of each parameter in a co-design approach, which can be separated according to their origin, and to estimate the amplitude of each peak received for a specific interrogation setup. Combined with the complete model, which enables more precise estimation of the received signal, an advanced analysis is possible. It is the basis for several analyses carried out to understand the behavior of the sensor and which parameters to optimize. Some of them are presented in this chapter.

### 5.5.2 Interrogation of multiple MEMS on one antenna

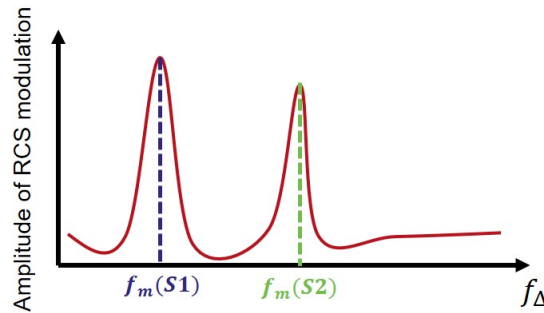


Figure 5.11: Example of the evolution of the amplitude of the modulation of the RCS with frequency, when two MEMS are placed on an antenna. In order to differentiate them, the two have different mechanical resonance frequency variation ranges.

This method of interrogation presents an interesting advantage: it allows to read and identify multiple MEMS on a single antenna. By taking the example of two different MEMS on an antenna, denoted S1 and S2. Each MEMS has different variation ranges of mechanical resonance frequency. The measurement is done in time-domain and then a Fourier transform is applied to extract the frequency spectrum. By shifting the frequency  $f_\Delta$  of the interrogation signal, the amplitude of the modulation of the RCS will be maximum for two frequencies, corresponding to the resonant frequencies of each MEMS. An illustration is presented in Figure 5.11.

This advantage can be used in two different ways: to enhance the precision of the measurement, by adding a reference MEMS on the same antenna as the MEMS sensor, or to measure multiple physical quantities with different MEMS on a single antenna.

By extension, multiple antennas can be interrogated and identified without the need of another differentiating criterion such as the antenna resonance frequency or polarization. It is the MEMS present on the antennas that acts as the identifying element. The low mechanical resonance frequency of the MEMS compared with the electrical resonance frequency of the antenna is then used to have several sensors while complying with frequency band usage regulations.

### 5.5.3 Amplitude of the peaks in the frequency spectrum

Eq. (5.25) and (5.36) show that this type of interrogation counters the clutter isolation issue. On the one hand, the peaks in the frequency spectrum of the response at the interrogation frequencies  $f_e$  and  $f_e + f_m$  will contain the clutter, the structural mode of the antenna and the static antenna mode (i.e., the response related to the out-of-resonance reflection coefficient  $\Gamma_0$ ). On the other hand, the two peaks at the intermodulation frequencies  $f_e - f_m$  and  $f_e + 2f_m$  contains only the terms due to the resonance of the MEMS. By reading the response at one of these frequencies, only the mechanical resonance of the MEMS is read, and then no background cancellation step on the signal processing is necessary.

Due to the limitation of the dynamic range of the measurement setup, it could be interesting in a co-design approach to lower the structural part of the response, in order to reduce the ratio between the power received at the interrogation frequency compared to the power received at the intermodulation frequencies.

## 5.6 Example of numerical applications of the models

This section presents on a first example of the application of the models presented above on a specific geometry of miniature antenna and MEMS. Even when the antenna and the MEMS were not specifically designed for an interrogation using intermodulation during this thesis, it is still possible to extract interesting information about the behavior of a sensor interrogated by this method.

### 5.6.1 Geometries used for this analysis

The MEMS used in this analysis has dimensions of ( $R = 150\mu m, t = 4\mu m, g_0 = 1\mu m$ ), a mechanical quality factor  $Q_m = 100$ , a pressure of 0.8 bar, while the antenna has a gain of 1.15. It is represented as a RC series circuit with a resistance of  $100\Omega$ , and a capacitance variation with pressure shown in Figure 5.12. The simulated capacitance variation is used because of the difference highlighted in section 2.6.2 with the capacitance calculated with the parallel plate representation. This electrical behavior was obtained in simulations on Ansys HFSS and the fitting is done using a polynomial equation of order 5.

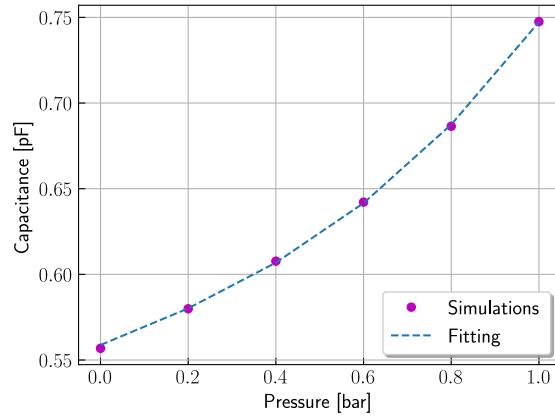


Figure 5.12: Variation of the capacitance of the MEMS with dimensions of ( $R = 150\mu\text{m}$ ,  $t = 4\mu\text{m}$ ,  $g_0 = 1\mu\text{m}$ ) with pressure, obtained by simulations on Ansys HFSS. The curve is obtained by a polynomial fitting of order 5.

The antenna geometry is based on the CLL antenna used for the analysis of the impact of the quality factor of the antenna in section 2.7.2, and is shown in Figure 5.13. It is printed on a  $35\mu\text{m}$  thick copper over  $0.787\text{ mm}$  thick Rogers RT5880 substrate ( $\epsilon_r = 2.2$ ,  $\tan \delta = 0.0009$ ). The lumped element is a  $0.3\text{pF}$  perfect capacitance and the MEMS is the antenna load. The antenna has a radius of the outer loop of  $15.4\text{mm}$ , and of the inner arc is  $11\text{mm}$  (electrical size  $ka = 0.28$ ). Its input impedance and variation of RCS with pressure are shown in Figure 5.14.

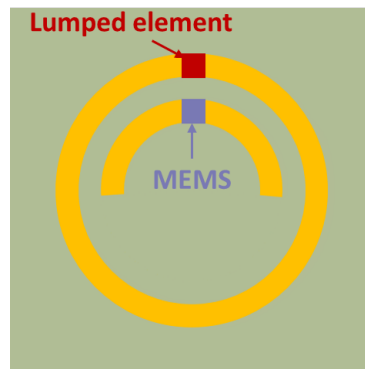


Figure 5.13: CLL antenna used for the application of the intermodulation model.

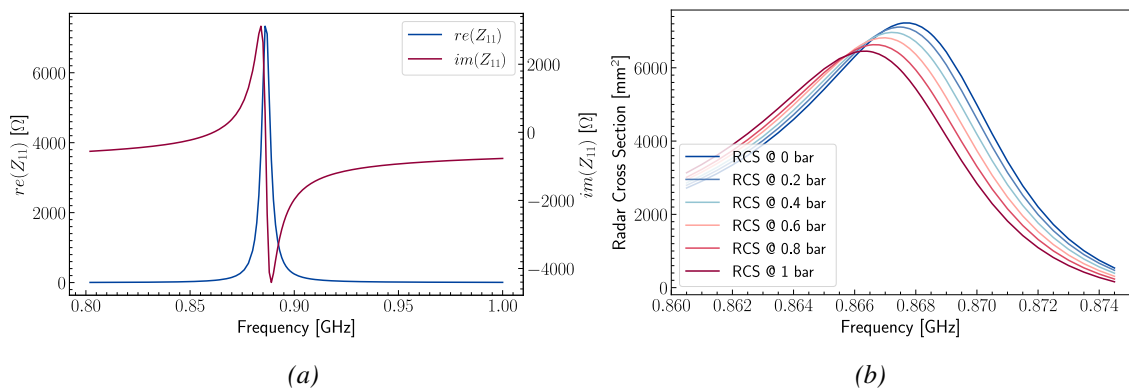


Figure 5.14: Input impedance (a) and evolution of the RCS with the pressure (b) for the CLL antenna used in this analysis.

The gain of the reading antenna in transmission and reception is assumed to be equal to 3, while the power sent is 1 W in order to respect French regulations. The sent signal is the sum of two sinusoids of equal amplitudes.

### 5.6.2 Validation of the voltage on the antenna

Among all the physical phenomena involved during the interrogation of resonant MEMS, the voltage is a phenomenon whose analytical formula can be compared with a HFSS simulation. Two simulations of the antenna were performed to extract the voltage: one with the load on the antenna to extract the voltage at the MEMS terminals, one without it to extract the open-circuit voltage. The antennas were excited using a plane wave with the same intensity of the electric field as in the analytical model. The voltage was calculated by integrating the electric field on a line at the MEMS location.

Figure 5.15a shows the comparison between the analytical formula of the open-circuit voltage of Eq. (5.10) and the simulation, and Figure 5.15b shows the comparison with the voltage at the MEMS terminals (Eq. (5.11)).

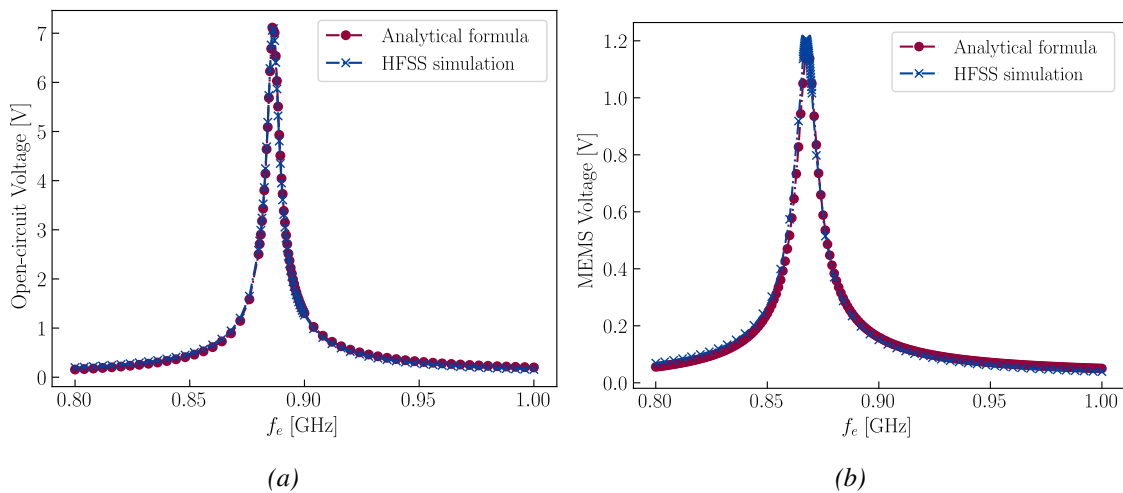


Figure 5.15: Comparison between simulation and analytical formula for the open-circuit voltage (a) and the voltage at the MEMS terminals (b).

Both analytical formulas match with the simulation. The peaks of the subfigures appear at different frequencies: the open-circuit voltage is maximal at the antiresonance of the antenna, where its impedance is the highest, while the peak of the MEMS voltage occurs at the impedance matching frequency.

### 5.6.3 Validation of the linear model

The linear model was then validated. To achieve that, the complete model were applied on the sensor setup presented in section 5.6.1. The evolution in time-domain of the parameters were plotted for the complete model in order to compare the values obtained with the linear model on one way, and to validate the approximations used on the other way. Figure 5.16 shows the example of the time-domain evolution of the voltage and the displacement of the membrane using the complete model.

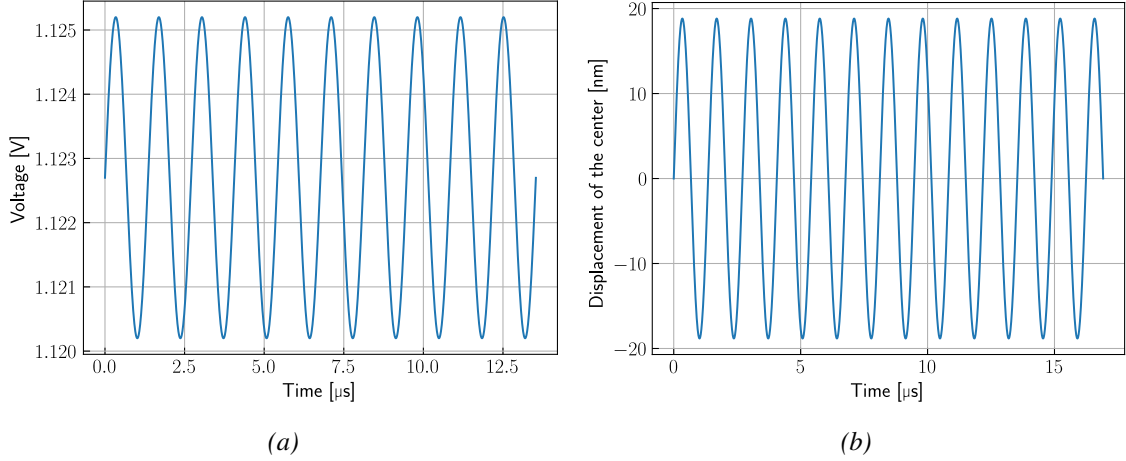


Figure 5.16: Example of voltage (a) and displacement of the center of the membrane (b) in time-domain and steady state, calculated using the complete model. Using the linearized model, the calculated voltage is  $V_S = 1.1226V$ , and the calculated displacement of the center of the membrane is  $\Delta x(t) = 18.839 \times 10^{-9} \sin \omega_m t$  (in meters).

By looking at both subfigures, the approximation of low variations of voltage can be validated, with a relative variation of the voltage of 0.45%. The low displacement condition can be validated too, as the maximal displacement is 18.827nm which is low compared to the  $1\mu\text{m}$  of the gap. By applying the linearized model, the values of the voltage  $V_S$  and the displacement  $\Delta x(t)$  are equal to:

$$V_S = |Z_{S0}| E^i \lambda \sqrt{\frac{G_A}{4\pi Z_0 R_S}} = 1.1226V \quad (5.37)$$

$$\Delta x(t) = \frac{C_0}{2\bar{g}(P)} |Z_{S0}|^2 (E^i)^2 \lambda^2 \frac{G_A}{4\pi Z_0 R_S} \frac{Q_m}{k_{eff}} \sin \omega_m t = 18.839 \times 10^{-9} \sin \omega_m t \quad (5.38)$$

which represents a relative error of 0.06% for the displacement of the center of the membrane, and less than 0.01% for the voltage by comparing to the mean value of the voltage. The voltage obtained by simulation on Ansys HFSS is equal to 1.1136 V.

To conclude, for this analysis the conditions to linearize the model were validated. The linearized model can be used in this context to predict the behavior of the sensor, as there are low differences with the complete model.

#### 5.6.4 Example of a received signal

The complete model allows to calculate the spectrum of the received signal under the conditions presented in section 5.6.1, by applying a Fourier transform to the calculated time-domain signal. The comparison between the sent and the received signal is shown in Figure 5.17. This response will lead to four peaks in the spectrum of the received signal: Two peaks at  $f_e$  and  $f_e + f_m$ , corresponding to the two signals sent, and two peaks at  $f_e - f_m$  and  $f_e + 2f_m$  corresponding to the intermodulation frequencies created by the vibration of the membrane. The spectrum of Figure 5.17 is calculated at a distance of 1 m for 1 W sent.

#### 5.6.5 Choice of the interrogation frequency

As the resonance of the membrane modulate the RCS, it seems interesting to compare the mean value of the RCS  $\sigma_{mean}$  with the amplitude of the variation of RCS  $\Delta\sigma = \max \sigma(t) - \min \sigma(t)$ .

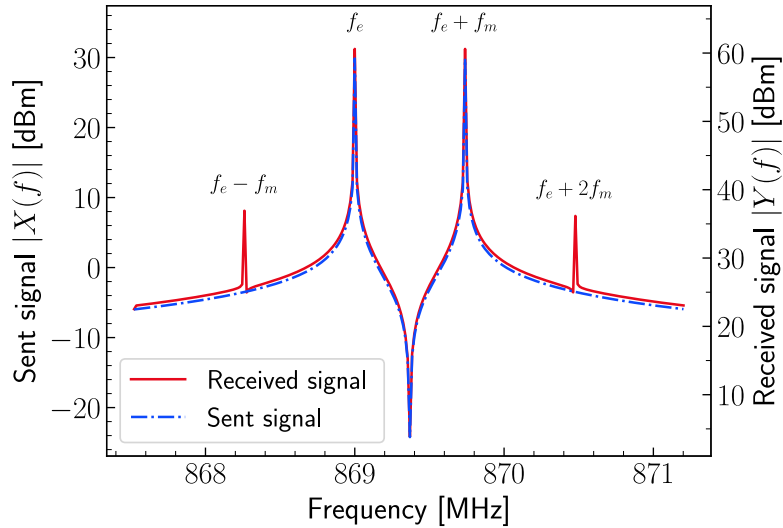


Figure 5.17: Example of FFT of sent and received signal under the conditions presented in section 5.6.1 calculated with the complete model.

Under the same interrogation condition as before, and by shifting the interrogation frequency  $f_e$ , the evolution of  $\sigma_{mean}$  and  $\Delta\sigma$  is then plot in Figure 5.18.

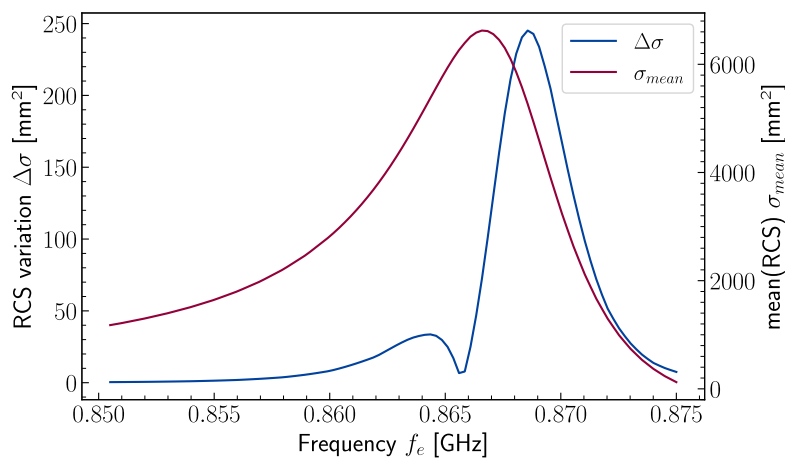


Figure 5.18: Variation of the mean value of the RCS  $\sigma_{mean}$  and the variation of RCS  $\Delta\sigma$  with the interrogation frequency  $f_e$ .

This figure shows an interesting property of this interrogation: the interrogation frequency at which  $\sigma_{mean}$  is maximal (i.e, at  $f_e = 866.6$  MHz) is not the frequency at which the modulation is the highest (which occurs at 868.6 MHz). It seems to be interesting to interrogate the sensor at a frequency slightly higher than the frequency of maximum RCS in the frequency response of the sensor in order to maximize the received signal.

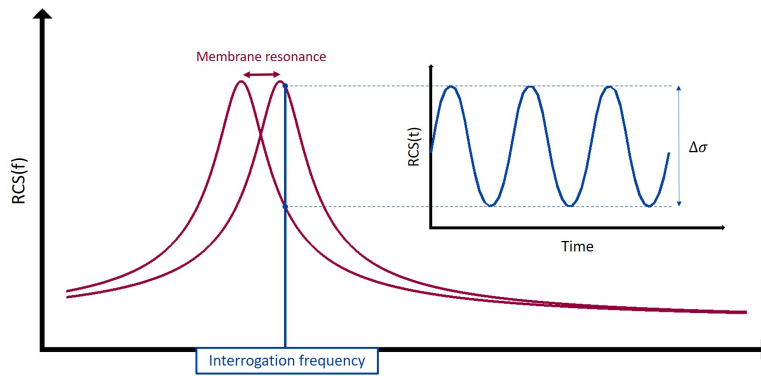


Figure 5.19: Illustration of the impact of the resonance of the MEMS on the RCS while interrogated at a frequency different than the maximum of RCS. The vibration of the membrane periodically shift the frequency response of the antenna, which periodically changes the value of the RCS at the interrogation frequency.

Figures 5.14b and 5.15b are important in order to explain this phenomenon. At 868.6 MHz, the voltage is not maximal, as the maximum of voltage is at 866.6 MHz, i.e., the same frequency as the maximum of RCS. However, another way to interpret the impact of the MEMS resonance on the RCS is shown in Figure 5.19. While interrogating the sensor, the frequency response of the antenna shifts periodically. As the interrogation is done at a fixed frequency, the RCS changes also with time. Because the interrogation frequency is different than the frequency of maximum RCS, this amplitude of the modulation is dependent on the slope of the response frequency of the sensor. The steeper the slope, the more the RCS is modulated. This phenomenon counterbalances the reduction in voltage at this interrogation frequency: the amplitude of the membrane vibration is lower, but it has a greater impact on the sensor response. Further studies are needed to investigate the impact of antenna and MEMS design parameters on this interrogation at a frequency other than the electrical resonance.

## 5.7 Measurement of the resonance of the MEMS

The measurements presented in this section were done with Zacharie Auray during his internship. The main goal was to extract the dynamical behavior of several MEMS, i.e., the evolution of their resonance frequency with pressure, their quality factor and the spectrum received under the effect of two nearby sinusoidal voltages. However, no wireless interrogation using the intermodulation principle was carried out. The choice of the MEMS to measure is based on the results of the characterization presented in chapter 3, while the goal was to measure MEMS with different geometries (metallized membrane or not, different radius etc.). This section focuses on the results of these characterizations.

### 5.7.1 Resonance frequency and pressure

The behavior of several MEMS membranes under a change of pressure was characterized on the PAV2000 prober, the same one which was used for the measurement of the MEMS under vacuum of section 3.5.2, connected to an impedance analyzer. These measurements were performed on MEMS chosen on a full wafer (based on the characterization of chapter 3), for values of pressure between 1 mbar and atmospheric pressure. A DC voltage of 10V and an AC voltage of 1V

were applied on the MEMS.

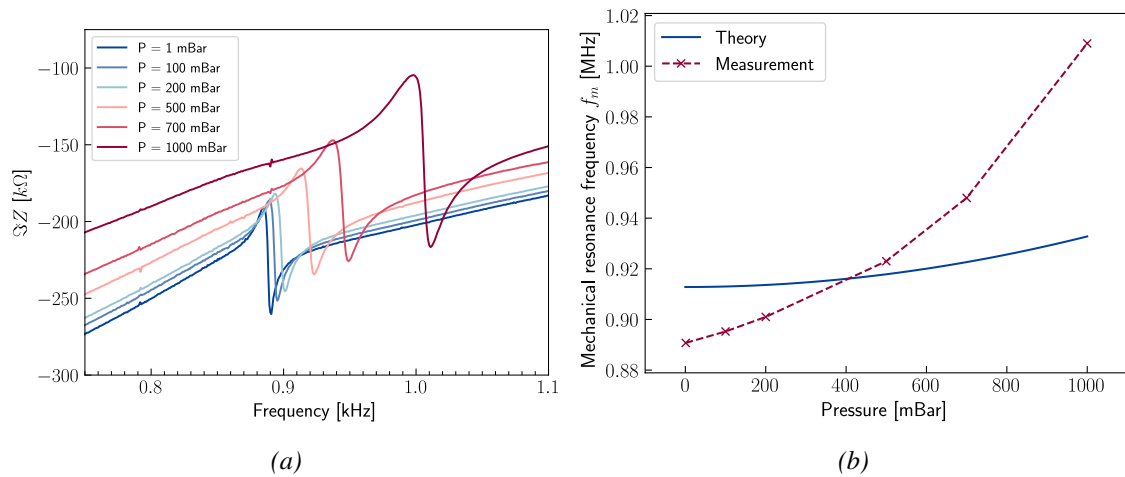


Figure 5.20: Example of variation of resonance frequency of a MEMS with pressure. (a) Imaginary part of the MEMS impedance with pressure, the resonance occurs when the curve decreases. (b) Variation of resonance frequency with pressure, the theoretical curve was calculated using Eq (5.17).

Figure 5.20 shows an example of the evolution of the frequency response and the resonance frequency and the imaginary part of the impedance of one MEMS with pressure. The measured variation of resonance frequency is higher than expected. It can be correlated with the measurement of the profile of the membranes with the DHM, as they are different than expected (the membrane is not flat under vacuum). If there is stress on the membrane added during the fabrication, it can change its mechanical behavior.

## 5.7.2 Quality factor of the MEMS

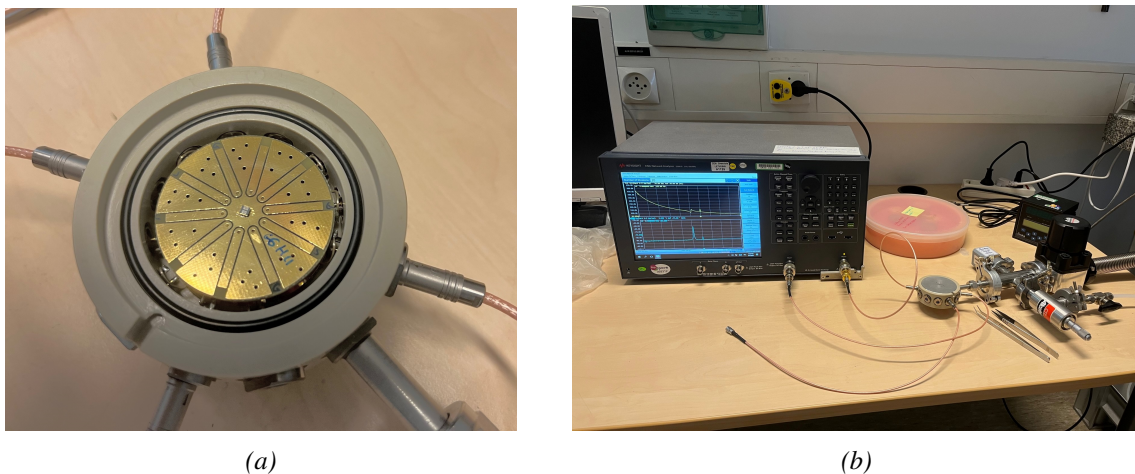


Figure 5.21: View of the PCB inside the vacuum chamber (a) and the measurement setup (b) including a Keysight E5061B ENA Vector Analyzer and a vacuum pump.

To estimate the quality factor of the MEMS, four chips were selected and wire-bonded to a PCB. These PCB were then placed inside a small vacuum chamber connected to a Keysight E5061B ENA Vector Analyzer, which are used when the impedance of the device under test is far from 50 $\Omega$ . The PCB on the vacuum chamber and the setup of measurement are shown in

Figure 5.21. The ENA was calibrated using an Open-Short-Thru-Load calibration. To extract the quality factor, the frequency response of the MEMS was fitted using a Modified Butterworth Van-Dyke (MBVD) circuit [12].

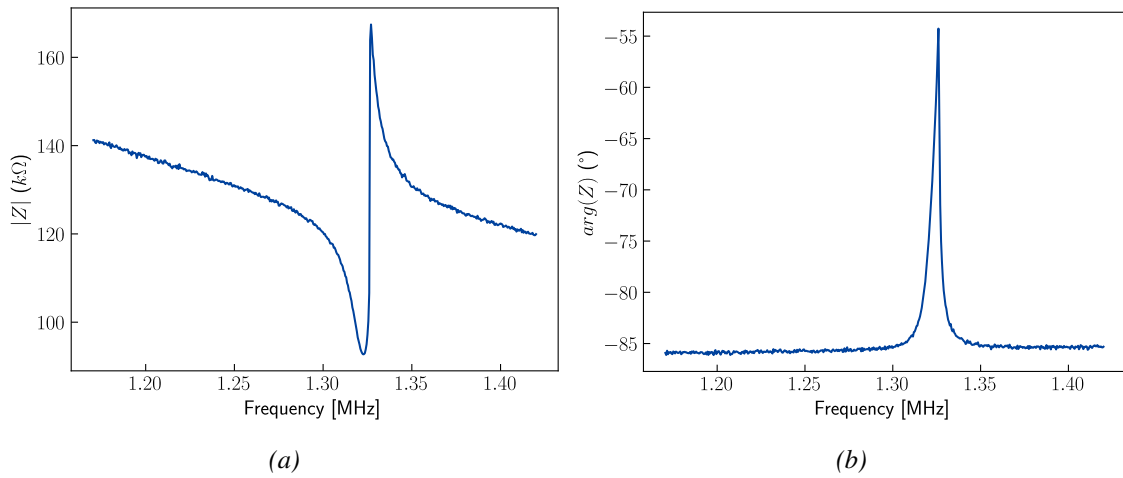


Figure 5.22: Modulus (a) and argument (b) of the non-metallized MEMS impedance under vacuum with electrostatic actuation. The ENA was calibrated using an Open-Short-Thru-Load calibration. The measured quality factor under vacuum, extracted thanks to a MBVD fitting, is 271.

The DC voltage applied is 5V while the AC voltage is 224mV. It was observed that the non-metallized MEMS presents a higher quality factor than the other MEMS which have their membrane metallized. The impedance of one non-metallized MEMS under vacuum is plotted in Figure 5.22. The measured resonance frequency is 1.32 MHz, with a quality factor of 271. At atmospheric pressure, the measured quality factor is 89. It shows clearly the effect of the air damping on the quality factor. By looking at the modulus of the impedance, the actuation is slightly non linear, as the part of the curve just before resonance is slightly wider than the part after resonance.

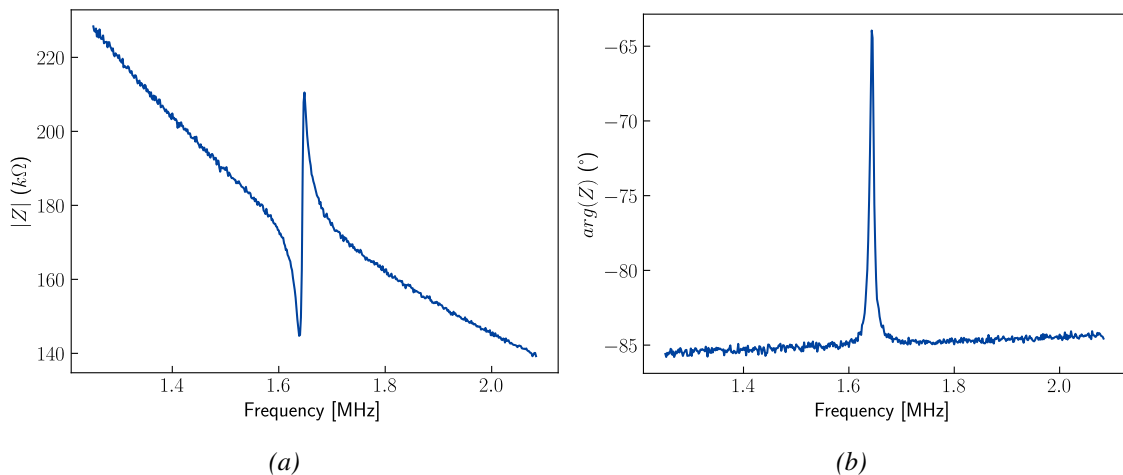


Figure 5.23: Modulus (a) and argument (b) of the metallized MEMS impedance under vacuum with electrostatic actuation. The ENA was calibrated using an Open-Short-Thru-Load calibration. The measured quality factor under vacuum, extracted thanks to a MBVD fitting, is 184.

For comparison purposes, the impedance of a metallized MEMS is plotted in Figure 5.23. Under the same conditions of actuation, the measured quality factor under vacuum is 184 at a resonance frequency 1.64 MHz. For this MEMS, the part of the curve just before resonance has

the same width as the part after resonance, this response is then linear. This change in the linearity between the two MEMS under the same voltage applied shows that the non-metallized MEMS has a higher amplitude of resonance, and so it became slight non-linear.

### 5.7.3 MEMS resonance and intermodulation

Finally, now that the resonance frequency of the MEMS is known, the MEMS were actuated using the intermodulation principle by sending two sinusoidal voltages generated by a lock-in amplifier. The measurement setup is shown in Figure 5.24. The goal of this measurement is to find the intermodulation peak created by the mechanical resonance of the MEMS, as it is the key element of the interrogation, because this peak creates the modulation of the backpropagated signal.

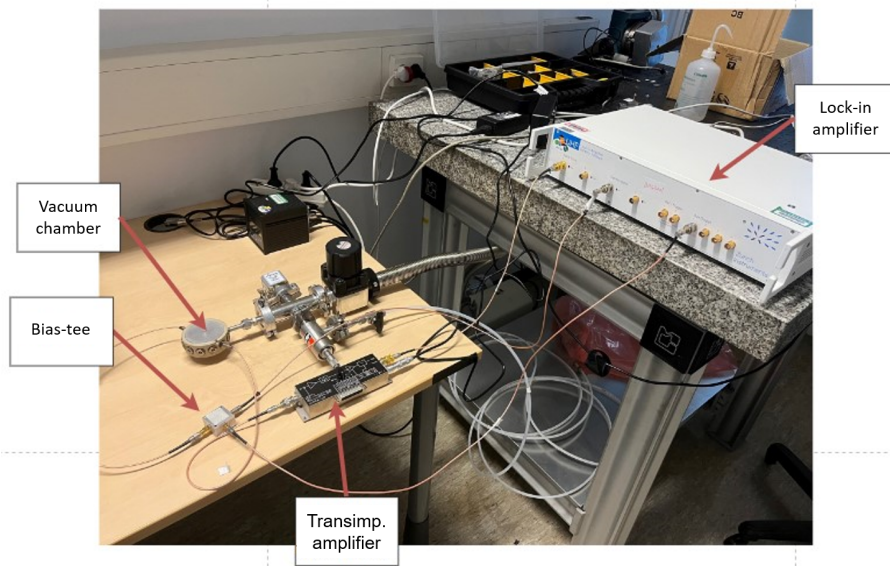


Figure 5.24: Setup of measurement of the peaks of intermodulation of the MEMS. The MEMS is placed on a PCB inside a vacuum chamber. The two sent signals were generated using a lock-in amplifier. A bias-tee is used at the output of the MEMS to separate the DC and the AC signals of the voltage, which is then converted into current thanks to a transimpedance amplifier.

The signal generated by the MEMS after the actuation was sent through a bias-tee in order to separate the AC and the DC components of the signal. The AC signal was then sent through a transimpedance amplifier to convert it into a voltage, which was sent back to the lock-in. The same MEMS as presented in the previous section was actuated under vacuum with a signal at  $f_e = 5$  MHz modulated by a signal at  $f_\Delta$ , with  $f_\Delta \in [1.28, 1.37]$  MHz. No DC voltage was generated by the lock-in amplifier, and the gain of the transimpedance amplifier was  $10^4$  V/A.

Figure 5.25 shows the current received by the lock-in amplifier at  $f_e - 1.5f_\Delta$  versus  $f_\Delta$  for different values of the AC voltage. A peak of intermodulation can be seen, with an amplitude which increase when the voltage increases, as expected. It shows that an intermodulation peak is generated by the MEMS, which proves the resonance of the MEMS.

### 5.7.4 Conclusion on the measurements

To conclude, these measurements shows that the MEMS designed for this thesis generate intermodulation peaks under the application of a two-frequencies voltage. It proves the resonance of the MEMS, and the evolution of this resonance frequency with pressure has been measured. Additional parameters has been measured, such as the quality factors or the frequency spectra

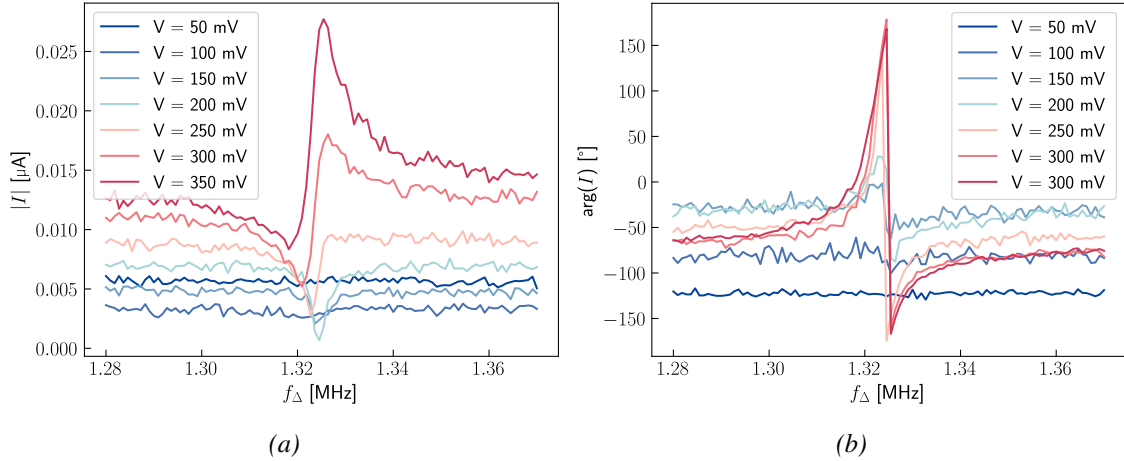


Figure 5.25: Modulus (a) and argument (b) of the received voltage by the lock-in amplifier at one intermodulation frequency versus the frequency  $f_{\Delta}$

received. All these measurements are important in order to design antenna specifically for these MEMS.

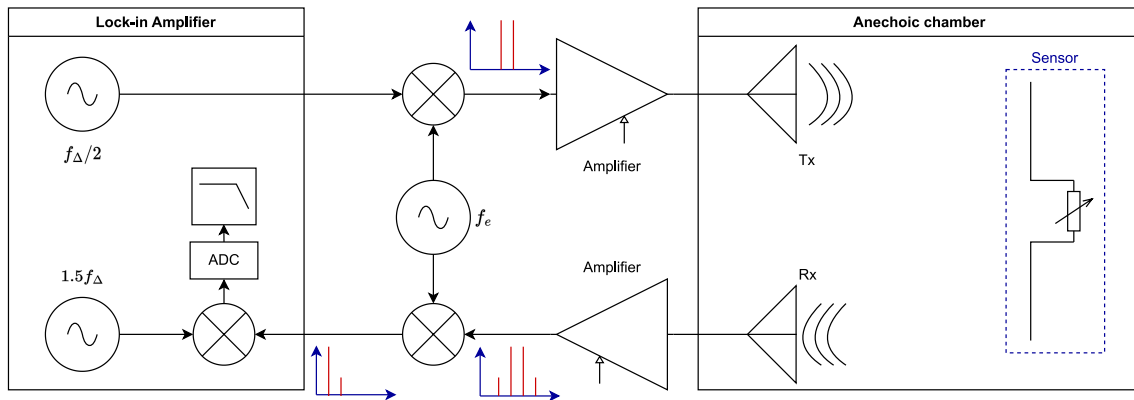


Figure 5.26: Measurement diagram for resonant sensors in anechoic chamber using intermodulation. The high-frequency signal at  $f_e$  is generated by a RF source, while the low-frequency signal at  $f_{\Delta}/2$  is generated by the lock-in amplifier. The signal received back by the Rx antenna contains the four peaks in its spectrum. It is converted to baseband by multiplying it again by  $f_m$ . It is sent to the lock-in amplifier, where the reference is set to  $1.5f_m$  to extract the amplitude of the intermodulation peak.

The following steps in this study are the application of the model presented here and the measurements results in order to design antennas specifically for the MEMS. Then, these sensors will be characterized in anechoic chamber. A first set-up of measurement in anechoic chamber is shown in Figure 5.26. The objective is to measure the amplitude of the intermodulation peaks with the lock-in amplifier. The lock-in amplifier generate and analyze the low frequencies components while an additional RF source is necessary to generate the interrogation frequency  $f_e$ . Particular attention must be paid to the choice of multipliers and amplifiers to ensure signal integrity.

These results on the MEMS developed in this thesis are important in order to validate the analytical model and design new MEMS for a wireless measurement in resonant mode.

## 5.8 Conclusion

As a conclusion, this chapter presented a new method of interrogation for our sensors. The measurement is done by wirelessly reading the value of the pressure-dependant mechanical resonance of this MEMS through an intermodulation interrogation principle, which has the added advantage of separating in frequency the direct response of the antenna and the sensing signal from the MEMS. A complete model was developed to predict precisely the behavior of the sensor, which was then linearized to extract a single equation which links the important parameters of the design.

This technique presents several advantages, such as the possibility to put multiple MEMS on the same antenna and interrogate them separately, a greater reading distance in real environments, as the reading is done at a frequency different from the interrogation frequencies, and an increased precision of the measurement.

This model was then applied on a specific sensor design, to extract first results such as the value of the voltage or the importance of the choice of the interrogation frequency.

Finally, some MEMS were characterized in resonance in order to extract their resonance frequency and their quality factor, and finally actuated under an amplitude-modulated signal to prove the presence of an intermodulation peak which is characteristic of membrane resonance.

However, a lot of work remains to be done on this subject, which looks very promising. The first step, following on from the resonance measurements carried out here, would be to design antennas for some of the MEMS designed in this thesis. The linearized model would then be very well suited to this design perspective.

In a second phase, it would be interesting to study the impact of the choice of antenna geometry on performance, its impedance, in order to design MEMS specifically intended to be interrogated using the intermodulation principle.

# Bibliography

- [1] Nicolas Barbot, Olivier Rance, and Etienne Perret. “Classical RFID Versus Chipless RFID Read Range: Is Linearity a Friend or a Foe?” In: *IEEE Transactions on Microwave Theory and Techniques* 69.9 (Sept. 2021), pp. 4199–4208. ISSN: 1557-9670. DOI: [10.1109/TMTT.2021.3077019](https://doi.org/10.1109/TMTT.2021.3077019).
- [2] Ashkan Azarfar, Nicolas Barbot, and Etienne Perret. “Towards Chipless RFID Technology based on Micro-Doppler Effect for Long Range Applications”. In: *2021 IEEE MTT-S International Microwave Symposium (IMS)*. 2021, pp. 819–822. DOI: [10.1109/IMS19712.2021.9575006](https://doi.org/10.1109/IMS19712.2021.9575006).
- [3] Ville Viikari and Heikki Seppä. “RFID MEMS sensor concept based on intermodulation distortion”. In: *IEEE Sensors Journal* 9 (Jan. 2010). DOI: [10.1109/JSEN.2009.2031809](https://doi.org/10.1109/JSEN.2009.2031809).
- [4] Ville Viikari et al. “Review of passive wireless sensors utilizing the intermodulation communication”. In: *2014 IEEE RFID Technology and Applications Conference (RFID-TA)*. Tampere, Finland: IEEE, Sept. 2014, pp. 56–61. ISBN: 978-1-4799-4680-8. DOI: [10.1109/RFID-TA.2014.6934200](https://doi.org/10.1109/RFID-TA.2014.6934200). URL: <http://ieeexplore.ieee.org/document/6934200/> (visited on 01/20/2021).
- [5] Constantine A Balanis. *Antenna theory: analysis and design*. John wiley & sons, 2015.
- [6] John D Kraus and Ronald J Marhefka. *Antenna for all applications*. McGraw-Hill, 2002.
- [7] S. Timoshenko and S. Woinowsky-Krieger. *Theory of Plates and Shells*. Engineering mechanics series. McGraw-Hill, 1959. ISBN: 978-0-07-085820-6. URL: <https://books.google.fr/books?id=rTQFAAAAMAAJ>.
- [8] W. Weaver, S.P. Timoshenko, and D.H. Young. *Vibration Problems in Engineering*. A Wiley-Interscience publication. Wiley, 1991. ISBN: 978-0-471-63228-3. URL: <https://books.google.fr/books?id=YZ7t8LgRqi0C>.
- [9] Robert Blair Green. “The general theory of antenna scattering”. PhD thesis. The Ohio State University, 1963. URL: [http://rave.ohiolink.edu/etdc/view?acc\\_num=osu1272988438](http://rave.ohiolink.edu/etdc/view?acc_num=osu1272988438).
- [10] Victor Engelhardt. “Contribution au développement d’antennes miniatures intégrant des fonctionnalités de capteurs”. PhD thesis. 2018. URL: <http://www.theses.fr/2018INPT0067/document>.
- [11] Binzhen Zhang and Dongming Fang. “Modeling and modification of the parallel plate variable MEMS capacitors considering deformation issue”. In: *Mechanism and Machine Theory* 44.4 (Apr. 2009), pp. 647–655. DOI: [10.1016/j.mechmachtheory.2008.12.006](https://doi.org/10.1016/j.mechmachtheory.2008.12.006). URL: <https://doi.org/10.1016/j.mechmachtheory.2008.12.006>.
- [12] J.D. Larson et al. “Modified Butterworth-Van Dyke circuit for FBAR resonators and automated measurement system”. In: *2000 IEEE Ultrasonics Symposium. Proceedings. An International Symposium (Cat. No.00CH37121)*. Vol. 1. 2000, 863–868 vol.1. DOI: [10.1109/ULTSYM.2000.922679](https://doi.org/10.1109/ULTSYM.2000.922679).



## Conclusion and perspectives

In this work, the development of wireless passive pressure sensors based on the combination of MEMS and miniature antennas has been presented. The work carried out in this thesis includes the bibliographical study leading to the choice of the sensor, the design and manufacture of the MEMS and antennas, and the characterization of the sensor, leading to a proof of concept for this technology of sensors. It enables the measurement on various physical quantities in harsh environments, with a great flexibility of design either on the antenna or the MEMS.

The analytical and numerical analyses presented in this work highlight the impact of each parameter of the MEMS and the antenna on the performances of the sensor, with a focus on the resolution and the sensitivity. For the MEMS, the key parameter to increase the sensitivity is the reduction of the resistive part of its impedance, while the reduction of the electrical size of the antenna reduces at the same time the sensitivity and the bandwidth.

Three different sensors were designed. The first two of them are based on the complementary of a dipole and a loop antennas, with an interrogation principle consisting of the variation of resonant frequency, with a sensitivity of 2 MHz/bar and 3 MHz/bar, and a maximal resolution of 146.56 mbar and 78 mbar at a distance of 3 meters. The last sensor is based on a PIFA miniature antenna geometry, and the reading is done by measuring the amount of power backpropagated at 868 MHz. The sensitivity is 6.7 %RCS/bar for a maximal resolution of 3.12 mbar at a distance of 3 meters. These sensors were characterized in anechoic chamber with a set-up specifically conceived for this thesis, which allows changing the pressure inside a vacuum chamber where the sensor is placed.

Considering the limitations of the developed sensor, a new method of interrogation has been presented, based on the mechanical resonance of the MEMS, which modulates the backpropagated signal. An analytical model has been presented, which allows to precisely predict the behavior of the sensor and to extract the key parameters to optimize in a co-design approach. The analysis of this model shows that this interrogation method presents several advantages, such as a better clutter isolation, or the possibility to read and identify multiple sensors with multiple MEMS on each sensor. First measurements under probes have been carried out. It allowed to characterize the dynamic properties of the MEMS, and to highlight the creation of the intermodulation frequencies in the signal generated by the MEMS under the application of a two-frequency voltage.

The work carried out in this thesis opens up many new avenues of study: for an interrogation based on the membrane deflection, it would be interesting to adapt this technology to severe environments. This implies a judicious choice of materials, whether for the antenna or the MEMS, and a study of the impact of the environment on the sensor (temperature stability, noise study, etc.). Designing a sensor for a specific application would be interesting to perform, bearing in mind the parameters to focus on for improving performance put forward in this thesis.

On the other hand, interrogation based on membrane resonance seems very promising to develop, as it overcomes many of the limitations of other interrogation methods. Some interesting advantages of this technique are a potentially higher reading range in real environments, the possibility of interrogating multiple MEMS on the same antenna or the increase of the measurement precision. Examples of lines of research include the in-depth study of the analytical model presented in this work or the interrogation of one of the sensors developed here to lead to the design

of a sensor specifically designed for resonant mode interrogation.



# List of Figures

1.1	Simplified representation of a reading procedure of a Passive Wireless Sensor using the backscattering technique. A reading antenna sends an EM signal, and the antenna-sensor will reflect a part of this power. This power will be received back by the reader and linked to the value of the physical quantity measured by the sensor.	7
1.2	LC pressure sensor proposed by Collins [6], which consists of two coils trapped between two membranes. The pressure brings the coils closer together and changes the capacitance between them.	8
1.3	LC pressure sensor proposed by Fonseca [11] for high-temperature applications. The sensor consists of two electrodes on two diaphragms, separated by a vacuum-sealed cavity, thus forming a capacitor, connected to a coil on one side of the sensor.	8
1.4	Working principle of a wireless surface acoustic wave sensor [15].	9
1.5	Time domain response of an AW wireless sensors based on a delay line [15].	9
1.6	Representation of an external sensor connected to a SAW device. The sensor impedance will change the reflection coefficient of the interdigital transducer. [15]	10
1.7	Example of radiation of a short dipole [33].	14
1.8	Equivalent circuit of a loaded antenna.	14
1.9	3D representation of a radiation pattern [33].	16
1.10	Comparison of the curves of the transfer functions of the antenna for high and low quality factors.	18
1.11	Examples of miniature antennas geometries.	19
1.12	Example of planar antenna geometries.	20
1.13	Working principle of a 1-axis MEMS accelerometer. The acceleration will move the mobile part, which will change the capacitance at the outer plates.	22
1.14	Example of etching process using photolithography depending on the photoresist polarity.	23
1.15	Operating principle of a capacitive pressure sensor. The membrane will deflect due to applied pressure. The deflection changes the value of the capacitance between the two electrodes (in pink).	24
1.16	Example of the two positioning configurations of the MEMS for the same antenna	25
2.1	Working principle of the capacitive pressure sensor: under vacuum (a), the membrane and the bottom electrode are parallel, while applying a pressure on the membrane (b), it will deflect and change the value of the capacitance.	37
2.2	Spring model of a circular membrane of surface $S$ under a pressure $P$ , modeled with a stiffness $k_m$ .	38
2.3	Example of curves used to determine MEMS dimensions sets for a radius $R = 150\mu m$ . The green area represents the zone where the thickness (in x-axis) and the gap (in y-axis) can be extracted. In this area, the triplet $(R, g_0, h)$ are considered as valid, as the deflection (red curve) is lower than the upper limit of the gap (orange line), and the stress (blue curve) is lower than the upper limit of breakage (dark blue line).	39

2.4	Simulation on Ansys Mechanical of the deflection of the membrane of the MEMS with dimensions of ( $R = 100\mu m, g_0 = 0.3\mu m, h = 3.5\mu m$ ) at 1 bar and comparison between the maximal deflection extracted from simulation and from equation 2.2.	41
2.5	Simulation on Ansys Mechanical of the constraint on the membrane of the MEMS with dimensions of ( $R = 100\mu m, g_0 = 0.3\mu m, h = 3.5\mu m$ ) at 1 bar and comparison between the maximal constraint extracted from simulation and from equation 2.4.	41
2.6	Photolithography and dopant implantation of Boron atoms at a concentration of $5 \times 10^{15}$ atoms/cm <sup>2</sup> and an energy of 240 keV on a 200mm high-resistivity (HR) silicon wafer to define the lower electrode, fixing the value of the radius $R$ . The implantation creates an area with free charges which locally increase the conductivity. It is followed by an annealing step at 1000°C for 12 hours, to activate and diffuse the doping agents in depth. The AlCu metallization is not possible for the lower electrode as few of the subsequent manufacturing stages include annealing at temperatures higher than the melting point of AlCu.	42
2.7	Photolithography and silicon dry etching to prepare for the SiO <sub>2</sub> deposition. This SiO <sub>2</sub> is used in a subsequent step to bond the membrane.	42
2.8	SiO <sub>2</sub> deposition using Plasma-Enhanced Chemical Vapor Deposition (PECVD). The etched parts of the previous steps are filled with SiO <sub>2</sub> . A Chemical Mechanical Polishing (CMP) is done in order to planarize the oxide.	43
2.9	Silicon etching to fix the values of the capacitor gap $g_0$ . The silicon is etched in the areas where there is no oxide. Two etching splits using two different masks are made on each wafer to get two different gap values.	43
2.10	Direct bonding under vacuum ( $P = 5 \times 10^{-2} mbar$ ) of a SOI wafer and thinning to create the pressure sensor highly resistive membrane layer 4μm thick. The buried oxide layer of the SOI wafer is 1μm thick and the top silicon 4μm thick. The bonded surfaces needs to be as planar as possible to have a high-quality bonding. After the bonding, the bulk is grinded in order to reduce its thickness up to 10μm. A wet etching is then performed to etch the remaining 10μm of silicon, followed a dry etching to remove the oxide 1μm thick.	43
2.11	Localized thinning of the top Si to fix the value of the membrane thickness $h$ . Two different etching steps with two different photolithography masks are done for each wafer in order to create two different values of membrane thickness.	44
2.12	Surface implant through a photoresist mask to create the upper electrode on the membrane. The implant dose is $2 \times 10^{15}$ atoms/cm <sup>2</sup> at an energy of 75 keV. The activation annealing is at 1000°C for 15 min.	44
2.13	Photolithography and Si top dry etching to access to the contact of the lower electrode. A hole is also etched at the center of the membrane of reference sensors (for them to be insensitive to pressure).	44
2.14	Deposition of AlCu for the metallization of contact pads, electrical lines and test structures. The input impedance of the transmission lines is 50Ω. A deoxidation using Hydrofluoric acid (HF) is carried out before the metal deposition in order to remove any thin layer of native oxide.	45
2.15	Variants of membrane stacks	45
2.16	Variants of the lines of the MEMS on the wafer.	46
2.17	Variants of RF test structures on the wafer.	46
2.18	Simulated structures with their corresponding $S$ matrixes and equivalent circuit. The ground planes are neglected in the representation of the MEMS itself.	47
2.19	MEMS geometry simulated on Ansys HFSS. The red rectangles are the lumped ports.	48
2.20	Simulated equivalent capacitance of the MEMS of the first set and comparison with analytical results.	49

2.21	Simulated equivalent capacitance of the MEMS of the second set and comparison with analytical results. . . . .	49
2.22	Simulated resistance of the MEMS of the first set. . . . .	50
2.23	Simulated resistance of the MEMS of the second set. . . . .	51
2.24	Characteristic impedance of a 1mm-long line . . . . .	52
2.25	EM simulation using Ansys HFSS of CPW and FGC lines with their dimensions and the electric field. . . . .	53
2.26	Transmission properties of the two types of lines . . . . .	53
2.27	FGC lines simulated to evaluate the cross-talk, with the electric field, the dimensions in red and the port number in blue. . . . .	54
2.28	Cross-talk between two lines on the same chip separated by 1000 $\mu$ m between the center of the signal lines. . . . .	54
2.29	EM simulation of two MEMS on Ansys HFSS to simulate the cross-talk, with the electric field plotted. . . . .	55
2.30	Cross-talk between two MEMS on the same chip separated by 1000 $\mu$ m between the center of the signal lines. . . . .	55
2.31	CLL antenna used for the analysis of the impact of the electrical size, with the position of the elements . . . . .	57
2.32	Sensitivity of the sensor vs antenna electrical size . . . . .	58
2.33	Representation by a simplified equivalent circuit of the antenna loaded by the MEMS. . . . .	58
2.34	Variation of antenna sensitivity with its quality factor. . . . .	59
2.35	Variation of the sensitivity $\Delta f$ with the resistive part of the impedance of the MEMS $R_S$ for two values of the quality factor. . . . .	60
2.36	Simulated wire-bonding geometry on Ansys Q3D. The lines are the shortest possible in order to extract only the inductance of the wire-bonding. . . . .	60
2.37	Variation of the inductance of a wire-bonding of 25 $\mu$ m of diameter as function of its length. . . . .	61
2.38	Geometry of the miniature antenna based on a SRR excited by a backside loop, with the positions of the load and the MEMS. . . . .	61
2.39	Variation of the resonance frequency of the SRR antenna with the MEMS as a perfect capacitance . . . . .	62
3.1	Picture of one of the wafers . . . . .	66
3.2	In-line characterization of the etching of the membrane. (a) Measurement of the topography of the MEMS using a profilometer after the etching of the membrane shown in Figure 2.13. (b) Side view of the MEMS at the corresponding step. . . .	67
3.3	In-line characterization of the bonding of the wafers. (a) SAM full-wafer view after the bonding. The light areas show where the wafer is not correctly bonded to the SiO <sub>2</sub> . (b) Side view of the MEMS at the corresponding step. . . . .	68
3.4	SEM view of one of the reference sensor centered on the hole. . . . .	68
3.5	(a) Zoomed-in view of the hole in the membrane. (b) View of the depth of the etching of the hole. The hole is not fully etched. . . . .	69
3.6	Visual defects observed on the metal after the forming gas annealing . . . . .	69
3.7	Van der Pauw structure for characterization of sheet resistance of materials. . . .	70
3.8	Mapping of the sheet resistance of AlCu over a wafer. . . . .	71
3.9	Mapping of the sheet resistance of the implant of the lower electrode over a wafer. . . . .	71
3.10	CBKR structure for the characterization of the contact resistance between a metal and a semi-conductor. . . . .	72
3.11	Intensity-Voltage (IV) curve for one contact between the metal and the lower implant. . . . .	73

3.12	Test structures to characterize the quality of etching of AlCu. (a) Test structure to characterize the over-etching and the sheet resistance. (b) Test structure to characterize isolation and continuity. . . . .	73
3.13	Comparison between the appearance of the two metals used AlCu and AlSi. (a) Cell of technological tests with AlCu. (b) Cell of technological tests with AlSi. . . . .	75
3.14	IV curves for all the contact resistances of a wafer with the correction steps. . . . .	75
3.15	Observations after etching holes using FIB to create a reference MEMS. (a) FIB image of the first etching test. It creates deposition of materials at the bottom of the hole. (b) SEM image of a hole etched using FIB next to the hole created during the microfabrication. . . . .	76
3.16	RF semi-automatic prober used for S-parameters measurement at atmospheric pressure. . . . .	77
3.17	Open (a) and short (b) geometries used for de-embedding . . . . .	77
3.18	Impact of the de-embedding on the real (a) and imaginary parts (b) of the A parameter of the ABCD matrix for the MEMS with dimensions of $R = 100\mu m$ , $h = 3.5\mu m$ and $g_0 = 0.3\mu m$ . . . . .	78
3.19	Equivalent resistance (a) and capacitance (b) of a MEMS with ( $R = 100\mu m$ , $h = 3.5\mu m$ , $g_0 = 0.3\mu m$ ). The dotted lines highlight the extracted equivalent resistance and capacitance of the MEMS at 868 MHz. . . . .	79
3.20	Mappings of resistance (a) and reactance (b) at 868 MHz of a MEMS with $R = 100\mu m$ , $h = 3.5\mu m$ and $g_0 = 0.3\mu m$ . . . . .	79
3.21	Plot of the relationship between the resistance and the reactance at 868 MHz of 4 MEMS with the same geometries over the wafer. A correlation between the value of the resistance and the reactance is observed. . . . .	80
3.22	View of the inside of the vacuum chamber of the PAV2000 prober. . . . .	81
3.23	Comparison of the measurements made by the two probers of the real (a) and imaginary part (b) of the impedance after de-embedding. . . . .	82
3.24	Resistance (a) and reactance (b) of a MEMS with $R = 100\mu m$ , $h = 3.5\mu m$ and $g_0 = 0.3\mu m$ as function of pressure. The dotted line highlights the resistance and reactance of the MEMS at 868 MHz. . . . .	82
3.25	Measurement of the profile of MEMS with a metallized membrane (a) and a non-metallized membrane (b), at different level of pressure. . . . .	83
4.1	Geometries of the antennas, where the yellow part is the copper, the green part the substrate and the blue part the position of the MEMS. The PIFA is designed to study the variation of RCS at 868 MHz and the two others ones the variation of the frequency of maximum of RCS. . . . .	89
4.2	Real (a) and imaginary parts (b) of the impedance of one of the 4 MEMS put in parallel as the load of the PIFA antenna at 1 bar. The points with the dotted lines correspond to the value of the impedance at 868 MHz. The small periodic variations in the curves are due to the prober used for the characterization of the MEMS. At 868 MHz and 1 bar, the 4 MEMS in parallel have an equivalent impedance of $137.9 - j65.57\Omega$ . . . . .	90
4.3	Electrical properties of the PIFA sensor. (a) Input impedance of the PIFA antenna at the location of the MEMS. (b) Reflection coefficient of the antenna loaded by the MEMS. . . . .	91
4.4	Electromagnetic behavior of the PIFA. (a) Realized gain of the PIFA sensor at 1 bar and 868 MHz. (b) RCS of the PIFA sensor at 1 bar. . . . .	91
4.5	Simulated RCS at 868 MHz versus pressure for the PIFA sensor. . . . .	91

4.6	Real (a) and imaginary parts (b) of the impedance of one of the 4 MEMS put in parallel as the load of the Loop antenna. The points with the dotted lines correspond to the value of the impedance at 868 MHz. The small periodic variations in the curves are due to the prober used for the characterization of the MEMS. At 868 MHz and 1 bar, the 4 MEMS in parallel have an equivalent impedance of $139.18 - j74.31\Omega$ . . . . .	92
4.7	Electrical properties of the Loop sensor. (a) Input impedance of the Loop antenna at the location of the MEMS. (b) Reflection coefficient of the antenna loaded by the MEMS. . . . .	93
4.8	Electromagnetic behavior of the Loop. (a) Realized gain of the Loop sensor (in dB) at 1 bar and 868 MHz. (b) RCS of the Loop sensor at 1 bar. . . . .	93
4.9	Real (a) and imaginary parts (b) of the impedance of one of the 2 MEMS put in parallel as the load of the Slot antenna. The points with the dotted lines correspond to the value of the impedance at 868 MHz. The small periodic variations in the curves are due to the prober used for the characterization of the MEMS. At 868 MHz and 1 bar, the 2 MEMS in parallel have an equivalent impedance of $310.37 - j146.86\Omega$ . . . . .	94
4.10	Electrical properties of the Slot sensor. (a) Input impedance of the Slot antenna at the location of the MEMS. (b) Reflection coefficient between the antenna and the MEMS. . . . .	94
4.11	Electromagnetic behavior of the Slot. (a) Realized gain of the Slot sensor at 1 bar and 868 MHz. (b) RCS of the Slot sensor at 1 bar. . . . .	95
4.12	Pictures of the sensors, where the antenna is made of copper over FR4. The MEMS are wire-bonded to the antennas. (a) PIFA sensor (b) Loop sensor (c) Slot sensor. . . . .	96
4.13	CEA-Leti anechoic chamber, for measurements up to 40 GHz, with the sensor to characterize in frequency placed on the support. . . . .	96
4.14	Time-domain (a) and frequency (b) response of the PIFA and comparison with the simulation. The colored area correspond to the window applied. . . . .	99
4.15	Time-domain (a) and frequency (b) response of the Slot and comparison with the simulation. The colored area correspond to the window applied. . . . .	99
4.16	Time-domain (a) and frequency (b) response of the Loop and comparison with the simulation. The colored area correspond to the window applied. . . . .	99
4.17	Measurement setup of the sensors in anechoic chamber. The sensor are placed inside a vacuum chamber. The pressure controller, connected to a vacuum pump, is used to change the pressure inside the vacuum chamber. The two antennas in Rx and Tx are used for the interrogation of the sensor. (a) Interior of the anechoic chamber (b) Vacuum pump and pressure controller outside the anechoic chamber. . . . .	100
4.18	RCS of the vacuum chamber. At 868 MHz, the vacuum chamber does not reflect a lot of power, as its RCS is $573.86 \text{ mm}^2$ . . . . .	101
4.19	Magnitude of the electric field at the surface of the vacuum chamber at 3 GHz. . . . .	101
4.20	Comparison of the raw RCS measurements of the Loop (a) and Slot (b) sensors at 100 mbar, 500 mbar and 1 bar. . . . .	103
4.21	Raw measurement of the Loop sensor before the time gating, at 100 mbar (a) and 1 bar (b) with the frequencies of the main peaks. . . . .	103
4.22	Raw measurement of the Slot sensor before the time gating, at 100 mbar (a) and 1 bar (b) with the frequencies of the main peaks. . . . .	103
4.23	Comparison of the raw RCS measurements of the PIFA sensor at 100 mbar, 500 mbar and 1 bar. . . . .	104

4.24	RCS of the Loop sensor extracted from the algorithm in time-domain (a) and frequency domain (b). The colored area in time-domain correspond to the window applied. The arrow indicates the reading direction for increasing pressure. 10 measurements are taken between 100 and 1000 mbar, in 100 mbar steps. . . . .	105
4.25	Variation of the frequency of maximum RCS of the Loop sensor with pressure. The points at 300 and 900 mbar are at the same frequencies at the previous ones due to the frequency resolution of the interrogation. . . . .	105
4.26	RCS of the Slot sensor with a maximum at 803MHz extracted from the algorithm in time-domain (a) and frequency domain (b). The colored area in time-domain correspond to the window applied. The arrow indicates the reading direction for increasing pressure. 10 measurements are taken between 100 and 1000 mbar, in 100 mbar steps. . . . .	106
4.27	Variation of the frequency of the maximum RCS of the Slot sensor at 800MHz with pressure. The point at 500 mbar is at the same value of frequency than 400 mbar due to the frequency resolution of the interrogation. . . . .	107
4.28	RCS of the PIFA sensor extracted from the algorithm in time-domain (a) and frequency domain (b). The colored area in time-domain correspond to the window applied. The arrow indicates the reading direction for increasing pressure. 10 measurements are taken between 100 and 1000 mbar, in 100 mbar steps. . . . .	107
4.29	Variation of the RCS of the PIFA sensor at 868 MHz (a) and at 896.75 MHz, the peak of the frequency response (b). . . . .	108
4.30	Evolution of the maximal resolution achievable in function of the distance for the PIFA sensor (a), the Loop sensor (b) and the Slot sensor (c). . . . .	110
5.1	Principle of wireless reading method using the MEMS mechanical resonance by intermodulation. . . . .	116
5.2	Block diagram of the interrogation of resonant MEMS using intermodulation. Two signals at $f_0$ and $f_0 + f_\Delta$ with $f_\Delta \ll f_0$ are sent to the sensor. Due to the non-linear aspect of the electrostatic force, the MEMS is put in mechanical resonance at $f_\Delta$ . This resonance modulates the backpropagated signal by adding peaks in the spectrum received back by the reader. Only the two first intermodulation peaks are considered here. . . . .	117
5.3	Block diagram of the interrogation of resonant MEMS using intermodulation, with the current step of the calculation highlighted. This section focuses on determining the voltage across the MEMS based on the incident electric field. . . . .	118
5.4	General equivalent circuit of a receiving antenna loaded by a MEMS. . . . .	118
5.5	Block diagram of the interrogation of resonant MEMS using intermodulation, with the current step of the calculation highlighted. This section focuses on determining an expression for the pressure-dependent mechanical resonance frequency of the membrane, and establishing the equation of motion of the membrane under the application of a pressure and an electrostatic force. . . . .	120
5.6	Representation of a circular parallel plate capacitor with a membrane and a fixed electrode under a voltage $V$ and a uniform pressure $P$ . . . . .	121
5.7	Block diagram of the interrogation of resonant MEMS using intermodulation, with the current step of the calculation highlighted. This section focuses on determining the expression of the capacitance variation and the impedance mismatch between the MEMS and the antenna. . . . .	124
5.8	Block diagram of the interrogation of resonant MEMS using intermodulation, with the current step of the calculation highlighted. This section focuses on determining the expression of the RCS of the antenna based on the reflection coefficient. Then, the expression of the electric signal received can be expressed. . . . .	125

5.9	Equivalent circuit of an sensor used for the simplified model. The parallel RLC representation is used to represent the input impedance of the antenna around the antiresonance. . . . .	128
5.10	Simplified block diagram of the interrogation of resonant MEMS using intermodulation. The feedback loop is no longer present due to the approximation of constant voltage. . . . .	128
5.11	Example of the evolution of the amplitude of the modulation of the RCS with frequency, when two MEMS are placed on an antenna. In order to differentiate them, the two have different mechanical resonance frequency variation ranges. . .	131
5.12	Variation of the capacitance of the MEMS with dimensions of ( $R = 150\mu m, t = 4\mu m, g_0 = 1\mu m$ ) with pressure, obtained by simulations on Ansys HFSS. The curve is obtain by a polynomial fitting of order 5. . . . .	133
5.13	CLL antenna used for the application of the intermodulation model. . . . .	133
5.14	Input impedance (a) and evolution of the RCS with the pressure (b) for the CLL antenna used in this analysis. . . . .	133
5.15	Comparison between simulation and analytical formula for the open-circuit voltage (a) and the voltage at the MEMS terminals (b). . . . .	134
5.16	Example of voltage (a) and displacement of the center of the membrane (b) in time-domain and steady state, calculated using the complete model. Using the linearized model, the calculated voltage is $V_S = 1.1226V$ , and the calculated displacement of the center of the membrane is $\Delta x(t) = 18.839 \times 10^{-9} \sin \omega_m t$ (in meters). . . . .	135
5.17	Example of FFT of sent and received signal under the conditions presented in section 5.6.1 calculated with the complete model. . . . .	136
5.18	Variation of the mean value of the RCS $\sigma_{mean}$ and the variation of RCS $\Delta\sigma$ with the interrogation frequency $f_e$ . . . . .	136
5.19	Illustration of the impact of the resonance of the MEMS on the RCS while interrogated at a frequency different than the maximum of RCS. The vibration of the membrane periodically shift the frequency response of the antenna, which periodically changes the value of the RCS at the interrogation frequency. . . . .	137
5.20	Example of variation of resonance frequency of a MEMS with pressure. (a) Imaginary part of the MEMS impedance with pressure, the resonance occurs when the curve decreases. (b) Variation of resonance frequency with pressure, the theoretical curve was calculated using Eq (5.17). . . . .	138
5.21	View of the PCB inside the vacuum chamber (a) and the measurement setup (b) including a Keysight E5061B ENA Vector Analyzer and a vacuum pump. . . . .	138
5.22	Modulus (a) and argument (b) of the non-metallized MEMS impedance under vacuum with electrostatic actuation. The ENA was calibrated using an Open-Short-Thru-Load calibration. The measured quality factor under vacuum, extracted thanks to a MBVD fitting, is 271. . . . .	139
5.23	Modulus (a) and argument (b) of the metallized MEMS impedance under vacuum with electrostatic actuation. The ENA was calibrated using an Open-Short-Thru-Load calibration. The measured quality factor under vacuum, extracted thanks to a MBVD fitting, is 184. . . . .	139
5.24	Setup of measurement of the peaks of intermodulation of the MEMS. The MEMS is placed on a PCB inside a vacuum chamber. The two sent signals were generated using a lock-in amplifier. A bias-tee is used at the output of the MEMS to separate the DC and the AC signals of the voltage, which is then converted into current thanks to a transimpedance amplifier. . . . .	140
5.25	Modulus (a) and argument (b) of the received voltage by the lock-in amplifier at one intermodulation frequency versus the frequency $f_\Delta$ . . . . .	141

---

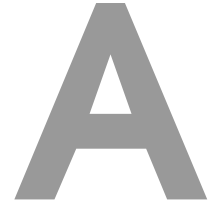
5.26	Measurement diagram for resonant sensors in anechoic chamber using intermodulation. The high-frequency signal at $f_e$ is generated by a RF source, while the low-frequency signal at $f_\Delta/2$ is generated by the lock-in amplifier. The signal received back by the Rx antenna contains the four peaks in its spectrum. It is converted to baseband by multiplying it again by $f_m$ . It is sent to the lock-in amplifier, where the reference is set to $1.5f_m$ to extract the amplitude of the intermodulation peak. . . . .	141
------	--	-----



## List of Tables

1.1	Summary table of advantages and disadvantages of LC sensors. . . . .	8
1.2	Summary table of advantages and disadvantages of AW wireless sensors. . . . .	11
1.3	Summary of advantages and disadvantages of wireless sensors based on electro-magnetic transduction. . . . .	12
1.4	Examples of RCS values in the X-band [34]. . . . .	18
1.5	Comparison of dry and wet etching. . . . .	24
2.1	Table of the dimensions triplet chosen for the MEMS . . . . .	40
4.1	Summary of the properties of the sensors. . . . .	95





## Appendix 1 : Python codes

---

*This appendix presents the Python algorithm used for the signal processing of the measurement of the sensors in anechoic chamber.*

---

## A.1 Time-gating algorithm for the frequency response

```

1 from scipy import io
2 import numpy as np
3
4 # Measurement import
5 S21 = io.loadmat('Sensor_measurement.mat')
6 H_meas = S21['data'][0][0][8][0]
7 H_cc_w = ((H_meas-H_cal))*(((4*pi)**(3/2))*(R1)*(R2)/((G)*(1/lbd))) #
   conversion into square root of RCS
8
9
10 # Zero padding
11 H_cc_p = np.concatenate((np.zeros(Nzero_moins), H_cc_w)) # Adding some
   zeros before
12 H_cc_p = np.concatenate((H_cc_p, np.zeros(Nzero_plus))) # Then after
13 Freq_w = df*np.array(range(0,len(H_cc_p))) # Array of the frequencies (
   only positives)
14 H_cc_p = np.concatenate((H_cc_p, np.flip(np.abs(H_cc_p[1:])*exp(-1j*np.
   angle(H_cc_p[1:]))) # Hermitian symmetry
15 Freq_p = np.fft.fftfreq(len(H_cc_p), 1/(len(H_cc_p)*df)) # Array of the
   frequencies (negatives and positive)
16
17
18 # Converting into time domain
19 h_cc = np.fft.ifft(H_cc_p)
20 dt = 1/(len(h_cc)*df)
21
22 # Time-gating
23 w_t = window(len(h_cc[Nmin:Nmax]))
24 h_cc_w = np.multiply(h_cc[Nmin:Nmax], w_t)
25 h_cc_z = np.concatenate((np.zeros(Nmin), h_cc_w))
26 h_cc_z = np.concatenate((h_cc_z, np.zeros(len(h_cc)-Nmax)))
27
28 # Converting into frequency domain
29 H_cc = np.fft.fft(h_cc_z)

```

## A.2 Time-gating algorithm for the pressure response

```

1 from scipy import io
2 import numpy as np
3 from scipy.stats import linregress
4
5 def RCS_optimize(N):
6     sigma_p = []
7     Nmin = int(N[0])
8     Nmax = int(N[1])
9     fres = [] # resonance frequencies
10    for p in press:
11        # Measurement import
12        S21 = io.loadmat('Sensor_measurement.mat')
13        H_meas = S21['data'][0][0][8][0]
14        H_cc_w = ((H_meas-H_cal))*(((4*pi)**(3/2))*(R1)*(R2)/((G)*(1/lbd))
   )) # conversion into square root of RCS
15
16

```

```

17     # Zero padding
18     H_cc_p = np.concatenate((np.zeros(Nzero_moins), H_cc_w)) # Adding
some zeros before
19     H_cc_p = np.concatenate((H_cc_p, np.zeros(Nzero_plus))) # Then
after
20     Freq_w = df*np.array(range(0,len(H_cc_p))) # Array of the
frequencies (only positives)
21     H_cc_p = np.concatenate((H_cc_p, np.flip(np.abs(H_cc_p[1:])*exp(-1j
*np.angle(H_cc_p[1:]))) # Hermitian symmetry
22     Freq_p = np.fft.fftfreq(len(H_cc_p), 1/(len(H_cc_p)*df)) # Array
of the frequencies (negatives and positive)
23
24
25     # Converting into time domain
26     h_cc = np.fft.ifft(H_cc_p)
27     dt = 1/(len(h_cc)*df)
28
29     # Time-gating
30     w_t = window(len(h_cc[Nmin:Nmax]))
31     h_cc_w = np.multiply(h_cc[Nmin:Nmax], w_t)
32     h_cc_z = np.concatenate((np.zeros(Nmin), h_cc_w))
33     h_cc_z = np.concatenate((h_cc_z, np.zeros(len(h_cc)-Nmax)))
34
35     # Converting into frequency domain
36     H_cc = np.fft.fft(h_cc_z)
37
38     sigma_p.append(H_cc)
39     fres.append(Freq_p[np.argmax(abs(H_cc)**2)])
40
41     linreg = linregress([int(px) for px in press],fres)
42     return(1-linreg.rvalue**2)

```



# "Capteurs télé-alimentés et interrogeables à distance"

---

## Résumé

Les capteurs sans-fil passifs sont des dispositifs capables de détecter et de transmettre des informations sans nécessiter de source d'énergie locale, en s'appuyant généralement sur des sources d'énergie externes telles que les ondes radiofréquences pour fonctionner et communiquer. La combinaison d'un capteur MEMS et d'une antenne miniature offre la possibilité d'un capteur à haute sensibilité, qui peut être interrogé à des distances de plusieurs mètres, avec une grande flexibilité de conception, et qui peut être conçu pour fonctionner en environnements sévères. Cette thèse présente la co-conception et la caractérisation d'un capteur de pression capacitif MEMS et d'antennes planaires, conçus pour fonctionner à 868 MHz. La procédure de lecture est basée soit sur la variation de la fréquence de résonance, soit sur la variation de la puissance rétro-propagée à une seule fréquence. Le modèle analytique d'une nouvelle méthode d'interrogation, basée sur la mise en résonance mécanique des MEMS, est présenté. Cette technique offre plusieurs avantages, tels que l'augmentation de la distance de lecture et de la précision de la mesure.

**Mots-clés :** Capteurs, MEMS, Radiofréquences, Antenne, Pression

---

## Abstract

Passive wireless sensors are devices that can detect and transmit information without requiring a local power source, typically relying on external energy sources such as radiofrequency waves to operate and communicate data. The combination of a MEMS sensor and a miniature antenna offers the possibility of a high-sensitivity sensor, which can be interrogated at distances of several meters, with a great design flexibility, and which can be designed to operate in harsh environments. This thesis presents the co-design and the characterization of a MEMS capacitive pressure sensor and planar antennas, designed to work at 868 MHz. The reading procedure is based on either the variation of resonance frequency or the variation of the power backpropagated at a single frequency. The analytical model of a new method of interrogation is presented, based on the mechanical resonance of the MEMS. This technique offers several advantages, such as an increasing of the reading distance and of the precision of the measurement.

**Keywords :** Sensor, MEMS, Radiofrequencies, Antenna, Pressure

